University of Alberta

Quantitative Microstructural Characterization of Microalloyed Steels

by

Junfang Lu

A thesis submitted to the Faculty of Graduate Studies and Research
in partial fulfillment of the requirements for the degree of

Doctor of Philosophy

in

Materials Engineering
Department of Chemical and Materials Engineering

Fall 2009
Edmonton, Alberta

Examining Committee

Hani Henein, Professor, Chemical & Materials Engineering - Co-supervisor

Douglas Ivey, Professor, Chemical & Materials Engineering - Co-supervisor

Jingli Luo, Professor, Chemical & Materials Engineering - Committee

Hao Zhang, Assistant Professor, Chemical & Materials Engineering - Committee

Gilbert Grondin, Professor, Civil and Environmental Engineering - Committee

Warren Garrison, Professor, Materials Science and Engineering, Carnegie Mellon University - External examiner

Abstract

Microalloyed steels are widely used in oil and gas pipelines. They are a class of high strength, low carbon steels containing small additions (in amounts less than 0.1 wt%) of Nb, Ti and/or V. The steels may contain other alloying elements, such as Mo, in amounts exceeding 0.1wt%. Microalloyed steels have good strength, good toughness and excellent weldability, which are attributed in part to the presence of precipitates, especially nano-precipitates with sizes less than 10nm.

Nano-precipitates have an important strengthening contribution, i.e. precipitation strengthening. In order to fully understand steel strengthening mechanisms, it is necessary to determine the precipitation strengthening contribution. Because of the fine sizes and low volume fraction, conventional microscopic methods are not satisfactory for quantifying the nano-precipitates. Matrix dissolution is a promising alternative to extract the precipitates for quantification. Relatively large volumes of material can be analyzed, so that statistically significant quantities of precipitates of different sizes are collected. In this thesis, the microstructure features of a series of microalloyed steels are characterized using optical microscopy (OM) and scanning electron microscopy (SEM). Matrix dissolution techniques have been developed to extract the precipitates from the above microalloyed steels. Transmission electron microscopy (TEM) and x-ray diffraction (XRD) are combined to analyze the chemical speciation of these precipitates. Rietveld refinement of the XRD pattern is used to fully quantify the relative amounts of the precipitates. The size

distribution of the nano-precipitates (mostly ≤10 nm) is quantified using dark field imaging (DF) in the TEM. The effects of steel chemistry and processing parameters on grain microstructure and the amount of nano-precipitates are discussed. Individual strengthening contributions due to grain size effect, solid solution strengthening and precipitation strengthening are quantified to fully understand the strengthening mechanisms of the steels.

Acknowledgements

This thesis and my whole PhD experience could not have been possible without the help and support of many people. It is a great pleasure to express my gratitude to all of them.

I would like to express my sincerest gratitude and appreciation to my supervisors, Professor H. Henein and Professor D.G. Ivey, for their continuous guidance and support for my research and study. They have provided me with a great deal of inspiration throughout the research. Working with them has been a great learning experience and I am impressed by their scientific knowledge, insight, energy and passion. Thanks also goes out to the Natural Sciences and Engineering Research Council (NSERC) of Canada and EVRAZ Inc. NA (previously IPSCO Inc.) for their financial support of this project.

I would also like to express my thanks to Dr. O. Omotoso and Dr. J. B. Wiskel for their invaluable help on a variety of technical aspects of my work. Many thanks also go to Dr. J. Chen and Dr. A. Prasad for ideas and motivation. Their guidance and encouragement has helped me overcome hardship during this work.

I would like to extend my appreciation to my colleagues who have provided a great research environment. To Xiujun Li, Hua Deng, Tonya Wolfe, Joel Pepin, Arash Ilbagi, Weifeng Wei, Nasseh Khodaie and other group members, thank you for your help and invaluable friendship.

My deepest gratitude must be given to my family: my parents, my parents-in law, my husband (Yang Cui) and my two lovely boys (Wentao and Allan). Thank you for your love, patience, sacrifice and encouragement. Without them, none of this could have been possible. You have always been a source of strength and encouragement in my life.

Table of Contents

List of Tables

List of Figures

List of Symbols and Abbreviations

A	Constant in solubility product expression
a_0	Lattice parameter for NbC, m
A_A	Atomic weight of element A, amu
A_B	Atomic weight of element B, amu
A_C	Atomic weight of carbon, amu
A_D	Atomic weight of element D, amu
AF	Acicular ferrite
A_{Fe}	Atomic weight of Fe, amu
a_{Fe}:	Lattice parameter of Fe matrix, nm
$a_{[M]}$	The activity of the dissolved microalloying element M
A_{Mo}	Atomic weight of Mo, amu
$a_{(MX)}$	The activity of the constituent phase MX
A_{Nb}	Atomic weight of Nb, amu
A_{NbC}	Atomic weight of NbC, amu
a_p:	Lattice parameter of nano-precipitates, nm
APFIM	Atom Probe Field-Ion Microscopy
API	American Petroleum Institute
A_{ppt}	Molecular weight of the precipitate, amu
Ar_1	A_1 temperature upon cooling, ºC
Ar_3	A_3 temperature upon cooling, ºC
$at\%_{Mo}$	Atomic fraction of Mo in the nano-precipitate (≤10 nm)
$a_{[X]}$	The activity of the dissolved interstitial element X
A'	Absorption factor
b	Magnitude of Burgers vector of a dislocation in ferrite, 2.5×10^{-10} m
B	Bainite
BF	Bainitic ferrite

B'	Temperature factor
BCC	Body-centered cubic
C	Constant in solubility product expression
C_A	Wt% of element A
C_B	Wt% of element B
CCT	Continuous cooling transformation
C_D	Wt% of element D
CE	Counter electrode (Pt)
C.E.	Carbon equivalent using the IIW equation
$[C]_e$	Wt% of C dissolved in the ferrite under equilibrium condition
C_i	Concentration of solute i, wt%
CR	Cooling rate, ºC/s
CSA	Canadian Standards Association
CT	Coiling temperature, ºC
C_T	Wt% of C in the alloy
$[Cu]_e$	Wt% of Cu dissolved in the ferrite under equilibrium condition
CVN	Charpy V-notch
d	Grain diameter, μm
D	Diffusion coefficient for Nb in ferrite at certain temperature, m^2/s
DBTT	Ductile to brittle transition temperature, ºC
d_{hkl}	The interplanar distance with h, k, l Miller indices
dN/dt	The nucleation rate of NbC in ferrite, number/(m^3.s)
DS	Divergent slit
$D_0(\alpha)$	Temperature-independent preexponential for Nb diffusion in ferrite, m^2/s
EDX	Energy dispersive X-ray (spectroscopy)
EELS	Electron Energy Loss Spectroscopy
EUL	Extension under load

f	Alloy multiplying factor for calculating hardenability
F	Repelling force of a particle
F_1	Line tension of a dislocation
FATT	Fracture appearance transition temperature, ºC
FCC	Face-centered cubic
F_{hkl}	Structure factor of reflection from the (hkl) plane
f_j	Structure factor for atom j
FRT	Finish rolling temperature, ºC
f_v	Volume fraction of nano-precipitates
FWHM	Full width at half maximum
f_ρ	Dislocation density factor
G	Shear modulus of the steel, 80.3 GPa
GF	Grain boundary ferrite
G_{psf}	Gaussian profile shape function
ICP	Inductively-coupled plasma
ICT	Interrupted cooling temperature, ºC
IF	Interstitial free
I_i	X-ray intensity of element i
I_k (cal)	Calculated integrated intensity of the kth Bragg reflection
I_k (obs)	Observed integrated intensity of the kth Bragg reflection
ITT	Impact-transition temperature
I_0	Peak intensity in profile shape functions
K	Work hardening coefficient, MPa
K'	Constant in the Scherrer Equation
k_{AB}	Cliff-Lorimer factor
k_i	Strengthening coefficient for solute i, MPa
K_s	Solubility product
k_y	Strengthening coefficient when grain size is used, MPa.mm$^{1/2}$

k_y'	Strengthening coefficient when mean linear intercept is used, MPa.mm$^{1/2}$
L	Effective particle spacing
L_k	Groups of Lorentz, polarization and multiplicity for reflection k
L_{psf}	Lorentzian profile shape function
L_{vol}	Volume weighted crystallite size (volume weighted mean column heights)
m	Shape parameter in PearsonVII profile shape function
M	Mass of the formula unit
[M]	Wt% of microalloying element M dissolved in the matrix
M/A	martensite/retained austenite
m.l.i.	Mean linear intercept, µm
[Mn]	Wt% of Mn dissolved in the matrix
M'	Taylor factor
Ms	Martensite-start temperature
MX	Binary precipitate compound
n	The order of the reflection
n'	Work hardening index
N	Number of precipitates per unit volume, m^{-3}
$N_{0\text{-}het}$	Number of sites per unit volume for heterogeneous nucleation, m^{-3}
$N_{0\text{-}hom}$	Number of sites per unit volume for homogeneous nucleation, m^{-3}
$N_{A:}$	Avogadro's number (6.023×10^{23} atoms/mol)
N/A	Not applicable
(NbC)	Wt% of NbC separated from the ferrite
$[Nb]_e$	Wt% of Nb dissolved the ferrite under equilibrium condition
Nb_{NbC}	Wt% of Nb present as NbC

Nb_T	Wt% of Nb in the alloy
N_j	Site occupancy (presence of vacancies)
N_v	Number per unit volume, m^{-3}
OM	Optical microscopy
P	Pearlite
P_{cm}	Carbon equivalent using the Ito-Bessyo equation
PF	Polygonal ferrite
P_k	Preferred orientation function for reflection k
P_{pfs}	Pearson VII profile shape function
PV_{psf}	Pseudo-Voigt profile shape function
q	Exponent in the strength superposition equation
Q	Heat of dissolution, $kJ.mol^{-1}$
QPF	Quasi-polygonal ferrite
$Q(\alpha)$	Activation energy for Nb diffusion in ferrite, J/mol.K
r	Radius of spherical precipitate embryo, nm
R_B	The R-Bragg index
R_c	Critical nucleation radius, nm
R_d	Radius of the curvature that the dislocation bows into an arc
R_g	Universal gas constant, 8.314 J/mol.K
RS	Receiving slit
RT	Reheating temperature, ^oC
R_{wp}	The R-weighted pattern index
$[S]$	Wt% of S dissolved in the matrix
SANS	Small angle neutron scattering
SCE	Saturated calomel electrode
ScS	Scatter slit
SEM	Scanning electron microscopy
SF	Scale factor
SL	Soller slit
SMYS	Specified minimum yield strength, MPa

STDEV	Standard deviation
S_v	Total interfacial area of near planar crystalline defects per unit volume, m^{-1}
T	Isothermal temperature, Kelvin
$T_{d\text{-}b}$	Ductile-to brittle transition temperature
TEL	Total elongation, %
TEM	Transmission electron microscopy
T_i	Atomic fraction of element i
TMCP	Thermo-mechanical controlled processing
T_{nr}	No-recrystalization temperature, ºC
$T_{5\%}$	Temperature for 5% recrystallization, ºC
$T_{95\%}$	Temperature for 95% recrystallization, ºC
UEL	Uniform elongation, %
UTS	Ultimate tensile strength, MPa
V	Volume of the unit cell, m^3
V_m	Molar volume of the species to precipitate, 1.34E-05 m^3/mol
Vol_{ppt}	Volume fraction of nano-precipitates, %
$Vol_{single:}$	Volume of a single nano-precipitate, nm^3
w_a	Relative weight fraction of phase a in a mixture of j phases
WE	Working electrode
w_i	Weighting factor for each observation point
wt_{Mo}	Total amount (weight) of Mo available for precipitation
wt_{ppt}	*A*mount (weight) of nano-precipitate (≤10 nm)
$wt\%_{ppt}$	Wt% of the nano-precipitates (≤10 nm)
X	Size of precipitate, µm
[X]	Wt% of an interstitial X dissolved in the matrix
X_C	Instantaneous concentration of C in mol fraction

X_C^e	Equilibrium concentration of C in mol fraction in the specified temperature
x_j	Coordinate in x-direction for atom j
X_{Nb}	Instantaneous concentration of Nb in mol fraction
X_{Nb}^e	Equilibrium concentration of Nb in mol fraction
XRD	X-ray diffraction
y_{bi}	Background intensity at position $2\theta_i$
$y_i(calc)$	Calculated intensities at each step
$y_i(obs)$	Observed intensities at each step
y_j	Coordinate in y-direction for atom j
YS	Yield strength (experimental), MPa
Z	Number of formula units per unit cell
ZA	Zone axis
z_j	Coordinate in z-direction for atom j
Z'	The Zeldovich factor
α-Fe	Ferrite
β	Integral breadth of a reflection located at 2θ
β'	Atomic impingement rate, s^{-1}
γ:	Surface energy of precipitate per unit area, 0.5 J/m^2
γ-Fe	Austenite
ΔG	Nucleation energy, J
$\Delta G_{dislocation}$	Dislocation core energy over the precipitate radius, which is used for precipitate nucleation, J
ΔG_{volume}	Volume energy term in nucleation energy, J
$\Delta G_{surface}$	Surface energy term in nucleation energy, J
ΔG_{strain}	Misfit strain energy term in nucleation energy, J
ΔG_ε	Misfit strain energy per unit volume of the phase formed, J/m^3
ΔG_v	Chemical driving force for nucleation, J/m^3
ΔG^*	Critical free energy for nucleation, J
δ	Zone misfit due to lattice parameter differences

ε	True plastic strain
η	Adjustable parameter for diffraction profile shape functions
θ	X-ray beam incident angle (the Bragg angle)
θ'	Half angle correspond to the arc of a dislocation
λ	X-ray wavelength, nm
ρ	Dislocation density, m^{-2}
ρ_{Fe}	Density of Fe, g/cm^3
ρ_{ppt}	Density of nano-precipitates, g/cm^3
σ_0	Peierls-Nabarro stress (intrinsic strength of ferrite lattice), MPa
σ_{dis}	Dislocation strengthening, MPa
σ_{fl}	Flow strength, MPa
σ_{gb}	Grain boundary strengthening, MPa
σ_i	Lattice friction stress of iron, MPa
σ_{ppt}	Precipitation strengthening, MPa
σ_{ss}	Solid solution strengthening, MPa
σ_{ys}	Yield strength, MPa
σ_{UT}	Ultimate tensile strength, MPa
τ	Shear stress, MPa
τ'	Precipitation incubation time, s
ϕ	Difference between a calculated profile $y(calc)$ and observed data $y(obs)$
$2\theta_0$	Peak position in profile shape functions
φ	Reflection profile function from $2\theta_i$ to $2\theta_k$
ω	Half of the full width at half maximum

Chapter 1: Introduction

1-1. Statement of the problem

During the past ten years, much steel research has focused on developing high strength steels for pipelines transporting oil and natural gas. The main driving force of these studies is to improve the transportation efficiency and to reduce the material and operation costs for large diameter pipes under high pressures. In order to improve the transportation efficiency and to reduce the material and operation costs, steels with higher strength, better low temperature toughness and field weldability are required.

Microalloyed pipeline steels have high strength, good toughness and excellent weldability and have been widely used in oil and gas pipelines. They are a class of high strength, low carbon steels containing small additions (in amounts less than 0.1 wt%) of Nb, Ti and/or V. The steels may contain other alloying elements, such as Mo, in amounts exceeding 0.1wt%. Thermo-mechanical controlled processing (TMCP) is used in the production of microalloyed pipeline steels.

Traditional strengthening mechanisms for high-strength microalloyed pipeline steels include grain refinement, solid solution strengthening and precipitation strengthening. Processing parameters associated with TMCP affect ferrite grain size and the precipitation behavior. Steel chemistry affects the precipitation behavior as well. A clear understanding of the effect of processing parameters and steel chemistry on steel microstructure and precipitation behavior is needed to understand the strengthening mechanisms and, therefore, to establish guidelines for the production of higher-strength microalloyed pipeline steels.

However, there are a few challenges associated with this study. First, precipitates have very low volume fractions in microalloyed steels. Second, the precipitates may also have a wide particle size distribution with sizes ranging from several microns down to less than 5 nm depending on steels. Third, the chemical composition of the precipitates varies because of the different precipitation sequences and formation temperatures. Finally, although the precipitates have size differences and chemical composition variations, they all

have the same NaCl-type FCC crystal structure, with similar lattice parameters, making it quite difficult to differentiate different phases. Therefore, conventional microscopic methods are not fully satisfactory for quantifying these precipitates due to the small volume of material being analyzed. Reliable quantitative techniques are required to be developed to achieve this goal, from which relatively large volumes of material can be analyzed and statistically significant quantities of precipitates of different sizes are characterized.

1-2. Objectives and methodology

Because of the above issues, the present study was undertaken with the following objectives:

1) To characterize the microstructural features of a series of microalloyed steels.
2) To characterize and quantify precipitates as a function of processing histories.
3) To understand the strengthening mechanisms and the contribution of each component to strengthening.

In order to achieve the above objectives, the following methods were used:

1) Microstructure examination of the base metal. This was carried out using optical microscopy (OM) and scanning electron microscopy (SEM) of the base metal for phase identification and grain size measurement of the microalloyed steels.
2) Precipitate extraction by matrix dissolution techniques. Matrix dissolution techniques were explored to extract significant quantities of precipitates of different sizes, making it possible to quantitatively determine the amount of precipitates.
3) Analysis of the overall precipitate chemistry. The overall chemistry of the extracted precipitates was analyzed by energy dispersive x-ray (EDX) microanalysis in the SEM.
4) Precipitate phase identification. Precipitate phases were identified using x-ray diffraction (XRD) of the extracted precipitates.

5) Mass balance determination. Inductively-coupled plasma spectroscopy (ICP) was used to analyze the concentration of the elements in solid solution. By comparing the steel chemistry with the ICP results, the amount of microalloying elements in the precipitates was determined.
6) Precipitate characterization in terms of size and chemistry. In order to supply the required information for precipitation quantification using Rietveld refinement, precipitates were characterized in terms of size and chemistry. This was carried out using SEM and transmission electron microscopy (TEM) imaging and EDX microanalysis via carbon replicas and matrix dissolution. The size distribution of the nano-precipitates (primarily ≤10 nm in size) was quantified using dark field imaging (DF) in the TEM via carbon replicas. Precipitate distribution and the orientation relationship with the base metal were studied as well. These were carried out using TEM of thin foil samples.
7) Precipitate quantification. Precipitate quantification was achieved via Rietveld refinement of the XRD patterns based on the classification of precipitates according to size and chemistry. The Rietveld refinement method refines precipitate structures and gives their relative abundance, leading to volume fraction determination of precipitates in the steel.
8) Strengthening contribution determination. Individual strengthening contributions were determined providing better understanding of the strengthening mechanisms.

Each of the above components of the research is presented in detail in the following chapters of this thesis.

1-3. Outline of the thesis

Chapter 2 covers a review of general information associated with high-strength microalloyed steels. Chapter 3 presents the experimental procedures that were used to achieve the objectives of the study. Chapter 4 presents the results for Grade100 steel in terms of the microstructure, grain size and precipitate characterization. Similar results are presented in Chapter 5 for API X70, X80

steels and in Chapter 6 for X100 steels. Chapter 7 discusses the effect of steel chemistry and processing histories on the grain microstructure. The volume fraction of nano-precipitates was determined for the above steels. The effects of microalloying content, finish rolling temperature and coiling temperature on the amount of nano-precipitates are discussed. Based on classical nucleation theory, critical free energy for nucleation was calculated for the Fe-Nb-C system under isothermal conditions. Individual strengthening contributions are quantified as well for the above steels. Finally, conclusions are made in Chapter 8 along with recommendations for future work.

Chapter 2: Literature review

2-1. Introduction

It is known that there are large reserves of crude oil and natural gas in the Arctic region. However, most refineries are located in West Europe and North America where most petroleum products are consumed. Therefore it is necessary to transport crude oil and natural gas from the drilling fields to the places where they are consumed. Pipelines have done a great job in transporting crude oil and natural gas over long distances in the past and will also be widely used in the future. Therefore, research on pipeline steels is on going.

In order to understand the current problems in the steel making industry and to develop steels with higher strength, better toughness and weldability, a literature review is presented in this thesis. In this chapter, six sections will be discussed. First, steel designation, developments of pipeline steels and high-strength low alloy steels will be presented in Section 2-1. Next, thermo-mechanical controlled processing and sequential precipitation will be presented in Section 2-2. Strengthening mechanisms in microalloyed steels and a review of precipitate characterization techniques will be presented in Section 2-3 and 2-4, respectively. Matrix dissolution and precipitate collection will be introduced in Section 2-5. X-ray diffraction and Rietveld refinement will be presented in Section 2-6 as a means of obtaining quantitative characterization of precipitates. Lastly, a summary and the research significance will be presented in Section 2-7.

2-1-1. Steel designation

API (American Petroleum Institute) is a very common designation for pipeline steels used in North America. API X70 and X80 pipeline steels have been widely used in the pipeline industry to transport crude oil and natural gas. API X100 is still under development for commercial production. The number (70, 80 and 100) is the specified minimum yield strength (SMYS) in ksi. API X70, X80 and X100 are simplified as X70, X80 and X100 in this thesis.

CSA (Canadian Standards Association) is another designation method. Grade80 and Grade100 are plate steels that have been widely used in the construction industry. The number (80 and 100) is the specified minimum yield strength (SMYS) in ksi.

2-1-2. Development of pipeline steels

Significant accomplishments have been made over the last fifty years with respect to pipeline steels, especially during the past ten years. Many research projects have been carried out focusing on developing high strength steels. The main driving force of the studies is to improve transport efficiency of oil and natural gas under high pressure and to reduce operation costs. In order to reduce the amount of material and operation costs, i.e. use thinner wall thicknesses, steels with high strength are required. These steels should also have good low temperature toughness and field weldability. It is known that steel toughness decreases with decreasing temperature due to its BCC structure. Therefore, good low temperature toughness is required for stable operation and maintenance of pipeline steels and it is especially important for those steels used under extremely low-temperature conditions.

Due to successful studies over the years, steel strength has doubled from the small diameter pipelines of the 1960s (API X60 grades) to the large diameter pipelines of API X80-X120 grades, while improving toughness and weldability. Figure 2-1 [1] shows the evolution of pipeline technology in the last fifty years along with the recent or near future development of API X120. Figure 2-2 shows the microstructure evolution and mechanical properties of steel for large diameter pipelines. [2,3] The astonishing advancements are mainly due to the combination of microalloying, low carbon contents and thermo-mechanical controlled processing (TMCP). [2]

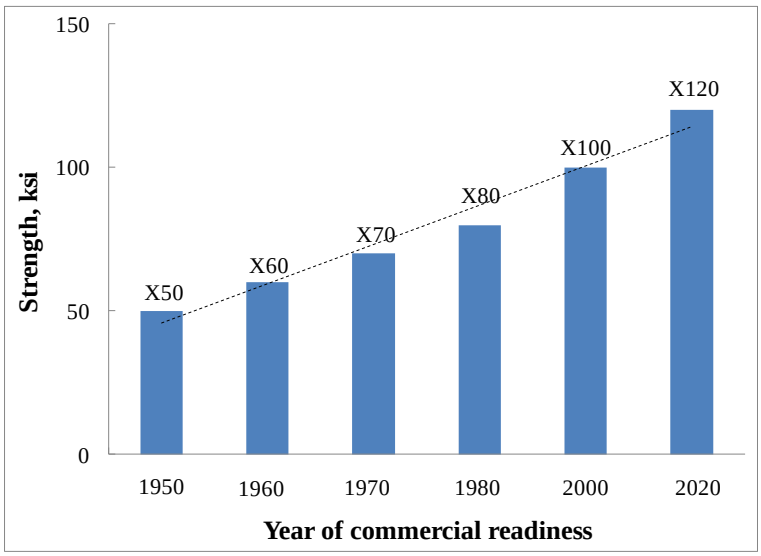

Figure 2-1 Evolution of pipeline technology. [1]

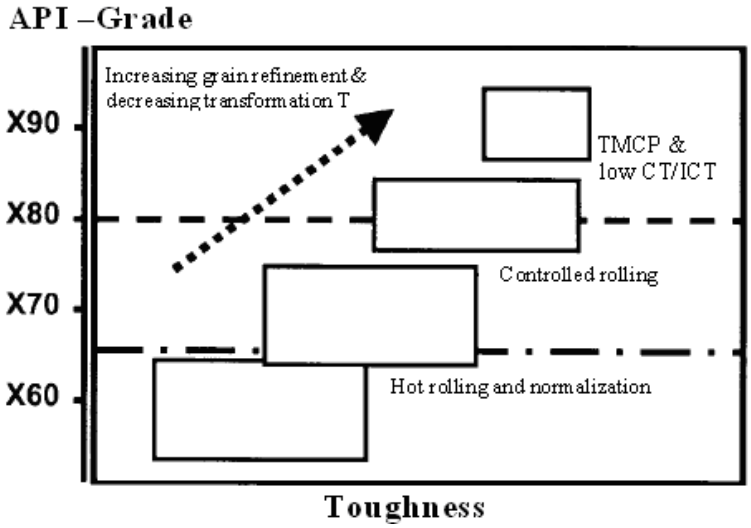

Figure 2-2 Evolution of plate steel for pipelines: microstructure and mechanical properties. [2,3]

In the mid-1960s, X60-65 grade steels were the best steels used in the pipeline industry. The approximate composition includes 0.1wt%C, 1wt%Mn, 0.3wt%Si and 0.03wt%Nb, with a transformation temperature of about 650-700ºC. These steels were mainly ingot cast and treated by either hot rolling or hot rolling followed by normalization. They had high carbon contents with coarse-grained polygonal ferrite (about 10-15 μm) and high amounts of pearlite. These steels had fairly low toughness, low ductility, high impact transition temperature and poor

weldability, due to the high carbon content, coarse grained ferrite and the large volume fraction of pearlite. This led to major research efforts to find ways of lowering steel carbon content while keeping high strength. [2]

In the 1970s, achievements were made by microalloying and controlled rolling. The improvement of mechanical properties was based on the suppression of recrystallization due to Nb. These steels were air cooled from the finish rolling temperature and the final microstructure was fine grained polygonal ferrite. Refinement of the ferrite grain size provides extra strength, allowing low carbon contents to be used, while improving toughness and weldability. However, polygonal ferrite is still a high temperature transformation product, with a maximum yield strength of only about 450 MPa or 65 ksi. [2]

In the late 1970s and early 1980s, the combination of microalloying and higher cooling rates associated with TMCP led to non-polygonal ferrite, i.e. acicular ferrite and bainitic ferrite. These are low temperature transformation products. This breakthrough gave the opportunity of producing higher strength steels without sacrificing toughness and weldability. Studies at about the same period of time showed that higher strength can also be obtained by rolling in the intercritical region near 600 ºC. X70-80 steels were produced by controlled intercritical rolling, resulting in ferrite-bainite microstructures and a certain level of precipitation. These steels had low carbon contents (<0.08wt%), higher Mn and Nb levels and about 0.2wt% Mo plus some Cr and Cu. Significant improvements in weldability and toughness were achieved due to the low carbon contents. [2]

Later, the combination of microalloying and higher cooling rates associated with TMCP and low interrupted cooling temperatures (ICT) led to a microstructure consisting of significant grain refinement of bainite with/without martensite. Steels with these low carbon microconstituents have higher strength, superior toughness and good weldability, which meet X100 requirements (minimum yield strength is 690 MPa or 100 ksi). Using a similar processing approach with the addition of boron (B) to increase hardenability, even higher mechanical properties can be developed - close to those needed for X120 grades. [2] Figure 2-3 [4] shows that boron markedly retards the ferrite reaction, likely by

preferential segregation to the prior austenite boundaries. Therefore, the steel hardenability can be effectively enhanced. Furthermore, the bainitic C-shaped curve is less affected by the B addition than that on ferrite reaction. Therefore, fully bainitic microstructures with little martensite can be obtained in low-alloy, low-carbon steels, containing small amounts of boron and molybdenum. The reduced alloy concentration gives better weldability and higher strength due to the refined bainitic microstructure as well.

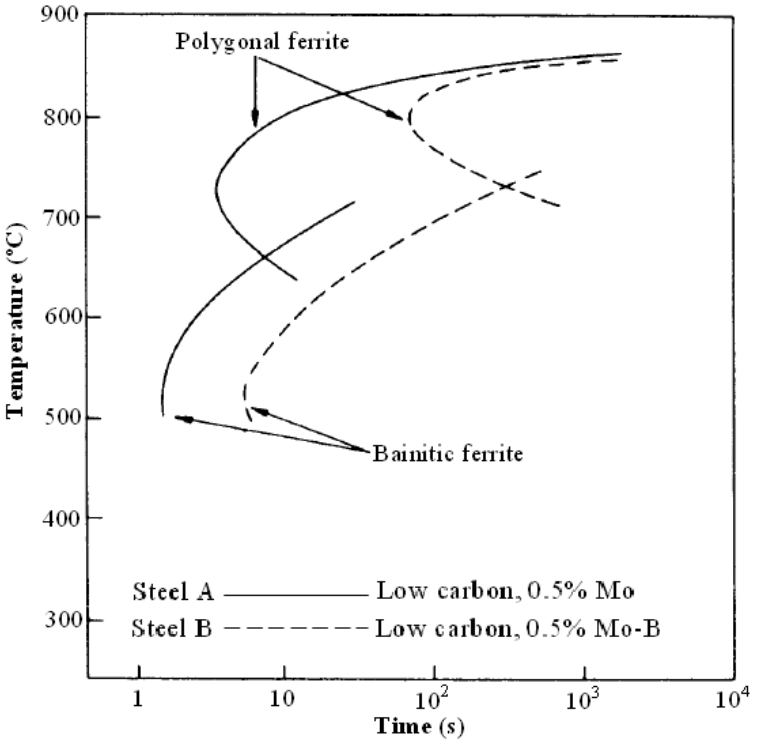

Figure 2-3 Effect of B addition (0.002 wt%) on polygonal ferrite and bainitic ferrite reaction of low carbon steel with 0.5% Mo. [4]

Figure 2-4 [5] shows that steel tensile strength is controlled by the transformation temperature and carbon content, because different microstructures are obtained. It also indicates that 400-500ºC is an ideal transformation temperature range, in which the bainite microstructure can be obtained and the steel has higher strength.

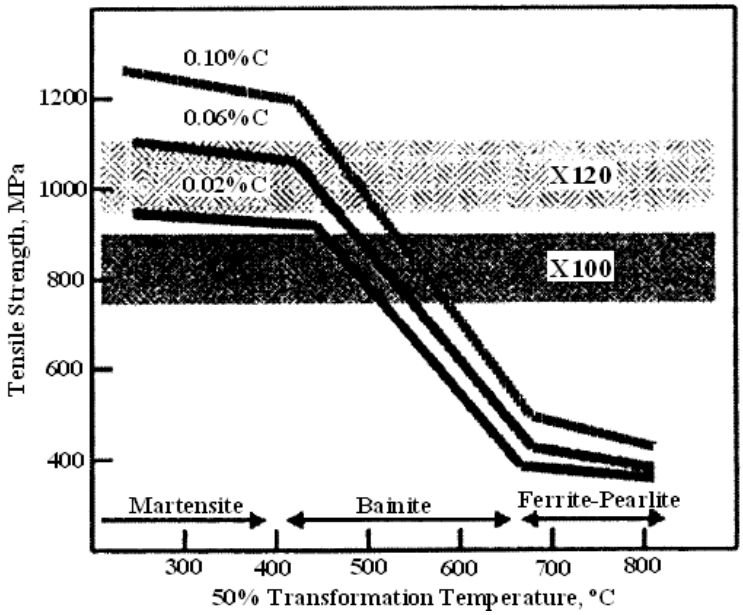

Figure 2-4 Schematic illustration on relationship between 50% transformation temperature and strength. [2,5]

Ferritic steels have a BCC structure, which undergoes a transition from ductile behaviour at high temperature to brittle behaviour at lower temperatures. The temperature at which this transition occurs is known as ductile to brittle transition temperature (DBTT). One method of defining the transition temperature is the temperature when the fracture surface is 50% ductile, which is known as the fracture appearance transition temperature (FATT). DBTT can be measured by a Charpy impact test using Charpy V-notch specimens (CVN specimens). The interrupted cooling temperature (ICT) has been found to have a strong effect on steel strength and toughness and it affects FATT as well, as shown in Figure 2-5. [2,5] Figure 2-5 indicates that an interrupted cooling temperature in the 400-450ºC range is ideal to produce steel with high strength and low FATT.

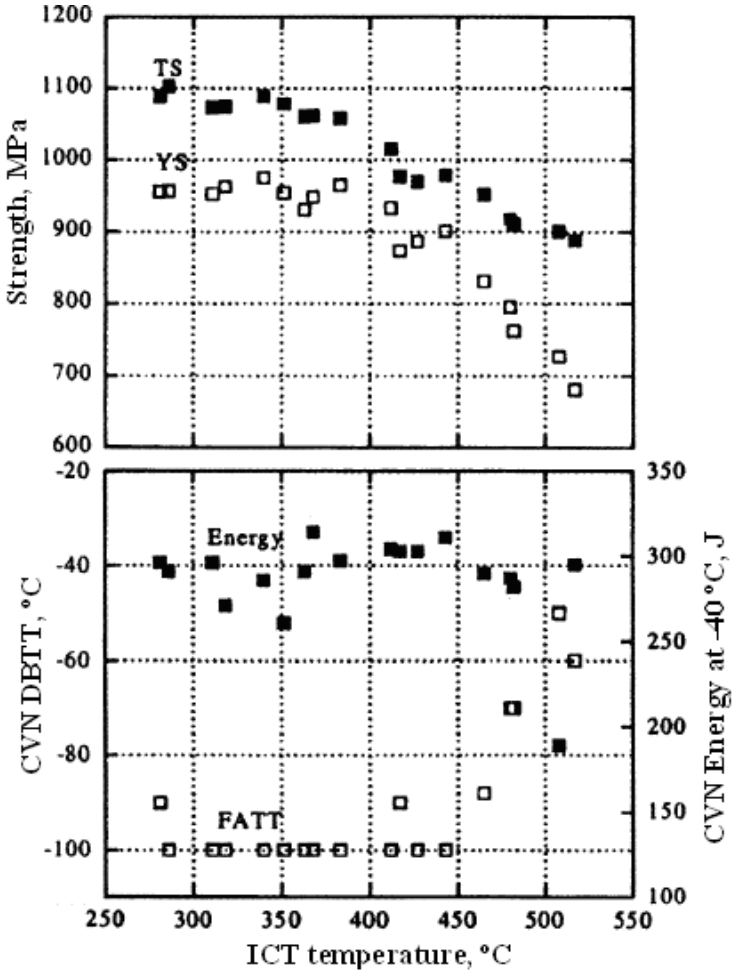

Figure 2-5 Effect of interrupted cooling temperature (ICT) on strength and toughness. [2,5]

2-1-3. High strength low alloy microalloyed steels (HSLA)

Microalloyed steels are a class of high-strength, low-carbon, low-alloy steels containing small additions (in amounts less than 0.1 wt%) of Nb, Ti and/or V. The steels may contain other alloying elements, such as Mo, in amounts exceeding 0.1wt%. The strength of the microalloyed steels is increased dramatically by the addition of the above microalloying elements through grain refinement and/or precipitation strengthening. Precipitation in these steels can be controlled through TMCP, leading to precipitates with sizes ranging from several microns to a few nanometers.

2-1-4. Effects of alloying elements

The alloying elements can be classified as austenite formers, ferrite formers and carbide formers. Austenite formers are the alloying elements that enlarge the austenite region, such as carbon, nitrogen, manganese, copper and nickel. Ferrite formers are the alloying elements that enlarge the ferrite region, such as aluminum, silicon, chromium, titanium, niobium, vanadium and molybdenum. Chromium, titanium, niobium, vanadium and molybdenum can form very stable carbides. [4,6] The following elements, which are listed in alphabetical order, are important alloying elements in steel.

Aluminum (Al)

Aluminum is not usually considered as a microalloying element. It is added primarily as a deoxidizer in steel [7] and works in conjunction with silicon. Aluminum is normally dissolved in austenite at high temperature prior to rolling, but the nitride phase is thermodynamically stable at lower temperatures. [8,9] Therefore, the other important role of Al in Al-killed steels is due to its precipitation properties. Aluminum nitride precipitates (AlN) help in the formation of optimum crystallographic texture (preferred orientation) in low-carbon sheet steels for deep-drawing applications. When Al combines with N, forming AlN, the amount of dissolved interstitial nitrogen is lowered; therefore, ductility is improved. However, AlN nucleates with some difficulty in steel unless precipitation is enhanced by thermal or mechanical treatments. [7] This is because of the high nucleation barrier due to its hexagonal crystal structure, i.e., a very different morphology from other nitrides. [9,10] Aluminum nitride particles are relatively coarse [11] and may cause embrittlement and cracking problems in casting products, ingots and rolled products. Aluminum carbide is not stable in steel. [12]

Boron (B)

Boron has received considerable attention since the introduction of low-carbon bainitic steels. The addition of a small amount of boron is favourable to obtain bainitic microstructures, because it can effectively increase steel

hardenability, by promoting the bainitic reaction. Boron can suppress the austenite/ferrite transformation by segregating to the austenite grain boundaries. Therefore, ferrite nucleation is prevented. [4,13] Secondly, the bainitic C-shaped curve is less affected by boron additions than that on ferrite reaction, so that fully bainitic microstructures with little martensite can be obtained. Furthermore, the addition of B can replace large additions of elements like Mn, Mo and Ni to obtain bainitic microstructures. The reduced alloy concentration gives higher strength and better weldability, due to the refined bainitic microstructure and reduced amount of Mn, Mo and Ni. [14] However, boron has a direct effect on susceptibility of steel to brittleness because of BN formation. It was found that the higher the concentration of B, the greater the susceptibility. [15] Therefore, the amount of boron needs to be strictly controlled.

Carbon (C)

Carbon is the most common alloying element in steel and has a strong effect on steel hardness and strength. Carbon is an interstitial element that occupies the interstitial sites in iron BCC and FCC lattices. Carbon can increase the yield strength of pure iron (0 wt% C) from 28 MPa (pure Fe) to 190 MPa at 0.005 wt% C, as shown in Figure 2-6. [16] However, carbon has very limited solubility in ferrite. The maximum solubility of carbon at room temperature is 0.005 wt%. [16] Any excess carbon, above 0.005 wt% C, is present in the form of cementite (Fe_3C) in steels, rather than in solid-solution. The other major effect of carbon is the precipitation strengthening effect when combined with Ti, Nb and V microalloying elements. Carbon content in pipeline steels is recommended to be <0.10 wt%, or even more conservatively between 0.01 and 0.05 wt%, in order to improve field weldability. [17]

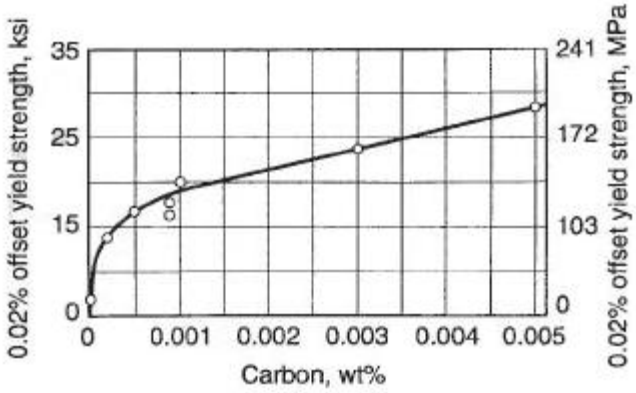

Figure 2-6 Effect of carbon in solid solution on the yield strength of iron. [16]

Chromium (Cr)

Chromium improves hardenability and corrosion resistance and is present in all stainless steels as a solid solution element. Chromium can also provide a small contribution to solid solution strengthening. [9] Chromium is a carbide former and chromium carbides are found in many tool steels for wear resistance. [16]

Copper (Cu)

Copper in amounts up to ~0.35 wt% is very effective in improving the atmospheric corrosion resistance of carbon and microalloyed steels. [18] When used in the amounts of about 1.3 wt%, copper can provide solid-solution strengthening or much greater strengthening by precipitation strengthening. [9]

Manganese (Mn)

Manganese is an important element in most steels and it is usually added in steels to combine with sulfur to form manganese sulfide (MnS). [9] Without manganese, sulfur would react with Fe and form FeS, which is a brittle compound with a low melting point. It causes a phenomenon called hot shortness (brittleness at high temperatures, which is usually caused by sulfur). Steel toughness and ductility are reduced accordingly. Manganese also plays an important role in ferrite grain refinement and dispersion strengthening. The reason is that Mn is an austenite stabilizer, which can provide a marked decrease in the austenite to ferrite transformation temperature, resulting in ferrite grain refinement and finer precipitate dispersion. [19] The proper amount of Mn (1.4-2.0 wt%) controls the

transformation temperature and enhances the formation of lower transformation temperature products, such as acicular/bainitic ferrite. [14] Manganese is not used specifically as a solid-solution strengthener; however, it is often added to trigger other strengthening mechanisms in structural steels. In V-microalloyed steels, the effect of Mn on the activity of V is especially important. Manganese is known to increase the activity coefficient of V and at the same time decrease the activity coefficient of C. [19] One disadvantage of Mn is that it increases the carbon equivalent and, hence, reduces steel weldability.

Molybdenum (Mo)

Molybdenum has a strong effect on hardenability. It shifts the ferrite and pearlite curves of the CCT diagram to the right (longer times); therefore, the formation of polygonal ferrite is suppressed and lower-temperature products, such as acicular/bainitic ferrite structures, are promoted. [12] It was reported that the addition of Mo to Nb-containing line-pipe steels improves transformation hardening through an increased volume fraction of acicular ferrite and M/A islands as well as through grain refinement and precipitation hardening. [20]

Molybdenum carbides are formed in many tool steels to improve wear resistance. [16] Uemori et al. [21] studied the effect of Mo addition on the microstructure in Ti-Nb steels. It was found that Mo has two important functions. One is that all Mo atoms are in solution in the ferrite matrix, resulting in Mo solid solution hardening. The other is that Mo atoms strongly segregate to the Nb(C,N)/ferrite matrix interfaces, likely suppressing the diffusion of Nb atoms into Nb(C,N) from the ferrite matrix. This directly results in fine precipitates in Ti-Nb-Mo steel. Some of the Nb atoms are replaced by Mo atoms, forming Nb(Mo)C.

Nickel (Ni)

Nickel is an austenite stabilizer and decreases the austenite-to ferrite transformation temperature. Nickel has a positive effect on hardenability and is an important alloying element in many alloy steels. Nickel is a substitutional element; however, it has a small effect on increasing yield strength. Nickel does not form carbides and remains in solid solution. [16]

Niobium (Nb)

The major application of Nb is in microalloyed steels. Niobium can affect the mechanical properties of the final product through three effects: dissolution in austenite, precipitation in austenite and precipitation in ferrite. [22] Because of its affinity for both carbon and nitrogen, niobium is also important in interstitial-free (IF) steels and is also used as a carbide stabilizer in many stainless steels. [16]

At high temperatures, Nb is dissolved in austenite and remains in solid solution. Niobium solute atoms slow down the austenite to ferrite decomposition kinetics and retard austenite recovery and recrystallization during rolling. During rolling, Nb has the largest effect on grain refinement and it has a more effective strengthening effect than V or Ti, because Nb can partially precipitate in austenite as nitrides, carbides or carbonitrides. These precipitates can inhibit austenite grain growth and delay the recrystallization of austenite grains. The remaining Nb in solution after rolling will precipitate as fine carbonitrides in ferrite, increasing the strength by a precipitation strengthening mechanism.

Nitrogen (N)

Similar to carbon, nitrogen is also an interstitial atom which has a strong strengthening effect on iron. Nitrogen is an essential microalloying element in microalloyed steels because of the interaction ability with other microallying elements such as titanium, niobium and vanadium. Nitrogen is especially important in V-steels because the solubility of VN is much lower than that of VC. It determines the density of precipitation and thereby the degree of precipitation strengthening. Since pure ferrite dissolves more N than C, the total N content of the steel is normally dissolved in the ferrite before precipitation in the absence of nitride-forming alloying elements, whereas only a fraction of the C content is dissolved in ferrite. However, when some nitride formers are present, some of the N will be removed from solid solution by the nitride formers. [12]

Compared with the effect of nitrogen on vanadium, nitrogen has a detrimental effect on niobium since Nb(C,N) is less soluble and tends to precipitate

excessively in austenite. Therefore, much of the precipitation strengthening effect in ferrite is lost. [23]

Silicon (Si)

Silicon is added to many steels as a deoxidizer to remove dissolved oxygen from the molten steel during the steel refining process. [16] Silicon has a solid solution strengthening effect, increases hardenability and reduces weldability.

Titanium (Ti)

Titanium is a strong deoxidizer and it can provide some solid-solution strengthening as a substitutional solute in the steel matrix. However, the major effect of titanium in microalloyed steels is in forming TiN and TiC precipitates. These precipitates can pin grain boundary movement in austenite and, therefore, provide grain refinement. Because of its affinity for both C and N, Ti is important in interstitial-free (IF) steels, which have exceptional formability. Titanium is also used as a carbide stabilizer in many stainless steels. [16]

Vanadium (V)

The largest use of V is in high-strength, low-alloy (HSLA) steels. Vanadium has a higher solubility in austenite than Ti or Nb. Prior to the austenite to ferrite transformation, V stays in solid solution. Vanadium has a strong affinity for nitrogen and carbon and forms fine carbides, nitrides or carbonitrides. [9] The addition of vanadium produces a finer ferrite grain size and also leads to significant precipitation strengthening. VC should have a higher precipitation strengthening effect than VN, because it has a much higher solubility. VC precipitates out at lower temperatures in ferrite than VN and is finer than VN.

For microalloyed steels, Nb, Ti, V and Mo are the major microalloying elements. Besides the effects explained previously, they also retard austenite recrystallization, affecting the austenite to ferrite transformation temperature. The effectiveness of these microalloying elements on the retardation of austenite recrystallization decreases in the order: Nb>Ti>Mo>V. [24] It is believed that retardation of austenite recrystallization can be caused by solute atoms and strain-induced precipitates. Solute atoms can significantly delay the onset of austenite recovery, which is referred to as the solute drag effect, and recrystallization of

austenite during rough rolling. [25] Due to the solute drag effect, the austenite to ferrite transformation temperature is lowered, leading to grain size refinement. The interaction between solute atoms and defects (vacancies and dislocations) as well as the solute diffusion behavior corresponds to different retardation abilities. [26] Strain-induced precipitates can also retard recrystallization by pinning dislocations, grain boundaries and subgrain boundaries, inhibiting the nucleation and growth process, causing retardation of recrystallization. [27,28,29] Due to the strong retardation and precipitation effect, niobium has the largest effect on retardation and grain refinement and it is more effective in increasing strength than Ti and V.

2-2. Thermo-mechanical controlled processing and sequential precipitation

2-2-1. Thermo-mechanical controlled processing (TMCP)

Thermo-mechanical controlled processing (TMCP) is a well-established industrial process which plays an important role in the production of many steels for pipelines, structural applications in bridges, buildings, etc. It involves combining controlled thermal and deformation treatments simultaneously to an alloy in order to change its shape and refine the microstructure. [4] TMCP can be simplified as controlled rolling followed by accelerated cooling. It is a highly controlled operation in which the rolling parameters, such as reheating temperature, strain, number of rolling passes, finishing temperature, etc., are predetermined and accurately defined. Therefore, very high levels of productivity and reproducibility can be achieved. TMCP allows one to achieve optimum mechanical properties with fewer alloying elements than would be required for regular hot rolling processes. A schematic TMCP schedule (time-temperature-transformation diagram) is illustrated in Figure 2-7 and it includes the following steps: [30]

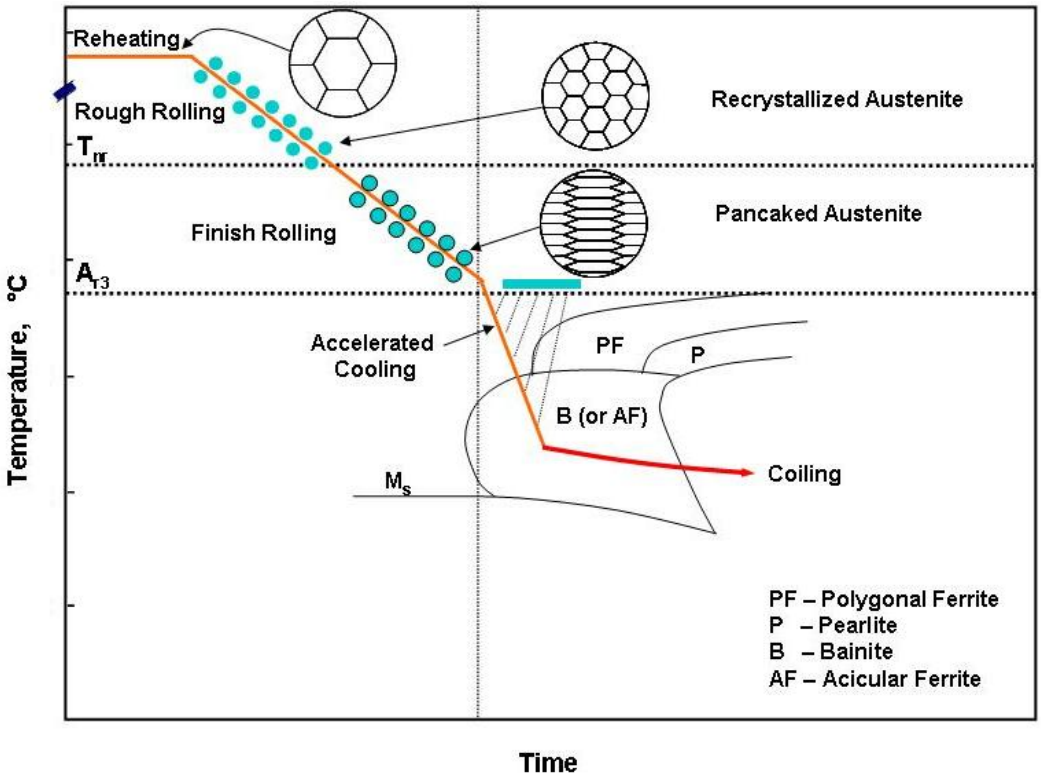

Figure 2-7 Schematic of a thermo-mechanical controlled processing schedule.[30]

1) Reheating the steel to a selected temperature (soaking temperature, about 1250ºC) for austenite (γ) homogenization so that elements that will form precipitates during subsequent processing (Nb, Ti, V, etc.) are substantially dissolved in the steel.
2) Rough rolling occurs at temperatures above the no-recrystalization temperature (T_{nr}) to break down the austenite grains through multiple recrystallization cycles. At this stage, the steel can be reduced by as much as 80% thickness. [31]
3) Finish rolling is carried out at temperatures below the no-recrystallization temperature (T_{nr}, recrystallization will not happen below this temperature), but above the austenite to ferrite transformation temperature (A_{r3}), to produce heavily pancaked austenite. Finish rolling is in the no-recrystallization temperature range for austenite. At this stage, 60% thickness reduction can be reached. [31]

4) The steel undergoes accelerated cooling from a temperature above A_{r3} down to an interrupted cooling temperature (ICT) at which the desired stable microstructure can be obtained.
5) The steel subsequently experiences strains from coiling. This introduces dislocations in the steel with the desired microstructure, so as to enhance precipitation kinetics. The final coils are then naturally slow cooled to room temperature (air cooling).

Stages 2 and 3 are the two rolling stages. Both stages are important to achieve ferrite refinement by maximizing the total interfacial area per unit volume, S_v, of near planar crystalline defects, i.e. austenite grain boundaries, deformation bands and incoherent twin boundaries. However, the approaches to increase S_v are quite different.

Stage 2 is most important for primary austenite grain refinement due to the dynamic recrystallization of austenite. It involves repeated recrystallization and inhibition of grain coarsening at temperatures above $T_{95\%}$ (temperature for 95% recrystallization). The increase in S_v is from the increase in grain boundary area per unit volume resulting from a decrease in average grain volume. [32,33] Because of the high temperature at this stage, austenite grain refinement is limited. The situation can be greatly improved by precipitation of some fine particles in the austenitic matrix. These particles form on austenite grain boundaries. Because of the pinning effect of particles on austenite grain boundaries, austenite grain size can be effectively restricted. These precipitates will be introduced in the next section.

Stage 3 occurs during the later stages of austenite deformation. Recrystallization does not occur at the lower temperature. It involves substantial deformation below $T_{5\%}$ (temperatures for 5% recrystallization). The increase in S_v is from the increase in grain boundary area per unit volume resulting from a change in grain shape and through the addition of the transgranular twins and deformation bands. [32,33] At this stage, austenite grains will be elongated and flattened, forming pancaked austenite, increasing the austenite grain boundary area per unit volume. Figure 2-8 [34] shows the variation of ferrite grain size with

austenite grain boundary area per unit volume for deformed and recrystallized austenite. Furthermore, deformation bands are formed inside the elongated austenite grains because of deformation, dividing the austenite grain into several subdivisions by deformation bands. For ferrite nucleation, the deformation bands are equivalent to austenite grain boundaries. [6,34,35] The pancaked microstructure increases the grain boundary area and generates deformation bands, providing more ferrite nucleation sites, resulting in finer grains.

In stage 4, accelerated cooling from the finish rolling temperature further suppresses austenite grain growth, allowing the austenite to ferrite transformation to take place. Because of the relationship between austenite and ferrite grain sizes, refinement of ferrite grain size is achieved through austenite grain refinement due to the combination of controlled rolling and fine precipitation. [36] Ferrite grains nucleate at both austenite grain boundaries and the austenite deformation bands. The elongation of austenite grains and the division of deformation bands inside the austenite grains allow for much more refined ferrite grain sizes. The formation of the deformed bands is one of the beneficial facts of controlled rolling. However, in conventional hot rolling, ferrite grains only nucleate at the austenite grain boundaries, resulting in a much coarser ferrite grain structure. [6]

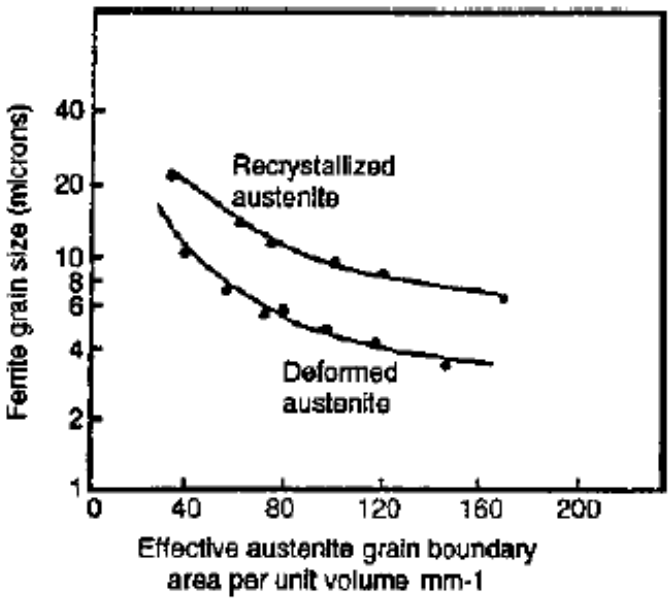

Figure 2-8 Variation of ferrite grain size with austenite grain boundary area. [34]

2-2-2. Effects of processing parameters

Reheating temperature (RT), finish rolling temperature (FRT), cooling rate (CR), coiling temperature (CT) and interrupted cooling temperature (ICT) all play important roles in steel microstructure formation, grain size refinement and precipitation effects and, therefore, affect the steel yield strength.

2-2-2-1. Effect of RT

The purpose of reheating the steel to the soaking temperature is to obtain austenite homogenization and dissolve all the precipitation substances (Nb, Ti, V, etc.) in the steel. Thus, reheating temperature is important in controlling the initial austenite grain size and the extent of microalloying element dissolution. Lower RT may result in incomplete dissolution. The initial austenite grain size will be increased as RT increases. However, an increase in RT helps maximize dissolution of the precipitation substances, leading to higher precipitation strengthening and higher yield strength. The common RT for plain carbon steel is in the 1200-1320ºC range. [9]

2-2-2-2. Effect of FRT

Finish rolling temperature has an effect on austenite grain size and, therefore, an effect on final ferrite grain size, yield strength and toughness.

A decrease in FRT produces a finer austenite structure, which enhances ferrite grain refinement, resulting in higher yield strength. Toughness improves as well, due to grain size refinement. The effect of FRT on yield strength and the impact-transition temperature (ITT) of hot-rolled Nb microalloyed steels is shown in Figure 2-9 and Figure 2-10, respectively. [9] However, the precipitation strengthening effect is reduced as FRT is decreased. [9] In spite of the latter effect, the yield strength always increases as the FRT decreases.

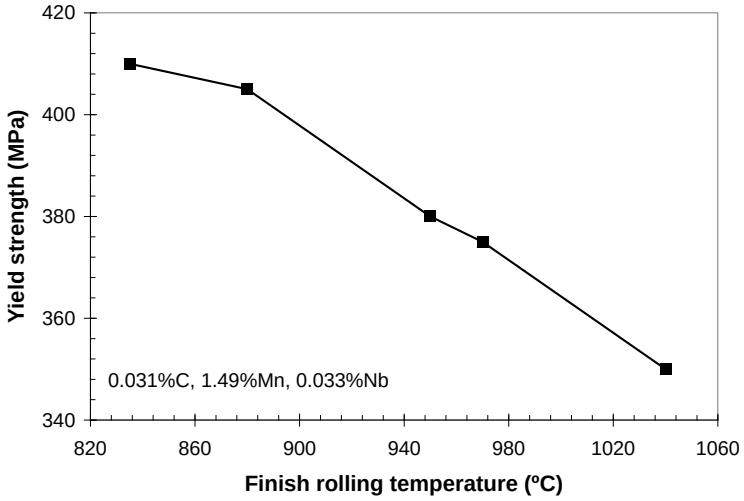

Figure 2-9 Effect of finish rolling temperature on yield strength of a hot-rolled Nb microalloyed steel. [9]

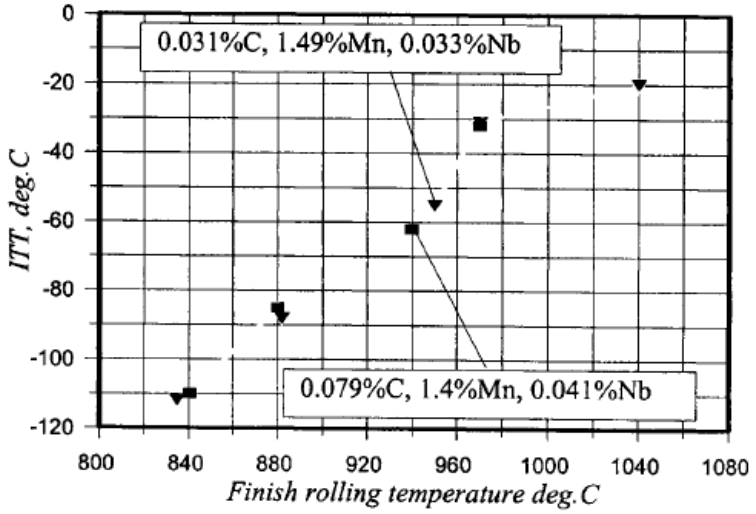

Figure 2-10 Effect of finish rolling temperature on impact-transition temperature (ITT) of hot-rolled Nb microalloyed steels. [9]

2-2-2-3. Effect of cooling rate (CR) on microstructure and grain size

2-2-2-3-1. Effect of CR on microstructure

Different microstructures can be formed during steel processing and CR is one of the determining parameters. According to the microstructural features, microalloyed steels can be categorized into three groups: polygonal ferrite-pearlite, polygonal ferrite-bainitic/acicular ferrite and bainitic ferrite. Small amounts of other phases may also be included, such as grain boundary ferrite

(GF) and martensite/retained austenite (M/A phase). Grain boundary ferrite refers to ferrite that nucleates at the corners of prior austenite grain boundaries and appears elongated or granular along the prior austenite grain boundaries. Martensite is formed at lower temperature, normally below 250ºC. Rapid cooling promotes the formation of martensite, which has a very fine grain size. Retained austenite refers to untransformed austenite. Figure 2-11 [14] is a continuous cooling transformation (CCT) diagram of a typical microalloyed steel; different phases can be obtained by controlling the CR.

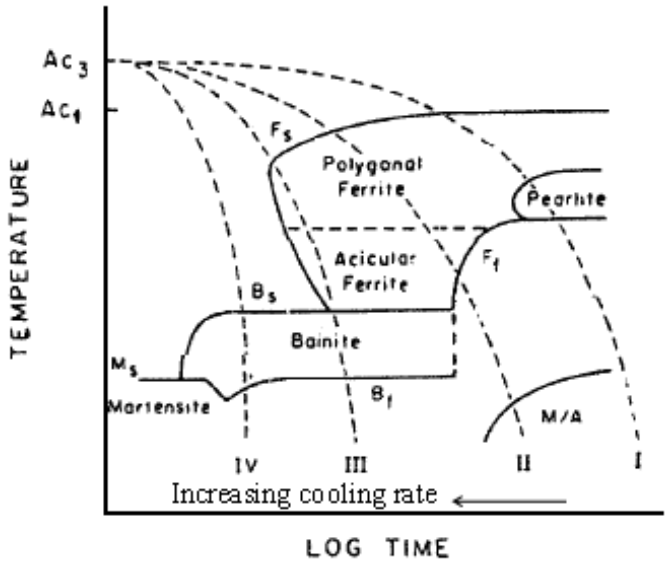

Figure 2-11 CCT diagram of a typical microalloyed steel. [14]

1) Polygonal ferrite (PF) -pearlite (P) microstructure

This is a mixture of PF and P. In low carbon steels, PF is the majority phase and P occupies a substantial amount of the microstructure. Polygonal ferrite, nucleated at prior austenite grain boundaries, is equiaxed and each grain has distinct grain boundaries, but may have irregular shapes or edges due to deformation. In some references, quasi-polygonal ferrite (QPF) is used to define coarse ferrite grains with irregular grain shapes. [37,38] Pearlite normally has a lamellar mixture of ferrite and cementite, formed at high temperatures between 550-700ºC. Thus, a PF-P microstructure is formed at the highest temperature and lowest CR in CCT diagram, shown as I in Figure 2-11. These steels usually have

lower strengths due to the larger grain size. Polygonal ferrite-pearlite microalloyed steels exhibit discontinuous stress-strain curves in a tensile test.

2) Polygonal ferrite (PF) - acicular ferrite (AF) microstructure

The main phases include PF and AF. Acicular ferrite is highly substructured, i.e., fine irregular ferrite. It is transformed from austenite at an intermediate temperature between 300-550ºC. This temperature range is just above the bainite start temperature. Compared to a PF-P microstructure, PF-AF is formed at much higher cooling rates, between II and III as shown in Figure 2-11. The CR is too fast for P to form, yet not rapid enough to produce martensite. Therefore, the grain size is relatively small due to the fast CR. Similar to PF-P microalloyed steels, the strength of microalloyed steels with this type of microstructure mainly comes from grain refinement and precipitation strengthening. However, the strength is highly improved due to the grain refinement effect. This type of microalloyed steel exhibits a continuous stress-strain curve. X70 and X80 steels that are investigated in the present research have a PF-AF microstructure, which will be discussed further in Chapter 5.

3) Bainitic ferrite (BF) microstructure

The distinction between BF and AF is not very clear in pipeline steels and sometimes they are considered as one phase in CCT diagrams. However, BF is believed to form at even higher CR, between III and IV as shown in Figure 2-11. However, the CR is not rapid enough yet to produce martensite. Bainitic ferrite grows in the form of thin plates, which are often referred to as ‘packets’ of lath ferrite. Therefore, BF has an even smaller grain size compared to the above two microstructures, leading to higher strength and good toughness. This type of microalloyed steel has a continuous stress-strain curve.

It is clear that CR has a direct influence on the evolution of steel microstructure. From the CCT diagram, a higher CR helps avoid the PF + P nose, leading to a final microstructure with a ferrite and bainite mixture or even a fully bainitic microstructure.

The PF+P and PF+AF microstructures are the traditional microstructures used for the linepipes with strengths up to those of the X80 designation. In order to improve the strength level, a microstructure of bainite is desirable; bainite has higher strength, good low-temperature toughness and field weldability. Grade100 and X100 steels that are investigated in the present research have mainly bainitic microstructures. The detailed microstructural information will be introduced in Chapter 4 and Chapter 6, respectively. In order to develop the bainitic microstructure during accelerated cooling of TMCP, the steels must have sufficient hardenability. Steels with inadequate hardenability tend to form mixtures of ferrite and bainite. However, attempts to improve hardenability usually lead to partially martensitic microstructures. Small additions of boron are used to effectively suppress the ferrite reaction and enhance bainite formation, while the bainitic C-shape is less affected; thus martensite formation is controlled. [4]

2-2-2-3-2. Effect of CR on grain size

Transformations are generally shifted to lower temperatures during cooling, which is called undercooling. Within a certain period of time, a faster CR causes a greater temperature drop, leading to a higher degree of undercooling. The nucleation rate increases with increasing undercooling and the ferrite grain size decreases accordingly with increasing nucleation rate. If other processing parameters are kept the same, the austenite/ferrite transformation temperature is reduced at higher CR, resulting in a finer ferrite grain size, leading to higher yield strength.

Figure 2-12 shows the combined effect of processing parameters on the yield strength and grain size of a Nb steel. [9,12] The parameters include RT, CR and FRT. The figure indicates that increasing RT, faster CR and lower FRT increase the steel yield strength. A lower FRT and faster CR decrease the grain size.

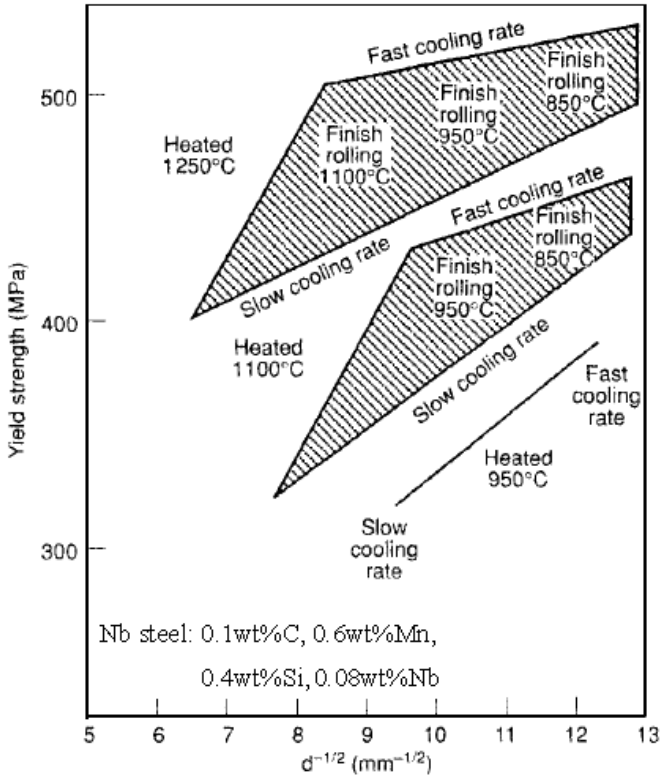

Figure 2-12 Effects of processing parameters on the yield strength of Nb steel. [9,12]

2-2-2-4. Effect of coiling temperature or interrupted cooling temperature (CT/ICT)

The CT/ICT is another important parameter determining the final microstructure. A mixture of PF and P forms at a high temperature range between 550-700ºC. Bainitic/acicular ferrite forms at lower temperatures between 300-550ºC. It was already explained in Section 2-1-1 that the CT/ICT has a strong effect on steel strength, toughness and the fracture appearance transition temperature (FATT). A combination of high CR and low CT/ICT with low carbon in microalloyed steels helps to produce a fully bainitic microstructure, making higher strength steels (X100, X120) possible. These steels also have superior toughness and good field weldability.

The CT/ICT can affect both ferrite grain size and precipitation behavior as well. Figure 2-13 shows that decreasing the CT decreases the ferrite grain size. [9]

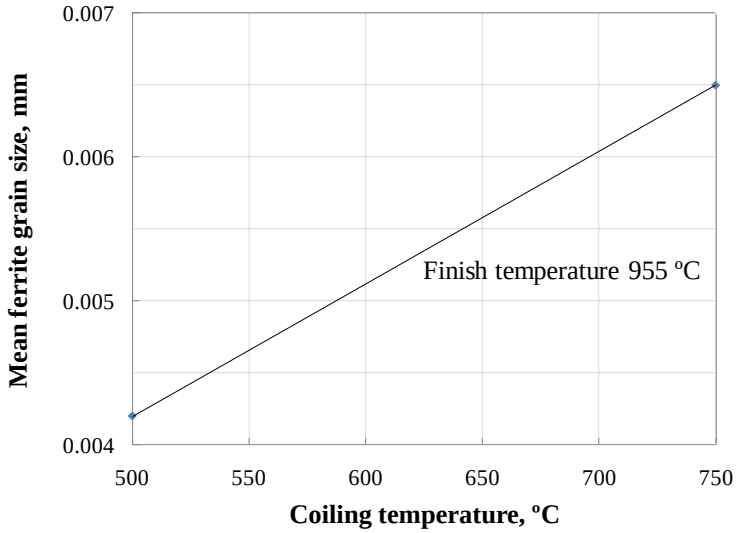

Figure 2-13 Effect of coiling temperatures on ferrite grain size for Nb-Ti microalloyed steels. [9]

Precipitate nucleation is a kinetic process and temperature influences the kinetics by altering the diffusivity, atomic impingement rate, the equilibrium solute concentrations (solubility) and the nucleation driving force. At high temperatures (higher than the critical temperature), the driving force is lower and therefore the critical nucleus size is larger; however, there is a higher species diffusivity and atomic impingement rate, which enhances the nucleation process. At low temperatures (lower than the critical temperature), the critical nucleus size is smaller; however, there is insufficient thermal energy, which hinders the nucleation process. These two competitive processes lead to a maximum nucleation rate at an intermediate temperature.

Figure 2-14 shows the combined effect of CT on the interphase precipitate size, ferrite grain size and the yield stress of a microalloyed steel after hot rolling and coiling. [9,12] The median size of nano-precipitates decreases with decreasing CT, as indicated in block a. The ferrite grain size is reduced as well due to austenite refinement with decreasing CT, as indicated in block b. Therefore, the yield strength is effectively improved due to ferrite grain refinement and precipitation strengthening, as indicated in block c. [9,12]

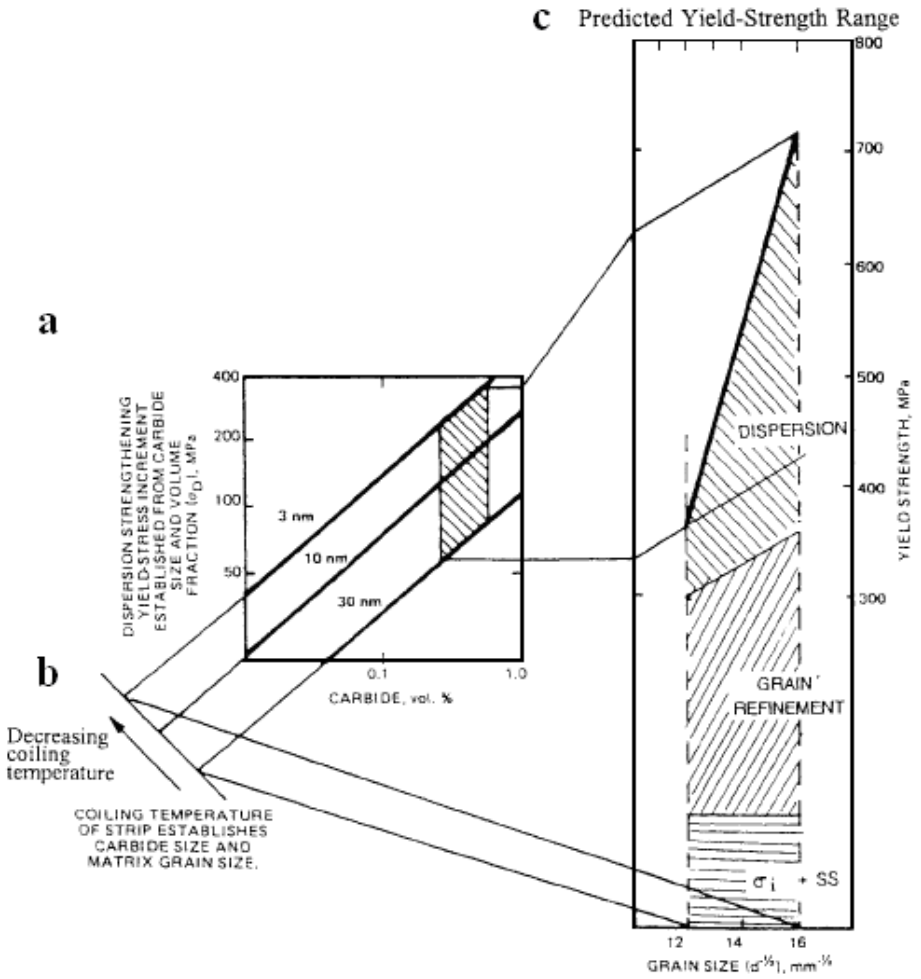

Figure 2-14 Schematic presentation of the effect of CT on interphase precipitate size, ferrite grain size and the yield stress of a microalloyed steel after hot rolling and coiling. [9,12]

2-2-3. Microalloyed precipitates and their solubility products

2-2-3-1. Microalloyed precipitates

When the solute concentration in an alloy exceeds the solubility limit in the matrix, second-phase particles will precipitate out. Figure 2-15 shows a portion of an equilibrium phase diagram. For an alloy with composition X, a single phase α is present at temperatures above T_s. Below the solvus line, two phases with α and β are stable. If this alloy is cooled from high temperature to below T_s, precipitation of β phase will happen within the α matrix.

In microalloyed steels, small additions of strong carbide- and nitride-forming elements, such as Nb, Ti and V are added intentionally. At high temperature, most of these microalloyed elements are all dissolved in the steel (some large TiN precipitates that form during casting, are not dissolved). During the cooling process, the solubilities of carbon, nitrogen and the alloying elements are reduced, causing precipitation to take place by combining with carbon or nitrogen to form dispersed precipitates. Precipitates may form within the austenite matrix prior to transformation, at the austenite/ferrite interface during the austenite to ferrite transformation because of the solubility drop of the carbides and nitrides associated with the transformation from austenite to ferrite, or in the ferrite matrix following the transformation. The precipitates that form within the austenite matrix act to pin the grain boundaries and prevent excessive grain growth, thereby reducing the overall size of the ferrite, providing Hall-Petch strengthening. Precipitates that form in the ferrite matrix are much finer in size and contribute to precipitation strengthening. [39] Table 2-1 shows the main precipitation strengthening systems in commercial HSLA steels. [40]

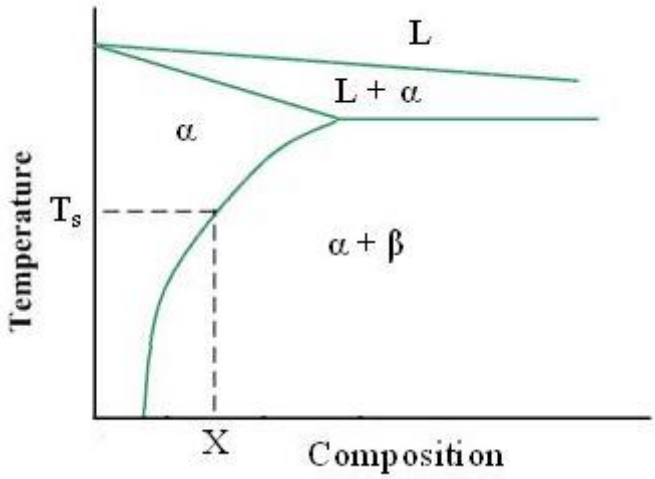

Figure 2-15 Portion of an equilibrium phase diagram showing precipitation of a second phase from a supersaturated solid solution.

Table 2-1 Main precipitation strengthening systems used in commercial HSLA steels [40]

Elements	Main precipitates
Titanium	Ti(C,N), TiC
Niobium	Nb(C,N), Nb_4C_3
Vanadium	V(C,N), V_4C_3
Niobium + vanadium	Nb(C,N), V(C,N), Nb_4C_3, V_4C_3
Vanadium + nitrogen	VN

2-2-3-2. Precipitate solubility products

A list of notation is defined here; these terms will be used in the following section.

$K_{s:}$ solubility product of precipitate *MX* in the matrix;

[*M*]: wt% of microalloying element *M* dissolved in the matrix;

[*X*]: wt% of an interstitial *X* dissolved in the matrix;

(*MX*): precipitate;

$a_{[M]}$: activity of the dissolved microalloying element *M*;

$a_{[X]}$: activity of the dissolved interstitial element *X*;

$a_{(MX)}$: activity of the constituent phase *MX*;

Q: heat of dissolution in $kJ.mol^{-1}$;

R_g: universal gas constant with a value of 8.314 J/mol.K;

T: temperature in Kelvin;

A, C: constants for a given system in solubility product expression;

c: constant in the Arrhenius equation.

The solubility product K_s is used as a measure of solubility for microalloying elements in steel. In a reaction

$$[M] + [X] \leftrightarrow (MX)$$

the solubility product is written as:

$$K_s = a_{[M]} \cdot a_{[X]} / a_{(MX)} \qquad (2\text{-}1)$$

The activity of a pure compound is equal to 1 and the activity of dilute elements can be replaced by their concentrations in wt%, i.e., [*M*] and [*X*]. Therefore, the solubility product can be written as:

$$K_s = [M][X] \tag{2-2}$$

The temperature dependence of K_s has an Arrhenius relationship

$$\ln K_s = -\left(Q/R_g T\right) + c \tag{2-3}$$

Therefore,

$$\log K_s = \log([M][X]) = A - C/T \tag{2-4}$$

The solubility of microalloyed carbides and nitrides in steel plays an important role in the precipitation strengthening mechanism, which will be introdued in the following section.

2-2-4. Solubility of precipitates and their sequential precipitation

2-2-4-1. Solubility of Ti, Nb and V carbides, nitrides in ferrite and austenite

Extensive work has been carried out on the determination of the solubilities of the carbides and nitrides of the microalloying elements. There still exist large differences between the data from different sources because the solubility is too small to measure exactly and solubility is very sensitive to the presence of contaminants, especially oxygen.

Table 2-2 shows the most frequently referenced solubility products for Ti-, Nb- and V- carbides and nitrides in austenite and ferrite. Figure 2-16 shows a comparison of the solubility products for microalloyed carbides and nitrides. [12]

Table 2-2 Values of solubility product constants for precipitate compounds

Compound	Matrix	A	C (K)	Reference
TiN	Liquid iron	5.90	16586	[12]
	δ iron	5.56	17205	[41]
	Austenite	3.82	15020	[12]
TiC	Austenite	5.12	10300	[12,42]
	Ferrite	4.40	9575	[12,42]
Nb(C,N)	Austenite	2.26	6770	[43]
NbN	Austenite	2.80	8500	[12]
	Ferrite	4.96	12230	[12]
NbC	Austenite	2.06	6700	[12]
	Ferrite	3.90	9930	[12]
VN	Austenite	3.46	8330	[12]
	Ferrite	6.63	12500	[44]
VC	Austenite	6.72	9500	[12]
	Ferrite	8.05	12265	[12]

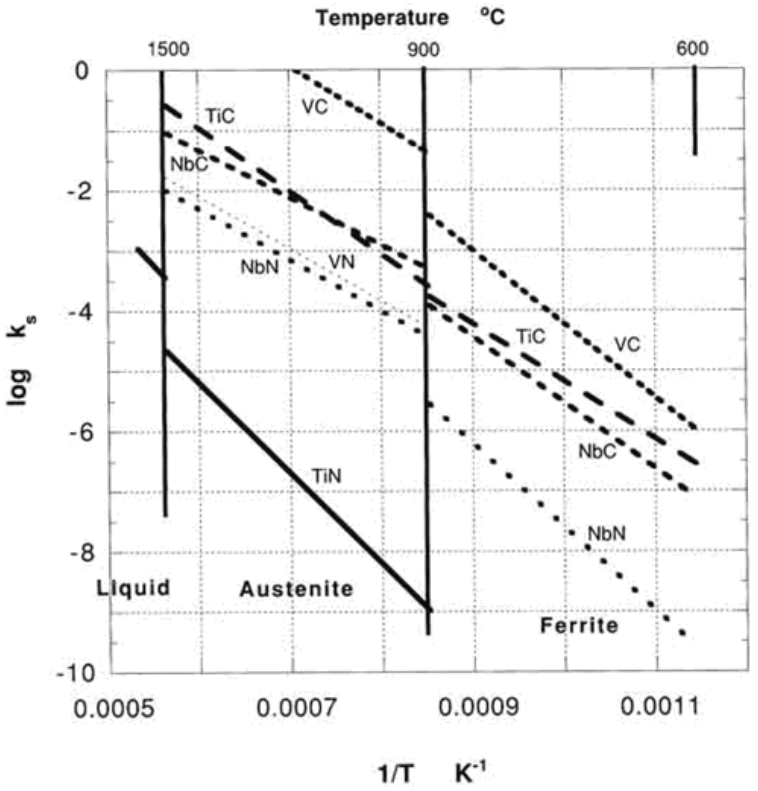

Figure 2-16 A comparison of the solubility products for microalloyed carbides and nitrides. [12]

The solubility of TiN in austenite is lower than that of all other nitrides and carbides of the microalloying elements. [45] TiN is extremely stable and can withstand dissolution at high temperatures during reheating prior to rolling. Therefore, Ti is intentionally added to react with N, forming TiN to restrict excessive grain coarsening at high temperatures. If larger Ti contents are present, the excess Ti can precipitate at lower temperatures as TiC, which can contribute to a precipitation strengthening effect. [46,47,48,49,50]

Niobium carbide and nitride have relatively low solubilities and may precipitate out in the later stages of rolling. [51,52] Therefore, further precipitation at lower temperatures is predominantly by Nb(C,N). However, in practice, some of the particles are frequently cored with Ti- and N-rich compounds in the interior of the particle, and are Nb- and V-rich towards the surface of the particle. [7] This reflects the high temperature stability of Ti- and N-rich compounds (primarily TiN). These particles can act as nucleation centres for subsequent precipitation at relatively low temperatures; for example, NbN forming around a core of TiN. [7]

The solubility of V(C,N) in austenite and ferrite is much higher than that of the other alloying element carbides/nitrides. Vanadium carbonitride has a high solubility in austenite at temperatures as low as 1050-1150°C. [7,53] It does not readily precipitate in austenite and therefore has little influence on austenite grain size control. This is an advantage of V as a microalloying element to maximize the precipitation strengthening in ferrite in the form of finely dispersed and stable particles. [7,54]

As temperature decreases, the probability of the nucleation of new V- and Nb-rich carbonitride precipitates increases because of the increasing driving force. (The driving force increases monotonically as the temperature decreases.) It has been found experimentally that larger particles formed at high temperatures are high in Ti and low in V or Nb, whereas smaller ones formed at low temperatures are low in Ti and high in V and Nb. [55,56]

It is usually considered that V gives little grain refinement on its own; it is advantageous to combine it with a small amount of Ti to control the austenite

grain size during hot rolling and thereby refine the resulting ferrite microstructure on cooling as nitrides and carbides after hot rolling. But recent studies strongly suggest that V can also be effectively used for ferrite grain refinement. [57,58] It was suggested that the VN particles, which precipitate inside austenite grains during/or after hot rolling, show a strong potential for nucleation of intragranular ferrite. Intragranular ferrite can nucleate on VN and maintain coherent, low energy interfaces with respect to VN. The presence of VN precipitates in austenite is the main factor governing the formation of intragranular ferrite is [58]

2-2-4-2. Sequential precipitation

From the comparison of the solubilities of the carbides and nitrides in Figure 2-16, it can be seen that precipitation is a sequential process because of solubility differences. It is believed that the solubility of nitrides is lower than that of the corresponding carbides in austenite or in ferrite, especially for Ti and V (i.e. $K_{TiN} < K_{TiC}, K_{VN} < K_{VC}, K_{NbN} < K_{NbC}$). [8,39] The solubility of VC and VN differ widely and the solubility of VN is about two orders of magnitude lower than that of VC. This means that VN will tend to react with N first and subsequently with C. The greater stability of vanadium nitride compared to the carbide makes nitrogen a useful and economical alloying element in many microalloyed steels. It has been verified that vanadium and titanium start to precipitate in austenite as pure nitrides. When the nitrogen is about to be exhausted, there is a gradual transition to form mixed carbonitrides. [7]

Although the solubility of NbN is lower than that of NbC, the difference is relatively small. Mixed carbonitrides form at all nitrogen contents.

The solubility of precipitates establishes guidelines to identify different phases at different processing stages. It is clear that TiN is the least soluble of the precipitates considered in austenite. TiN should precipitate out at higher temperatures in earlier processing stages and can be several microns in size. Nb(C,N) has a much higher solubility and will precipitate out at lower temperatures in the later processing stages with a much smaller size. VC has the highest solubility and is expected to precipitate last with the finest crystallite size.

Thus, precipitates can be categorized into different groups according to their chemistry, crystallite size and their precipitation sequence.

2-2-5. Crystal structure and lattice parameters of the binary precipitates

Titanium, niobium and vanadium nitrides and carbides all have an FCC structure (NaCl-type structure) with two interpenetrating FCC lattices. The metal atoms are on one set of FCC lattice set and interstitials on the other set. [59] The respective lattice parameters are shown in Table 2-3. [60] Carbonitrides of Ti, Nb and V also have the FCC structure and the lattice parameters vary systematically with the carbo/nitrogen ratio and are intermediate between those of the individual carbonitrides. [12]

Table 2-3 Lattice parameters of binary carbides and nitrides (nm) [60]

	Nitride	Carbide
Titanium	0.42417	0.43274
Niobium	0.43927	0.44698
Vanadium	0.41392	0.41820

2-3. Strengthening mechanisms in microalloyed steels

The combination of microalloying additions, such as Nb, Ti and/or V, to the steel and thermo-mechanical controlled processing (TMCP) can enhance the strength and ductility of the steel. The improvement of mechanical properties mainly results from the refinement of ferrite grain size, precipitation, solute strengthening and dislocation strengthening, of which the most important are grain refinement and precipitation strengthening. [12,30,61]

The strengthening mechanism in metals is the relationship between dislocation motion and mechanical properties of the material. For all the strengthening methods, hindering dislocation motion improves strength. In other words, the more difficult it is for dislocations to move, the higher the strength of the material.

2-3-1. Strengthening by grain size refinement

Grain size refinement of ferrite provides one of the most important strengthening mechanisms in the steel. Because of the atomic disorder at the grain boundary, grain boundaries act as a barrier to the motion of a dislocation. When a dislocation passes through the grain boundary, it has to change its direction of motion. Therefore, the finer the grain size, the larger the area of grain boundaries that impedes dislocation motion.

Usually the effect of grain size on strength follows a Hall-Petch type equation. [62]

$$\sigma_{ys}(MPa) = \sigma_i + k_y\, d^{-1/2} \tag{2-5}$$

σ_{ys}: yield stress;

σ_i: lattice friction stress (or Pierls-Nabarro force) of iron; σ_i is equal to 54 MPa according to Pickering and Gladman; [12]

k_y: strengthening coefficient for the grains; k_y lies in the range of 21.4-23.5 MPa.mm$^{1/2}$; [12]

d: average grain diameter in microns.

The strengthening contribution due to grain size refinement can be expressed as

$$\sigma_{gb}(MPa) = k_y\, d^{-1/2} \tag{2-6}$$

In practice, the grain diameter d cannot be measured directly. Therefore, the mean linear intercept (*m.l.i.*) is introduced and is measured on a planar metallographic section. For the measurement of *m.l.i.*, random lines are drawn and the number of grain boundaries intercepted by each line is counted. The ratio of the line length (l) to the number of grains (n) provides an estimation of the grain size ($i = l/n$). Equation (2-6) is transformed into:

$$\sigma_{gb}(MPa) = k_y d^{-1/2} = k_y'(m.l.i.)^{-1/2} \quad (2\text{-}7)$$

σ_{gb}: strengthening contribution due to grain boundaries;

k_y: strengthening coefficient when grain size (d) is used;

k_y': strengthening coefficient when mean linear intercept (*m.l.i.*) is used. Since k_y lies in the range of 21.4-23.5 MPa.mm$^{1/2}$, the equivalent to k_y' is 17.5 to 19.2 MPa.mm$^{1/2}$. [63]

An increase in strength usually leads to a decrease in toughness. However, grain size refinement improves toughness simultaneously. The relationship between toughness and grain size can be explained by the following equation: [34]

$$\beta T_{d-b} = \log \beta - \log C - \log d^{-½} \quad (2\text{-}8)$$

β, C: constants;

$T_{d\text{-}b}$: ductile-to brittle transition temperature;

d: ferrite grain size.

2-3-2. Strengthening by solid solution (solute strengthening)

Interstitial or substitutional atoms, located in interstitial or lattice positions, contribute to solute strengthening. They distort the crystal lattice, causing lattice strain. Dislocations are effectively anchored, the strength is improved accordingly. Interstitial elements are more effective in solid solution strengthening than substitution elements.

Table 2-4 shows the atomic sizes of elements in iron. [62,64] Carbon and nitrogen atoms are sufficiently small relative to iron, so that these elements enter the γ- and α-Fe lattices, forming interstitial solid solutions in iron. The metallic alloying elements, such as Mn, Ni and Cr have much larger atom sizes, so they form substitutional solid solutions when entering iron lattices.

Table 2-4 Atomic sizes of elements in iron [62,64]

Element	Atomic radius, r (nm)	r/r_{Fe}	Element	Atomic radius, r (nm)	r/r_{Fe}
α-Fe	0.124	1.00	Mo	0.136	1.10
C	0.077	0.62	Ni	0.125	1.01
N	0.071	0.57	Cr	0.125	1.01
Si	0.118	0.95	Ti	0.145	1.17
Cu	0.128	1.03	Nb	0.143	1.15
Mn	0.112	0.90	V	0.132	1.06

2-3-2-1. Solid solution strengthening by interstitials in ferrite

Carbon or N interstitial atoms occupy the asymmetrical octahedral interstitial sites in BCC α-Fe. Both hydrostatic and shear strains are produced, having strong interactions with both edge and screw dislocations. However, C and N, especially C, have very limited solubilities in ferrite. The solubility of N is higher than that of C because of the slight decrease in atom size and the increase in electronegativity. [64] Table 2-5 shows the solubilities of C and N in γ-Fe and α-Fe. [65] Austenite can take up to 2 wt%C and 2.8 wt%N into solid solution; however, the solubilities of both C and N in α-Fe are extremely low at lower temperatures. The maximum solubility of C is less than 0.005 wt % at room temperature. [16] No detailed solubility data of N in α-Fe at room temperature has been found. The solubility of N at 590 ºC is 0.10wt%. Therefore, it is expected that excess C and N will precipitate out at room temperature.

Table 2-5 Solubilities of carbon and nitrogen in austenite and ferrite [16,64,65]

Element	Sold solution	Temperature (ºC)	Solubility (wt%)
C	in γ-Fe	1150	2.04
		723	0.80
	in α-Fe	723	0.02
		20	<0.005 [16]
N	in γ-Fe	650	2.8
		590	2.35
	in α-Fe	590	0.10

Figure 2-17 shows the yield strength as a function of the interstitial C and N content. [12] Within the limited solubility range, the yield strength increases linearly with increasing interstitial C and N content.

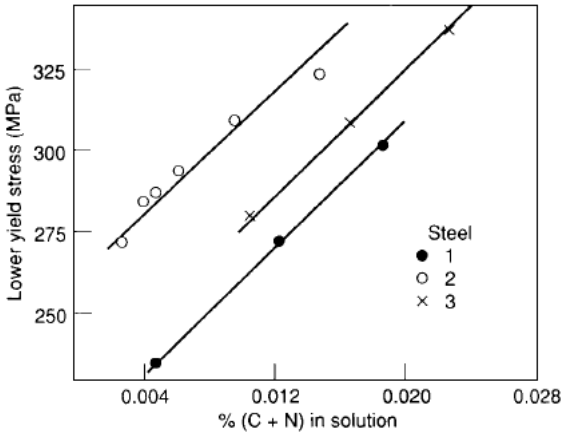

Figure 2-17 Yield strength as a function of the interstitial C and N content. [12]

2-3-2-2. Solid solution strengthening by substitutional atoms in ferrite

It has been mentioned that C or N interstitial atoms in ferrite cause asymmetrical distortion, with both hydrostatic and shear components. However, substitutional solute atoms only give rise to a hydrostatic distortion. Therefore, substitutional solute atoms have much lower strengthening effects compared to interstitial solutes. [12,66]

In BCC metals, the interaction of substitutional solute atoms with dislocations is quite complex and is temperature dependent. Increasing the solute concentration for many solute species at low temperatures results in solid solution softening, rather than strengthening. [67] From the standpoint of microalloyed steels and their room temperature properties, only room temperature effects are discussed.

The relationship between $\Delta\sigma_{ys}$ and the solute content in BCC α-Fe at room temperature is shown in Figure 2-18. [65] The figure indicates that $\Delta\sigma_{ys}$ increases linearly with increasing solute content and different alloying elements have different strengthening factors. Phosphorus and Si are more efficient for strengthening; Cu, Mn and Mo also have a positive effect on solid solution strengthening. Nickel does not have any solid solution strengthening effect and Cr

has a negative effect. In industrial steels, solid solution strengthening is achieved by adding a number of alloying elements, e.g., Mn, Si, Cu, Mo, etc. These alloying elements are usually added for other reasons, e.g., Mn to combine with S, Si to achieve deoxidation, Cu to obtain atmospheric corrosion protection and Mo to promote hardenability. Therefore, the solid solution strengthening contribution can be viewed as a useful bonus.

The effect of solid solution strengthening, including interstitial and substitutional, can be expressed by the equation below and Table 2-6 shows the solid solution strengthening coefficients for the most commonly used microalloying elements in ferrite-pearlite steels. [63,65,68,69,70] It should be noticed that k_i for Nb is very high compared to other substitutional elements. However, it is the only data found in literature for Nb. [70]

$$\sigma_{ss}(MPa) = \sum k_i C_i \tag{2-9}$$

σ_{ss}: strengthening contribution due to solid solution strengthening;

k_i: strengthening coefficient for solute strengthening of solute i;

C_i: concentration of solute i (wt%).

One thing that needs to be noted is that the solid solution strengthening effect is independent of the grain size, which indicates that strengthening contribution due to solid solution strengthening and grain size refinement are independent. [12]

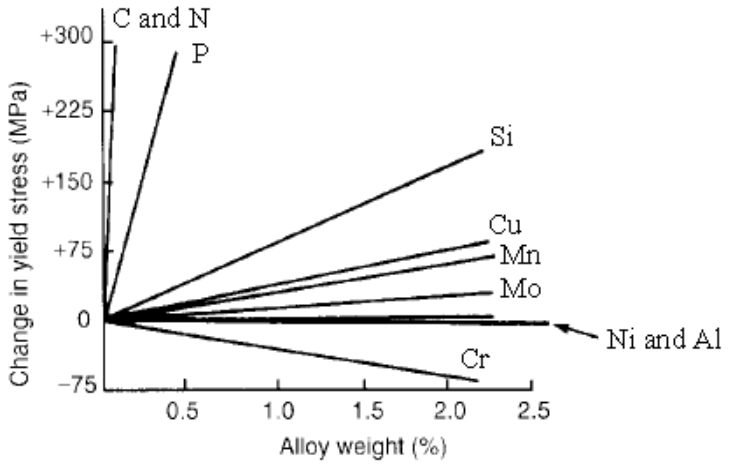

Figure 2-18 Solid solution strengthening effects (σ_{ys} vs. solute contents in wt%) in ferrite-pearlite steels. [65]

Table 2-6 Solid solution strengthening coefficients in ferrite-pearlite steels [63]

Solute	C, N	Si	Cu	Mn	Mo	Ni	Cr	Ti	Nb
k_i (MPa)	4620, 5544	83	39	31[68], 32[69]	11	0	-31	80	2400 [70]

2-3-3. Precipitation strengthening due to second-phase particles

2-3-3-1. Precipitation strengthening mechanism - precipitate and dislocation interaction

Precipitation or dispersion strengthening is another strengthening method using second phase particles as obstacles to impede dislocation motion. Different strengthening mechanisms have been proposed in the literature depending on how the dislocations interact with the precipitates, such as chemical strengthening, stacking fault energy strengthening, modulus strengthening due to differences in shear modulus, coherency strengthening and order strengthening due to ordered precipitates. [71] It is not within the scope of this thesis to go into the details for these different mechanisms. Refer to Ardell [71] for a more comprehensive understanding. To summarize briefly, the interaction between precipitates and dislocations can be classified into two categories: precipitate cutting (shearing) and Orowan looping (bypassing). For the first condition, the dislocations cut and penetrate the precipitates. For very hard particles, the dislocations will not likely be able to shear the precipitates; Orowan looping becomes the primary strengthening mechanism.

The precipitate cutting mechanism is shown in Figure 2-19, [12] where an edge dislocation cuts through a deformable precipitate. In the precipitate cutting mechanism, precipitates are involved in plastic deformation and this mechanism occurs with deformable particles.

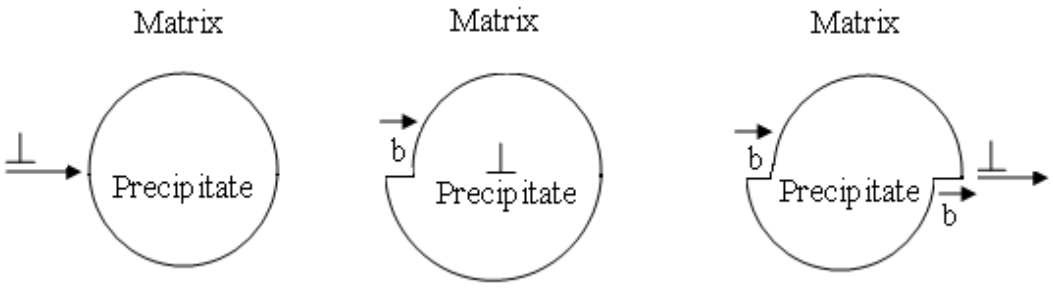

Figure 2-19 Schematic illustration of an edge dislocation cutting a deformable precipitate. [12]

Orowan looping happens when the precipitates are non-deformable. The dislocation is pinned by the strong undeformable precipitates, making the dislocation bow around the precipitate. The bowing process creates more dislocation lines and increases the energy of the system. Eventually, the dislocation line from adjacent loops will touch, allowing the dislocation to glide leaving behind a dislocation loop. [12,72] Figure 2-20 shows a dislocation line meeting a line of hard second-phase particles and the loops between them. [12]

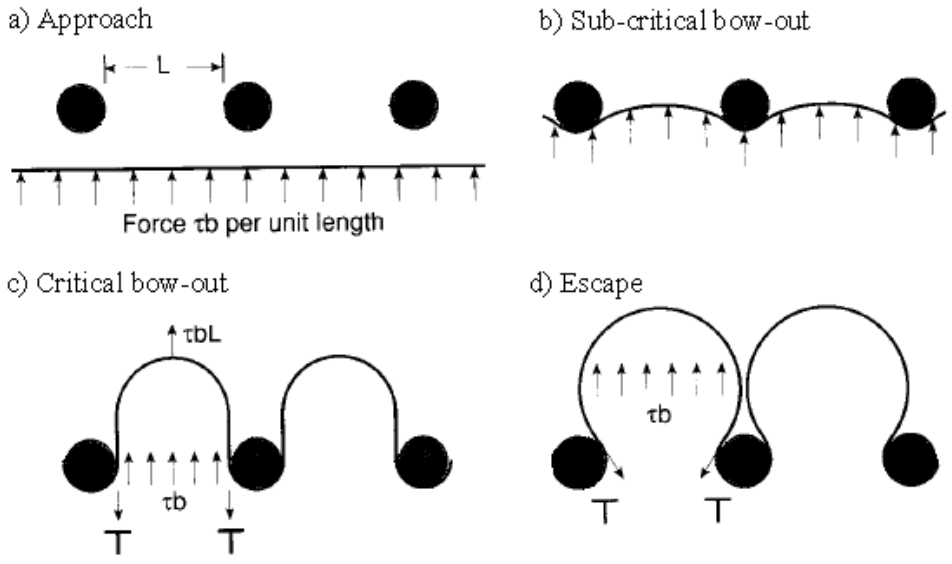

Figure 2-20 Schematic illustration of a dislocation bowing around a line of hard undeformable precipitates - Orowan looping. [12]

2-3-3-2. Precipitation strengthening based on Orowan looping model

The basic model for dislocation looping was developed by Orowan. [73] Figure 2-21 shows a dislocation pinned by three precipitates. [12] A list of notations used in this section is shown as follows.

F: repelling force of the particle;

F_1: line tension of a dislocation;

L: effective particle spacing;

θ': half angle corresponding to the arc of the dislocation;

R_d: radius of the curvature of the bowing dislocation;

τ: shear stress;

b: Burgers vector of the dislocation;

G: shear modulus of the material, i.e., steel in this work.

The general theory of Orowan looping model is related to the resisting force (F), the effective particle spacing (L) and the shear stress (τ). At the force balance condition,

$$F = 2F_1 \cos(90 - \theta') \tag{2-10}$$

Assuming F_1 is independent of the character of the dislocation (edge, screw, or mixed), then

$$\tau \cdot b = \frac{F_1}{R_d} \tag{2-11}$$

From geometry:

$$R_d = \frac{L}{2\sin(\theta')} \tag{2-12}$$

Thus:

$$\tau \cdot b = \frac{2F_1 \sin(\theta')}{L} \tag{2-13}$$

From Equation (2-10) and (2-13) gives:

$$\tau = \frac{F}{bL} \tag{2-14}$$

When θ' reached 90º, $F = 2F_1$

$$\tau = \frac{2F_1}{bL} \tag{2-15}$$

The dependency of the line tension of the dislocation on the shear modulus of the material gives

$$F_1 \approx \frac{Gb^2}{2} \tag{2-16}$$

Expressing Equation (2-17) in terms of τ yields the Orowan equation:

$$\tau = \frac{Gb}{L} \tag{2-17}$$

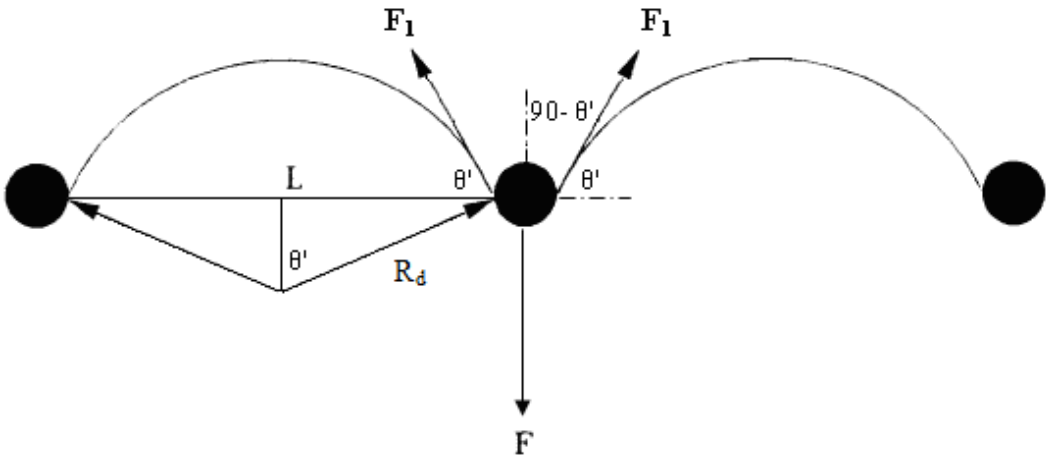

Figure 2-21 A dislocation line is pinned by precipitates with separation *L*. [12]

Ashby further modified the effect of precipitation strengthening on the strength of a material based on the Orowan model and came up with the Ashby-Orowan model.

$$\tau = 0.84\left(\frac{1.2Gb}{2\pi L}\right)\ln\left(\frac{x}{2b}\right) \tag{2-18}$$

where *x* is the average diameter of the precipitates in the intersection plane, which is related to the actual precipitate diameter (*X*) according to

$$X = \left(\frac{3}{2}\right)^{\frac{1}{2}} x \tag{2-19}$$

x can be related to the precipitate volume fraction (f_v) and the number of precipitates per unit area (n_A) as follows:

$$f_v = n_A \cdot \pi \cdot x^2 / 4 \tag{2-20}$$

$$L = \left(\frac{1}{n_A}\right)^{\frac{1}{2}} \tag{2-21}$$

Substituting G = 80.3 GPa, $b = 2.5\times10^{-10}$ m and multiplying the shear stress (τ) by the Taylor factor (M' = 3), [12] gives the precipitation effect on the strength of the material (Ashby-Orowan equation).

$$\sigma_{ppt}\,(MPa) = \left(\frac{10.8\, f_v^{\,1/2}}{X}\right) \ln\left(\frac{X}{6.125\times10^{-4}}\right) \tag{2-22}$$

σ_{ppt}: the strength increase due to precipitation strengthening;

X: the size of precipitates in microns;

f_v: the volume fraction of a given precipitate size (X).

It can be seen that precipitation strengthening increases as the square root of the volume fraction of the precipitates. Strength also increases as the average precipitate size decreases, since the effect of particle size ($1/X$) dominates over $Ln(X/6.125\times10^{-4})$. For a given volume fraction of precipitates, refinement of particle size means a higher number density of precipitates, which means a higher number of interactions between precipitates and the matrix. Thus, a significant increase in yield stress can be produced. Therefore, refining the precipitate size and increasing the volume fraction of precipitates are very important issues to improving material strength.

2-3-3-3. Precipitate-matrix interface

Precipitates usually have a different crystal structure and composition from the matrix. They can generate stresses and strains similar to solute atoms in solid

solution. The precipitation strengthening effect depends on the precipitate-matrix interface structure, so that precipitates can be categorized into coherent, semi-coherent or incoherent precipitates.

A coherent precipitate is one where the lattice planes of the precipitate and the matrix are perfectly aligned and in complete coincidence. Complete continuity between the lattice planes exists. The interface between the coherent precipitate and the matrix is called a coherent interface, where the atoms match up on a one to one basis (perfect atomic matching at the boundary.) In almost all cases, the lattice parameter of the precipitate is different from that of the matrix, as shown in Figure 2-22. [74] In this example, the precipitate has a larger lattice parameter than the matrix, generating a compressive strain field in the surrounding matrix.

If there is not complete continuity in the lattice planes between the precipitate and the matrix, the precipitate and matrix interface is called semi-coherent or incoherent. This type of precipitation usually happens when a coherent structure is not allowed because of the crystal structure of precipitate and the matrix, or when the lattice parameter difference between the precipitate and the matrix is too large.

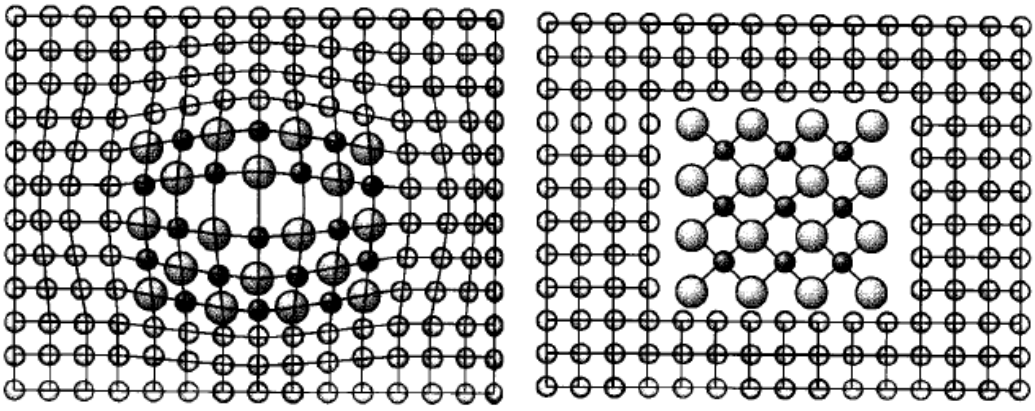

Figure 2-22 Precipitate - matrix interface. [74]

Coherent precipitate (left): complete continuity between the lattice planes.

In-coherent precipitate (right): no relationship between the lattice planes.

Coherent precipitates usually have the largest stress field associated with them and offer the greatest resistance to dislocation glide due to the elastic dislocation-precipitate interaction, even if the dislocation merely passes near the coherent

precipitate. Non-coherent precipitates cannot effectively impede dislocation motion except when they lie in the dislocation path.

It is possible that a precipitate may nucleate coherently initially, but lose its coherency as the particle grows larger. The loss of coherency happens when the stress field around the precipitate is large enough for dislocations to be generated.

2-3-4. Dislocation strengthening

Dislocation strengthening is achieved by an increase in dislocation density and a change in dislocation arrangement (e.g., forest dislocations, cell structures or sub-grain structures) through cold plastic deformation. [12] The dislocations may mutually tangle with each other, hinder dislocation motion and increase the strength. Forest dislocation strengthening is generally calculated as follows. [75, 76]

$$\sigma_{dis} = \alpha M' G b \rho^{1/2} \tag{2-23}$$

σ_{dis}: strengthening contribution due to dislocations;

α: dimensionless coefficient with a value of 0.38 when the stress is calculated in kg/mm^2;

M': Taylor factor;

G: shear modulus of the steel;

b: magnitude of Burgers vector;

ρ: dislocation density.

Dislocation strengthening is not included in hot-rolled or normalized microalloyed steels by Gladman because cold deformation is not commonly used in these steels. [12] Therefore, it is expected that dislocation strengthening does not have a significant contribution to strengthening. Dislocation strengthening should be considered in steels substantially deformed below ~700ºC. These steels usually have substructures in the form of dislocation cells or sub-grains and each sub-grain is separated by a low angle sub-grain boundary. [12]

2-3-5. Texture strengthening

Texture effects are related to differences in the tensile strength along the rolling direction and transverse to the rolling direction. However, texture strengthening does not have a significant contribution and was addressed by Gladman because the development of texture is difficult in steels having a dispersed second phase. [12]

2-3-6. Combined strengthening mechanisms (interaction and superposition of strengthening mechanisms) in steel

As explained previously, material strengthening is always related to the hindering of dislocation motion in metals. Dislocation motion is controlled by the microstructure of a material which includes short and long-range barriers to dislocation motion. The short-range barriers affect a dislocation by changing its position within the lattice and include the lattice friction stress (also called Peierls-Nabarro barrier) and dislocation forests. The lattice friction stress is the controlling short-range barriers in BCC metals, while dislocation forests are the controlling short-range barriers in FCC and HCP metals. The inter-barrier spacing of longe-range barriers is several orders of magnitude greater than the lattice spacing. Long-range barriers include point defects (solute and vacancies), precipitates, boundaries (twin, grain, etc.) and other dislocations in the material. [77]

In steels, there are normally several phases present in the microstructure. The matrix, which is usually BCC ferrite or FCC austenite, strengthened by grain size refinement and solid solution strengthening, is further strengthened by precipitation strengthening through the control of dispersions in the microstructure. The most common other phases are carbides formed as a result of the low solubility of carbon in α-Fe. In plain carbon steels this carbide is normally Fe_3C (cementite), which can occur in a wide range of structures from coarse lamellae (pearlite) to fine rod or spheroidal precipitates (tempered steels). In alloy steels, the same range of structures is encountered, except that in many cases iron

carbide is replaced by more stable dispersed phases, which include Ti, Nb and/or V-carbides, nitrides or carbonitrides.

2-3-6-1. Linear model

The strength contributions from the lattice friction stress of iron, grain boundary strengthening, solid solution and dispersion effects are superimposed and the effect of individual strengthening contributions can be quantitatively estimated by a linear model. [12]

$$\sigma_{ys}(MPa) = \sigma_i + \sigma_{gb} + \sigma_{ss} + \sigma_{ppt} = \sigma_i + k_y\, d^{-1/2} + \sum k_i C_i + \sum \left(\frac{10.8 f_v^{1/2}}{X} \right) \ln \left(\frac{X}{6.125 \times 10^{-4}} \right) \quad (2\text{-}24)$$

σ_{ys}: yield stress;

σ_i: lattice friction stress of iron (or Peierls-Nabarro barrier);

σ_{gb}: strengthening contribution due to grain boundaries;

σ_{ss}: strengthening contribution due to solid solution;

σ_{ppt}: strengthening contribution due to precipitation;

k_y: strengthening coefficient for grain size;

d: grain diameter in microns;

k_i: strengthening coefficient for solute strengthening of solute i;

C_i: concentration of solute i;

X: size of precipitates in microns;

f_v: volume fraction of a given precipitate size (X).

When the structural scales of the strengthening contributions are very different or the strengthening mechanisms are independent, linear superposition can be assumed to be valid. [78] One example is the lattice friction stress of iron and grain boundary strengthening; the former is on the scale of atomic distances and the latter is on the scale of microns. Linear superposition of these two strengthening contributions should be valid because of their different structural scales. Solid solution strengthening and grain size refinement have independent strengthening mechanisms. [62] Linear superposition of these two individual

contributions should also be valid. However, when commercial microalloyed steels treated by TMCP are studied, the linear model usually overestimates the yield strength. [75] It is believed that synergy between different strengthening mechanisms exists.

There is little evidence to show that solid solution strengthening and precipitation strengthening are independent. Solutes, which have a substantial effect on the matrix deformation character, can affect the stresses at which the precipitates become shearable. Therefore, the matrix slip character may change the precipitation strengthening mechanism from Orowan looping to precipitate cutting by changing the interaction between dislocation and precipitates. However, the solute concentration is relatively low for microalloyed steels. Solid solution strengthening and precipitation strengthening effects appear to be linear if the matrix deformation character does not change appreciably. [79,80] Similarly, the strengthening contribution due to solute strengthening and dislocation strengthening can be considered in a linear relationship.

It has been reported that there is strong synergism between grain boundary and particle hardening. [81] Due to thermo-mechanical controlled processing and solubility changes in precipitates, there is mutual interaction between grain refinement and precipitation strengthening in microalloyed steel systems. Precipitation occurs in austenite, which helps maintain a fine austenite grain size prior to transformation. These precipitates, typically carbides, nitrides and/or carbonitrides of Nb and Ti, are >20nm in size. [82] Deformation in the recrystallization region will assist in the formation of fine ferrite grains [83], dislocation strengthened forms of ferrite [84] and strain-induced precipitation. [33] The remaining precipitation materials will be able to form fine particles (<20nm), especially those smaller than 5 nm in size that form during or after transformation from austenite to ferrite and contribute significantly to dispersion strengthening. [8]

No detailed information has been reported about the interaction between precipitation strengthening and dislocation strengthening. However, from the mechanism of precipitation strengthening, precipitates must affect the distribution

and movement of dislocations as well as the deformation character of the matrix. A change in dislocation structure, such as density and the mean free path, will also affect precipitation strengthening. This indicates that precipitation strengthening and dislocation strengthening interact with each other rather than act independently. The relationship between precipitation strengthening and dislocation hardening is no longer linear. [80] In microalloyed steels, the interaction between precipitation strengthening and dislocation strengthening cannot be ignored due to the high amount of precipitates present.

It is known that dislocation motion can be effectively impeded by grain boundaries. It has been found that dislocations can be created at grain boundaries and subgrain boundaries during the yielding process. [85] Many of the dislocations can form cell or subgrain boundaries by deformation as well. [85,86] This indicates that there is an interaction between grain boundary strengthening and dislocation strengthening. As mentioned in Section 2-3-4, steels with substantial deformation below ~700ºC usually have substructures in the form of dislocation cells or sub-grains and each sub-grain is separated by a low angle sub-grain boundary. [12] The dislocation strengthening contribution may be included to some degree in the grain size term in the form of sub-grain boundaries. However, dislocation strengthening does not have a significant strengthening contribution in hot-rolled or normalized microalloyed steels because cold deformation is not commonly used in these steels. [12]

Because of the belief of synergism between different strengthening mechanisms, different models have been proposed, which will be briefly discussed below.

2-3-6-2. General superposition [71,87,88,89,90,91]

If more than one type of strengthening mechanisms is present in a grain, the total critical resolved shear stress (CRSS) of the grain will be a superposition of the individual strengthening contributions. A general approximation of the strengthening can be expressed as:

$$\tau^q = \sum \tau_i^q \qquad (2\text{-}25)$$

Thus, the superposition problem is changed to finding the values for *q*, an adjustable parameter that is appropriate for the system. The exponent *q* has a value between 1.0 and 2.0. Values of *q* equal to 1.0 and 2.0 would yield a linear model and a Pythagorean model, respectively.

2-3-6-3. Pythagorean superposition [75,92,93]

The root mean square summation is used to determine the flow stress due to different strengthening contributions, and is applicable to a wider range of situations.

$$\sigma = \sqrt{\sigma_1^{\,2} + \sigma_2^{\,2}} \tag{2-26}$$

σ_1, $\sigma_{2:}$ flow stresses associated with different strengthening modes.

It can be seen that the superposition of strengthening mechanisms is not straightforward and there is no general method to approach this problem. There are a number of ways to evaluate the experimental data in order to differentiate between different strengthening contributions.

In order to understand the strengthening mechanisms and to optimize the strengthening effects by controlling processing parameters, it is necessary to study steel microstructure and to quantify the size distribution, volume fraction and chemical speciation of different sized precipitates. However, it is challenging work because of fine particle sizes, wide particle size distributions and low volume fractions of precipitates. Another difficulty is that precipitates with different sizes all have the same crystal structure, with similar lattice parameters. In the past, researchers have mainly relied on conventional metallographic methods to characterize precipitates. However, the results are not satisfactory for quantifying these precipitates because of the sampling issue. For example, a very small volume of material is analyzed using TEM. Reliable quantitative techniques are required to be developed, from which relatively large volumes of material can be analyzed and statistically significant quantities of precipitates of different sizes are characterized.

2-4. Characterization of precipitates

2-4-1. Conventional metallographic methods

Microscopic methods are commonly used for characterizing precipitates. Only very large precipitates, several microns in size can be seen by optical microscopy (OM). Precipitates with sizes down to 100 nm can be observed through scanning electron microscopy (SEM) and the chemistry can be determined through energy dispersive x-ray (EDX) spectroscopy. Transmission electron microscopy (TEM) has superior imaging resolution, which can be used to observe precipitates with sizes down to a few nm and the chemistry can also be determined by EDX analysis. However, when it comes to precipitate quantification, microscopy methods do have limitations because of the limited resolution in OM and SEM and sampling issues in TEM.

Thin foils and replicas are the two main sample methods used in TEM. Thin foils are good for precipitate-matrix orientation and precipitate distribution studies. Extraction replicas have been widely used for studying different precipitates because of the ease of sample preparation. [94,95,96] Carbon and non-carbon replicas (such as Ni [97]) have traditionally been use in the past. Currently, carbon replicas are the most widely used method.

For both sample types used in TEM, the sample size is quite small, i.e. less than 10 μm^3 in volume. Therefore, the first issue associated with TEM is whether the sample examined is representative of the bulk material which is produced from ingots or slabs larger than 1 m^3 in volume. Secondly, quantification may be in error, because of particle overlap; small particles may be obscured by a larger particle. [98] Thirdly, for thin foil samples, particles may intersect the thin foil surface. If the particle center is outside the foil sample, the particles are partially removed or attacked by the polishing agent during the sample preparation process and consequently show a smaller radius. [98,99] Finally, accurate determination of sample thickness for both thin foil and carbon replicas is a critical problem for the precipitate quantification.

Carbon replicas have been mainly used to qualitatively analyze precipitates, i.e., imaging and chemistry studies. Some researchers have tried to use this

technique combined with TEM to determine the volume fraction of precipitates. However, determination of the volume fraction of the precipitates depends on the accurate determination of the sample thickness, from which the particles were extracted. This is not straightforward and prone to significant errors. Abrams [100] has derived an analytical expression to measure the sampling thickness of an extraction replica, i.e., a preshadowed extraction replica technique which is based on shadow length, shadowing angle and diameter of the largest particle. This assumption is valid if there is a large size difference between the maximum and the average particle diameters. Under this condition, the volume of the largest particle plays a more crucial role in determining when the replica will detach and float free. If particle dispersion is more uniform, which means a large volume fraction of precipitates of uniform size is present, the effective replica thickness may not be directly related to the maximum particle diameter. The volume fraction values obtained by the preshadowed extraction replica technique will then be in error. McCall and Boyd used the preshadowed extraction replica technique to determine the volume fraction of γ' particles in γ'-strengthened superalloys, which have a uniform dispersion of particles. Later Abram [101] modified their calculations. However, a wide scatter in the volume fraction values was obtained (ranging from 0.40 to 6.40 vol%).

Other microscopic methods, such as scanning transmission electron microscopy (STEM), atomic-force microscopy (AFM) and field ion microscopy (FIM) with atom probe (AP) also provide high resolution information, but suffer from many of the above limitations, as well as others, which limit their applicability to quantification. Because of the low volume of precipitates in the steel and possibly large errors involved in microscopy techniques, microscopy methods are not completely satisfactory for quantification of the volume fraction of precipitates in steels.

2-4-2. Precipitate volume quantification by small angle neutron scattering (SANS)

Small-angle neutron scattering (SANS) can be used to measure the size and volume fraction of nano-precipitates. Staron et al [102] used the SANS technique to determine precipitate size distributions and volume fractions in a maraging steel. Perrard and co-workers [103] also successfully measured the volume fraction and size of NbC precipitates in model interstitial free (IF) steel using the SANS method.

The size range of conventional SANS is approximately 2 nm to 100 nm. Larger sizes may be obtained for strong scatterers. With this method, a larger volume of material is used because of the large penetration depth of neutrons. The ferromagnetic matrix is magnetized to saturation and scattered neutrons are recorded. Because the precipitates are non-magnetic, they can be treated as "magnetic holes" in the ferromagnetic matrix. Therefore, precipitate size distribution and volume fraction of the precipitates can be obtained from the magnetic cross section. [102] This method cannot distinguish between different types of precipitates; only the size distribution of all precipitates is measured. An additional technique, such as XRD or TEM, must be used to identify specific types of precipitates.

2-4-3. Matrix dissolution combined with other techniques

The matrix dissolution method is a very promising technique to quantify precipitates in microalloyed steels, based on samples that are more representative of the steel strip. Relatively large volumes of material, e.g., a few cm^3, are analyzed, so that statistically significant quantities of precipitates of different sizes are collected. The extracted precipitates can be specifically identified using TEM to study the size, distribution and chemistry (EDX) without interference from the matrix. X-ray diffraction (XRD) can also be used to analyze the extracted precipitates, providing valuable crystallographic information. Rietveld refinement based on XRD data can be used for refining precipitate structures and to obtain

their relative abundance, making it possible to determine the volume fraction of precipitates in the steel.

In summary, examination of the isolated precipitates obtained by dissolution of the steel matrix can yield more information about shape, size and amount of the precipitates compared with conventional metallographic methods.

2-5. Matrix dissolution and precipitate collection

Matrix dissolution is a method to selectively dissolve the matrix while leaving the precipitates unattacked, which can then be extracted. In the following section (especially Table 2-7 and Table 2-8), it is clear that matrix dissolution has previously been used mainly to qualitatively characterize the nature of inclusions or precipitates. Only in a few instances have the size distributions been analyzed. This technique has not been used to quantify the volume fraction of precipitates yet, particularly nano-precipitates. Matrix dissolution, combined with centrifuging, is a promising technique to accurately determine the volume fraction of precipitates, which can then be correlated to the strengthening and processing history of microalloyed pipeline steels. This approach will be used in the present thesis for microstructural quantification.

Matrix dissolution can be done either chemically or electrolytically. [104,105,106] Chemical dissolution can be further classified into two broad categories: acid dissolution and halogen-based, mildly alcoholic dissolution [104], such as bromine in methanol, iodine in methanol and iodine-methanol-methyl acetate. [104,107]

2-5-1. Chemical dissolution method

2-5-1-1. Chemical dissolution- acid dissolution method

Various acids, such as HCl, H_2SO_4 and HNO_3, have been reported in the literature to extract different particles. Only those phases stable in acids, such as silica, alumina [104] and some carbides and nitrides, have been successfully extracted. Unstable phases, such as MnS and Fe_3C, were not extracted, as reported by Kanazawa and Bandi [108,109].

ASTM designation E194-99 [110] is a standard test method to determine acid-insoluble content of iron powders. In this standard, a dilute HCl solution is used. Insoluble matter, such as carbides, silica, insoluble silicates, alumina, clays and other refractory materials, can be collected.

HCl can be used to extract insoluble precipitates, such as Ti and Nb carbonitrides, from steel. The reaction product $FeCl_2$, from the reaction of Fe and HCl, is soluble in HCl, H_2O and ethanol. Therefore, it is possible to remove $FeCl_2$ from the solution, leaving insoluble particles.

Fernandes et al. [111] studied the morphology (shape), size, amount and chemical composition of nonmetallic inclusions by dissolving the ferrite matrix in HCl and HNO_3. They extracted micron size non-metallic oxide inclusions (Al_2O_3, SiO_2 and TiO_2), carbides and nitrides by a filtering process with a micron size filter.

Kanazawa et al. [108] used HCl acid extraction, combined with a centrifugal process, and successfully separated insoluble NbC and Mo_2C precipitates from steel. Using a combination of Scherrer and TEM diffraction, they determined the particle size of the NbC precipitates to be in the range of 12 to 21 nm. Mori and Fujita [112] extracted Nb carbonitrides from steel with 6N- HCl acid.

Brunckovan and Niznik have reported the extraction of Ti and Nb carbonitrides using 3 M H_2SO_4 followed by filtration using a filter pore size of 0.25 mm. [113] HNO_3 and HF acids are not recommended for many microalloyed steels, because TiC can be dissolved in HNO_3. FeF_2 is insoluble in ethanol [114] and only slightly soluble in H_2O and HF.

2-5-1-2. Chemical dissolution- halogen based, mildly alcoholic solutions

Halogen-based separation is perhaps the oldest dissolution technique. There are several chemical combinations: bromine in methanol or ethanol, iodine in methanol or ethanol and iodine-methanol-methyl acetate. [115] Br_2 and I_2 have good solubility in organic solvents, such as ethanol, methanol and methyl acetate. The reaction products of Br_2 and I_2 with the steel matrix ($FeBr_2$ and FeI_2) also have good solubility in H_2O and in ethanol. Therefore, they can be removed from the solution, leaving undissolved particles to be collected. The solubility of Br_2

and I_2 is very low in water; therefore, water is not suggested as the extraction reagent.

An alcoholic solution of iodine, which was first proposed by Willems in 1928, is the mildest treatment. [116] This procedure is still in use to isolate chemically unstable phases such as Fe_3C [115], MnO, MnS [117] and FeS [109]. It also has been used to isolate carbides such as Cr_2C, Cr_7C_3, and $Cr_{23}C_6$. [109] The reaction rate for this method is very slow, and the temperature is always kept at 60-65ºC. [107,115] A number of solvents other than alcohol have been used, such as acetone, benzene and carbon tetrachloride, but the results have not been satisfactory, which is mainly because of the insolubility of iron iodine. [117]

It is generally considered that treatments with Br_2 and non-aqueous solvents are the best methods for separating stable oxides (Al_2O_3, Cr_2O_3, Fe_2O_3, FeO, ZrO, etc) and nitrides (AlN and ZrN) from the steel. [109,115,118] The Br_2 mixtures should not be used for separation of carbides, because too many carbides dissolve, leaving a residue of amorphous carbon. [109,119] One difference between the iodine and bromine methods is that Br_2 mixtures can dissolve away nitrides of iron and manganese and sulphides of iron at ordinary temperatures together with the matrix, all of which are insoluble by the iodine method even at 60ºC. [120,121] Bromine has one interesting property. It does not react with the steel in the absence of the solvent, even on prolonged contact with the steel at the boiling temperature of bromine. However, a few drops of the solvent will initiate the reaction. [118] The reaction, once initiated, is very strong even at room temperature; the temperature will rise to the boiling point of the solvent because of the exothermic reaction. Therefore, the reaction must be controlled. Smerko and Flinchbaugh [115] proposed several experimental procedures, such as drop-wise addition of the solvent to restrict the amount of methanol in contact with the bromine and then to control the vigorous dissolution reaction. Performing the dissolution in an ice water bath (Pasztor and Raybeck procedure) is also a good way to control the reaction. [115]

A summary of the various chemical extraction methods, based on the precipitates to be identified, is shown in Table 2-7.

Table 2-7 Chemical extraction

Solution	Condition	Residues Extracted	Size
50 vol% HCl	Room temperature	Insoluble carbides, silica, silicates, alumina, clays and other refractory materials [110]	
HCl, HNO_3		Al_2O_3, SiO_2, TiO_2, carbides and nitrides [111]	1-10 μm
HCl,		NbC and Mo_2C [108]	12-21 nm
6N- HCl acid		Nb carbonitrides [112]	
H_2SO_4		BN [122,123], AlN [124], Ti and Nb carbonitrides [113]	
$CuCl_2.2H_2O$, KCl, $HOOC[CHOH]_2COOH$, HCl, H_2O		Cr-N precipitate [125]	
Alcoholic solution of iodine	60-65°C	Fe_3C, MnO, MnS, [119] FeS, Cr_2C, Cr_7C_3 and $Cr_{23}C_6$ [109]	
Br_2 and non-aqueous solvents	Room temperature	Al_2O_3, Cr_2O_3, Fe_2O_3, FeO, ZrO, AlN and ZrN [109,115,118]	

2-5-2. Electrolytic dissolution

Electrolytic dissolution is a selective dissolution process, during which an anode and cathode are suspended in a cell with an electrolyte. Different dissolution behaviors of the various precipitates and the steel matrix make it possible to selectively extract precipitates from steel, i.e. the ferrite matrix is dissolved at low anodic potentials, while precipitates are more noble and are dissolved at higher potentials.

During electrolytic dissolution, the steel sample works as the anode and a voltage or current is supplied across the anode and cathode. With the combination of the electrolyte and either an applied voltage or current, the steel matrix is dissolved while the second phases are retained as a residue. Inclusion and precipitate extraction can be altered by choosing different electrolytes from the more than one hundred electrolytes that have been proposed in the literature. [126,127,128,129,130] A partial list is given in Table 2-8 according to the precipitates to be identified. Voltages can be adjusted to dissolve the less stable phases and to allow only the electrochemically stable phases to be isolated. [104]

Read et al. [105] extracted nano-sized Nb carbonitrides from HSLA steel by electrolytic dissolution using a 'slime' cell. Only the size distribution was studied; volume fractions were not determined. In their work, the cathode was a stainless steel mesh and the electrolyte was a 15% $FeCl_2$ aqueous solution. A current density of 30mA/cm^2 was maintained throughout electrolysis at the electrodes. Iron was deposited at the cathode and slime was collected at the base of the cell. The slime was composed of cementite, iron rust, basic iron salts, metallic iron and inclusions. The electrolyte was centrifuged to separate the solid and liquid. Chemical treatments of the slime were then carried out, followed by centrifuging to dissolve the metallic iron and separate inclusions and precipitates.

Although electrolytic dissolution methods have been used for a long time, several difficulties exist. First of all, selective dissolution often results in the loss of electrochemically unstable phases such as FeS, MnO and Fe_3C, as well as certain nitrides and carbides. [131] Therefore, the current or potential applied has to be carefully controlled so that only the matrix is dissolved, while the precipitates are unaffected. Secondly, careful selection of the electrolyte must be done, because the electrolyte has a significant influence on the electrolysis process and on the extraction ratio. The electrolyte should: (a) be chemically inert with respect to the extracted residues, (b) protect the metallic ions dissolved from a specimen against oxidation and subsequent sedimentation and (c) protect a specimen from passivation. [132]

Therefore, the electrolytic method is more complex than chemical dissolution. The dissolving parameters, such as current and potential should be closely controlled. Bandi [109] found that potentiostatic dissolution is not the best method for isolating stable nitrides and not generally the best method for isolating carbides. However, it is often the only method applicable for specific chemically unstable phases. This is why Brunckova extracted MnS inclusions by electrochemical methods. [124]

It should be noted that matrix dissolution is good at supplying enough precipitates for quantification. However, it cannot be used exclusively to characterize precipitates, such as precipitate-matrix orientation. Since the steel

matrix is dissolved, the location of a precipitate, and its relationship with respect to the matrix, cannot be identified. TEM or other techniques must, therefore, be used in a complimentary manner.

Table 2-8 Electrolytic extraction

Electrolyte	Condition	Residues Extracted	Size
Mixture of concentrated hydrochloride acid, acetic acid, hydrogen peroxide	1.2 V vs. SCE, 50°C	(Nb, Ti)C [133]	5-1000 μm
15% $FeCl_2$, then 10% HCl, 10% bromine/ethanol	30 mA/cm^2	Nb(C,N) [105]	2-120 nm
20% H_3PO_4	20 mA/cm^2, room temperature	Ni_3Mo, Ni_3Ti, FeMo [134]	
10% acetyl acetone, 1% TMAC, methanol			
1% salicilic acid, 4% salicilic methyl, 1% TMAC, methanol			
1% salicylic acid, 4% methyl salicylate, 1% TMAC, methanol	20 mA/cm^2, Ar	TiN, TiS, MnS, $Ti4C_2S_2$ [106]	
10% $FeCl_2$	Current 5-10 A	Al, Si-inclusions [135]	> 50 μm
LiCl	-50 mV vs. SCE	TiC, Fe_3C [129]	< 0.1 μm
TMAC	-120 mV vs. SCE	Ti(C, N), Nb(C, N), Si_4N_3, AlN, Zr(C, N), Fe_3C [129]	
	-100 mV vs. SCE	(Ca,Mn,Fe)S [129]	
TMAC + BaO	40 mA/cm^2		
10% acetylacetone, 1% TMAC, MeOH	-150 mV vs. SCE, room temperature	(Ca, Fe, Mn)S, CaO-Al_2O_3, CaO-SiO_2 [130]	
4% salicylic acid, 2% LiCl, MeOH			
3% methyl salicylate, 1% salicylic acid, 1% TMAC, MeOH	-100 mV vs. SCE, room temperature		
2% triethanolamine, 1% TMAC, 0.04% BaO, MeOH	40 mA/cm^2, room temperature		
5% EDTA+1% NaF (or NaCl, LiCl, NaBr, NaI, KCl to increase the conductivity)	-470 mV vs. SCE, N_2, room temperature	Cementite [132]	
EDTA	-200 mV vs. SCE	BN, Fe_3C [123]	
10% HCl-methanol	1-2 V vs. Pt cathode	Mo_2C [136]	
$HNO_3/H_3PO_4/H_2SO_4$, Vol%= 41/12/47	7-8 Volts, 0.18A/cm^2, room	(Cb, Ti, Al)C [137]	

or HCl/H_2O, Vol%= 10/90	temperature		
20% NaCl, 6% trisodium acetate, and 2% citric acid, H_2O, pH= 4.1		MnS [124]	
5% sodium citrate, 1.2% KBr, 0.5% ascorbic acid, H_2O, pH= 5.6-5.8			
1% $(NH_4)_2SO_4$, 1% tartaric acid, H_2O or 1% $(NH_4)_2SO_4$, 1% citric acid, H_2O or 3% HNO_3, 2% $HClO_4$, methyl alcohol	850 or 1350 mV vs. Ag/AgCl	γ', γ", carbides [138,139]	

TMAC: tetra-methyl ammonium chloride;

γ': $(Ll_2)Ni_3Cb$; γ": $(DO_{22})Ni_3Cb$.

2-5-3. Precipitate collection

For matrix dissolution, there are two main methods to collect particles from the solution: centrifuging or filtering. Filtering is widely used to extract micron-sized particles. Centrifuging is a better choice to collect submicron precipitates. Once the precipitates are collected, the overall precipitate chemistry can be analyzed by SEM-EDX. Phase identification and the relative abundance can be determined by x-ray diffraction (XRD).

2-6. X-ray diffraction and Rietveld refinement

2-6-1. X-ray diffraction (XRD)

2-6-1-1. Bragg's law

X-rays are a form of electromagnetic radiation with high energies and short wavelengths. When a beam of x-rays impinges on crystals, interference occurs because of the periodic atomic structure of crystals, which is called x-ray diffraction (XRD). The constructive interference between x-rays and crystals follows Bragg's law, as shown in Figure 2-23, and is expressed in the following equation.

$$n\lambda = 2d_{hkl}\sin\theta \qquad (2\text{-}27)$$

n: order of the reflection;

λ: wavelength of the x-rays;

d_{hkl}: interplanar distance with h, k, l Miller indices;

θ: x-ray beam incident angle.

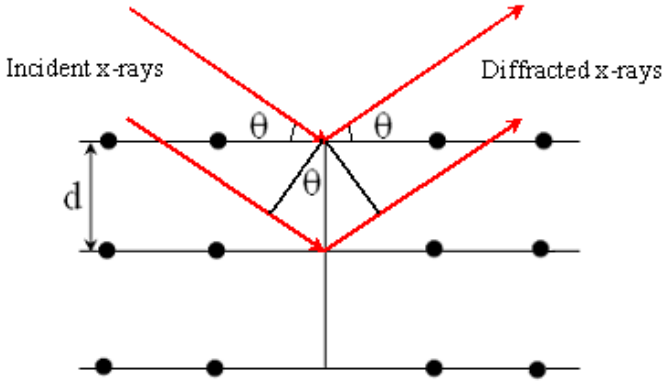

Figure 2-23 Schematic of Bragg's law.

The interplanar distance d_{hkl} is a function of the Miller indices (h, k and l) as well as the lattice parameter(s). For example, for cubic phases, the relationship between d_{hkl} and lattice parameter (unit cell edge length a) can be expressed as

$$d_{hkl} = \frac{a}{\sqrt{h^2 + k^2 + l^2}} \qquad (2\text{-}28)$$

Because of the relationship between the interplanar distance, Miller indices and lattice parameters, XRD is best known for crystal structure determination. It has also been used in qualitative phase identification (phase identification by comparison with standard patterns) as well as residual stresses and crystal size determination. With the developments in quantitative phase analysis of crystalline mixtures, for example, determination of the relative abundance of different phases, x-ray diffraction is widely used because of the speed and simplicity of data collection.

2-6-1-2. XRD equipment setup

Figure 2-24 shows the XRD setup (θ: θ goniometer). The main components include an x-ray source, a divergent slit (DS), soller slits (SL), scatter slits (ScS),

a receiving slit (RS) and a detector. Soller slits are parallel plates, which are used to create a parallel incident beam. The scatter slits on the incident beam side are used to control the width of the beam that impinges on the specimen. The receiving slits are used to control the width of the beam entering the detector.

A sample should be centered in the measuring circle and be tangent to the focusing circle. The focusing circle changes radius with angle θ. For the θ: θ goniometer, the sample is stationary in the horizontal position. The x-ray tube and the detector move simultaneously over the angular range θ.

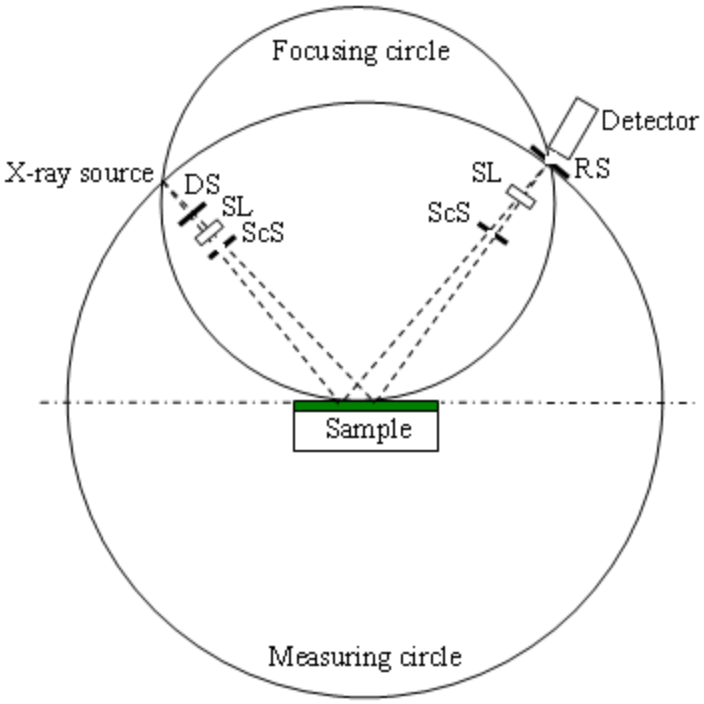

Figure 2-24 Schematic of XRD goniometer setup (Bragg-Brentano θ: θ).
DS: divergence slit; SL: soller slit; ScS: scatter slit; RS: receiving slit.

2-6-2. Rietveld refinement of XRD data

2-6-2-1. Least squares profile fitting (minimization procedure)

Rietveld refinement uses a least squares approach to refine a theoretical line profile until it matches the experimental step-scanned diffraction profile. In other words, the principle of Rietveld refinement is to minimize a function ϕ which

represents the difference between a calculated profile *y(calc)* and the observed profile *y(obs)*. [140,141,142]

$$\phi = \sum_i w_i (y_i(obs) - y_i(calc))^2 = Minimum \qquad (2\text{-}29)$$

w_i: weighting factor for each observation point; [142]

$y_i(obs)$: observed intensities at each step - the sum i occurs over all data points in the diffraction pattern;

$y_i(calc)$: calculated intensities at each step.

The calculated intensity $y_i(calc)$ includes the contributions of the $|F_{hkl}|^2$ structure factors, Lorentz and polarization factors, preferred orientation functions and the background noise contribution.

$$y_i(calc) = SF \times \sum_k L_k \mid F_{hkl} \mid^2 \varphi(2\theta_i - 2\theta_k) P_k A' + y_{bi} \qquad (2\text{-}30)$$

$y_i(calc)$: calculated intensity of a Bragg reflection at position $2\theta_i$;

SF: scale factor;

L_k: groups of Lorentz, polarization and multiplicity for reflection k;

F_{hkl}: structure factor of reflection from the (hkl) plane;

φ: reflection profile function from $2\theta_i$ to $2\theta_k$;

P_k: preferred orientation function for reflection k;

A': absorption factor, which depends on the instrument geometry;

y_{bi}: background intensity at position $2\theta_i$;

k: Miller index for Bragg reflection.

The minimization of equation (2-29) using equation (2-30) is processed using the least-squares method.

The contribution of the $|F_k|^2$ structure factors is obtained by the summation of the adjacent reflection contributions. The structure factor $|F_k|$ depends on positions of each atom j within each Miller plane and is calculated from the crystal structure

data, which includes site occupancy, cell dimensions and a temperature factor. [143]

$$F_{hkl} = \sum N_j f_j \exp\left[2\pi i\left(hx_j + ky_j + lz_j\right)\right]\exp\left(-B'\frac{\sin^2\theta}{\lambda^2}\right) \qquad (2\text{-}31)$$

F_{hkl}: structure factor of reflection from the (hkl) plane;

N_j: site occupancy (presence of vacancies);

f_j: structure factor for atom j;

x_j, y_j, z_j: coordinates for atom j;

B': temperature factor;

$\frac{\sin\theta}{\lambda}$: form factor.

2-6-2-2. Information from Rietveld refinement

2-6-2-2-1. Crystal structural parameters

A diffraction pattern includes information about peak position and intensity. Peak positions of the reflections are indicative of the crystal structure and phase symmetry; therefore, the peak positions are directly related to the unit cell dimensions, lattice parameters and space group. Therefore, lattice parameters can be deduced and refined from the peak positions.

Peak intensities indicate the total scattering from each plane in the crystal structure, which means that peak intensities are directly dependent on the atom distribution in the crystal structure. Thus peak intensities are related to phase structure, i.e. atomic positions and phase composition (atomic occupancies).

2-6-2-2-2. Quantitative phase analysis (relative weight fraction of phases)

Quantitative phase analysis measures the relative abundance of the constituent crystal phases in the sample. With the development of whole pattern fitting methods and Rietveld refinement techniques, quantitative phase analysis is becoming one of the most important applications of powder diffraction. The percentage content of phases in a sample is calculated from scale factors. The scale factors, derived from Rietveld refinement of powder diffraction data, are related to the phase composition of the mixture by the following relationship. It involves the mass, number and volume of the unit cell of each phase. [142,144]

$$w_a = \frac{SF_a (MZV)_a}{\sum_j SF_j (MZV)_j} \quad (2\text{-}32)$$

w_a: relative weight fraction of phase a in a mixture of *j* phases;

SF: Rietveld scale factors derived from the refinement;

M: mass of the formula unit;

Z: number of formula units per unit cell;

V: volume of the unit cell.

Rietveld refinement is a full pattern profile refinement and achieves simultaneous crystal structure refinement. Due to the development of profile refinement techniques, quantitative phase analysis is the most important recent application of x-ray diffraction.

2-6-3. Instrument alignment, sample preparation and data collection

Quantitative analysis requires high quality data; therefore, the XRD data should be collected as accurately as possible in terms of peak positions and intensities for the following Rietveld refinement. The accuracy of XRD data collection depends on both the instrument and the specimen.

2-6-3-1. Instrument calibration

For XRD measurement, the sample should be centered in the measuring circle and be tangent to the focusing circle as shown in Figure 2-24. The focusing circle changes radius with angle θ.

In order to minimize the instrument error, the geometry of the instrument and the alignment must be calibrated, which mainly includes the zero error and specimen displacement. Zero error is the error in the zero 2θ position, which means that the x-ray source, sample and detector need to line up horizontally, as shown in Figure 2-25. The sample is always equal-distant between the source and detector as well (*e.g.*, R1 = R2).

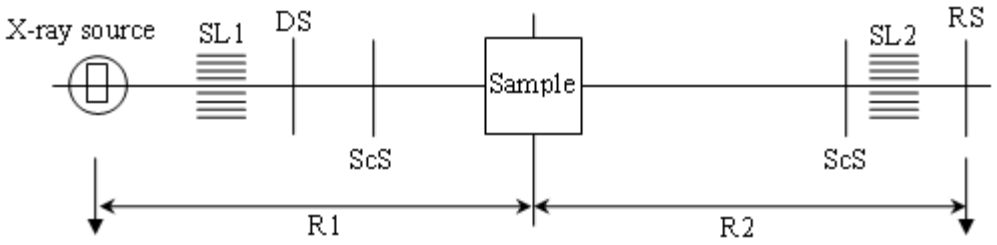

Figure 2-25 Axial alignment.

SL1, SL2: soller slits; DS: divergent or primary slit; ScS: primary scatter slit; RS: receiving slit; R1: $R_{incident}$; R2: $R_{reflected}$.

Specimen displacement means that the sample is off the diffractometer focusing circle due to instrumental misalignment or the way that the sample is packed into the sample holder. Figure 2-26 shows an example of specimen displacement, leading to a peak shift. The bottom rectangle in Figure 2-26 is the ideal sample location and the top rectangle is the actual sample location.

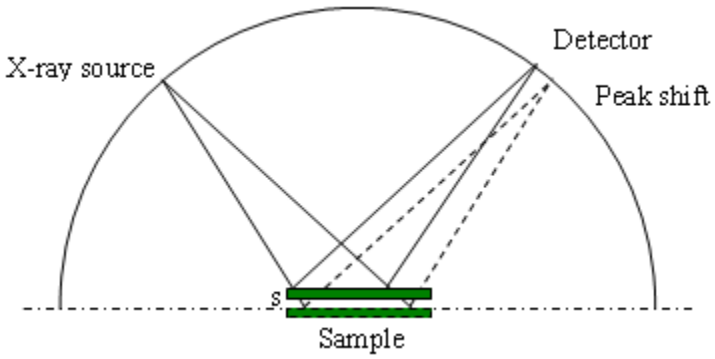

Figure 2-26 The effect of sample displacement by distance s on error in the measurement of 2θ.

2-6-3-2. Divergence slit selection

Both fixed and variable divergence slits (divergence aperture) have been used to determine the width of the x-rays that impinge on a sample surface. A fixed slit has a fixed aperture, whereas a variable slit has a variable aperture.

Figure 2-27 schematically shows the goniometer optics during data collection using a fixed divergence slit. If a fixed slit is used, the divergence angle is fixed

during the scan through all diffraction angles. Thus, the irradiated width changes with a change in the diffraction angle. As a result, the irradiated area on the sample varies with a change in the diffraction angle. [145] At low and high angles, the irradiated depth is smaller compared to medium angles. Due to the variation of irradiated area and the irradiated depth during the scan, the irradiated volume from the specimen is relatively fixed in a fixed slit condition. The error occurring in a fixed slit condition is that the divergence slit may be too wide at low angles, so the measured intensities are too low at low angles. The same thing happens at high diffraction angles. There is a gradual decline of intensity with increasing 2θ because x-ray scattering has a form factor ($\sin\theta/\lambda$), as the scatter (size of the electron cloud) is the same magnitude as the x-ray wavelength λ. The intensity at high diffraction angles drops further if a fixed divergence slit is used.

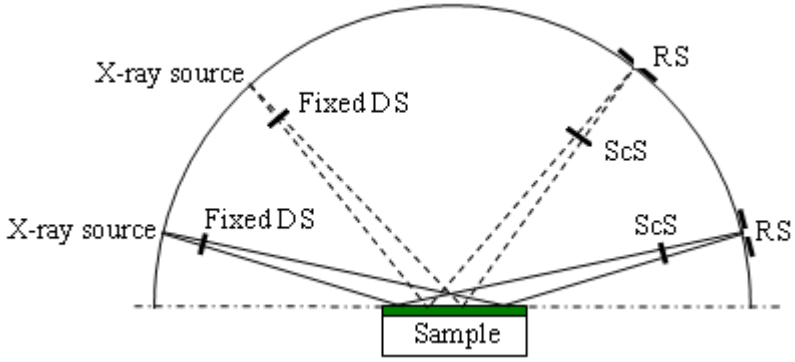

Figure 2-27 Schematic of goniometer optics during data collection using a fixed divergence slit changing the irradiated area. [145]
Fixed DS: fixed divergence slit; RS: receiving slit; ScS: scatter slit.

Figure 2-28 shows the goniometer optics during data collection using a variable divergence slit. [143] If a variable slit is used, the divergence angle is controlled as the diffraction angle changes such that the irradiated width stays fixed. However, the irradiated volume changes due to a variation in the irradiated depth during the scan. The main purpose of a variable slit is to increase the intensities of reflections at high angles. However, correction of the measured intensity using a variable aperture for the incident beam introduces additional errors into the experimental data. This error may become very severe if the

diffractometer is misaligned or when the incident beam is inhomogeneous. [143] For structural work, it is best to stay with a fixed slit and no modifications are needed for the profile function.

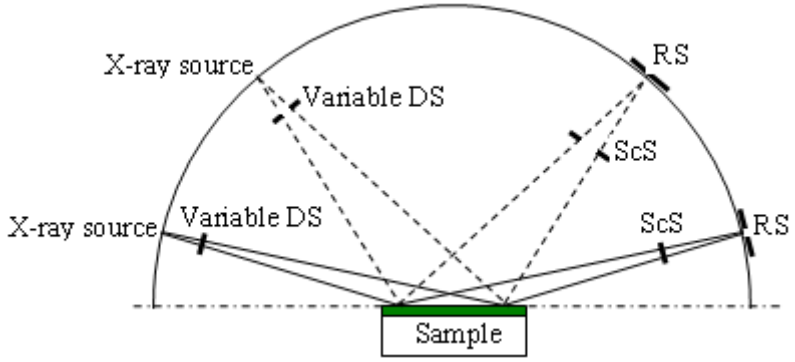

Figure 2-28 Schematic of goniometer optics during data collection using variable divergence slit maintaining the same irradiated area. [143]
Variable DS: variable divergence slit; RS: receiving slit; ScS: scatter slit.

2-6-3-3. Specimen preparation

Specimen preparation is another important aspect for accurate XRD data collection. Most analysis requires that the specimen meet certain requirements to produce repeatable diffraction data that can accurately reflect the structure and composition of the sample, i.e. a large number of randomly oriented, uniformly sized powder particles and an infinitely thick powder specimen. Particle size, preferred orientation and specimen thickness are the common errors associated with specimen preparation. [142] The recommended crystallite size is less than a few microns. Larger crystallite sizes will easily cause problems as fewer crystallites diffract the x-rays, so that the random distribution requirement is not met.

There are three borderline cases concerning preferred orientation. The first is real texture in the sample, e.g., in a steel pipe introduced by rolling. The second is preferred orientation as a result of cleavage properties in the crystals. The third is non-random distribution because of the impossibility to achieve 100% randomness in the specimen. The first two have to be treated differently compared with the third case. For the third case, this phenomenon is observed in almost all

specimens used in powder diffraction, which means that a completely random orientation of the crystallites is difficult to prepare. [142]

In order to prepare nearly random specimens, especially for extremely small amounts of powder samples, a slurry mounting technique can be used. This can minimize preferred orientation, produce homogeneously distributed specimens and specimens can be easily crushed, spread and packed flat. For example, ethanol can be used to prepare ethanol insoluble materials and it can easily evaporate afterwards. A zero-background quartz plate is widely used as a sample holder, and it can effectively minimize scatter from the substrate because of sample thickness or not enough material to fill the holder.

2-6-3-4. Step size and counting time

Step size $\Delta(2\theta)$/step and counting time/step directly determine the total scanning time. Proper step size and counting time per step must be selected in order to obtain high quality data.

2-6-4. Refinement parameters in Rietveld refinement

Rietveld refinement requires that a sufficiently good structure model must be first known to carry out the refinement. Therefore, qualitative analysis of the diffraction pattern to determine the crystal structure, space group and the approximate lattice parameters is the starting point, which can be obtained by comparing the sample XRD data (peaks and relative intensities) with a standard database provided by the International Center for Diffraction Data (ICDD). Rietveld refinement is therefore based on this starting point to refine a series of parameters to achieve the best fit to the experimental data. The parameters include instrument correction parameters, profile shape functions, background fitting functions, preferred orientation functions, scale factors and thermal factors. [142]

2-6-4-1. Instrument correction parameters

The instrument correction parameters such as the zero error and specimen displacement need to be corrected in a Rietveld refinement.

2-6-4-2. Profile shape functions

Profile shape functions describe the shape of the diffraction peaks. Four profile shape functions have been widely used in profile fitting programs; these include the Gaussian (G_{psf}), the Lorentzian (L_{psf}), the Pseudo-Voigt (PV_{psf}) and the Pearson VII (P_{psf}) functions, expressed by the following equations. [142]

$$G_{psf} = I_0 \exp\left(-\ln 2\left(\frac{2\theta - 2\theta_0}{\omega}\right)^2\right) \quad (2\text{-}33)$$

$$L_{psf} = I_0\left(1+\left(\frac{2\theta - 2\theta_0}{\omega}\right)^2\right)^{-n}, \text{ n=1; 1.5; 2} \quad (2\text{-}34)$$

$$PV_{psf} = \eta L + (1-\eta)G, (0 \leq \eta \leq 1) \quad (2\text{-}35)$$

$$P_{psf} = I_0\left(1+\left(\frac{2\theta - 2\theta_0}{ma^2}\right)^2\right)^{-m} \quad (2\text{-}36)$$

$2\theta_0$: peak position;

I_0: peak intensity;

ω: half of the full width at half maximum (FWHM);

η: adjustable parameter;

m: shape parameter.

The Gaussian profile is equivalent to a normal distribution and the graph is a characteristic symmetric bell shape curve that quickly falls off towards infinity. The Lorentzian profile is equivalent to a Cauchy–Lorentz distribution and it has flatter tails than a Gaussian distribution with equal FWHM (full width at half maximum). Figure 2-29 shows a comparison between Gaussian and Lorentzian distributions. When a small crystallite size is responsible for the profile broadening, a Lorentzian function is used. However, a Gaussian function is used when microstrain is responsible for the profile broadening. Usually, the instrument contribution is Gaussian and the sample contribution is Lorentzian. The Pseudo-Voigt function (PV_{psf}) is used in most programs for Rietveld refinement and it is a linear combination of G_{psf} and L_{psf} by applying an adjustable

parameter η. When η = 0, it is a pure Gaussian function; when η = 1, it is a pure Lorentzian function.

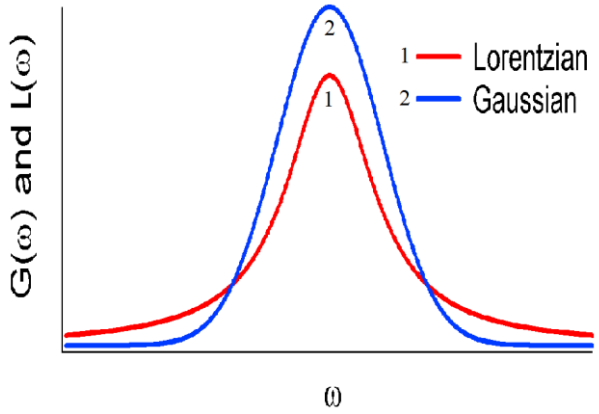

Figure 2-29 Gaussian and Lorentzian distributions.

2-6-4-3. Background fitting functions

Background can be produced from a number of sources, such as fluorescent radiation emitted by the specimen, diffraction of a continuous spectrum of wavelengths, diffraction scattering from materials other than the specimen including soller slits, sample mount and air and diffuse scattering from the specimen itself, including incoherent and coherent scattering. Amorphous content in the sample gives non-uniform contributions to the background as well.

There are two mathematical approaches to do background fitting. The first is a linear interpolation between selected data points between reflections, which is preferred for simple patterns. The second uses a Chebyshev polynomial function, which is preferred for complex patterns. [142]

2-6-4-4. Preferred orientation function

The determination of the true relative intensities by powder diffraction is based on many fully random, statistically distributed crystallites. However, preferred orientation is present due to the difficulty in preparing non-randomly distributed specimens, which produce systematic distortions of the reflected intensities. Preferred orientation functions are used to define an intensity correction factor based on the deviation from randomness.

There are two main parameters for preferred orientation correction. One is based on a March-Dollase function and the other is based on spherical harmonics ordering according to Jarvinen. [146] The latter approach is more complex and more powerful; so it is used more often.

2-6-4-5. Scale factors

Scale factors are the most important parameters for quantitative phase analysis and are determined by the mass, number and volume of the unit cell of each phase. The scale factors can be derived from Rietveld refinement of powder diffraction data [142,144] and have been explained in Section 2-6-2-2.

$$w_a = \frac{SF_a (MZV)_a}{\sum_j SF_j (MZV)_j} \qquad (2\text{-}32)$$

w_a: relative weight fraction of phase a in a mixture of j phases;

SF: scale factors derived from the Rietveld refinement and is proportional to the number of unit cells of phase *a* in the specimen;

M: mass of the formula unit;

Z: number of formula units per unit cell;

V: volume of the unit cell.

2-6-4-6. Temperature factor (thermal factor)

Atoms undergo thermal vibrations around their mean positions and the vibration amplitude increases as the temperature increases. Increased thermal vibration of the atoms expands the unit cell and changes the planar spacing, leading to changes in the 2θ positions of the diffracted lines. Thermal vibrations also decrease the intensities of the diffraction lines and increase the background intensity between diffraction lines. [147] Therefore, most Rielveld refinement programs include a temperature factor to allow for thermal vibrations of the atoms.

2-6-5. Criteria of fit

There are different criteria for a successful refinement. However, the overall best criteria for a fit is the difference plot between the observed and calculated data, $y_i(obs)$-$y_i(calc)$ or difference plot. There should not be large deviations at any point in the difference plot. The other two main criteria include two R-indices, R_{wp} and $R_{B,}$ which should be low for the profile fit. R_{wp} is the R-weighted pattern index and it is statistically the most meaningful indicator of the overall fit, because it is the residual that is minimized in the least squares procedure. R_B is the R-Bragg index, which is based on the integrated intensities deduced from the model. [142]

$$R_{wp} = \left\{ \frac{\sum w_i (y_i(obs) - y_i(calc))^2}{\sum w_i (y_i(obs))^2} \right\}^{1/2} \quad (2\text{-}37)$$

$y_i(obs)$: observed intensity at each step;

$y_i(calc)$: calculated intensity at each step;

w_i: weighting factor for each observation point, which is assumed to be proportional to the square root of the count rate $y_i(obs)$ following Poisson counting statistics.

$$R_B = \frac{\sum | I_K(obs) - I_K(calc) |}{\sum I_K(obs)} \quad (2\text{-}38)$$

$I_K(obs)$: observed integrated intensity of the kth Bragg reflection;

$I_K(calc)$: calculated integrated intensity of the kth Bragg reflection.

2-6-6. Programs for Rietveld refinement

There are many available programs for Rietveld analysis for general profile and structure analysis for powder diffraction data. GSAS (General Structure Analysis System) and TOPAS are two of the most widely used. Both packages use a least squares refinement program for Rietveld refinement and they support all types of x-ray and neutron crystallography instruments.

GSAS is free software that is available for Windows, Linux and Macintosh systems. It uses an EXPGUI graphical user interface, which provides many useful utilities for viewing fits and refinement results. [148]

TOPAS is powerful software for the analysis of powder diffraction data. There are two forms of TOPAS: BRUKER-AXS TOPAS and TOPAS-Academic. TOPAS-Academic is an academic version of BRUKER-AXS TOPAS (2004), which is used in the present research work. It comprises all the functionality of BRUKER-AXS TOPAS including all graphics and an OpenGL structure editor and viewer. TOPAS-Academic is operated using input and output files. The input files (.inp) contain all information for controlling and accessing all the features of TOPAS. The text based input file can be created and modified using a text editor, e.g. Jedit, allowing for control of TOPAS. TOPAS is more user-friendly compared with GSAS.

2-7. Summary and research significance

From the above literature review, significant accomplishments have been made over the last fifty years with the development of pipeline steels, especially during the past ten years. Steel development is motivated by the requirement to increase mechanical properties and to reduce cost. Therefore, many research projects have been carried out focusing on developing high strength steels. Microalloying and TMCP have been combined and played a big role in improving steel mechanical properties.

In order to understand the strengthening mechanisms, researchers relied on different qualitative techniques. Conventional microscopic methods are most commonly used. Different techniques, such as optical microscopy, SEM, TEM, STEM, AFM, FIM with atom probe have been used. The microstructural features of the steel matrix and precipitates have been observed. The qualitative methods may have been sufficient to increase steel strength to date. However, it may not be sufficient for future steels.

In order to effectively improve steel mechanical properties for future development of new steels with higher strength, better toughness and weldability,

such as X100, X120 and beyond, a more quantitative understanding of the strengthening mechanism is required. The relative importance and contribution of different strengthening mechanisms need to be determined. However, this quantitative information is lacking.

In this thesis, the microstructure and strengthening mechanisms of a series of microalloyed steels are studied. A quantitative approach - matrix dissolution, is sought and quantitative characterization of precipitates is carried out. Precipitate quantification was achieved via Rietveld refinement of the XRD patterns based on the classification of precipitates according to size and chemistry by SEM and TEM.

From literature, matrix dissolution has been used to qualitatively determine the composition of inclusions and large precipitates (mainly >100 nm). The chemical compositions of nano-precipitates have been studied only in a few cases. Several researchers have extracted and studied nano-precipitates in industrial steels using the TEM. However, the reported chemical composition of these steels has been limited to general statements about the mutual substitution of Nb and Ti and of C and N. For the development of stronger steels with more complex chemistries and processing histories, a more rigorous and quantitative approach is desired and will be presented in this thesis. The quantitative analysis increases the accuracy about the contribution of different strengthening components.

Rietveld refinement has been used in mineral characterization. However, it has not been applied to study precipitates with complex chemistries in industrial steels. This is a new application of the Rietveld refinement method. In this thesis, Rietveld refinement is used to study the extracted precipitates, i.e. it yields the relative abundance of precipitates, leading to volume fraction determination of precipitates in the steel. The contribution of each individual strengthening component, such as precipitation strengthening, grain size effect and solid solution strengthening is determined, providing better understanding of the strengthening mechanisms for these microalloyed steels. In this thesis, the nucleation of nano-precipitates in ferrite or bainite is studied as well, providing better understanding of precipitate nucleation after austenite to ferrite phase

transformation. It should be noted that the nucleation of precipitates in austenite has been studied in the literature, but not in ferrite or bainite.

Chapter 3: Experimental procedures

3-1. Introduction: experimental outlines

Nine microalloyed steels were characterized in this work. The types of steels, their compositions, processing histories and mechanical properties will be presented in Section 3-2. This will be followed by a description of the methods used and developed to quantitatively describe each steel in terms of its microstructure, grain size, quantity and types of precipitates. Thus, in Section 3-3, microstructural examination of the steels using optical microscopy (OM) and scanning electron microscopy (SEM) will be described. The method for quantifying grain size will also be addressed in this section. In Section 3-4, matrix dissolution techniques will be introduced to extract precipitates. The mass balance performed via inductively coupled plasma spectroscopy (ICP) will be introduced as well. The concentration of the elements in solid solution will be analyzed using ICP. By comparing the steel chemistry with the ICP results, the amounts of microalloying elements in the precipitates can be determined. In Section 3-5, x-ray diffraction (XRD) will be used to identify the phases of the extracted precipitates. In Section 3-6, precipitate characterization using SEM and TEM (transmission electron microscopy) will be addressed. Chemical composition of the precipitates is determined by SEM/TEM-EDX microanalysis. The size distribution of the nano-precipitates and the orientation relationship with the base metal through TEM will be introduced in this section as well. In Section 3-7, Rietveld refinement of XRD patterns will be introduced to refine precipitate structures and the relative abundance of different precipitate phases will be quanitified, leading to volume fraction determination of precipitates in the steel.

3-2. Materials analyzed

3-2-1. Chemical composition, processing histories and mechanical properties

Four grades of microalloyed steels: Grade100, X70, X80 and X100 were supplied by EVRAZ Inc. NA and were used in this study. The main reason for using this Grade100 steel is that it has the highest amount of microalloying

content (Nb+Ti+Mo+V); therefore it is possible to extract a larger amount of precipitates for further quantification. The knowledge gained from the study of Grade100 steel served as a basis for further study of other grades of steels. X70, X80 and X100 steels are intended for production of pipelines. X70 steel is currently most widely used in industry and X80 steel will be more popular in the near future. X100 steel is a type of new steel for future development. The collection of these steels (going from X70 and increasing to X100) allows the exploration of the differences in chemistry and processing that yield their respective property values. There are several steels at the same strength level designation (four X80 steels and three X100 steels). Including those steels would allow the exploration of how the same final strength using different chemistries and/or processing may be obtained.

The steel chemical compositions and finish processing histories, namely, finish rolling temperatures (FRT) and coiling temperatures or interrupted cooling temperatures (CT/ICT) are given in Table 3-1 and Table 3-2. [149] The data in Table 3-1 and Table 3-2 were provided by EVRAZ. Because of confidentiality issues, the actual FRT and CT/ICT temperatures are not shown. The normalized FRT and CT/ICT are shown in Table 3-2. The respective FRT and CT/ICT temperatures for steel X80-B4F were used as the base values. The temperatures for other steels are reported relative to those for this steel. The mechanical properties of these steels are presented in Table 3-3.

From the effects of alloying elements that were introduced in Section 2-1-4, the alloying strategy for developing these high strength steels mainly includes C, Mn, Ti, Nb and Mo. A lower C content gives better impact toughness and good weldability. Manganese is added to the steels to combine with S to form MnS and avoid hot shortness. [9] Manganese also plays an important role in ferrite grain refinement and dispersion strengthening. A proper amount of Mn (1.4-2.0 wt%) controls the austenite to ferrite transformation temperature and enhances the formation of lower transformation temperature products, such as acicular/bainitic ferrite, resulting in ferrite grain refinement and finer precipitation dispersion. [19] The major effect of Ti is to form Ti(C,N) precipitates, which can pin grain

boundary movement in austenite and, therefore, provide grain growth control during recrystallization rolling. Niobium plays a key role for high strength steels by three major functions. When Nb is in solution, it slows down the austenite to ferrite decomposition kinetics and retards austenite recovery and recrystallization. During rolling, Nb can partially precipitate in austenite as Nb(C,N), which can inhibit austenite grain growth and delay austenite recrystallization. Therefore, Nb has the largest effect on grain refinement and it has a more effective strengthening effect than Ti. Upon completion of the austenite to ferrite transformation, the ferrite is supersaturated with Nb and C. The remaining Nb will precipitate as fine precipitates in ferrite, increasing the strength by precipitation strengthening. Molybdenum has a strong effect on hardenability. It shifts the ferrite and pearlite curves of the CCT diagram to the right (longer times); therefore, the formation of polygonal ferrite is suppressed and lower-temperature products, such as acicular/bainitic ferrite structures, are promoted. Most Mo atoms are in solution in the ferrite matrix, resulting in solid solution hardening. A small amount of Mo precipitates as fine particlees in ferrite, leading to precipitation strengthening.

The X70 and X80 compositions listed in Table 3-1 have lower C levels to improve weldability, while Grade100 steel has higher amounts of carbon and other alloying elements to achieve the minimum yield strength. Grade100 steel has a much higher Ti content compared to other microalloyed steels as well. Compared to X70 steel, the X80 steels have a higher Nb content except for the X80-A4F steel. All the alloys contain small amounts of Cu, Ni and Cr, with Cu + Ni + Cr total shown in Table 3-1 for each alloy. The amount of Mn, Al, Mo and Ti are also slightly different. The amount of C in the X100 steels is a little bit higher than that of the X80 steels. The Nb content in the X100 steels is much lower; however, there are higher amounts of Cu, Ni, Cr and Mo in the X100 steels. In the X100-2A steel, a small amount of B is added with the intention to increase steel hardenability and promote the formation of bainite. X100-2B steel has a higher amount of V. Increasing C content can effectively improve the tensile strength; however, the weldability will be reduced.

Carbon equivalent is normally used to evaluate steel weldability. Two

equations are introduced here for the carbon equivalent calculations. One is the IIW equation (International Institute of Welding) as expressed by equation (3-1). [150] The IIW equation works well for steels with C levels above 0.15wt%. The other is the Ito-Bessyo equation as expressed by equation (3-2). [150] The Ito-Bessyo equation is more accurate and most widely used for pipeline steels with carbon levels less than 0.15%. [150] The carbon equivalents (*C.E.* and P_{cm}) for the microalloyed steels using the two equations were calculated with the values shown in Table 3-1. Microalloyed steels have low carbon equivalents and reduced hydrogen induced cracking (HIC) susceptibility; hence, they exhibit improved weldability.

$$C.E. = \%C + \frac{\%Mn + \%Si}{6} + \frac{\%Cu + \%Ni}{15} + \frac{\%Cr + \%Mo + \%V}{5} \quad (3\text{-}1)$$

$$P_{cm} = \%C + \frac{\%Mn + \%Cr + \%Cu}{20} + \frac{\%Si}{30} + \frac{\%Ni}{60} + \frac{\%Mo}{15} + \frac{\%V}{10} + 5\%B \quad (3\text{-}2)$$

In terms of the processing conditions, the Grade100, X70 and X80 steels have similar FRT, CT and the same nominal CR. The X100 steels are laboratory steels produced at CANMET Ottawa and are not coiled. They have much lower interrupted cooling temperatures (ICT) and higher CR. X70 and X80 steels are coiled at the CT and the Grade100 and X100 steels are deformed by leveling or rolling at the ICT to achieve specified degree of flatness.

Table 3-1 Chemical composition (wt%) and carbon equivalent of the microalloyed steels [149]

Sample ID	C	Mn	Si	Al	N	Cu+Ni+Cr	Mo	Nb	Ti	V	C.E.	P_{cm}
Grade100	0.080	1.800	0.244	0.05	0.011	0.877	0.301	0.094	0.060	0.047	0.58	0.24
X70-564	0.0398	1.654	0.23	0.022	0.0118	0.432	0.2	0.069	0.023	0.001	0.43	0.16
X80-462	0.03	1.69	0.27	0.044	0.0098	0.45	0.297	0.091	0.013	0.002	0.45	0.16
X80-A4B	0.035	1.7	0.283	0.044	0.0058	0.66	0.305	0.094	0.017	0.003	0.48	0.17
X80-B4F	0.052	1.62	0.128	0.02	0.0061	0.62	0.299	0.077	0.009	0.002	0.45	0.17
X80-A4F	0.052	1.77	0.115	0.016	0.0055	0.64	0.404	0.044	0.009	0.003	0.50	0.19
X100-2A	0.039	1.81	0.11	0.018	0.0050	0.98	0.41	0.037	0.013	0.003	0.53	0.19
X100-2B	0.065	1.87	0.22	0.032	0.0059	0.77	0.40	0.047	0.009	0.070	0.58	0.22
X100-3C	0.064	1.88	0.33	0.024	0.0063	0.74	0.40	0.046	0.009	0.003	0.59	0.22

Table 3-2 Processing histories for the microalloyed steels [149]

Sample ID	Type	FRT (°C/°C)	CT (°C/°C)	ICT (°C/°C)	CR (°C/sec)
Grade100	plate	1.07		1.09	15*
X70-564	pipe	0.94	1.04		15*
X80-462	pipe	0.94	1.04		15*
X80-A4B	pipe	1.05	0.93		15*
X80-B4F	pipe	1.00	1.00		15*
X80-A4F	pipe	1.00	0.90		15*
X100-2A	plate	1.00*		0.71	35
X100-2B	plate	1.00*		0.64	34
X100-3C	plate	1.00*		0.80	19.1

FRT: Normalized finish rolling temperature; for X100 steels, the FRT are the intended values.

CT: Normalized coiling temperature;

ICT: Normalized interrupted cooling temperature.

CR: Cooling rate; for X70, X80 and Grade100 steels, the CR are the intended values.

Table 3-3 Mechanical properties for the microalloyed steels [149]

Sample ID	σ_{ys} (MPa)	σ_{UT} (MPa)	UEL (%)	TEL (%)	CVN	
					Test temperature (°C)	Absorbed energy (J)
Grade100	788	928	-	17	-	-
X70-564	520	650	-	-	-	-
X80-462	588	703	-	34	-7	173
X80-A4B	568	694	-	35	-7	211
X80-B4F	592	735	-	37	0	123
X80-A4F	589	717	-	39	0	131
X100-2A	810	907	5.2	17	-15	178
X100-2B	691	793	6.2	20	-15	241
X100-3C	744	846	5.8	21	-15	175

* Specimen for tensile testing: 10 mm in diameter, 40.6 mm gauge length.
Specimen for charpy testing: full size (10 mm x 10 mm).
$\sigma_{ys:}$ yield strength; $\sigma_{UT:}$ ultimate tensile strength;
UEL: uniform elongation; TEL: total elongation.

3-2-2. Continuous cooling transformation diagrams (CCT)

Figure 3-1 shows the continuous cooling transformation (CCT) diagram for the Grade100 steel studied here. [149] Figure 3-2 and Figure 3-3 show the CCT diagrams for representative X70 and X80 steels, respectively. [149] Because of confidentiality issues, the temperature scale is not shown. If the cooling rate is 15ºC/s, the expected microstructure for the Grade100 steel is a mixture of bainite with small amounts of polygonal ferrite. The expected microstructure for the X70 steel is a mixture of polygonal ferrite, bainite and a small amount of pearlite, with polygonal ferrite as the primary phase. For the X80 steels, the microstructure should be mostly bainite with a small amount of polygonal ferrite. Higher amounts of microalloying elements (Nb, Ti and Mo) will shift the CCT curves to longer times and lower temperatures, leading to more bainitic ferrite content.

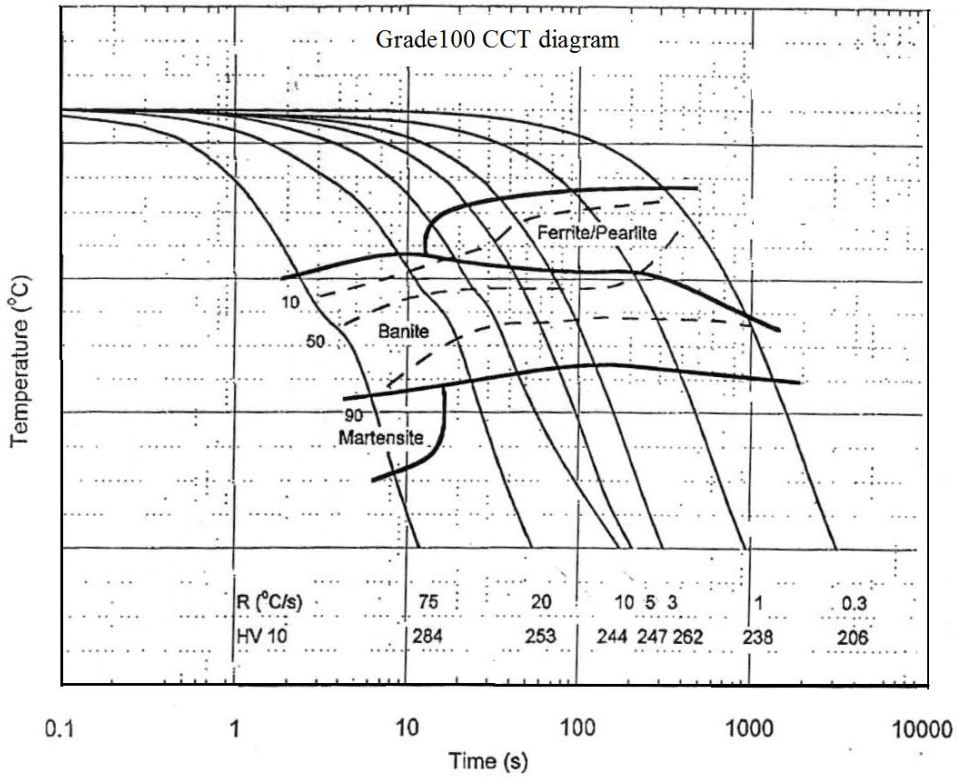

Figure 3-1 CCT diagram for Grade100 steel. [149]

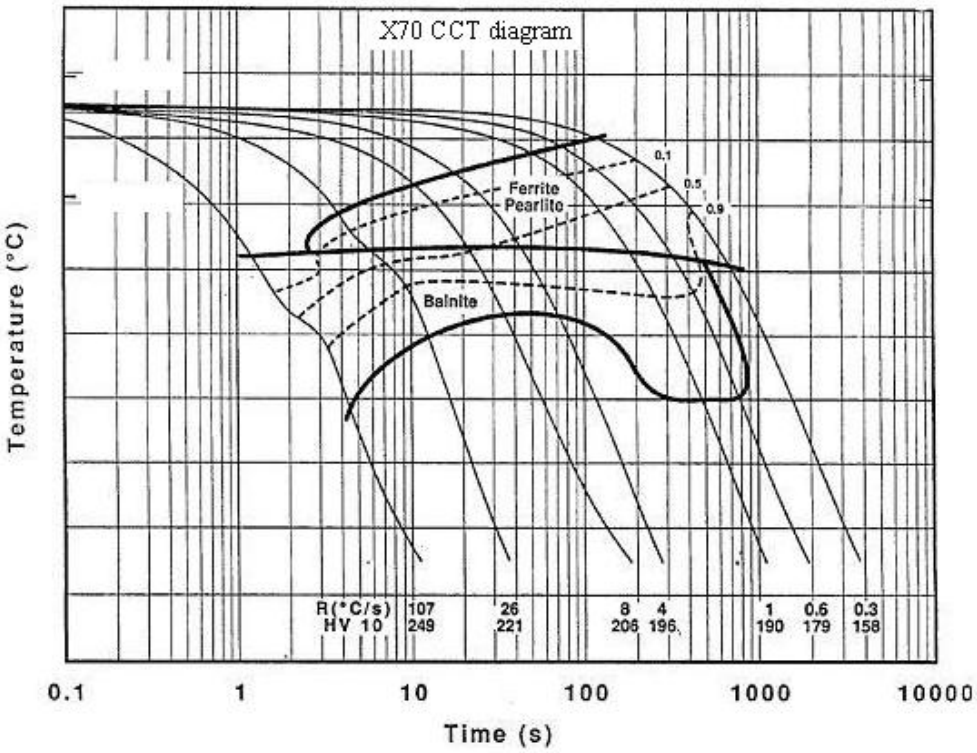

Figure 3-2 CCT diagram for X70 steel. [149]

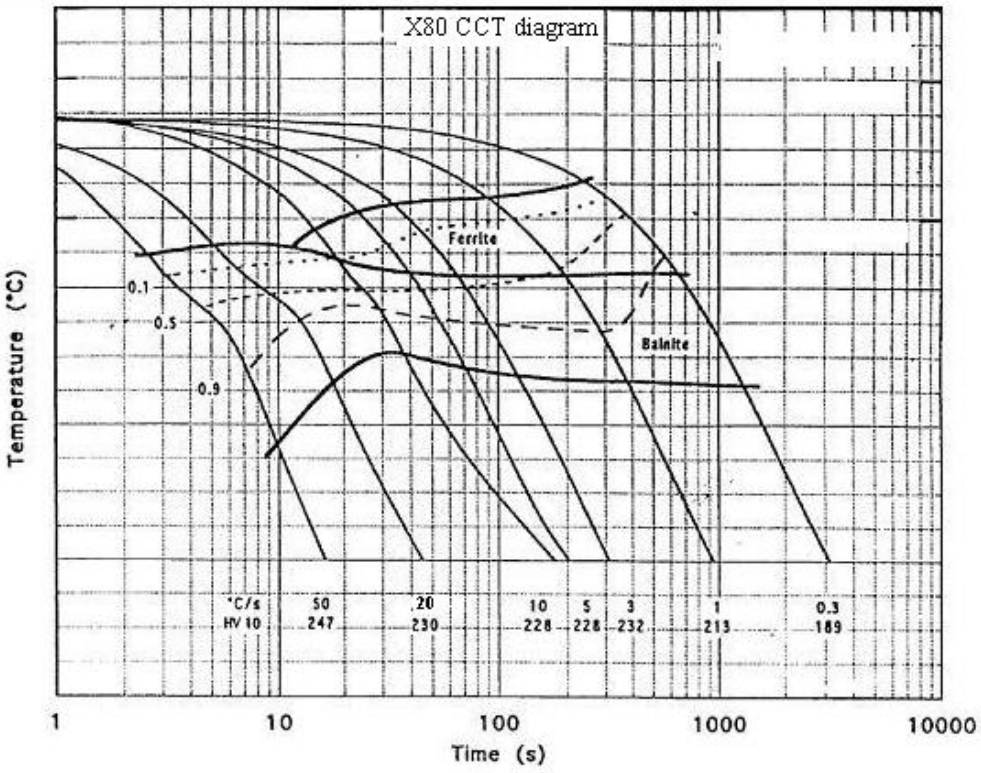

Figure 3-3 CCT diagram for X80 steel. [149]

3-3. Equipment for steel microstructure analysis and grain size measurement

Small pieces of steels were cut and mounted in Bakelite using a hot press. The exposed sample surface was through the pipe/plate thickness and perpendicular to the rolling direction for microstructure observation and grain size measurement. Once mounted, the samples were ground in sequence with 240, 320, 400 and 600 grit SiC sand papers. Sample surfaces were pre-polished using 3μm diamond paste followed by final polishing with 0.05 μm alumina. Samples were then etched with 2% Nital to reveal their microstructure features. The etched specimens were examined in an optical microscope.

A Hitachi S-2700 SEM, operated at 20 kV, was used to take secondary electron images (SE-SEM) for more detailed microstructural analysis of steel samples; for example small amount of pearlite was observed in Grade100, X70 and X80 steels, but not in X100 steels. This qualitative microstructure observation was made for the whole sample thickness. Sample preparation for SEM analysis was similar to that for optical microscopy.

A JSM6301 (JEOL) field emission source SEM with an IMIX energy-dispersive X-ray detector was used to take SE-SEM images for steel grain size measurement. Because secondary electrons have low energies (below 50eV) and are generated within 5nm of the surface, they are used for imaging. In order to obtain better surface resolution, the SEM was operated at lower accelerating voltage, i.e., 5kV. At lower accelerating voltages, electron beams have less penetration, allowing for better surface resolution. The images were taken within 1/8 to 3/8 of the pipe/plate thickness for the grain size measurement.

Because the grains are non-equiaxed, i.e., they are highly deformed and irregular in shape, standard ASTM techniques were not used for grain size measurement. Mean linear intercepts (*m.l.i.*) were used to measure the grain size, as shown in Figure 3-4. Lines (horizontal, vertical and at 45 and 135º, three of each) were drawn and the number of grains (grain boundaries) intercepted by each line was counted. The ratio of the line length (l) to the number of grains (n) provides an estimation of the grain size ($i = l / n$). At least three SEM images were analyzed. The standard deviation was obtained from the above measurements.

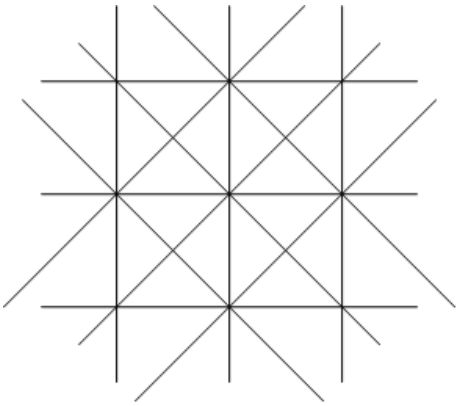

Figure 3-4 Grain size measurement using mean linear intercept method.

3-4. Precipitate extraction by matrix dissolution

In order to obtain a significant amount of precipitates, matrix dissolution was used to extract the precipitates from the steel matrix. Chemical dissolution, by HCl solution and iodine-ethanol solution, and electrolytic dissolution were used to

extract precipitates from Grade100 steel. Both an iodine-ethanol solution and electrolytic dissolution were very time consuming; therefore, the dissolution for other steels was done chemically using the HCl solution.

3-4-1. Chemical dissolution and ICP analysis of the supernatant

The sample surface was ground using 240 grit SiC sand paper to remove oxides and dirt. The ground samples were cleaned with acetone under ultrasonic conditions. An analytical balance with an accuracy of 0.1 mg was used to measure the weight of the sample before dissolution.

Chemical dissolution was used for all steels to extract the Ti, Nb and/or V carbonitride precipitates using an HCl acid solution at 65-70°C, according to ASTM Standard Test Method E 194-90 [110] (1:1 mixture by volume of HCl acid, with a specific gravity of 1.19, and distilled water). A schematic of the experimental setup is shown in Figure 3-5.

After the whole steel sample was completely dissolved in the acid solution, the acid solution with a soluble ferrous chloride ($FeCl_2$) and precipitates was transferred to centrifuge tubes. A Sorvall RC-6 superspeed centrifuge, made by Mandel, was used to separate solid particles from the solution by rapidly rotating the material at up to 40,000 RCF (relative centrifugal force) at 4°C. The supernatant was carefully removed from the centrifuge tube using a pipette and then distilled water was added to dilute the solution and to clean the residues. The centrifuging process was repeated several times, until the dark brown colour was gone. At this point, the soluble ferrous chloride was removed from the centrifuge tube and solid particles had settled at the bottom of the centrifuge tube. Most of the water was removed and ethanol was added into the centrifuge tube. The tube containing the solid particles and ethanol was vibrated in an ultrasonic bath for about 10 minutes until the solid particles were removed from the wall of the centrifuge tube. At this point the solid particles were well mixed with the ethanol solution. Then the mixture was poured into a collection beaker (the weight of the collection beaker was pre-measured). This procedure was repeated several times to ensure that all particles were collected from the centrifuge tube. The sample

was dried on a hot plate at low temperature, about 40ºC, to evaporate the ethanol. The weight of the beaker containing the extracted residues was measured with a scale with a 0.1 mg accuracy so that the weight of the extracted residues was obtained. The amount of extracted residues was compared to the original weight of the dissolved steel sample. At this stage, the chemistry and phase identification of the isolated residues were ready to be analyzed by SEM, TEM and XRD.

After the steel matrix was dissolved using HCl dissolution, precipitates were separated from the supernatant using centrifuging. In order to perform a mass balance, inductively coupled plasma mass spectrometry (ICP-MS), with a Perkin Elmer Elan 6000 ICP-MS, was used to analyze the concentration of the elements dissolved in the supernatant (mixture of $FeCl_2$, HCl and water). Calibration was done using four calibration levels (four point calibration curve) for each element, i.e., Ti, Nb, Mo and V. The solution to be analyzed was diluted to keep the analyte concentration well within the linear working range.

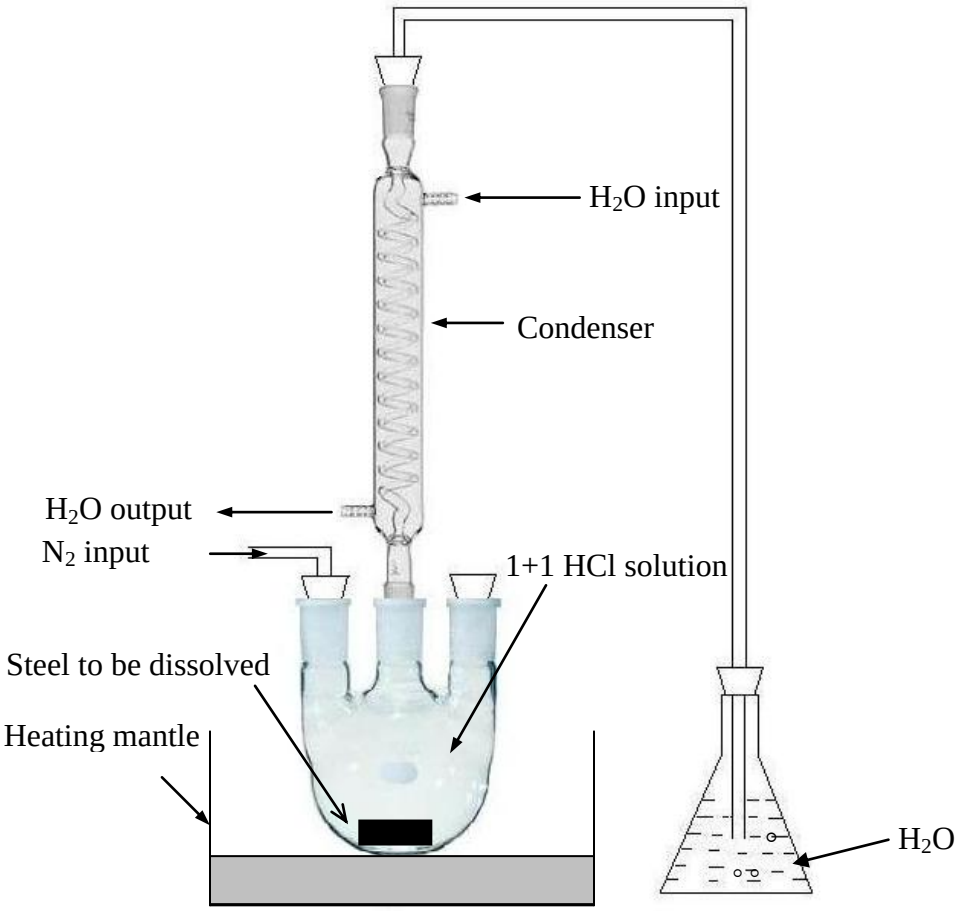

Figure 3-5 Schematic of the experimental set up for chemical dissolution of steel samples using HCl solution.

Chemical dissolution using I_2 was also explored to extract precipitates from Grade100 steel. Ethanol was used as the extraction reagent to dissolve solid I_2. Based on the reaction between Fe and I_2, enough iodine was added to reagent-grade ethanol until all the I_2 was dissolved. The matrix dissolution was conducted at 65-70°C and the experimental set up is similar to that for HCl dissolution (Figure 3-5). After the whole steel sample was completely dissolved in the I_2-ethanol solution, the solution with soluble FeI_2 and precipitates was transferred to centrifuge tubes. The same centrifuge was used to separate solid particles from the FeI_2 + ethanol solution. The centrifuge and precipitate collection procedures were the same as that used in HCl extraction, except that ethanol was used for all the dilution keeping the unreacted I_2 dissolved in the solution.

3-4-2. Electrolytic dissolution and potentiodynamic scans

Electrolytic dissolution was employed for the Grade100 steel, using a 10% AA solution, composed of 10% acetylacetone, 1% TMAC (tetramethylammonium chloride) and methanol. [129,130]. Because precipitates have different stabilities, i.e., TiN and TiC are less stable than NbN and NbC (this will be discussed further in Section 4-7-1 in Chapter 4), it is theoretically possible to selectively extract different precipitates by applying different potentials. However, due to the voltage limitations of the Gamry Potentiostat/Galvanostat system (Gamry PC4/750), it was not feasible to apply potentials over 1.5 volts for samples with a $1cm^2$ surface area. Therefore, based on the polarization results (introduced in the following paragraph) for the steel and binary Ti and Nb carbides and nitrides, the potential was set at 300 mV vs. SCE to dissolve the steel matrix and to leave behind all the precipitates. The experimental setup for electrolytic dissolution is shown in Figure 3-6. After the iron matrix was dissolved, the electrolyte, composed of iron salts, precipitates and inclusions, was centrifuged and residues were collected. The centrifuging of the solution and precipitate collection procedures were the same as that used in HCl and I_2 extraction, except that methanol was used for all the dilutions.

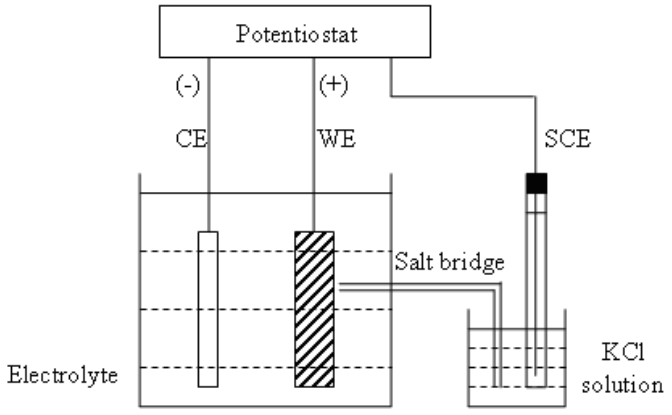

Figure 3-6 Experimental setup for electrolytic dissolution.
CE: counter electrode (Pt); WE: working electrode (steel or pure carbides and nitrides); SCE: saturated calomel electrode.

As mentioned previously, selection of the appropriate dissolution potential is based on the different dissolution behaviors of the various precipitates and the steel matrix, which provides the selective extraction of precipitates in terms of composition. The ferrite matrix is dissolved at low anodic potentials, while precipitates are nobler and are dissolved at higher potentials. Some precipitates are nobler than others, thereby allowing for selective extraction. In order to determine the appropriate potential used for electrolytic dissolution, a Gamry Potentiostat/Galvanostat (PC4/750) was used to determine polarization curves for the Grade100 steel (ferrite matrix) and several binary carbides and nitrides. The experimental setup is shown in Figure 3-7. The electrolyte used was a 10% AA solution.

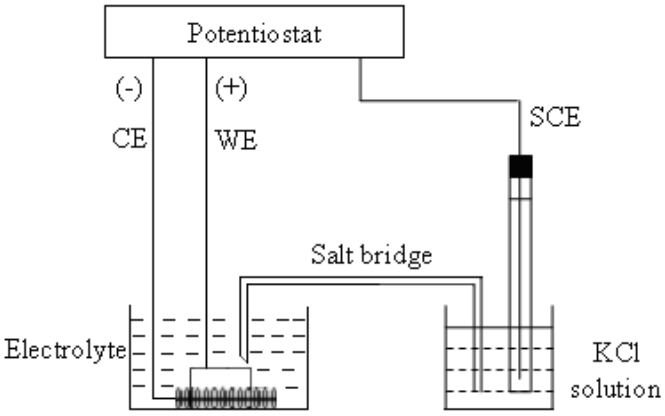

Figure 3-7 Corrosion cell used in potentiodynamic measurement.
CE: counter electrode (Pt); WE: working electrode (steel or binary carbides and nitrides); SCE: saturated calomel electrode.

3-5. X-ray diffraction (XRD) of the extracted precipitates

About 100 mg of extracted precipitate as dry powder was used to collect a high resolution X-ray diffraction pattern. The sample was slurry mounted to minimize preferred orientation. A wet (with methanol) drop pipette was used to remove the precipitates from the bottle and place them in a mortar. More methanol was added and the sample was passively crushed. The slurry was then

transferred to a quartz sample holder using the drop pipette and tapped to spread it evenly and allow for drying in air.

For phase identification, the XRD experimental conditions are shown in Table 3-4. Most of the diffraction data, except for sample X80-A4F, was collected with a Bruker D8 Advance X-ray Diffractometer, equipped with a Co X-ray source and a VANTEC-1^{TM} linear detector. Initially, a variable divergence slit (4mm x 4mm) was used for the sample extracted from the Grade100 steel using 10%AA dissolution. A fixed 0.3^{o} divergent slit was used for the remaining samples in order to avoid the error associated with variable slits regarding intensity correction. For precipitates extracted from the X80-A4F141 steel, a Rigaku Geigerflex 2173 X-ray Diffractometer, equipped with a Co X-ray source was used. A fixed 1º divergent slit was used for data collection.

Table 3-4 Experimental conditions for XRD analysis

	X80-A4F	Other steels
Diffractometer	Rigaku Geigerflex 2173	Bruker D8 Advance
Radiation	Co, wavelength 0.178899 nm	
Detector	Vertical Goniometer	VANTEC-1TM linear detector
2θ angular range	10 -125º	10 -125º
Step scan increment	0.02º (2θ)/step	0.022º (2θ)/step
Counting time	0.5 º (2θ)/minute	0.08 º (2θ)/minute
Receiving slit length	0.6mm	50mm
Primary soller angle	1º	2.3º
Divergent slit	Fixed 1º	Variable (4mm x 4mm) for Grade100 10%AA, fixed at 0.3º for all others
Sample holder	Quartz (zero-background plate) to minimize scatter from the substrate because of sample thickness problems.	

3-6. Precipitate characterization by SEM and TEM

3-6-1. Equipment for specific precipitate characterization

The Hitachi S-2700 SEM was used for overall chemical analysis of precipitates that were extracted by matrix dissolution. The JSM6301 SEM was used for characterization of specific precipitates extracted by carbon replicas or

matrix dissolution. SE-SEM and BSE-SEM images (back-scattered electron images) were taken. The compositions of the coarse precipitates (larger than 100 nm) were determined by SEM-EDX analysis. The precipitates in the steels are mainly Ti, Nb and/or V carbonitrides. Titanium, Nb and V are high atomic number elements, which can be clearly identified in BSE-SEM images giving good compositional contrast.

A JEOL 2010 TEM, operated at 200 kV and equipped with an EDX detector, was used for characterization of specific precipitates. Three techniques for sample preparation were used for TEM: precipitates extracted by carbon replicas and matrix dissolution as well as thin foil samples. The chemical composition of the precipitates extracted by carbon replicas and matrix dissolution was determined by EDX microanalysis. The weight percents (wt%) of each element were related to the measured intensities with the use of the Cliff-Lorimer factor assuming the thin film criterion was satisfied. [151]

$$\frac{C_A}{C_B} = k_{AB}\frac{I_A}{I_B} \tag{3-3}$$

C_A, C_B: wt% of element A and B;

I_A, I_B: x-ray intensity of element A and B - the K_α lines for the measured intensities were used;

k_{AB}: Cliff-Lorimer factor.

For a binary system,

$$C_A + C_B = 100\% \tag{3-4}$$

The precipitate composition in terms of atomic fraction, can be obtained from weight percent via equations (3-5) and (3-6) for element A and B respectively.

$$T_A = \frac{\frac{C_A}{A_A}}{\frac{C_A}{A_A} + \frac{C_B}{A_B}} \tag{3-5}$$

$$T_B = \frac{\frac{C_B}{A_B}}{\frac{C_A}{A_A} + \frac{C_B}{A_B}} \tag{3-6}$$

T_A, T_B: atomic fraction of element A and B;

A_A, A_B: atomic weight of element A and B.

For a ternary system, the atomic fraction of each element can be determined in a similar way using the following equations.

$$\frac{C_A}{C_D} = k_{AD}\frac{I_A}{I_D} \tag{3-7}$$

$$C_A + C_B + C_D = 100\% \tag{3-8}$$

$$T_A = \frac{\frac{C_A}{A_A}}{\frac{C_A}{A_A} + \frac{C_B}{A_B} + \frac{C_D}{A_D}} \tag{3-9}$$

$$T_B = \frac{\frac{C_B}{A_B}}{\frac{C_A}{A_A} + \frac{C_B}{A_B} + \frac{C_D}{A_D}} \tag{3-10}$$

$$T_D = \frac{\frac{C_C}{A_C}}{\frac{C_A}{A_A} + \frac{C_B}{A_B} + \frac{C_D}{A_D}} \tag{3-11}$$

C_A, C_B, C_D: wt% of element A, B and D;

I_A, I_B, I_D: x-ray intensity of element A, B and D;

T_A, T_B, T_D: atomic fraction of element A, B and D;

A_A, A_B, A_D: atomic weight of element A, B and D.

Because of the presence of intermediate and high atomic number elements, such as Ti, Nb, V and Mo, there is strong interference from the L- and M-family x-rays of these elements with the K peaks of the low atomic number elements.

Therefore, the amount of C and N in a precipitate cannot be accurately determined by conventional SEM/TEM-EDX. [152] The main focus of this research work was to quantitatively determine the amount of different precipitates. The C and N concentrations were chosen according to precipitate solubility, i.e., precipitates formed at higher temperatures (above the rough rolling temperature) are assumed to be nitrides because nitride precipitates have lower solubilities than the carbides. Precipitates formed at lower temperatures (during or after coiling) are assumed to be carbides because carbide precipitates have higher solubilities than the nitrides. Precipitates formed at intermediate temperatures are assumed to be carbonitrides because the solubility of theses precipitates are in between nitrides and carbides. Detailed information will be presented in Chapter 4, 5 and 6.

3-6-2. TEM sample preparation

Three types of samples were used for TEM observation and EDX microanalysis: precipitates extracted by carbon replicas and matrix dissolution, as well as thin foil samples. The sample preparation procedure will be briefly discussed in the following.

For preparation of carbon replicas, sample surfaces were prepared as for optical microscopy. A light etch of the specimen surface for 30s in 2% Nital was used to remove some of the iron matrix, so that the precipitates protruded from the surface. A thin carbon film (about 20nm) was evaporated onto the etched specimen surface from a carbon rod in a DV-502A vacuum evaporator. The replica was sectioned into small squares with a surgical knife to facilitate removal from the steel surface. Then, the sample was immersed into a 5-10% Nital solution. Carbon pieces, containing the precipitates, were lifted off from the surface. The replicas were transferred to a solution with 50% deionized water and 50% methanol to rinse off the nital solution. Then the replicas were transferred to a beaker filled with deionized water, where the replicas floated to the surface and spread out due to the surface tension of the water. Replicas were collected on 300 mesh copper grids and were ready for SEM/TEM observation. The chemical composition for the different precipitates was determined by EDX microanalysis.

The size distribution of the nano-precipitates (mainly ≤ 10nm) was characterized using dark field (DF) imaging.

For TEM samples prepared from precipitates that were extracted by matrix dissolution, the extracted precipitates were collected on carbon coated, 300 mesh Cu grids. Precipitate size was measured by TEM imaging and the chemical composition of the different precipitates was determined by EDX microanalysis.

Thin foil samples for TEM were prepared by mechanically thinning the base metal to a thickness of about 50 μm and then punching out 3 mm discs. These disks were electropolished in a Fischione Twin-Jet Electropolisher at 90 mA (voltage about 60V), with a solution of 90 vol% acetic acid and 10 vol% perchloric acid for about 2 minutes at room temperature. Thin foil samples were examined to determine precipitate distribution in the ferrite matrix and to study precipitate-matrix orientation relationships.

3-7. Rietveld refinement based on XRD data

After the XRD pattern was collected (experimental file or .raw file), the reflections were indexed using Jade-7 software. Preliminary phase identification was processed using the ICDD data base, from which the space group and approximate lattice parameters of precipitate phases were determined. The crystallographic information file, i.e., .cif file, was obtained from American Minerologist Crystal Structure Database. The .cif file contains the unit cell and atomic parameters, which is required for structure refinement.

Based on the experimental file of the XRD pattern, TOPAS Academic software was used for Rietveld analysis to refine the precipitate structures and to determine the relative abundance of different phases. The technique uses a non-linear least squares method to refine instrument and structural parameters contributing to a calculated diffraction pattern, until a good match was generated. [140,141] The scale factors and lattice parameters (with tight restraints) were refined to reduce strong parameter correlations. The relative weight fraction of different phases was derived from the Equation below. [144]

$$w_a = \frac{SF_a (MZV)_a}{\sum_j SF_j (MZV)_j} \quad (2\text{-}32)$$

w_a: relative weight fraction of phase a in a mixture of *j* phases;

SF: Rietveld scale factors derived from the refinement and is proportional to the number of unit cells of phase *a* in the specimen;

M: mass of the formula unit;

Z: number of formula units per unit cell;

V: volume of the unit cell.

To start with the Rietveld refinement, an initial structural model has to be used, which has roughly accurate lattice constants, correct space group and atomic positions. The program input information and parameters to be refined are listed in Table 3-5. The refinement procedures are explained below.

1) Read the .raw file in Jedit.
2) Add the experimental parameters, which include starting and ending values of 2θ, X-ray wavelength and slit information.
3) Read the .cif files; add all the phases one by one by starting with the major phase.
4) Add instrument zero-error correction parameters and specimen displacement. Both parameters will be refined.
5) 1st order Chebyshev polynomial function is used for background fitting.
6) The Pseudo-Voigt function (PV_{psf}) is used as profile shape function for peak shape refinement.
7) Add crystal structural refinement parameters, such as lattice parameters, atom positions, element occupancies and atomic thermal parameters. Atom positions are fixed. The element occupancies were fixed as well, which were based on the precipitate chemical composition obtained by EDX analysis. Lattice parameters (with tight restraints), which are related to the peak positions, are refined.
8) Preferred orientation, which is related to peak height, is refined using spherical harmonics.

9) The scale factors, which are related to the relative abundance of different phases, were refined.
10) Create the input file (.inp file) and import it into the TOPAS.
11) Run TOPAS.
12) The lattice parameters can be refined and the relative abundance of different phases was determined.

Table 3-5 Input information and parameters to be refined in Rietveld analysis

Initial values of variable parameters	Error correcting parameters (instrument)	Zero error correction (error in zero 2θ position)	Refined
		Specimen displacement (shift of peak position)	Refined
	Background	Background function (1st order polynomial)	Refined
	Peak shape	Peak shape function (Pseudo-Voigt)	Refined
	Crystal structural parameters	Lattice parameter (with tight restraints)	Refined
		Atomic positions (x,y,z)	Fixed
		Atomic site occupancies based on the precipitate chemistry obtained by SEM/TEM-EDX	Fixed
		Atomic thermal parameters, isotropic or anisotropic	Refined
		Preferred orientation (Spherical Harmonics)	Refined
	Quantification	Scale factor (determination of the relative abundance of each phase)	Refined
Other input information	Experimental	Step-scan data in equal increments 2θ	Fixed
		2θ limits (starting and ending values of 2θ)	Fixed
		X-ray wavelength	Fixed
		Slit information (receiving slit width, soller angle, divergent slit aperture)	Fixed

Chapter 4: Grade100 steel

4-1. Introduction

Grade100 steel was the steel first and most extensively studied in this thesis. The main reason for starting with this steel is that it has the highest amount of microalloying content (Nb+Ti+Mo+V); therefore it is possible to extract a larger amount of precipitates for further quantification compared with other steels. The knowledge gained from the study of Grade100 steel served as a basis for further study of other grades of steels.

To study Grade100 steel, in Section 4-2, the microstructural features were first examined using various analytical tools and methods, which include OM and SEM. Grain size was measured based on the secondary electron (SE) images taken by SEM. Precipitates were extracted by matrix dissolution using chemical dissolution, with HCl and I_2, and electrolytic dissolution. Thus, in Section 4-3, the overall chemistry of the precipitates collected was analyzed by SEM-EDX. This was followed by XRD analysis for phase identification in Section 4-4. The results of these three methods are compared and contrasted. In Section 4-5, the supernatant from HCl matrix dissolution was analyzed by ICP for element concentration analysis. In Section 4-6, precipitate size and chemistry were determined by SEM/TEM imaging and EDX microanalysis, which was used as the basis for Rietveld refinement. The orientation relationship of the very finest precipitates (≤10 nm) with the ferrite matrix was studied by TEM in Section 4-6 as well. In Section 4-7, Rietveld refinement was used based on XRD data and precipitate chemistry to determine the relative abundance of each precipitate phase. The amount of nano-precipitates (≤10 nm) was determined based on the amount of Mo as well. Comparison was made for the amount of nano-precipitates (≤10 nm) based on Rietveld refinement and Mo-based calculations.

4-2. Microstructural analysis and grain size measurement

Figure 4-1 shows the microstructure of Grade100 steel by OM at magnifications of 500x and 1,000x. Grade100 steel is made up primarily of

bainitic ferrite and smaller amounts of polygonal ferrite. [63] Figure 4-2 shows SE-SEM images at magnifications of 3,000x and 10,000x. The microstructure is fairly uniform with small amounts of pearlite-like structure in some regions, as shown in Figure 4-2b (labeled as P). The grain size was measured by a modified mean linear intercept method based on the inverted SE-SEM images shown in Figure 4-3 at magnifications of 2,500x and 6,000x. For the grain size measurement, the images were taken at 1/8 to 3/8 of the plate thickness. The measured mean linear intercept (*m.l.i.*) with standard deviation is shown in Table 4-1 and was in a good agreement with reference [63].

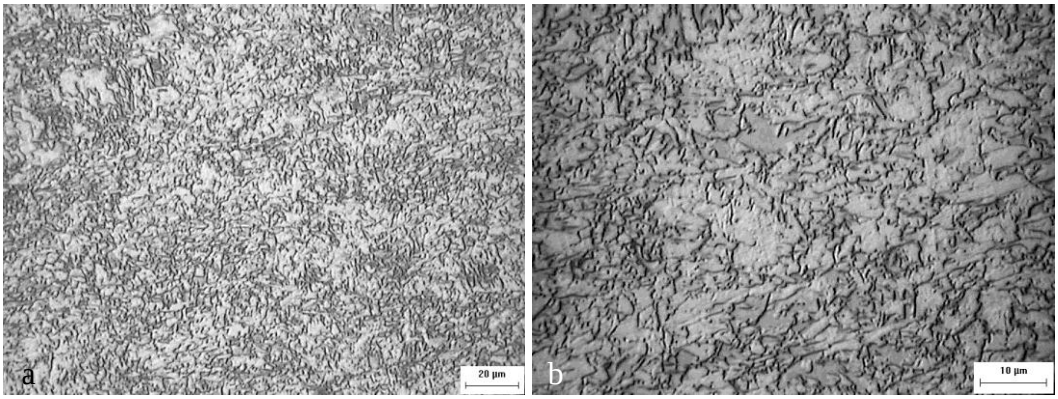

Figure 4-1 OM images of Grade100 steel at a) 500x and b) 1,000x.

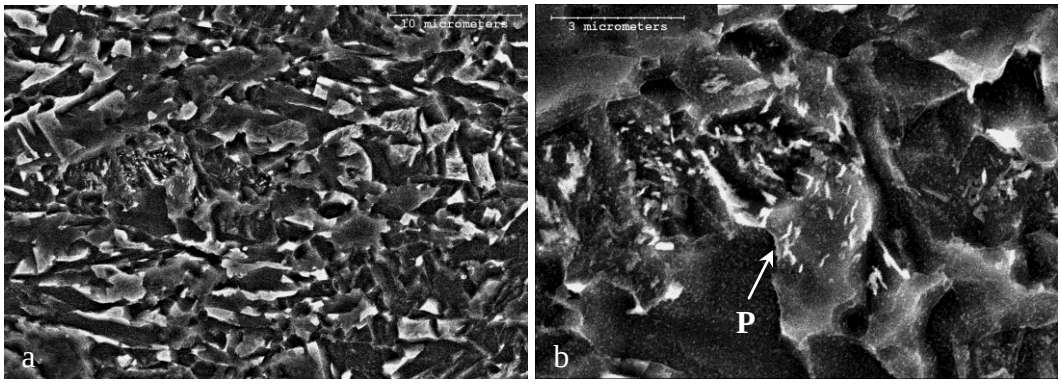

Figure 4-2 SE-SEM images (using 20kV) of Grade100 steel at
a) 3,000x and b) 10,000x. (P: Pearlite-like microstructure)

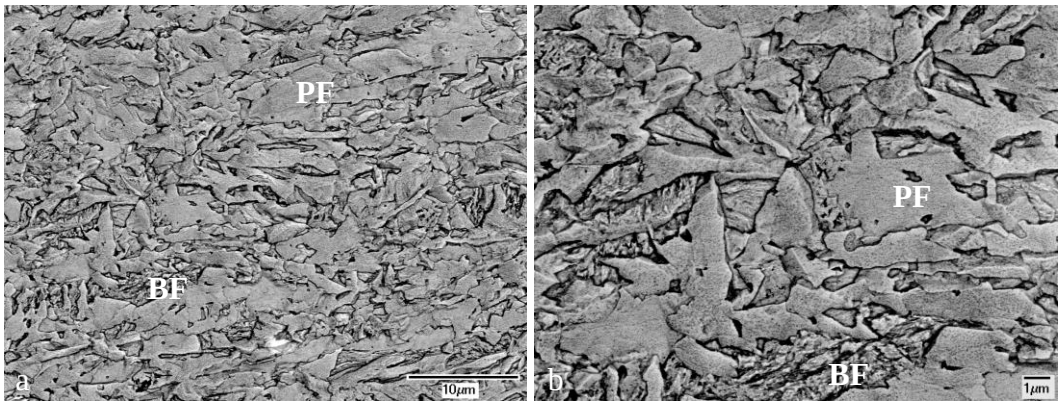

Figure 4-3 Inverted SE-SEM images (using 5kV) of Grade100 steel used for grain size measurement at a) 2,500x and b) 6,000x.

Table 4-1 Mean linear intercept (*m.l.i.*) for Grade100 steel

m.l.i. (μm)	STDEV (standard deviation) (μm)
1.28	0.03
1.2	0.1 [63]

4-3. Overall SEM-EDX analysis of the extracted precipitates

Precipitates were extracted by different dissolution techniques, including chemical dissolution using HCl and I_2, and electrolytic dissolution. Comparing the different dissolution methods, HCl was more efficient with about 1g of steel dissolved per day. The rate for HCl dissolution was about ten times faster than I_2 and electrolytic dissolution. The other advantage of HCl dissolution is that it takes about eight centrifuging cycles to separate the precipitates from the supernatant. However, I_2 and electrolytic dissolution are very time consuming due to the slow dissolution rate and the centrifuging process. More than twenty centrifuging cycles were needed due to the dark solution.

The supernatant from HCl matrix dissolution was analyzed by ICP in order to perform a mass balance, which will be presented in Section 4-5. For HCl dissolution, the extraction yield was 0.792wt% compared to the weight of the original steel. For electrolytic dissolution, the extraction yield was 0.361wt%. Characterization of the extracted residue will be introduced in Section 4-6 and further quantitative information will be introduced in Section 4-7.

4-3-1. SEM-EDX analysis of precipitates extracted by HCl and I_2 dissolution

Precipitates were collected after the ferrite matrix was chemically dissolved using HCl and I_2 dissolution. The overall chemical analysis of the extracted residues was done by EDX spectroscopy in the SEM and a representative EDX spectrum from a sample obtained using HCl dissolution is shown in Figure 4-4. The spectrum qualitatively shows the presence of various elements and indicates that there are intense peaks for Si, Nb, Mo and Ti. Other elements, such as Fe, Cl and O were also detected in the residues. Nb, Mo and Ti come from the precipitates. There is a significant amount of Si present in the steel, either in solid solution in the Fe matrix or as oxide/silicate inclusions. A Si-O phase forms during the matrix dissolution process, which will be explained in more detail later. Iron and Cl arise from the incomplete removal of Fe ions from the solution.

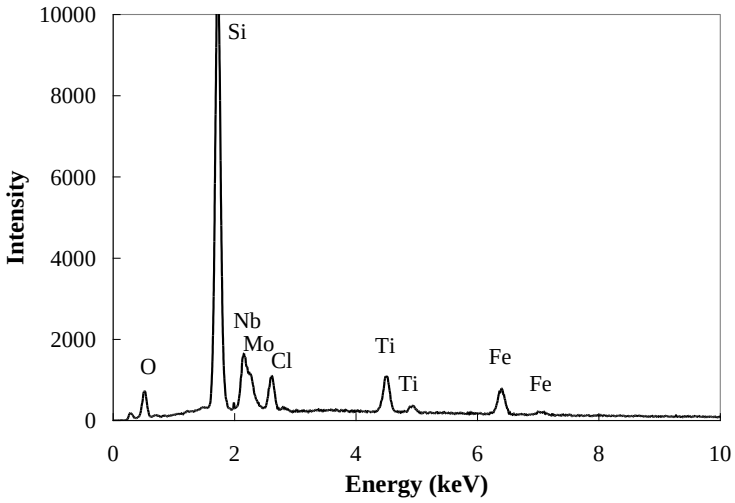

Figure 4-4 SEM-EDX chemical analysis of a group of precipitates from Grade100 steel, extracted by chemical dissolution using HCl.

Figure 4-5 shows an SEM-EDX spectrum of the extracted residues produced by chemical dissolution using I_2 from Grade100 steel. There are intense peaks for Fe, Si, Nb, Mo, Ti and V. Other elements, such as Al, O, Sn, Cr and Mn were also detected in the residues. Nb, Mo, Ti and V come from the precipitates. Si, Al, O and Mn are from the inclusions. Tin and Cr likely come from the steel matrix. The steels are produced from scrap steel; very small amount of impurities, such as Sn,

may be present, but are not reported. After the steel matrix is dissolved, the solution is very dark, making it difficult to completely remove the Fe ions from the solution by centrifuging. Therefore, Fe shows up in the residue. Inclusions were extracted by I_2 dissolution because an alcoholic solution of iodine is very mild and can be used to extract inclusion phases; these inclusions, such as MnS and FeS, are unstable in the acid solutions. [116,117] Therefore, inclusions were not extracted by acid dissolution methods.

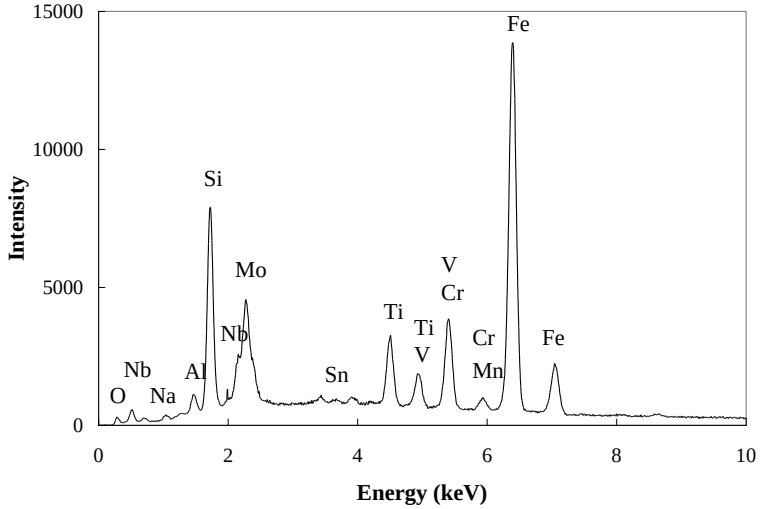

Figure 4-5 SEM-EDX chemical analysis of the extracted precipitates from Grade100 steel by chemical dissolution using I_2.

4-3-2. Polarization behaviour of Grade100 steel, binary precipitate materials and SEM-EDX analysis of the precipitates extracted by electrolytic dissolution

Polarization curves for electrolytic dissolution in the 10% AA solution for the Grade100 steel (ferrite matrix) and several pure carbides and nitrides are shown in Figure 4-6. Clearly, the steel matrix is the most soluble followed by TiN, TiC and then- NbC and NbN. The matrix can be selectively dissolved, at potentials <1000 mV vs SCE. In addition, TiN (the largest of the precipitates in the steel) are electrolytically dissolved preferentially, leaving behind the other compounds. If a high potential, i.e., 1500 mV, is supplied within the current range of the equipment, smaller-sized precipitates can be extracted with the ferrite matrix and

TiN selectively dissolved. However, this has been shown to be impractical for the Gamry system. If a significant amount of precipitates is to be extracted, the total surface area of the steel to be dissolved needs to be several cm^2, which means the current will exceed the current range of the system. This issue could be overcome by the use of several power supplies and smaller specimens; however, the number and availability of other Gamry's systems was limited, so this approach was impractical.

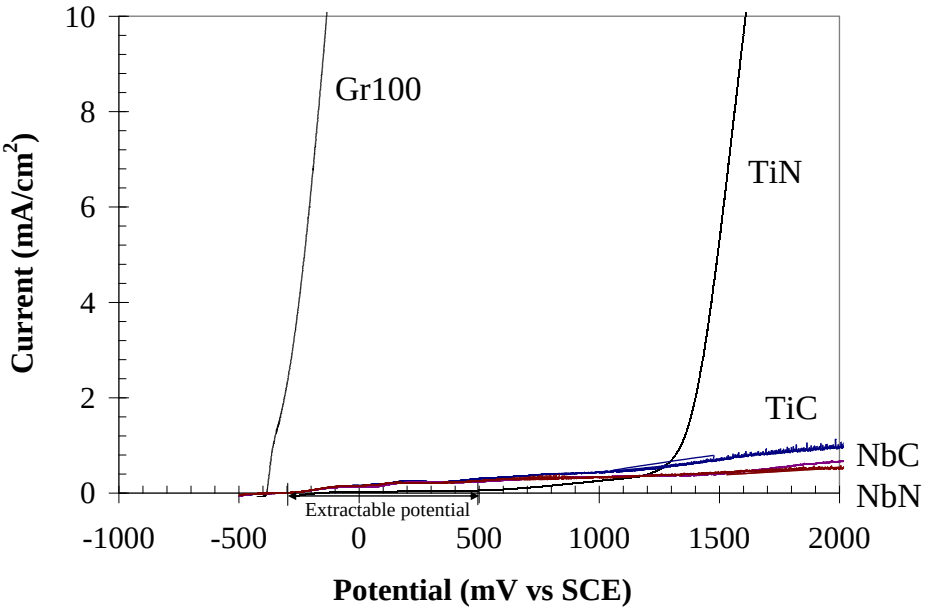

Figure 4-6 Polarization curves for Grade100 steel and pure precipitates in the 10% AA solution.

Figure 4-7 shows the overall chemical composition (SEM-EDX) of the extracted residues produced by 10% AA electrolytic dissolution. There are intense peaks for Si, Nb, Mo, Ti and V. Other elements, such as Al, Ca, Fe and O were also detected in the residues. As before, Nb, Mo, Ti and V come from the precipitates. The Si, Al, Ca and O are from inclusions that are present in the steels; these must have a dissolution potential higher than 300 mV and were extracted during matrix electrolytic dissolution. Fe arises from the incomplete removal of Fe ions from the solution.

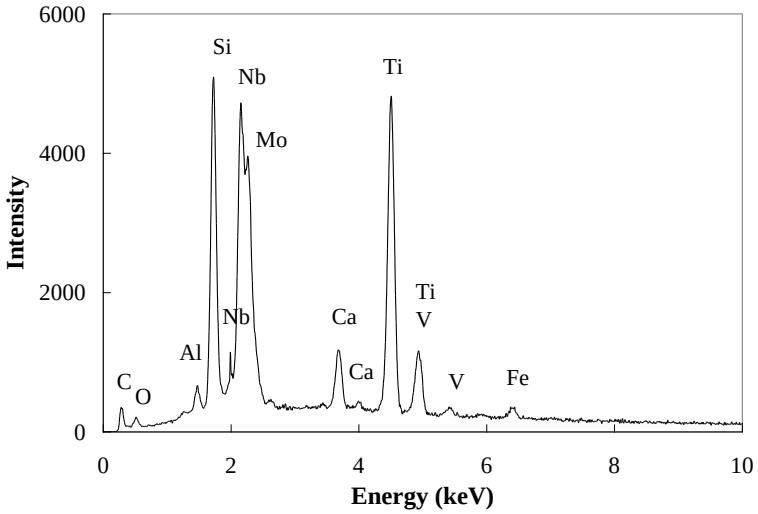

Figure 4-7 SEM-EDX chemical analysis of the extracted precipitates from Grade100 steel by electrolytic dissolution using 10%AA.

4-4. XRD analysis of the extracted residues

Figure 4-8 and Figure 4-9 show XRD patterns for residues extracted from Grade100 steel; samples were obtained through chemical (HCl) and electrolytic (10%AA) dissolution, respectively. The main difference for the two matrix dissolution techniques is the presence of a broad peak for chemical dissolution (HCl) between the 2θ angles of 20° and 30°, which is due to the presence of an amorphous phase, identified by TEM analysis as silica (Section 4-6). The broad peak was not found in the XRD pattern for residues extracted by electrolytic dissolution (10% AA), which is advantageous for the profile fitting and is explained in the Section 4-7. Different dissolution methods will be compared and discussed in Section 4-6-3 and 4-7-2-1.

Preliminary analysis of the diffraction patterns shows the presence of two crystalline phases with similar structures. One set of peaks (indicated by circles in Figure 4-8 and Figure 4-9) appears to represent NbC-based precipitates (larger d spacings) and the other set (squares in Figure 4-8 and Figure 4-9) corresponds to TiN-based precipitates. Both types of precipitates have a NaCl-type structure and belong to the cubic (NaCl-FCC) crystal system with an $Fm\bar{3}m$ space group. There are intensity differences, particularly for the {111} and {200} peaks among the

two patterns, which is due to sample orientation effects during XRD measurements. Sample preparation was discussed in Section 2-6-3-3, in which it was indicated that a sample with a completely random orientation of the crystallites is difficult to prepare. [142]

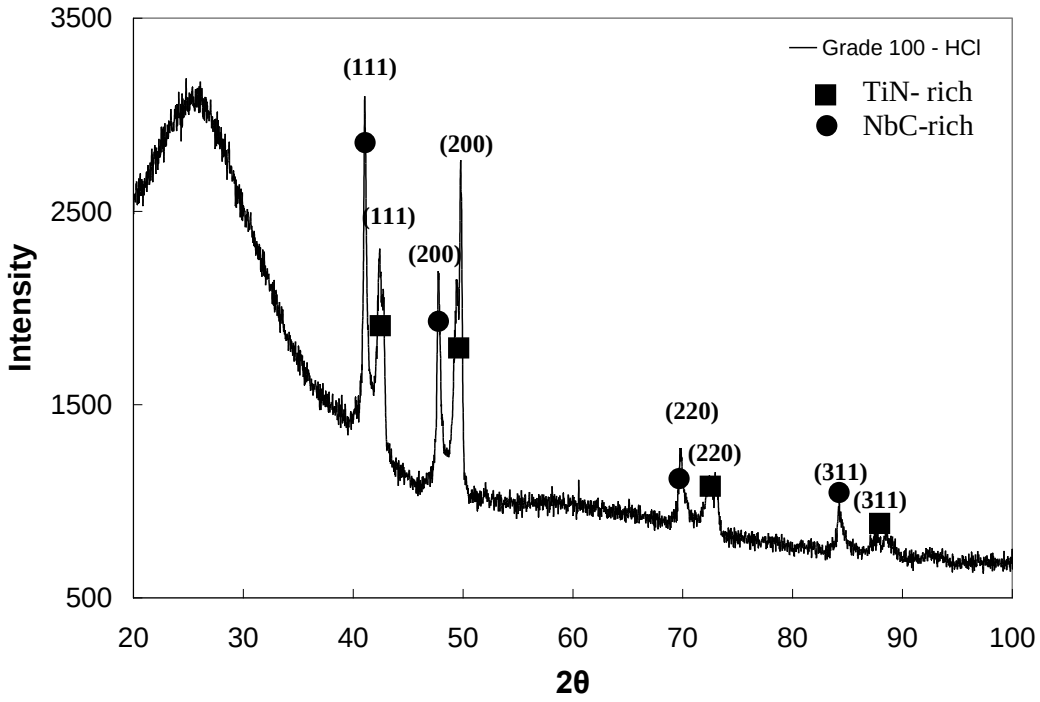

Figure 4-8 XRD pattern for residues extracted from Grade100 steel by chemical dissolution using HCl.

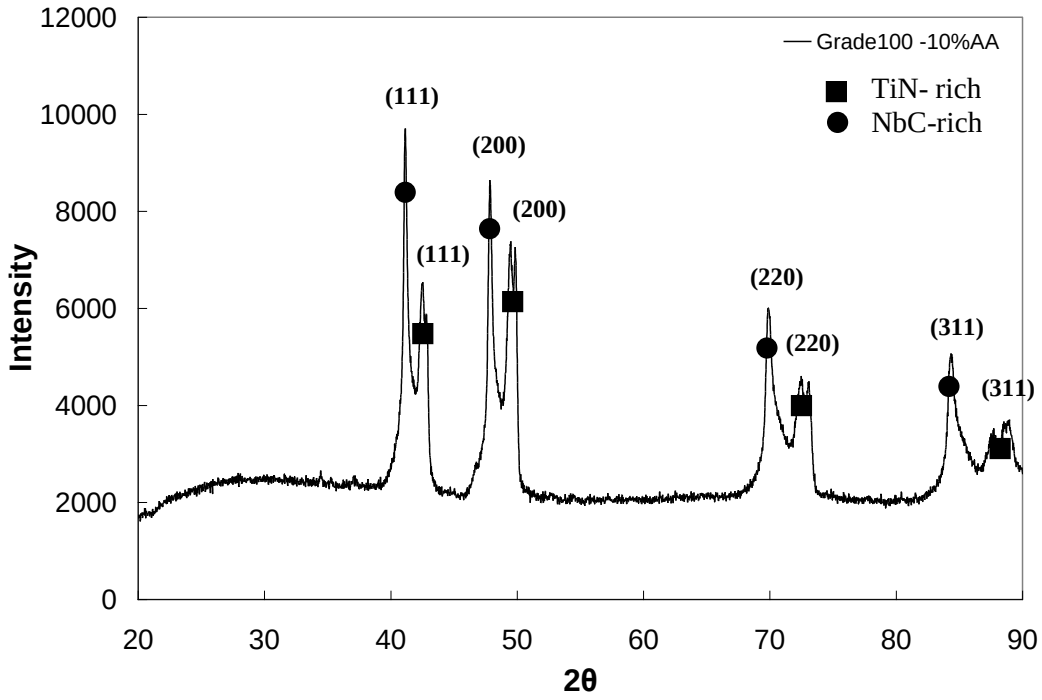

Figure 4-9 XRD pattern for residues extracted from Grade100 steel by electrolytic dissolution using 10%AA.

Actually, precipitates from Grade100 steel can be categorized into five groups, rather than two, according to their size and chemical composition. [82] There are three reasons that it is difficult to differentiate between the various carbides, nitrides and carbonitrides from the preliminary XRD analysis. First, the precipitates all have the same crystal structure (NaCl-type). Second, the lattice parameters of the precipitates are similar. Lastly, the lattice parameters of the precipitates vary with composition. Therefore, detailed information from the XRD patterns were obtained using Rietveld refinement, which will be discussed in Section 4-7.

4-5. Mass balance of the supernatant and the extracted residue

After the precipitates had been extracted from the solution, ICP analysis was performed on the supernatant. Because of evaporation of the ethanol or methanol solution, only the supernatant produced by HCl matrix dissolution was analyzed by ICP. By comparing the chemical composition of the steel with the ICP analysis

of the solution, the amount of each element extracted from the steel as part of the residue was obtained, as shown in Table 4-2. Supernatant chemistry (wt%) is defined as the amount of element in the supernatant per unit of steel being dissolved. Most of the Si in the steel matrix was collected in the residue, which agrees with the overall composition analysis by SEM. It is expected that Si combines with O forming amorphous SiO_2, which was identified in the TEM and will be presented in Section 4-6-2. Most of the Nb in the steel was in precipitate form. There were lower yields for Ti, Mo and V, especially for Mo and V, which means that most of the Mo and V were dissolved in the ferrite matrix. The mass balance performance helps to determine the amount of elements that are present in solid solution, from which the solid solution strengthening contribution can be determined.

Table 4-2 ICP analysis of the supernatant from Grade100 steel by HCl dissolution

Element	Si	Nb	Ti	Mo	V
Steel chemistry (wt%)	0.244	0.094	0.06	0.301	0.047
Supernatant chemistry (wt%)	0.021	0.003	0.014	0.257	0.045
Extraction yield of precipitates	91.6%	97.2%	76.3%	14.5%	5.0%

4-6. Precipitate characterization

4-6-1. TEM analysis of extracted precipitates by carbon replicas

Precipitates with different sizes and various chemistries can be extracted via carbon replicas. In the following section, size and chemistry information for some of the coarse precipitates is given. Size distribution and chemistry of the nano-precipitates (≤10 nm) extracted by carbon replicas are characterized by TEM DF imaging and EDX microanalysis, respectively.

Figure 4-10a shows a TEM BF image of a coarse precipitates with cuboidal shape. The corresponding EDX spectrum is shown in Figure 4-10b. The size and chemistry of this precipitate is listed in Table 4-3, which indicates that it is Ti-rich with some Nb. The Cu peaks in the EDX spectrum are from the Cu grid (sample holder). This cuboidal precipitate is a few hundred nanometres in size. The

chemistry (at% of element Ti and Nb) was determined using Equations (3-3) to (3-6) explained in Chapter 3.

In this thesis, precipitate compositions are determined from SEM/TEM-EDX, where a standardless approach was used. The difference between standard and standardless approach is that the former uses standard samples to determine the appropriate weighting factors; the latter has the weighting factors calculated from a number of parameters such as ionization cross section, fluorescence yield and detector efficiency. The errors in a standardless approach can exceed 10%.

In addition to the above error for the standardless approach, counting statistics is another error source which applies to both standard and standardless approaches. The relative error from counting statistics for a single measurement can be estimated from the equation (4-1) [151], i.e., the relative error is about 10% if there are 1000 counts in the peak. For most EDX analysis in this thesis, 200-1500 counts are used most often, so the corresponding error is between 8% - 21%. This error range applies to most of the precipitate chemistry.

$$\text{Relative error} = 3(\text{intensity})^{0.5}/(\text{intensity}) \times 100\% \qquad (4\text{-}1)$$

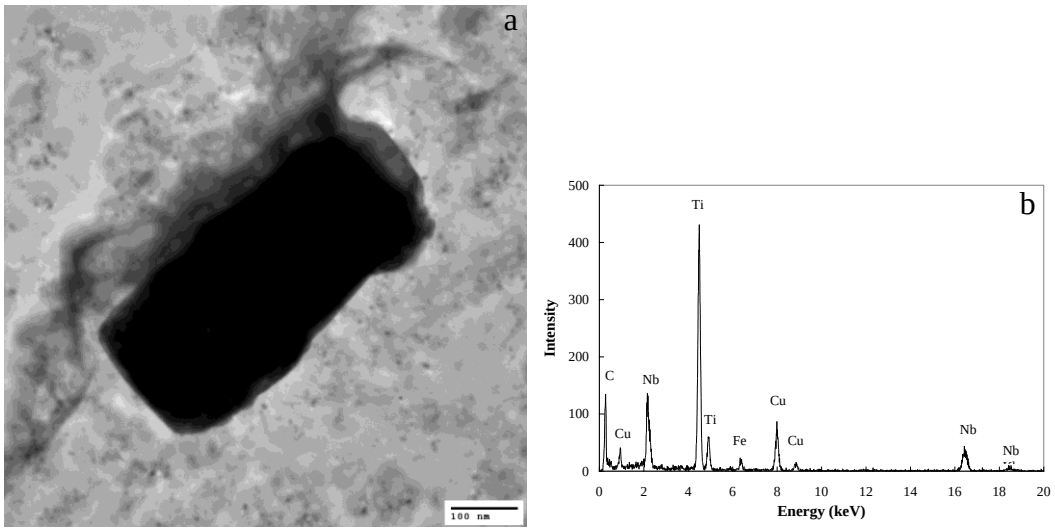

Figure 4-10 A coarse precipitate from Grade100 steel extracted by carbon replicas. a) TEM BF image; b) EDX spectrum.

Table 4-3 Chemistry (metallic elements) and size of precipitate shown in Figure 4-10

Image	Chemistry	Largest dimension (nm)	Morphology
a	$Ti_{0.78}Nb_{0.22}$	510	Cuboidal

Nano-precipitates (most are ≤10 nm) were observed in Grade100, X70 and X80 steels. They were all characterized using carbon replicas and the same procedures were followed which are explained next. The chemistry and size distribution of the nano-precipitates was analyzed by TEM-EDX and DF images, respectively. Nano-precipitates form after austenite-ferrite transformation, which will be explained in Section 4-6-5. From their solubility, they are assumed to be carbides.

Figure 4-11a shows an example of a TEM BF image of nano-precipitates from Grade100 steel via carbon replicas. It shows that these precipitates are less than 10 nm in size and spherical in shape. The inset in Figure 4-11a shows the corresponding SAD pattern from the field of view. Several intermittent rings are visible and correspond to the fine precipitates with a NaCl-type crystal structure. From the lattice parameter anaysis, the nano-precipitates from carbon replicas are the same precipitates seen in thin foil samples, which will be discussed in Section 4-6-5. Figure 4-11b shows a DF image, taken using part of the {111} and {200} diffraction rings. The size distribution of the nano-precipitates was investigated using similar DF images. Several DF images were taken by varying the position of the objective aperture around the diffraction rings, so that all particles in the field of view were selected. From these DF images, more than two thousand nano-precipitates (mainly ≤10 nm) were counted for the size distribution analysis. To avoid multiple counting of precipitates, image processing software (ImageTool and Photoshop) was used to combine and merge the DF images taken from the same imaging area, but with different objective aperture locations, into a single image (e.g., Figure 4-11c). Particle analysis was then done on the merged image. The relative frequency versus diameter of nano-precipitates in the Grade100 steel is shown in Figure 4-11d. The relative frequency (n/N) is defined as the ratio of

the number of particles (n) within a given size range to the total number of particles counted in that region (N). Although most of these nano-precipitates are less than 10 nm in size, the largest number of precipitates is in the 4-5 nm size range.

Figure 4-11e shows an EDX spectrum from some of the nano-precipitates. They are Nb/Mo-rich with some Ti and a small amount of V. Although there is C present in the precipitates, the large C peak arises primarily from the carbon replica. The Cu peaks are an artifact arising from the Cu support grid. The small Fe peak is from the matrix. These Nb/Mo-rich nano-precipitates are dispersed in the ferrite matrix and can be seen everywhere. Table 4-4 shows the composition range of the nano-precipitates from the Grade100 steel using carbon replica and matrix dissolution techniques. The chemistry is the average composition obtained from the EDX microanalysis of groups of nano-precipitates (most are ≤10 nm).

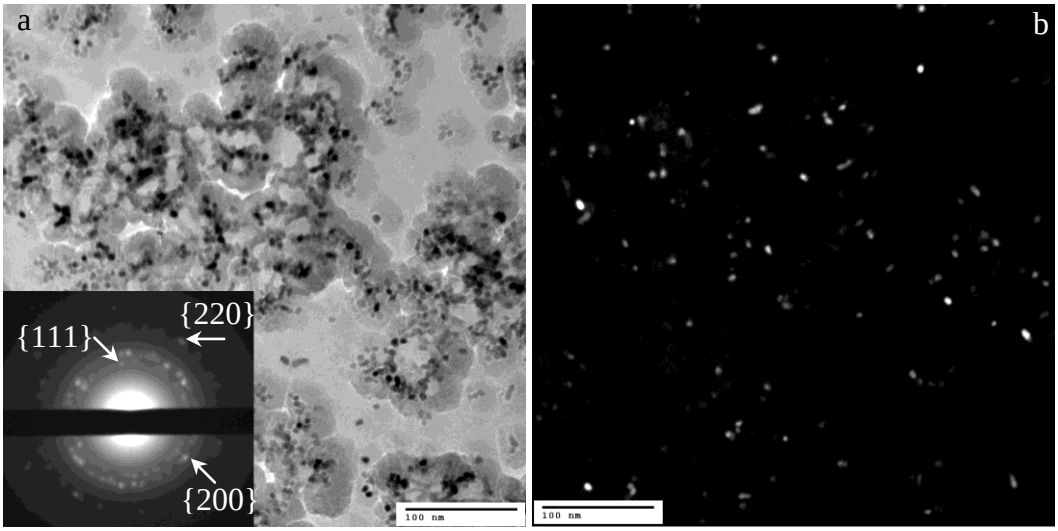

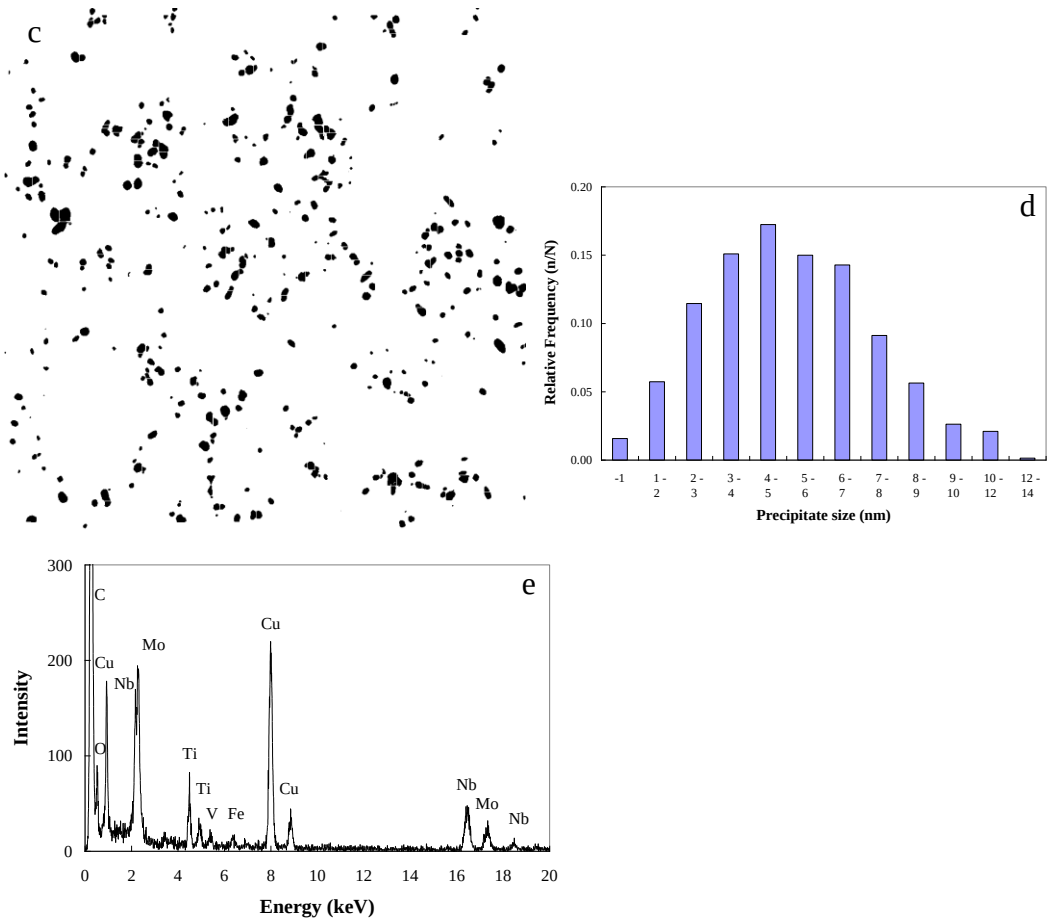

Figure 4-11 Nano-precipitates (mostly ≤10 nm) extracted via carbon replicas from Grade100 steel.

a) TEM BF image of nano-precipitates; b) TEM DF image of the same region as a; c) Merged image based on inverted DF images, used for size distribution analysis; d) Size distribution of nano-precipitates; e) EDX spectrum from a cluster of Nb/Mo-rich precipitates.

Table 4-4 Composition range and size of nano-precipitates (most are ≤10 nm) from Grade100 steel

Precipitate chemistry	STDEV of composition in atomic fraction			Size range (nm)
	Ti	Nb	Mo	
$Nb_{0.48}Mo_{0.28}Ti_{0.21}V_{0.03}C$	0.07	0.07	0.03	≤10, spherical

STDEV: standard deviation.

4-6-2. TEM analysis of precipitates extracted by HCl dissolution

The size and chemistry of the extracted precipitates were characterized by TEM imaging and EDX microanalysis in this section. Since the steel matrix was dissolved and precipitates were extracted, the interference of the steel matrix was avoided. From the precipitate analysis, five groups of precipitates were identified in terms of size and composition. Large Ti-rich nitride with sizes between a few hundred nanometres and 3 microns are formed during or soon after casting. Intermediate-sized Ti-rich (100-500 nm), Ti/Nb-rich (100-200 nm) and Nb-rich (100-200 nm) precipitates are formed during rolling. Nano-precipitates (≤10 nm, Nb/Mo-rich) are formed during or after coiling. Compared to carbon replica methods, a large amount of precipitates are extracted by matrix dissoution, making it possible for phase quantification.

4-6-2-1. Large and intermediate-size precipitates extracted by HCl dissolution

Figure 4-12 shows some of the TEM BF images and EDX spectra for the large and intermediate-sized precipitates extracted by HCl dissolution. A summary of the composition and approximate sizes of these precipitates is presented in Table 4-5. The size and chemistry difference between the various precipitates is because of a variation in the nucleation temperature and nucleation time.

Figure 4-12a shows a TEM BF image of a large cuboidal precipitate about 3μm in size. EDX analysis indicates that it is Ti-rich with a small amount of Nb. It is likely that the large cuboidal precipitates are formed at high temperature, in the liquid, during or soon after casting. They are too large to affect austenite grain size refinement during reheating. As such, it is desirable to avoid the formation of this type of precipitates. [153]

Figure 4-12b shows a group of intermediate-sized precipitates (about a few hundred nanometres in size). Most are cuboidal, except particle 5 in Figure 4-12b. EDX shows that particle 5 is composed of 30 at% Ti and 70 at% of Nb ($Ti_{0.3}Nb_{0.7}$). The other particles are Ti-rich precipitates with a relatively small amount of Nb. Precipitates in this group are likely Ti(Nb)CN, which are formed at intermediate temperatures during rolling.

Figure 4-12c and d show two groups of precipitates both with two Nb-rich precipitates attached to a Ti-rich precipitate. In both images, EDX analysis shows that the center precipitate is Ti-rich, while the Nb-rich particles have grown epitaxially on the pre-existing Ti-rich precipitate. Because TiN has a lower solubility in Fe (either austenite or ferrite) than NbC, NbN or Nb(CN), it precipitates first in the steel on cooling and can act as a heterogeneous nucleation site for Nb-rich precipitates. [154] EDX spectra of the Ti-rich precipitate and one of the Nb-rich precipitates from Figure 4-12c are shown in Figure 4-12e and f, respectively. The epitaxially-nucleated precipitates are the intermediate-sized Ti-rich and Nb-rich precipitates that are formed during rolling. Besides the epitaxially-nucleated precipitates in Figure 4-14c and d, some much finer particles are present as background in both images. They are nano-precipitates (≤10 nm in size and Nb/Mo-rich) and the amorphous Si-O phase, which will be discussed in the next section.

Figure 4-12g and h show two precipitates about 100 nm in size. EDX analysis indicates that both precipitates have similar amounts of Ti and Nb ($Ti_{0.5}Nb_{0.5}$). They are intermediate-sized Ti/Nb-rich carbonitrides.

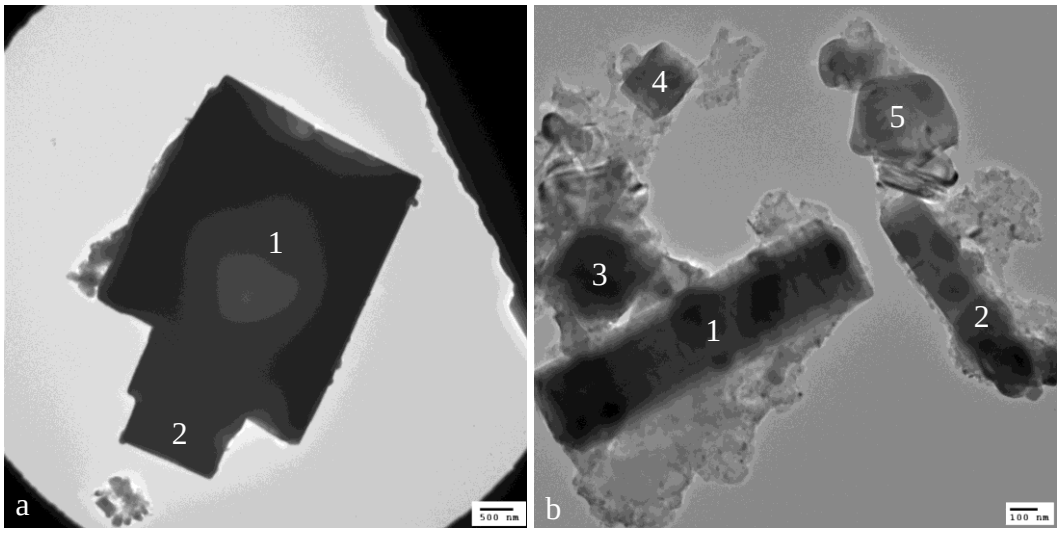

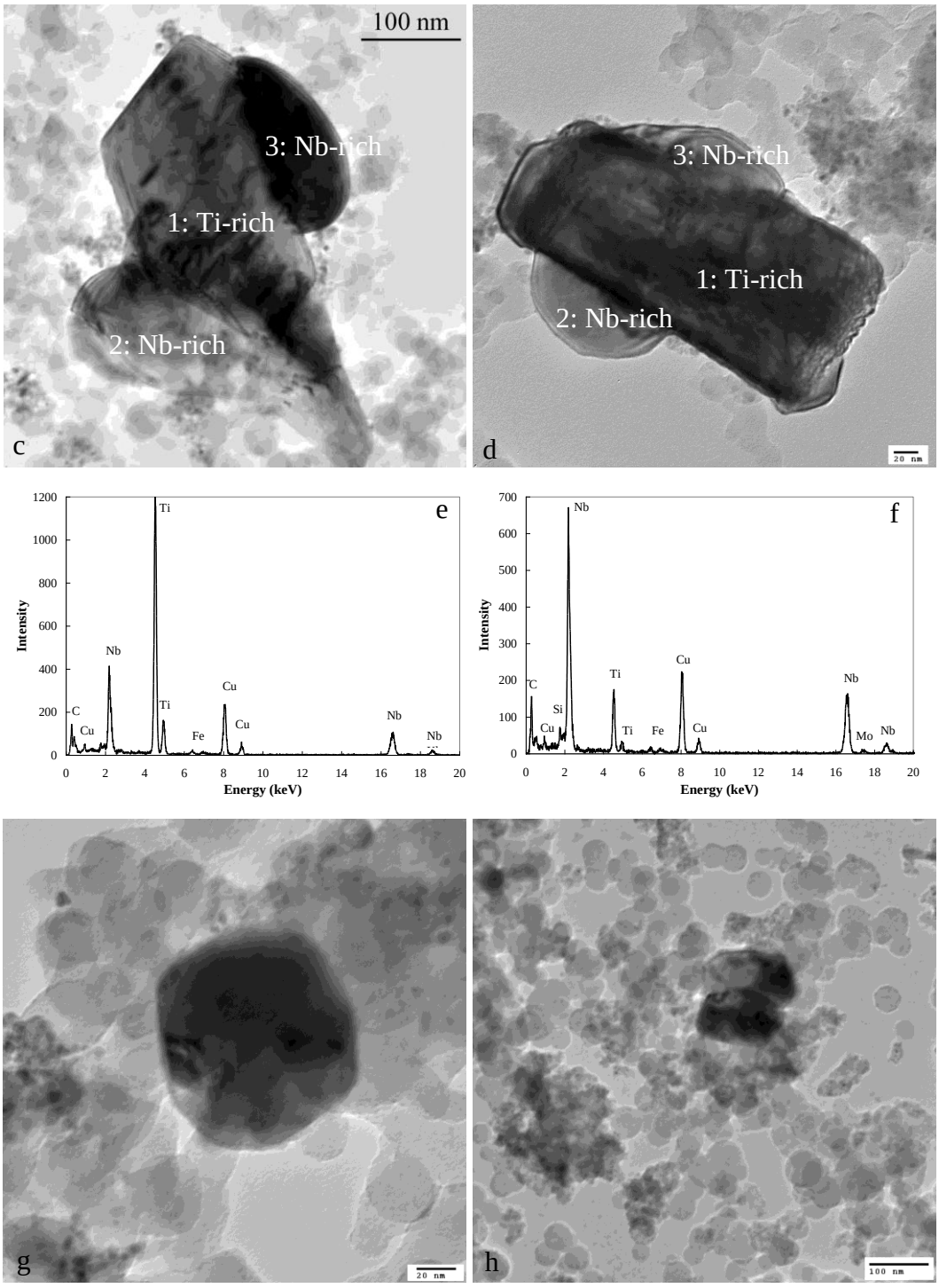

Figure 4-12 TEM BF images and EDX spectra of large and intermediate-size precipitates from Grade100 steel, extracted by HCl dissolution.

a) TEM BF image of a large Ti-rich precipitate; b) TEM BF image of intermediate-sized Ti-rich and Nb-rich precipitates; c, d) TEM BF images of epitaxial-nucleated precipitates; e) EDX spectrum from Ti-rich precipitate in c; f)

EDX spectrum from Nb-rich precipitate in c; g, h) TEM BF images of intermediate-sized Ti/Nb-rich precipitates.

Table 4-5 Chemistry (metallic elements) and size of large and intermediate-sized precipitates extracted by HCl dissolution

Image	Position	Chemistry	Largest dimension (nm)	Group
a	1	$Ti_{0.89}Nb_{0.11}$	3750	Large, Ti-rich, cuboidal
	2	$Ti_{0.93}Nb_{0.07}$	1770	
b	1	$Ti_{0.8}Nb_{0.2}$	1250	
	2	$Ti_{0.85}Nb_{0.15}$	800	
	3	$Ti_{0.81}Nb_{0.19}$	300	Intermediate, Ti-rich, cuboidal
	4	$Ti_{0.82}Nb_{0.18}$	250	
	5	$Nb_{0.7}Ti_{0.3}$	320	Intermediate, Nb-rich
c	1	$Ti_{0.82}Nb_{0.18}$	400	Intermediate, Ti-rich, cuboidal
	2	$Nb_{0.69}Ti_{0.31}$	200	Intermediate, Nb-rich
	3	$Nb_{0.64}Ti_{0.36}$	200	
d	1	$Nb_{0.64}Ti_{0.36}$	130	
	2	$Nb_{0.69}Ti_{0.31}$	120	
	3	$Ti_{0.82}Nb_{0.18}$	1000	Large, Ti-rich, cuboidal
g		$Ti_{0.49}Nb_{0.51}$	100	Intermediate, Ti/Nb
h		$Ti_{0.51}Nb_{0.49}$	100	

4-6-2-2. Nano-precipitates (≤ 10 nm) extracted by HCl dissolution

Figure 4-13 shows TEM BF images and EDX spectra of the extracted fine precipitates from the Grade100 steel by HCl dissolution. Figure 4-13b shows the nano-precipiates in Figure 4-13a at higher magnification. The finest precipitates extracted are less than 10 nm in size. EDX analysis (Figure 4-13c) reveals that they are Nb and Mo-rich, containing Ti and small amounts of V. The Ca peak in Figure 4-13c may come from the water used to dilute the supernatant. The chemistry of these nano-precipitates is shown in Table 4-4. An amorphous Si-O phase (Figure 4-13d and e), seen as spherical particles in Figure 4-13a, is also present in the residue. This phase is expected to be SiO_2 and was confirmed through Rietveld refinement by comparing its d-spacing with the modelling phase

(cristobalite). The specific peak positions of this amorphous SiO_2 will be presented in Section 4-7. To determine whether the source of O for the Si-O particles in the residue was the HCl solution (i.e., dissolved oxygen), N_2 was bubbled through the solution both prior to and during dissolution. However, SiO_2 was stilled extracted in the residue in the same quantities. Therefore, the source of O was likely oxide inclusions in the steel. It is known that Si is present in the steel, either in solid solution in the Fe matrix or as oxide/silicate inclusions. During steel dissolution, the oxide inclusions are dissolved in the HCl solution and the dissolved Si combines with dissolved O to precipitate out as Si-O phase.

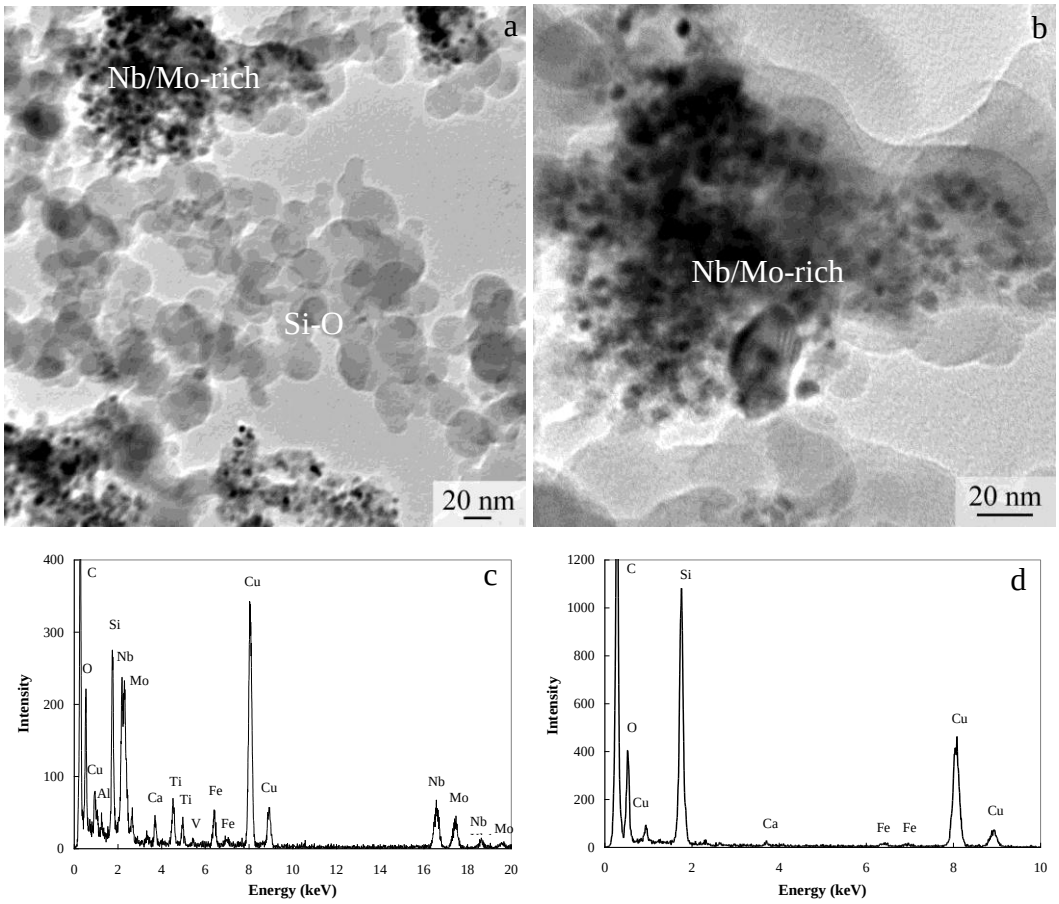

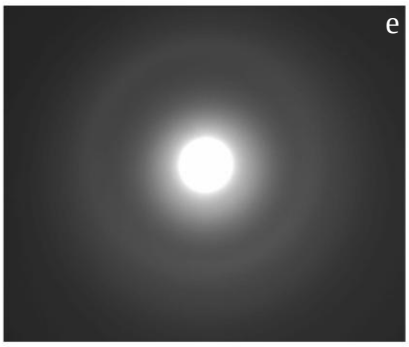

Figure 4-13 TEM BF images and EDX spectra from nano-precipitates (≤10 nm) extracted from Grade100 steel by HCl chemical dissolution.
a) TEM BF image of fine Nb/Mo-rich precipitates and SiO_2 particles;
b) TEM BF image of fine Nb/Mo-rich precipitates (high magnification);
c) EDX spectrum from Nb/Mo-rich precipitates; d) EDX spectrum from SiO_2;
e) SAD of SiO_2, indicating amorphous structure.

4-6-3. TEM analysis of precipitates extracted by I_2 dissolution

Figure 4-14 shows some of the TEM BF images and the corresponding EDX spectra of the precipitates extracted by chemical dissolution using I_2. Chemistry and precipitate size of these precipitates are listed in Table 4-6. Five groups of precipitates were also identified in terms of size and composition: large Ti-rich, intermediate-sized Ti-rich, Nb-rich, Ti/Nb-rich and nano-precipitates (≤10 nm, Nb/Mo-rich).

Figure 4-14a shows a TEM BF image of an intermediate-sized Ti-rich precipitate with the corresponding EDX spectrum shown in Figure 4-14b.

Figure 4-14c is a TEM BF image of a large Ti-rich precipitate and a cluster of nano-precipitates (≤10 nm). Figure 4-14d shows an intermediate-sized Ti/Nb-rich precipitate and a group of nano-precipitates (≤10 nm). EDX spectra from the intermediate size and nano-precipitates (≤10 nm) from Figure 4-14c are shown in Figure 4-14e and f, respectively.

Figure 4-14g shows a TEM BF image of an intermediate-sized Nb-rich precipitate and the corresponding EDX spectrum is shown in Figure 4-14 h).

Figure 4-14i shows an intermediate-sized Ti/Nb-rich precipitates with a cluster of nano-precipitates (≤10 nm). Figure 4-14j is a TEM BF image of the nano-precipitates (≤10 nm) in i at higher magnification. EDX spectra of the intermediate-sized precipitate and the nano-precipitates (≤10 nm) are shown in Figure 4-14k and l, respectively. EDX analysis of the nano-precipitates shows that they are Nb/Mo-rich with small amounts of Ti and V. The chemistry of the nano-precipitates is in good agreement with that obtained from carbon replicas and HCl dissolution. They correspond to the fine precipitates with composition corresponding to $Nb_{0.48}Mo_{0.28}Ti_{0.21}V_{0.03}C$ which has been presented in Table 4-4.

It can be seen that different sized precipitates can be extracted using I_2 dissolution and the extracted precipitates have similar information in terms of size and composition compared to the precipitates extracted by HCl dissolution. However, I_2 dissolution is very time consuming because of the slower matrix dissolution rate and tedious supernatant removal. Therefore, I_2 dissolution is not recommended and is not be used in precipitate extraction for other steels.

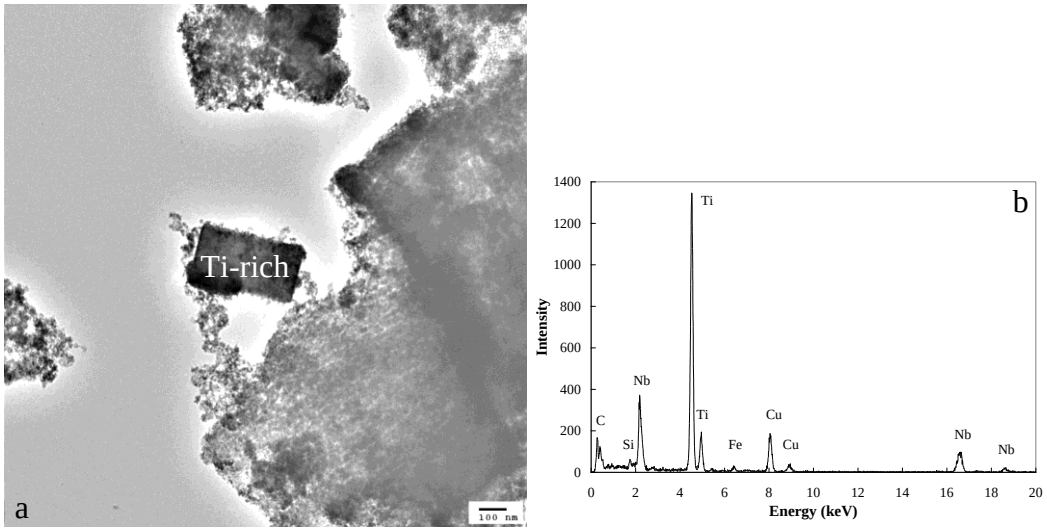

a, b) TEM BF image and EDX spectrum of an intermediate-sized Ti-rich precipitate.

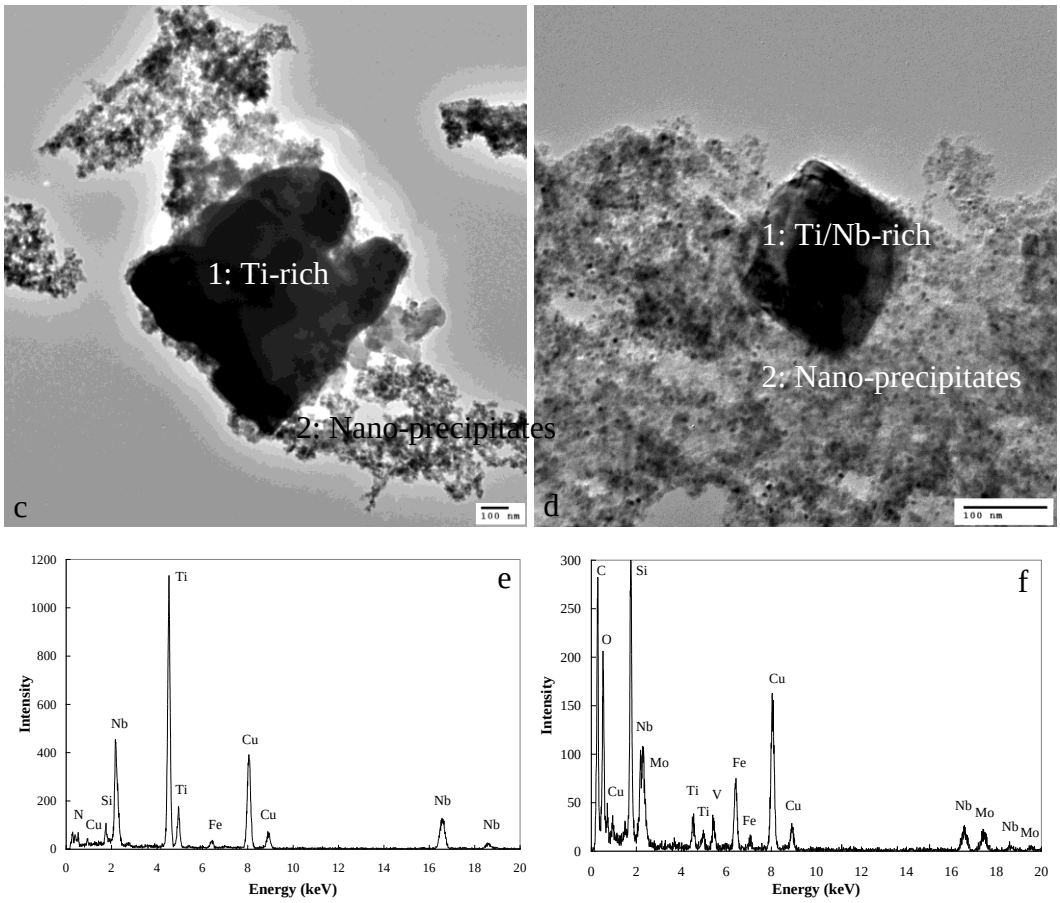

c) TEM BF image of a large Ti-rich precipitate and clusters of nano-precipitates; d) TEM BF image of an intermediate-sized Ti/Nb-rich precipitate and a cluster of nano-precipitates; e) EDX spectrum of the large Ti-rich precipitate in c; f) EDX spectrum of nano-precipitates in c.

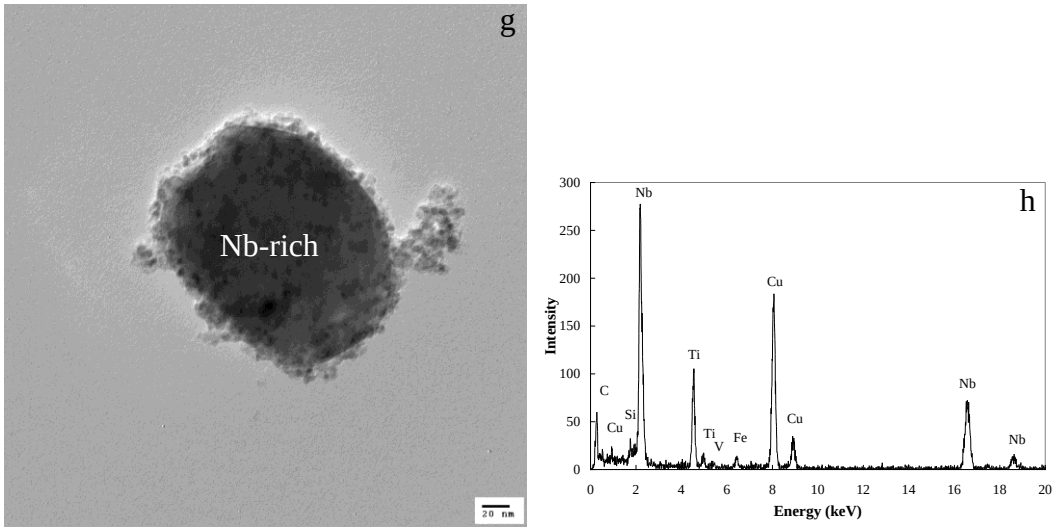

g, h) TEM BF image and the EDX spectrum of an intermediate-sized Nb-rich precipitate.

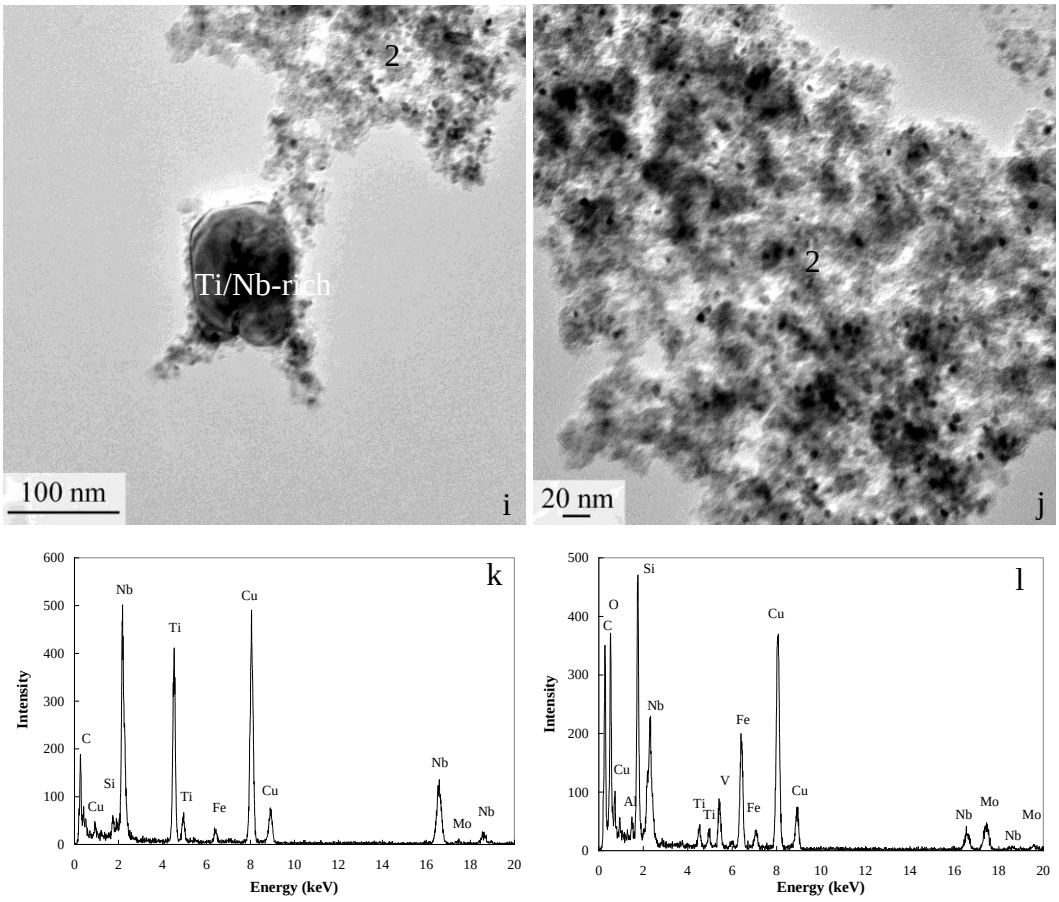

i) TEM BF image of an intermediate and nano-precipitates (mainly ≤10 nm);

j) TEM BF image of nano-precipitates in i with higher magnification;

k) EDX spectrum of the intermediate-sized precipitate in i;

l) EDX spectrum of nano-precipitates in j.

Figure 4-14 TEM BF images and EDX spectra of precipitates extracted using I_2 dissolution.

Table 4-6 Chemistry (metallic elements) and size of precipitates from Grade100 steel extracted by I_2 dissolution

Particle	Position	Chemistry	Largest dimension (nm)	Group
a	1	$Ti_{0.84}Nb_{0.16}$	350	Intermediate, Ti-rich, cuboidal
c	1	$Ti_{0.84}Nb_{0.16}$	800	Large, Ti-rich, cuboidal
	2	$Nb_{0.48}Mo_{0.28}Ti_{0.21}V_{0.03}$	≤10	Nano, spherical
d	1	$Ti_{0.55}Nb_{0.45}$	100	Ti/Nb-rich
	2	$Nb_{0.48}Mo_{0.28}Ti_{0.21}V_{0.03}$	≤10	Nano, spherical
g		$Nb_{0.64}Ti_{0.36}$	250	Intermediate, Nb-rich
i	1	$Ti_{0.69}Nb_{0.31}$	150	Intermediate, Ti-rich, cuboidal
i, j	2	$Nb_{0.48}Mo_{0.28}Ti_{0.21}V_{0.03}$	≤10	Nano, spherical

4-6-4. Characterization of precipitates extracted by 10%AA electrolytic dissolution

4-6-4-1. SEM analysis of coarse precipitates and inclusions

Relatively large precipitates extracted by 10%AA were identified by SEM. Figure 4-15 shows some of the SEM images (Figure 4-15a, c, d and e) and EDX spectra from these precipitates (Figure 4-15b, f, g and h). The chemistry and size measurements are listed in Table 4-7. They correspond to the large and intermediate-sized precipitates extracted by other methods.

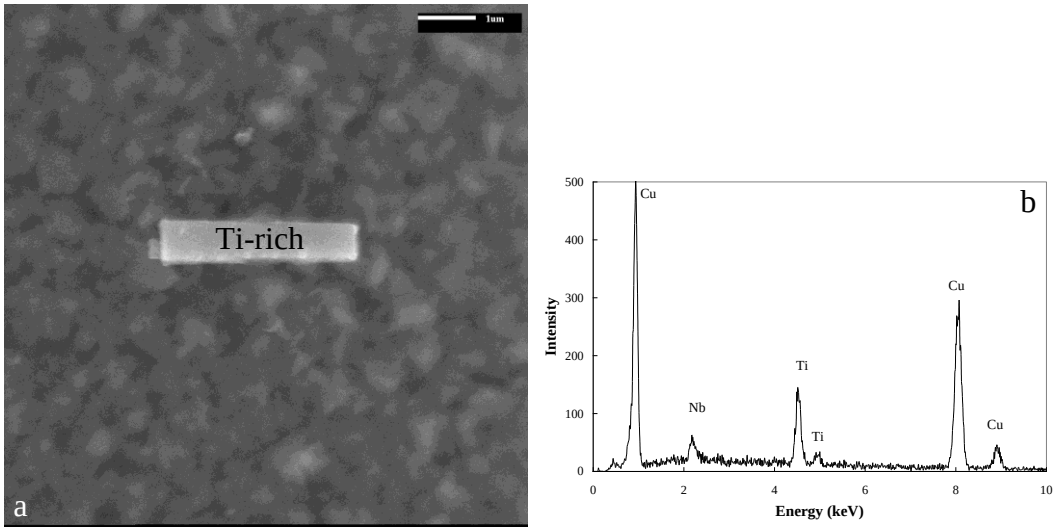

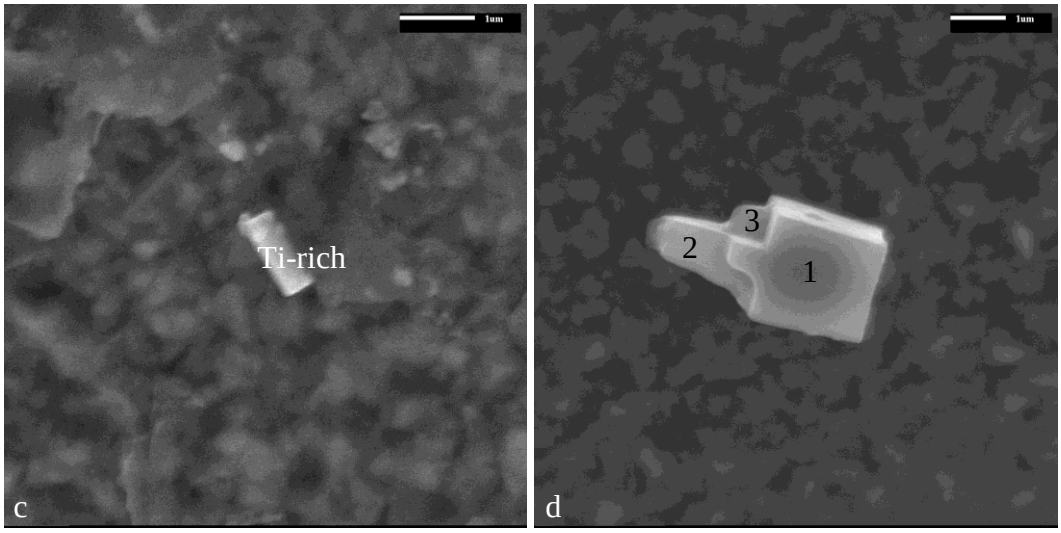

Figure 4-15 Large Ti-rich precipitates from Grade100 steel, extracted by 10%AA dissolution. a, c,d) SE-SEM images; b) EDX spectrum of precipitate shown in a.

Table 4-7 Chemistry (metallic elements) and size of large precipitates from Grade100 steel extracted by 10%AA dissolution

Image	Position	Chemistry	Size in length (nm)	Group
a		$Ti_{0.82}Nb_{0.18}$	3400	Large, Ti-rich, cuboidal
c		$Ti_{0.91}Nb_{0.09}$	1100	
d	1	$Ti_{0.93}Nb_{0.07}$	2100	
	2	$Ti_{0.96}Nb_{0.04}$		
	3	$Ti_{0.94}Nb_{0.06}$		

In addition to precipitates, some inclusions were extracted by 10%AA dissolution. Figure 4-16a and b show an SEM image of an Al-Ca-O-rich inclusion and the corresponding EDX spectrum. Significant amounts of Ti and a small amount of Nb were present in the inclusion. The rounded shape of the inclusion indicates the efficiency of inclusion shape control during steel making.

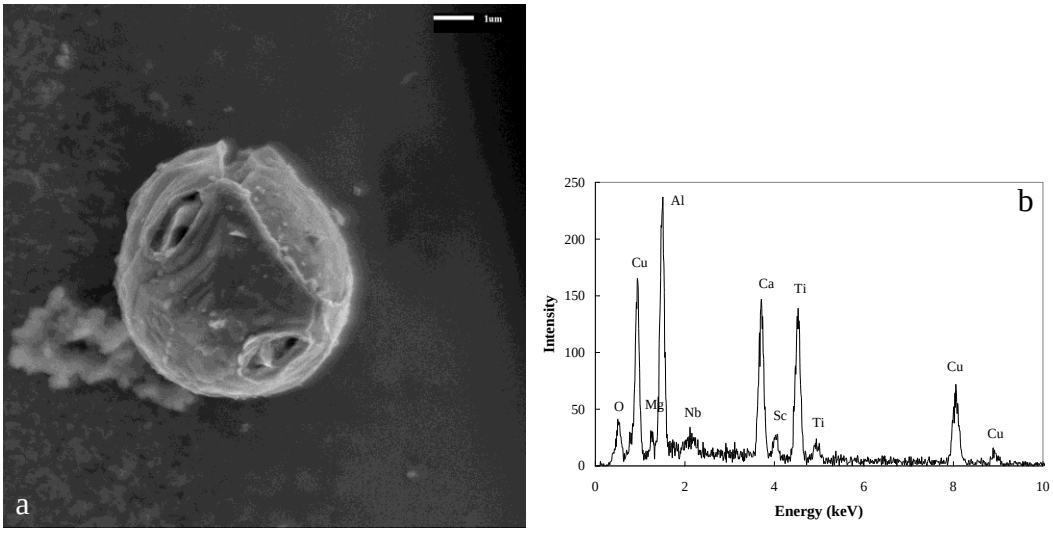

Figure 4-16 An inclusion from Grade100 steel, extracted by 10%AA dissolution. a) SE-SEM image; b) EDX spectrum of the inclusion shown in a.

4-6-4-2. TEM analysis of precipitates extracted by electrolytic dissolution

Figure 4-17a and b show TEM BF images of two groups of epitaxially-nucleated precipitates which were extracted by 10%AA dissolution. Figure 4-17c and d show EDX spectra of the Ti-rich precipitate and one of the Nb-rich precipitates in Figure 4-17a. An SAD pattern, with a zone axis (ZA) close to $[\bar{1}14]$, of the overlapping Ti-rich precipitate and Nb-rich precipitate is shown in Figure 4-17e. Figure 4-17f shows an SAD pattern of the Ti-rich precipitate in Figure 4-17a. The reflection $\{2\bar{6}2\}$ in Figure 4-17e, indicated by an arrow, shows spot splitting due to different lattice parameters from the different phases. From Table 2-3, Ti-rich precipitates have smaller lattice parameters than Nb-rich precipitates. Therefore, spots A (smaller d spacing) and B (larger d spacing) in Figure 4-17e come from Ti-rich and Nb-rich precipitates, respectively. It is expected that the coarse Ti-rich nitrides (cuboidal in shape) are formed during or soon after casting, the Nb-rich precipitates form in the austenite phase. This indicates that the Nb-rich particles grow epitaxially on the Ti-rich precipitate. The chemistry and size of the precipitates are listed in Table 4-8.

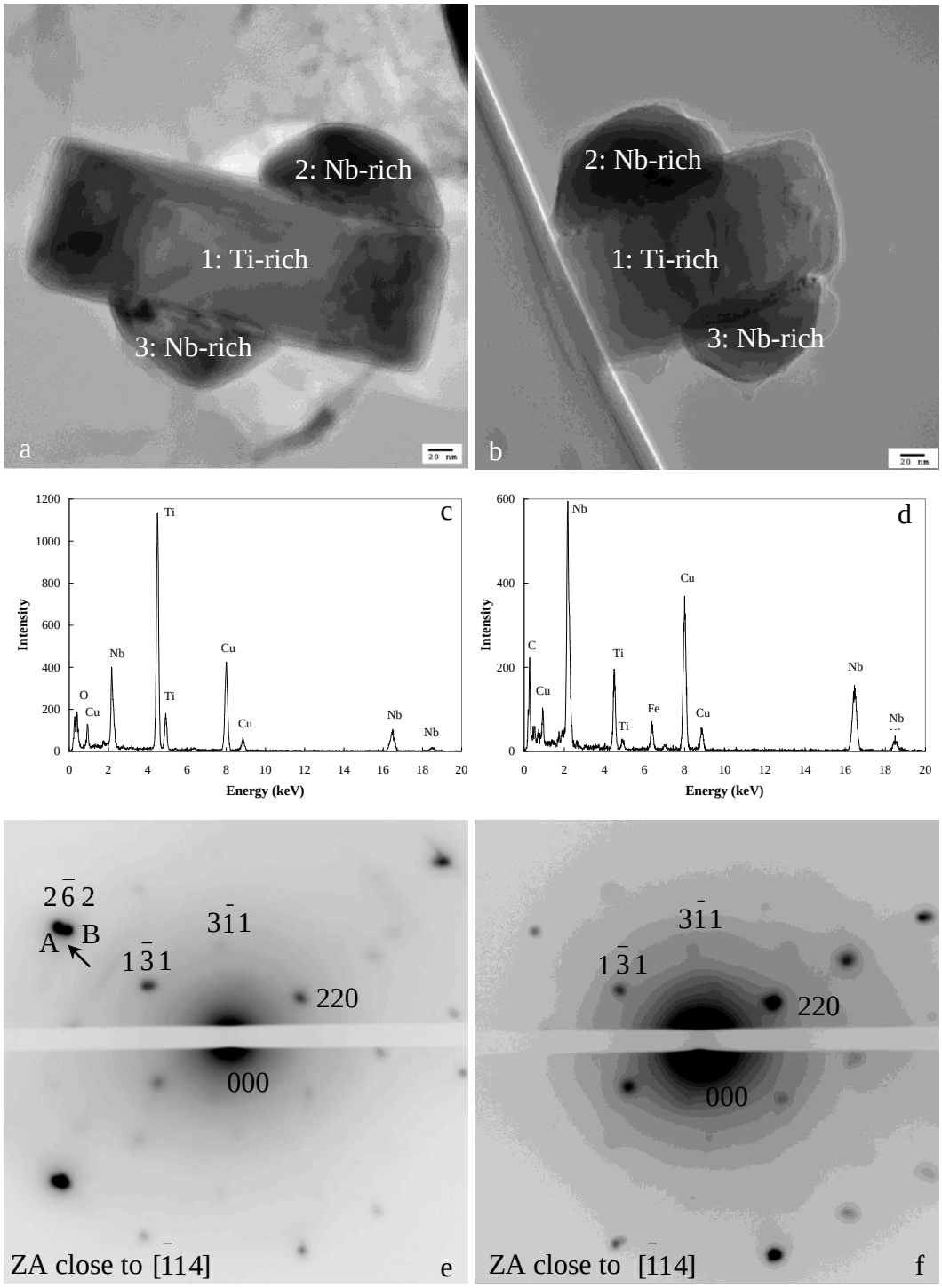

Figure 4-17 TEM BF images and the EDX spectra of epitaxially-nucleated precipitates from Grade100 steel, extracted by 10%AA dissolution.

a, b) TEM BF images of two groups of epitaxially-nucleated precipitates; c) EDX spectrum of Ti-rich precipitate in a; d) EDX spectrum from one of the Nb-rich

precipitate in a; e) SAD pattern from overlapping Ti-rich and Nb-rich precipitates (interface 1/2) in a; f) SAD pattern from Ti-rich precipitate in a.

Table 4-8 Chemistry (metallic elements) and size of intermediate-sized precipitates from Grade100 steel extracted by 10%AA dissolution

Image	Position	Chemistry	Largest dimension (nm)	Group
a	1	$Ti_{0.83}Nb_{0.17}$	360	Intermediate, Ti-rich, cuboidal
	2	$Nb_{0.68}Ti_{0.32}$	170	Intermediate, Nb-rich
	3	$Nb_{0.63}Ti_{0.37}$	160	
b	1	$Ti_{0.75}Nb_{0.25}$	240	Intermediate, Ti-rich, cuboidal
	2	$Nb_{0.76}Ti_{0.24}$	160	Intermediate, Nb-rich
	3	$Nb_{0.77}Ti_{0.23}$	130	

In addition to the intermediate-sized precipitates, nano-precipitates (≤10 nm) can also be extracted by 10%AA electrolytic dissolution. Figure 4-18 shows several TEM BF images (a, b, c and d) and corresponding EDX spectra (e and f) of the fine precipitates extracted by 10%AA dissolution. EDX analysis shows that they are Nb/Mo-rich with some Ti and V. The nano-precipitates have similar chemistry compared with those extracted by carbon replicas and HCl dissolution.

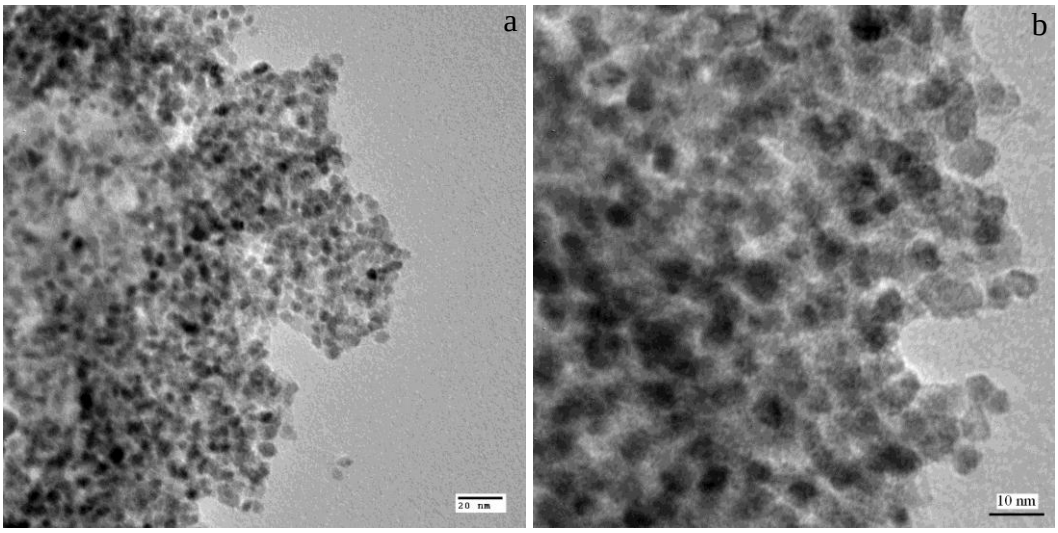

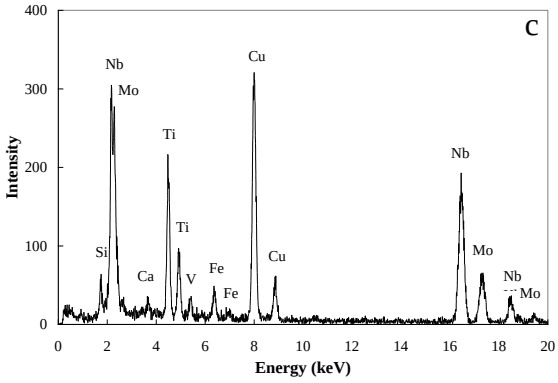

Figure 4-18 TEM BF images and EDX spectra of fine Nb/Mo-rich precipitates extracted by electrolytic dissolution (10%AA).

a, b) TEM BF images; c) EDX spectrum from the nano-precipitates shown in a.

From the above SEM/TEM imaging and EDX microanalysis, different size precipitates with various compositions can be successfully extracted by matrix dissolution, including chemical dissolution using HCl or I_2 and electrolytic dissolution using 10%AA. The precipitates extracted by the different methods all have similar information and can be categorized into five groups according to precipitate chemistry and size. For Grade100 steel, more than 70 precipitates (>10 nm) were characterized. More than 2000 nano-precipitates (mainly ≤10 nm) were counted for the size distribution and chemistry analysis. However, C and N were not quantified due to analysis difficulties of elements with low atomic numbers. Table 4-9 summarizes the precipitate information from Grade100 steel. The composition shown in Table 4-9 is the average composition measured for precipitates of a particular size. It is believed that large Ti-rich precipitates (500-3000 nm) are formed at higher temperature (during or soon after casting) and are expected to be Ti(Nb)N. Intermediate-sized Ti-rich (100-500 nm), Nb-rich and Ti/Nb-rich (100-200 nm) precipitates are formed during the rolling process. In order to simplify the calculations, it is assumed that they have similar amounts of C and N. (The actual composition could be different from this simplifying assumption.) Nano-precipitates (≤10 nm, Nb/Mo-rich) are formed at much lower temperature (during or after coiling). It is expected that they are carbides. The

expectation and assumptions are based on precipitate solubilities, which have been discussed in Section 2-2-4.

Table 4-9 Classification of precipitates from Grade100 steel according to composition and size range

Precipitate chemistry	STDEV of composition in atomic fraction			Size range (nm)
	Ti	Nb	Mo	
$Ti_{0.9}Nb_{0.1}N$	0.05	0.05	N/A	500-3000
$Ti_{0.77}Nb_{0.23}C_{0.5}N_{0.5}$	0.05	0.05	N/A	100-500
$Ti_{0.5}Nb_{0.5}C_{0.5}N_{0.5}$	0.07	0.07	N/A	100-200
$Nb_{0.7}Ti_{0.3}C_{0.5}N_{0.5}$	0.05	0.05	N/A	100-200
$Nb_{0.48}Mo_{0.28}Ti_{0.21}V_{0.03}C$	0.07	0.07	0.03	≤10, spherical

STDEV: standard deviation; N/A: not applicable.

4-6-5. TEM analysis of precipitates from thin foil samples

A TEM BF image of a coarse precipitate about 150 nm in size is shown in Figure 4-19a; a large number of nano-precipitates (≤10 nm), indicated by arrows, can also be seen. The corresponding EDX spectrum of this coarse precipitate is shown in Figure 4-19b, and indicates that it is Ti/Nb-rich precipitate. Iron peaks are from the ferrite matrix, as the sample is a thin foil. From the TEM images, it is clear that the coarse precipitates have a much lower number density than the fine precipitates.

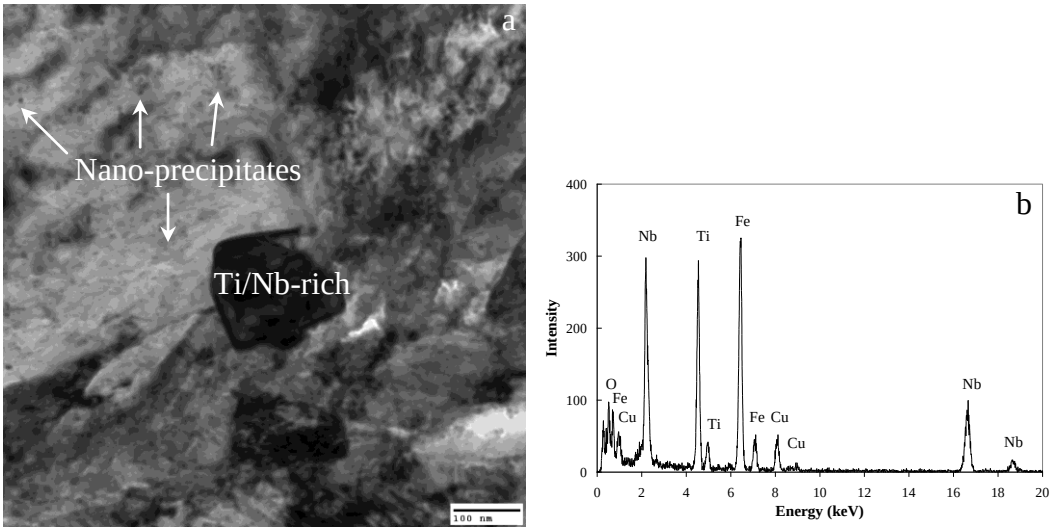

Figure 4-19 A coarse precipitate in the ferrite matrix from a thin foil sample. a) TEM BF image; b) EDX spectrum of the coarse Ti/Nb-rich precipitate shown in a.

Figure 4-20 shows a thin foil TEM sample prepared from the as-processed Grade100 steel. A BF image and the corresponding selected area diffraction (SAD) pattern from the field of view shown are given in Figure 4-20a. Several intermittent rings are visible (indexed as {111}, {200} and {220}) and correspond to fine precipitates which have a NaCl-type crystal structure, but are not visible in the BF image. The lattice parameter of the nano-precipitates is close to that of NbC. The other four diffraction spots, indexed as 200, $\bar{2}00$, 310 and $\bar{3}\bar{1}0$, are from the ferrite matrix. A DF image, taken using part of the {111} and {200} rings, is shown in Figure 4-20b; some of the fine precipitates (mostly ≤10 nm in size) are clearly visible as white spots.

Figure 4-21a and b show BF and DF images from another ferrite region containing the nano-precipitates. It is clear that the nano-precipitates have a high concentration compared to the coarse precipitates. Most of them are dispersed within the ferrite grains throughout the ferrite matrix. Several nano-pecipitates are aligned in a row as seen in Figure 4-21.

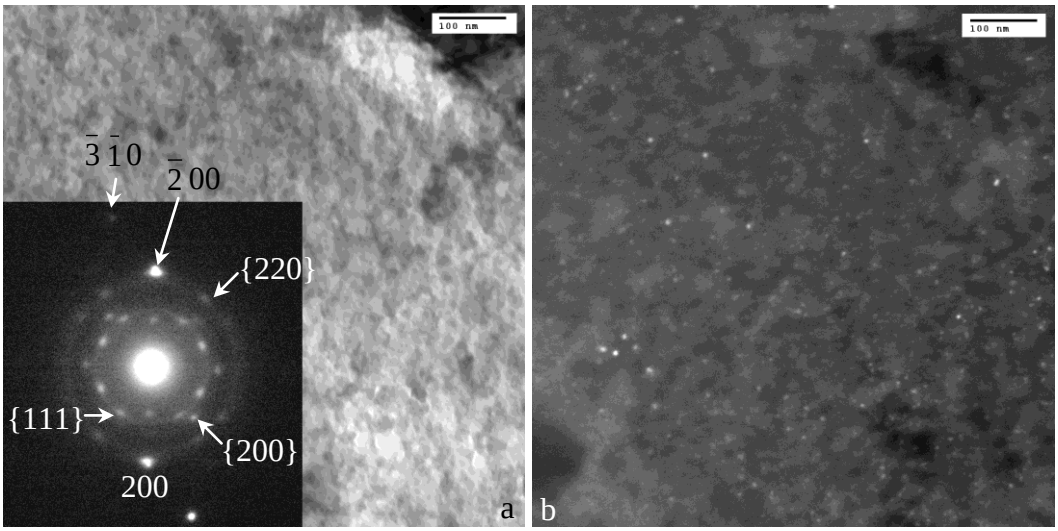

Figure 4-20 Fine NbC-based precipitates dispersed in the ferrite matrix from a thin foil sample. a) BF image; b) DF image.

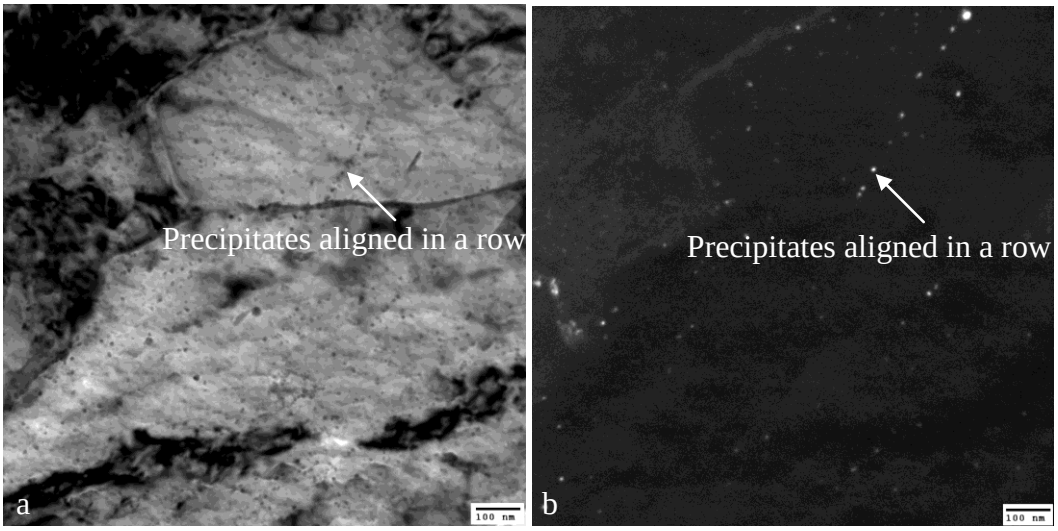

Figure 4-21 Fine NbC-based precipitates dispersed in the ferrite matrix from a thin foil sample. a) BF image; b) DF image.

It is known that there are two types of crystallographic orientation relationships (OR) for the precipitates with the matrix: the Kurdjumov-Sachs or Baker-Nutting relationship [63,155]. The precipitates and austenite both have a FCC crystal structure. For Ti, Nb and V carbonitrides that nucleate in austenite, like planes and directions are parallel, i.e., $(100)_{M(CN)}$ is parallel to $(100)_{\gamma}$ and is written as:

$$(100)_{M(CN)} \parallel (100)_{\gamma}$$
$$[010]_{M(CN)} \parallel [010]_{\gamma}$$

Ferrite has a Kurdjumov-Sachs (K-S) OR with the parent austenite, i.e., $(110)_{\alpha}$ is parallel to $(111)_{\gamma}$ and is written as:

$$(110)_{\alpha} \parallel (111)_{\gamma}$$
$$[111]_{\alpha} \parallel [110]_{\gamma}$$

Therefore, Ti, Nb and V carbonitrides that nucleate in austenite will have a K-S relationship with ferrite at room temperature, i.e.,

$$(111)_{M(CN)} \parallel (110)_{\alpha}$$
$$[110]_{M(CN)} \parallel [111]_{\alpha}$$

The OR between the precipitates that nucleate in ferrite (e.g., nano-NbC-rich precipitates with sizes less than 10 nm) is known as the Baker-Nutting OR with ferrite matrix [155], i.e., $(100)_{NbC}$ is parallel to $(100)_{\alpha}$ and is written as:

$$(100)_{NbC} \parallel (100)_{\alpha}$$
$$[100]_{NbC} \parallel [100]_{\alpha}$$

Two possible precipitation modes may happen during cooling after hot rolling. One way is interphase precipitation. [57] Nucleation occurs along the austenite-ferrite phase boundary. This precipitation mode appears as rows of particles in the TEM. Interphase precipitates usually form at moving interfaces during the austenite to ferrite transformation. Faster cooling rates lead to rapid movement of the austenite/ferrite interface which means that the interface velocity is too high to allow interphase precipitates to nucleate. [156,157] Therefore, it is believed that interphase precipitation is only possible at relatively high transformation temperatures or slower cooling rates after finish rolling. [158] The other precipitation mode is general, uniform nucleation of nano-precipitates in the newly formed ferrite. The general nano-precipitates follow a Baker-Nutting orientation relationship with the ferrite matrix. [57,159,160]

In Grade100 steel, both types of nano-precipitates (general and interphase precipitates) are identified. A small amount of interphase precipitates can be seen lining up in rows in Figure 4-21. The general nano-precipitates are in the majority and they are distributed throughout the ferrite matrix.

Figure 4-22 shows an SAD pattern of BCC α-Fe with a zone axis close to the [100] direction and the general nano-precipitates shown in Figure 4-21. The low order reflections are indexed and confirm the Baker-Nutting orientation relationship with the ferrite matrix.

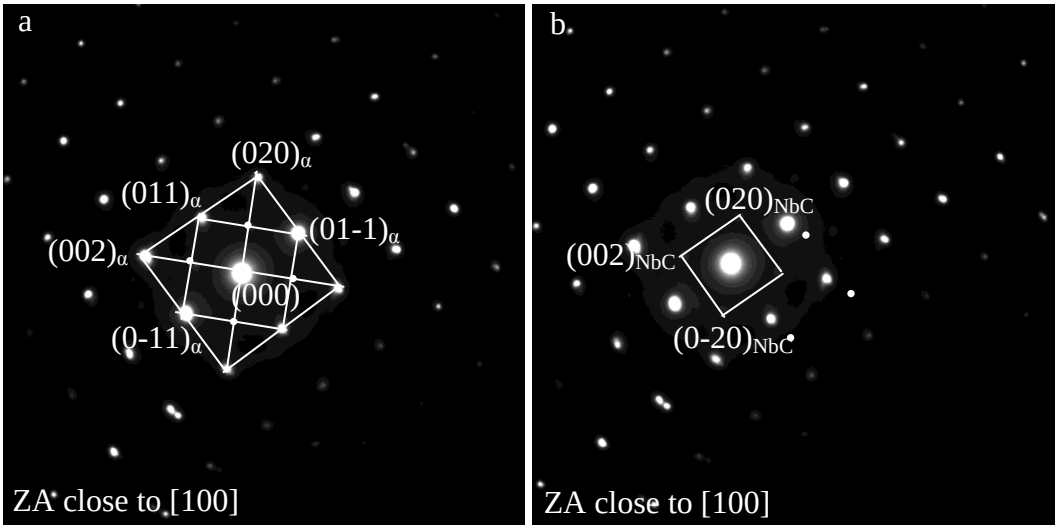

Figure 4-22 a) SAD pattern of BCC α-Fe close to the [100] zone axis;
b) the same SAD pattern highlighting the nano-precipitates.

Because of the OR of the nano-precipitates with the ferrite matrix, their chemistry and particle size, the nano-precipitates (mostly ≤10 nm in size) are expected to be formed mainly during coiling after austenite-to ferrite transformation. It is expected that CT/ICT should affect nano-precipitate nucleation, which will be discussed in Section 7-4-4-4.

It should be noted that thin foil samples are good for crystallographic orientation relationship analysis between precipitates and the steel matrix. They are not, however, good for precipitate chemistry analysis because of the fine sizes of the precipitates as well as the strong interference effect of the steel matrix.

Figure 4-23 shows two TEM BF images of dislocations that are effectively pinned by precipitates, as shown by arrows in the circled areas. Fine precipitates have a higher density per unit volume and can effectively impede dislocation movement compared to coarse precipitates.

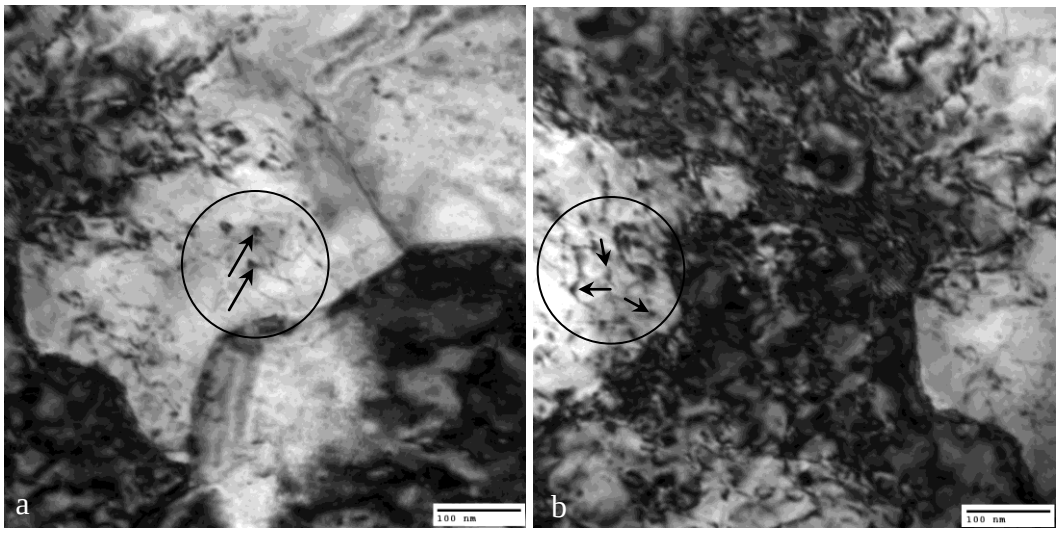

Figure 4-23 TEM BF images from thin foil samples, showing dislocations pinned by precipitates.

4-7. Rietveld refinement of the XRD data and determination of the relative abundance of different phases

4-7-1. Rietveld refinement of the XRD data

Detailed analysis of the XRD patterns was obtained via Rietveld refinement. From comparison of the XRD patterns from the HCl (Figure 4-8) and 10%AA dissolution (Figure 4-9), the absence of the broad amorphous peak in the sample produced by 10%AA dissolution allows for a better signal-to-noise ratio and peak resolution in the diffraction pattern, making Rietveld refinement less error prone. However, electrolytic dissolution is time consuming, making it impractical to implement.

From the previous section, precipitates were classified into five different groups according to size and chemical composition. These precipitates were used as the basis for Rietveld refinement, from which these five phases can be superimposed on the observed diffraction pattern. The relative abundance of each phase was determined and is presented in Section 4-7-2. Figure 4-24 shows the

profile fitting for the XRD pattern for the residue obtained from the Grade100 steel by 10%AA dissolution. Figure 4-24a shows the overall profile fitting and the difference between the calculated and observed spectrum. The calculated diffraction patterns for $Ti_{0.9}Nb_{0.1}N$, $Ti_{0.77}Nb_{0.23}C_{0.5}N_{0.5}$, $Ti_{0.5}Nb_{0.5}C_{0.5}N_{0.5}$, $Nb_{0.7}Ti_{0.3}C_{0.5}N_{0.5}$ and $Nb_{0.48}Mo_{0.28}Ti_{0.21}V_{0.03}C$ are shown in Figure 4-24b, c, d, e and f, respectively, as shown by arrows. The tick marks in the bottom of the figures indicate the positions of the above phases.

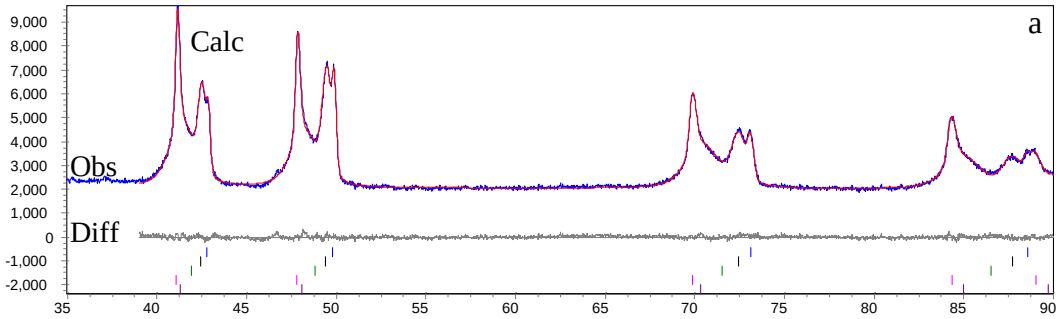

Obs: observed diffraction pattern; Calc: calculated diffraction pattern;

Diff: difference between the calculated and observed pattern.

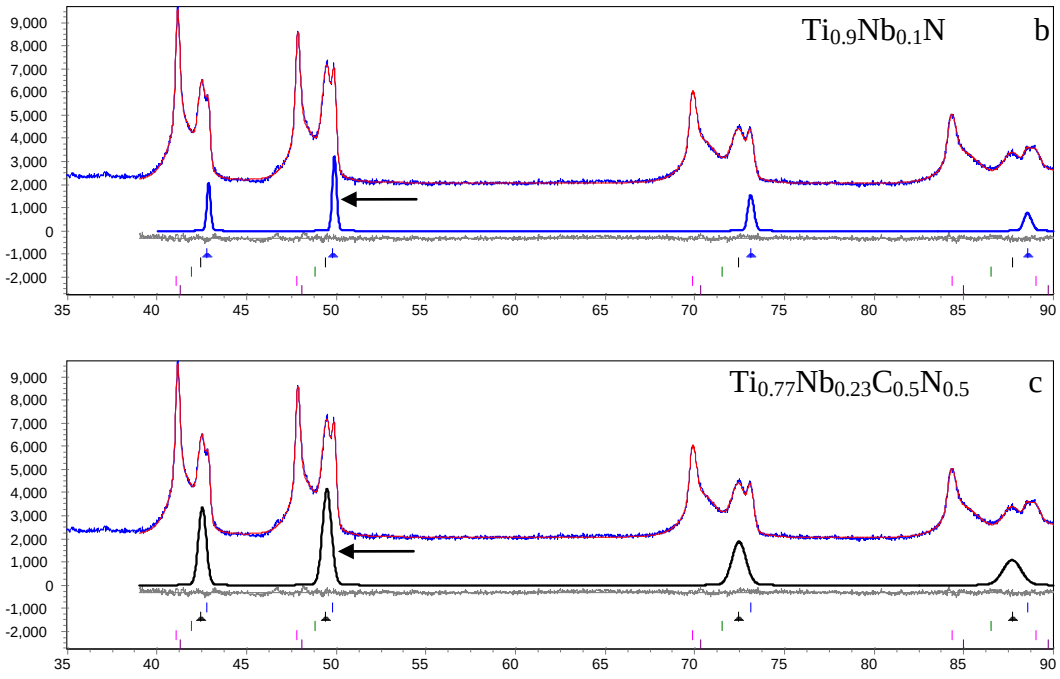

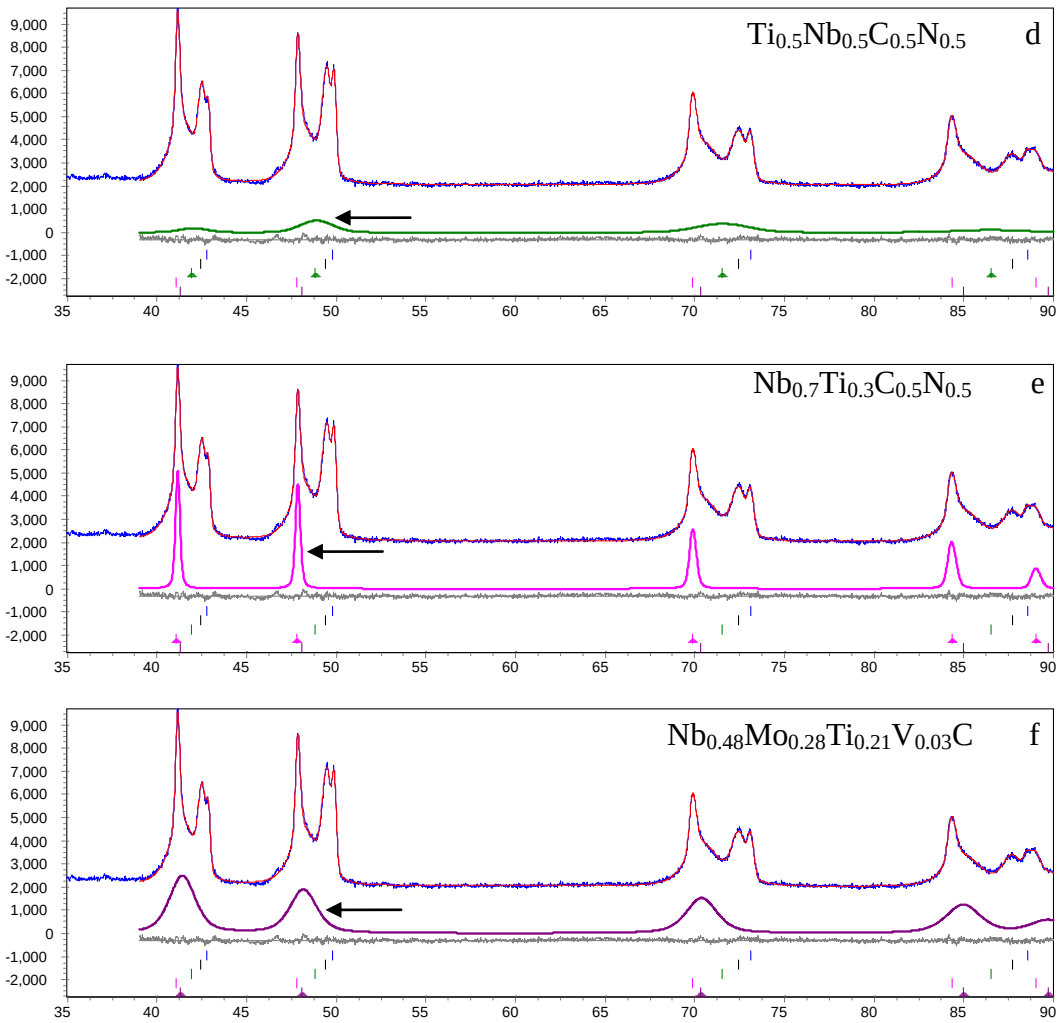

Figure 4-24 Profile fitting of XRD pattern by Rietveld refinement for precipitates from Grade100 steel, electrolytically dissolved using 10% AA dissolution. a) Overall XRD pattern profile fitting; b) calculated diffraction pattern for $Ti_{0.9}Nb_{0.1}N$; c) calculated diffraction pattern for $Ti_{0.77}Nb_{0.23}C_{0.5}N_{0.5}$; d) calculated diffraction pattern for $Ti_{0.5}Nb_{0.5}C_{0.5}N_{0.5}$; e) calculated diffraction pattern for $Nb_{0.7}Ti_{0.3}C_{0.5}N_{0.5}$; f) calculated diffraction pattern for $Nb_{0.48}Mo_{0.28}Ti_{0.21}V_{0.03}C$.

Profile fitting of the XRD pattern for the residue obtained from the Grade100 steel by HCl dissolution, shown in Figure 4-25, is slightly different from that by 10%AA dissolution. Because nano-precipitates (mostly ≤10 nm) with chemistry $Nb_{0.48}Mo_{0.28}Ti_{0.21}V_{0.03}C$ have broad peaks, there is a strong correlation with amorphous SiO_2, i.e., the nano-precipitate information is contained within the

amorphous SiO_2 information. Therefore, the nano-precipitate phase and amorphous SiO_2 are considered as one phase in the Rietveld refinement. The correlation between nano-precipitates and amorphous SiO_2 and determination of the nano-precipitates will be explained in Section 4-7-2-1. Figure 4-25a shows the overall profile fitting and the difference between the calculated and observed spectrum. Figure 4-25b, c, d, e and f show the calculated diffraction patterns for $Ti_{0.9}Nb_{0.1}N$, $Ti_{0.77}Nb_{0.23}C_{0.5}N_{0.5}$, $Ti_{0.5}Nb_{0.5}C_{0.5}N_{0.5}$, $Nb_{0.7}Ti_{0.3}C_{0.5}N_{0.5}$ and the amorphous SiO_2, respectively, as shown by arrows. The tick marks in the bottom of the figures indicate the positions of the above phases. This indicates that because of the strong correlation between the nano-precipitates (≤10 nm) and amorphous SiO_2, the amount of nano-precipitates cannot be determined directly from the Rietveld refinement and will be explained in the following section. In order to apply the Rietveld refinement to the amorphous SiO_2 structure, a crystalline form of silica, cristobalite, is used to approximate the amorphous phase. Cristobalite has a tetragonal structure (a=0.49732nm, c=0.69236nm), [60] with the same composition and similar d-spacings to the major d-spacings of amorphous SiO_2.

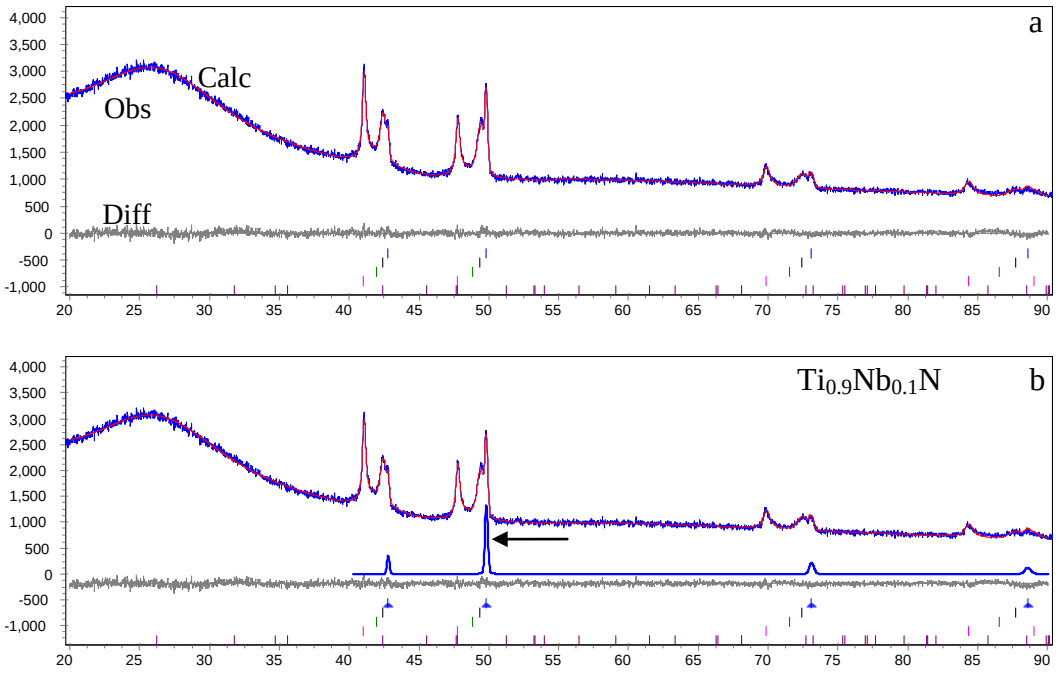

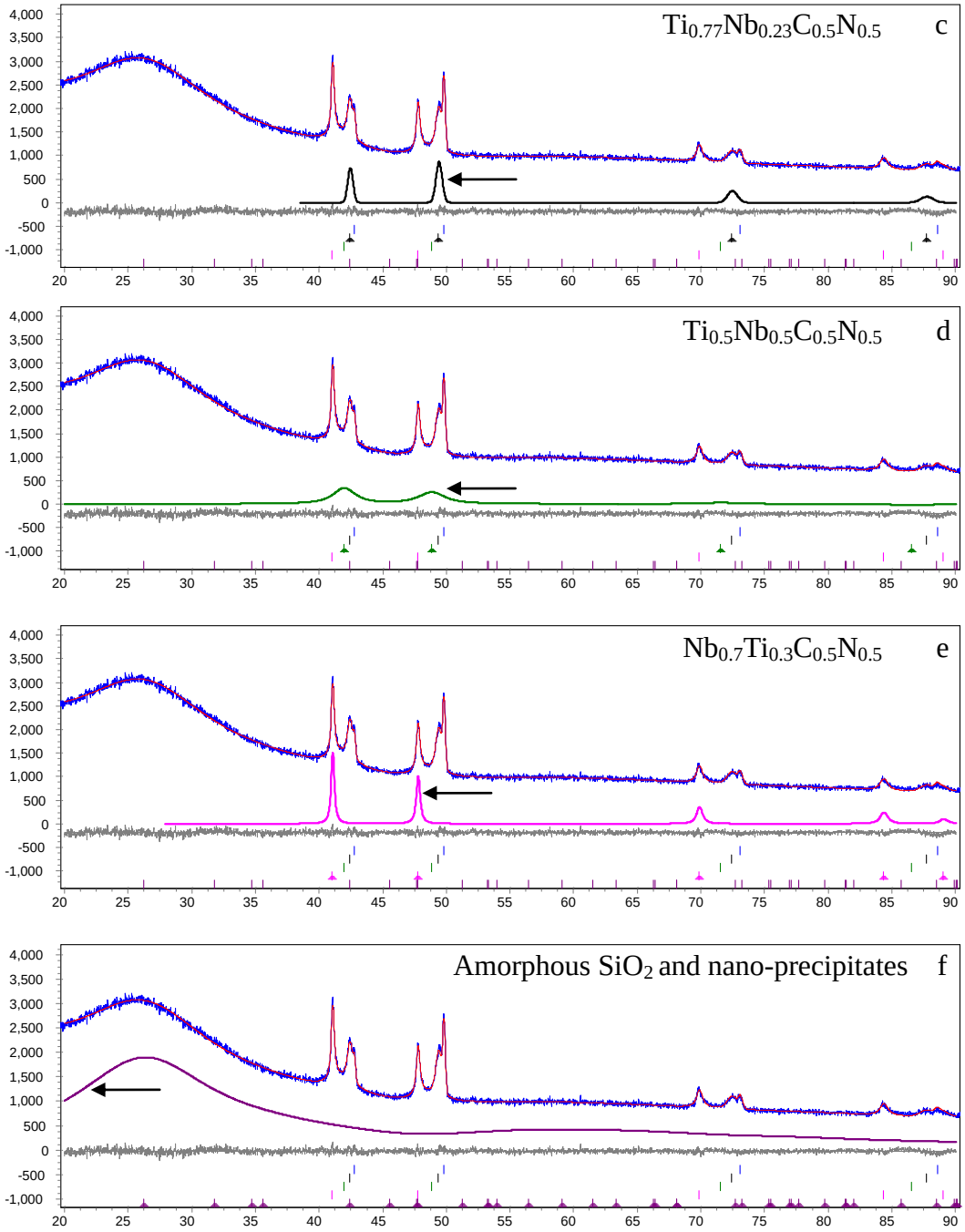

Figure 4-25 Profile fitting of XRD pattern by Rietveld refinement for residue from Grade100 steel, chemically dissolved using HCl dissolution.

a) Overall XRD pattern profile fitting; b) calculated diffraction pattern for $Ti_{0.9}Nb_{0.1}N$; c) calculated diffraction pattern for $Ti_{0.77}Nb_{0.23}C_{0.5}N_{0.5}$; d) calculated diffraction pattern for $Ti_{0.5}Nb_{0.5}C_{0.5}N_{0.5}$; e) calculated diffraction pattern for

$Nb_{0.7}Ti_{0.3}C_{0.5}N_{0.5}$; f) calculated diffraction pattern for amorphous SiO_2 and nano-precipitates.

4-7-2. Determination of the amount of nano-precipitates (≤10 nm)

4-7-2-1. Determination of the relative abundance of different phases via Rietveld refinement

The relative abundance (percentage content) of the constituent crystalline phases in the sample was determined from equation 2-32. The scale factors, determined by the mass, number and volume of the unit cell of each phase, were derived from Rietveld refinement of the XRD data.

$$w_a = \frac{SF_a (MZV)_a}{\sum_j SF_j (MZV)_j} \tag{2-32}$$

w_a: relative weight fraction of phase a in a mixture of *j* phases;

SF: Rietveld scale factors derived from the refinement which are proportional to the number of unit cells of phase *a* in the specimen;

M: mass of the molecular formula unit;

Z: number of formula units per unit cell;

V: volume of the unit cell.

The precipitate information from Rietveld refinement is shown in Table 4-10 and Table 4-11. The data corresponds to the residue extracted by 10%AA and HCl dissolution, respectively. The data includes the refined lattice parameter and relative abundance of the constituent crystal phases. According to the experimental extraction yield, the wt% of different precipitates compared to the weight of steel can be obtained and are shown in Table 4-10 and Table 4-11 as well.

As mentioned in the last section, the nano-precipitate phase and amorphous SiO_2 have a strong correlation (peak overlap) for the residues extracted by HCl dissolution. The correlation is due to the amorphous SiO_2 background extending up to the base of the whole XRD pattern, making it difficult to deconvolute the

crystalline phases from the SiO_2 amorphous background. The correlation is very strong especially for the nano-precipitates because the nano-precipitates have broad peaks according to the Scherrer Equation shown in Equation (4-2). [161] When parallel monochromatic radiation impinges on many random oriented crystals, the diffracted beam is broadened when the crystallite size is small.

$$L_{Vol} = K'\lambda / \beta_{hkl} \cos\theta_{hkl} \tag{4-2}$$

L_{vol}: the volume weighted crystallite size;

K': constant (K'= 0.9 for cubic crystallites);

λ: wavelength of the radiation;

θ: Bragg angle;

β: integral breadth of a reflection *hkl* (in radians 2θ) located at 2θ.

Because of the strong correlation between the nano-precipitates and the amorphous SiO_2, they are considered as one phase in the Rietveld refinement. Therefore, the amount of nano-precipitates is not determined directly from the Rietveld refinement. SiO_2 was used as an internal standard and the resulting residual amorphous content is ascribed to the nano-precipitates (mainly ≤10 nm). The amount of SiO_2 is determined from the reaction between Si and O, where the Si content in the residue was obtained from the total amount of Si in the steel and that in the supernatant via ICP analysis. In addition, the lattice parameter of the nano-precipitates extracted by HCl dissolution is not refined in Rietveld refinement. However, the nano-precipitates, extracted by the two dissolution methods, are both from Grade100 steel, so they should have the same lattice parameter.

Table 4-10 The relative abundance (wt%) of the constituent crystalline phases for Grade100 steel electrochemically dissolved using 10%AA dissolution

Phases	Lattice parameter nm	Relative abundance of precipitates in the extracted residue (wt%)	Experimental extraction yield (wt%)	Wt% compared to the weight of steel being dissolved
$Ti_{0.9}Nb_{0.1}N$	0.4248	10.85%	0.361%	0.038%
$Ti_{0.77}Nb_{0.23}C_{0.5}N_{0.5}$	0.4282	26.49%		0.096%
$Ti_{0.5}Nb_{0.5}C_{0.5}N_{0.5}$	0.4329	8.59%		0.031%
$Nb_{0.7}Ti_{0.3}C_{0.5}N_{0.5}$	0.4418	15.50%		0.056%
$Nb_{0.48}Mo_{0.28}Ti_{0.21}V_{0.03}C$	0.4392	38.84%		0.140%

Table 4-11 The relative abundance (wt%) of the constituent crystalline phases for Grade100 steel chemically dissolved using HCl dissolution

Phases	Lattice parameter nm	Relative abundance of precipitates in the extracted residue (wt%)	Experimental Extraction yield (wt%)	Wt% compared to the weight of steel being dissolved
$Ti_{0.9}Nb_{0.1}N$	0.4250	1.65%	0.792%	0.013%
$Ti_{0.77}Nb_{0.23}C_{0.5}N_{0.5}$	0.4282	3.43%		0.027%
$Ti_{0.5}Nb_{0.5}C_{0.5}N_{0.5}$	0.4329	0.77%		0.006%
$Nb_{0.7}Ti_{0.3}C_{0.5}N_{0.5}$	0.4419	3.15%		0.025%
$Nb_{0.48}Mo_{0.28}Ti_{0.21}V_{0.03}C$	0.4392	19.78%		0.157%

Comparing Table 4-10 and Table 4-11, the lattice parameters for similar phases agree very well, which is expected because the precipitates are from the same Grade100 steel; only the extraction methods are different. For the different precipitate phases, $Ti_{0.9}Nb_{0.1}N$ has the smallest lattice parameter. The lattice parameter increases with increasing Nb content, which is in good agreement with the lattice parameters for binary Ti and Nb carbides or nitrides shown in Table 2-3.

It is clear that nano-precipitates with an average composition of $Nb_{0.48}Mo_{0.28}Ti_{0.21}V_{0.03}C$ ($\leq$10 nm) are the majority crystalline phase in the extracted residues from both 10%AA and HCl extraction methods. The wt% of this type of precipitate is 0.140% (10%AA dissolution) and 0.157% (HCl

dissolution), respectively. The difference in the amount of this type of precipitate is within 10%, which is acceptable. If the precipitation strengthening is calculated using equation (2-2), the difference of precipitation strengthening is not significant, i.e, 195.0MPa using 0.157% and 184.5MPa using 0.140%. However, there is poor agreement for the other types of precipitates with the two extraction methods. There are several possible reasons for the discrepancy. First, the other types of precipitates have much lower amounts compared to the nano-precipitates, so that higher errors may be incurred. Second, there is a strong correlation between amorphous SiO_2 and the nano-precipitates. Determination of the relative abundance of different precipitate phases is interfered by SiO_2 in the HCl dissolution method. Third, a smaller amount of precipitates produced by 10%AA dissolution were used for XRD analysis (about 10% of the mass used for HCl dissolution) due to the inefficiency in precipitate extraction. Lastly, there is a detection limit for XRD. Therefore, certain errors are involved in precipitate quantification, especially for the minor precipitate phases. Overall, if the same amounts of residues are collected by both HCl and 10%AA dissolution methods, the latter method is more reliable because determination of the relative abundance of nano-precipitates is not interfered by SiO_2. But 10%AA dissolution method is much slower than HCl method. It is impractical to extract large amount of precipitates by 10%AA method for further analysis. Therefore, HCl method is used for all steels.

4-7-2-2. Determination of the amount of nano-precipitates based on the amount of Mo

The other way to determine the amount of nano-precipitates (≤10 nm) is based on the amount of Mo. The ICP analysis of the supernatant indicates that most of the Mo is present in solid solution in the ferrite. The remaining Mo (Table 4-2) is only attributed to the nano-precipitates (≤10 nm), as confirmed by TEM-EDX analysis (see Figure 4-11, Figure 4-13, Figure 4-14 and Figure 4-18). Therefore, the amount of nano-precipitates (≤10 nm) can be determined using equation (4-3). This is based on the chemistry of the nano-precipitates and the total amount of Mo available for precipitation.

$$\frac{wt_{Mo}}{A_{Mo}} = \frac{wt_{ppt}}{A_{ppt}} * at\%_{Mo} \quad (4\text{-}3)$$

wt_{Mo}: total amount (weight) of Mo available for precipitation, which is determined from the total amount of Mo in steel and that in the supernatant via ICP analysis;

wt_{ppt}: amount (weight) of nano-precipitate (≤10 nm), to be determined;

A_{Mo}: atomic weight of Mo;

A_{ppt}: molecular weight of nano-precipitate (≤10 nm);

$at\%_{Mo}$: atomic fraction of Mo in the nano-precipitate (≤10 nm), from the nano-precipitate composition determined from TEM-EDX microanalysis, i.e., 0.28.

Figure 4-26 shows a comparison of the amount of nano-precipitates based on Rietveld refinement (via HCl and 10%AA dissolution) and that based on the Mo amount. The amount of nano-precipitates (≤10 nm) determined by the different methods are very close.

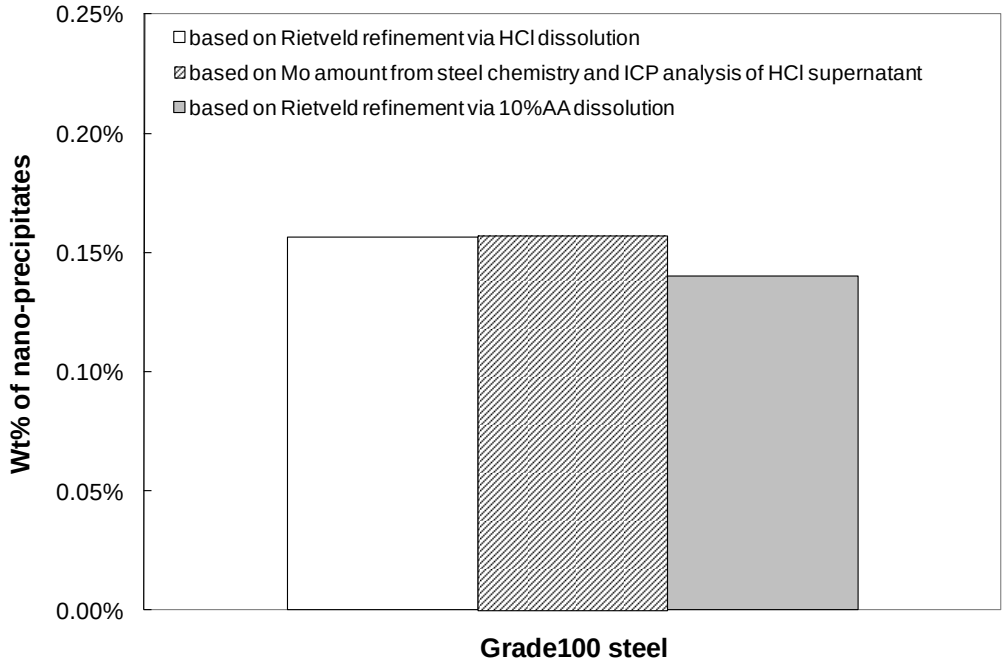

Figure 4-26 The amount of nano-precipitates (≤10 nm) compared with the original weight of the steel.

4-8. Summary

From the microstructural studies of Grade100 steel, the main results are summarized as follows.

Different sized precipitates can be successfully extracted using chemical dissolution (HCl and I_2) and 10%AA electrolytic dissolution. HCl dissolution is more efficient in extracting these precipitates. However, SiO_2 comprises a large portion of the residue in HCl dissolution.

The overall chemistry of the extracted precipitates can be obtained using SEM-EDX. The crystal structure of the extracted precipitates can be identified by XRD analysis and it was found that all precipitates have the NaCl-FCC structure. However, detailed precipitate information, i.e., lattice parameters and relative amounts of the precipitates, requires Rietveld refinement. Furthermore, the successful use of Rietveld refinement is based on the known chemical compositin of precipitates.

Based on SEM/TEM imaging and EDX microanalysis, five groups of precipitates were identified in Grade100 steel in terms of size and composition. It is clear that nano-precipitates (≤10 nm) with average chemistry $Nb_{0.48}Mo_{0.28}Ti_{0.21}V_{0.03}C$ are the majority crystalline phase in the extracted residues from both 10%AA and HCl extraction methods.

Most of the Mo present in the steel is dissolved in ferrite, with the remaining Mo present in the nano-precipitates (≤10 nm). Therefore, the amount of nano-precipitates (≤10 nm) can also be determined based on the amount of Mo. The amount of nano-precipitates (≤10 nm) determined by the above two methods are quite similar.

The knowledge gained from the study of Grade100 steel serves as a basis for further study of other grades of steels.

Chapter 5: X70 and X80 steels

5-1. Introduction

In Chapter 4, the steel microstructure and grain size of the Grade100 steel were studied. Precipitates were extracted by matrix dissolution. The results indicate that chemical dissolution using HCl is an efficient technique to extract a significant amount of precipitates for further quantitative analysis. Based on the precipitate chemistry from SEM/TEM-EDX, the relative abundance of different precipitates was successfully determined using Rietveld refinement of XRD data. From this information, the wt% of different precipitates was determined.

Based on the knowledge gained from the study of Grade100 steel, the microstructure and precipitate information for the X70 and X80 steels are studied in this Chapter. The microstructural features are studied using OM and SEM and are presented in Section 5-2. Grain size is measured based on SEM SE images. Precipitates were extracted by matrix dissolution using HCl. Thus, in Sections 5-3 and 5-4, the overall chemistry of the extracted precipitates is analyzed by SEM-EDX and then subjected to XRD analysis for phase identification. In Section 5-5, the supernatant is tested using ICP for element concentration analysis. In Section 5-6, precipitate size and chemistry are determined by SEM/TEM imaging and EDX microanalysis, which is used as the basis for Rietveld refinement. In Section 5-7, the relative abundance of each precipitate phase is determined by Rietveld refinement based on XRD data. The amount of nano-precipitates ($\leq$10 nm) is determined based on the amount of Mo as well. Comparison is made about the amount of nano-precipitates based on Rietveld refinement and Mo-based calculations.

Representative results are shown in this chapter. This includes overall microstructural images from X70-564 and X80-462 steels, SEM/TEM images and EDX spectra of the precipitates from X80-462 steel and the profile fitting of the XRD patterns from X70-564 and X80-462 steels. Additional microstructural images, SEM/TEM images and EDX spectra for the other steels are shown in

Appendix A. Additional profile fitting of the XRD patterns from the other steels is shown in Appendix B.

5-2. Microstructural analysis and grain size measurement

5-2-1. X70-564 steel

Figure 5-1 shows the microstructure of the X70-564 steel. Figure 5-1a was taken by OM at a magnification of 1,000x. Figure 5-1b is an SE-SEM image taken at a magnification of 10,000x. It is made up of coarse polygonal ferrite (PF) and acicular ferrite (AF) with a small amount of a pearlite-like structure (P) in some regions, as seen in Figure 5-1b. A large Ti-rich precipitate with a small amount of Nb can be seen in Figure 5-1b; the EDX spectrum is shown in Figure 5-1c. This cuboidal precipitate nucleated on a round Ca-Al-Mn inclusion at its center. The inclusion acts as a nucleation site for the large cuboidal TiN precipitate, a phenomenon which has been reported previously. [162] Iron is from the steel matrix. The grain size was measured by a modified mean linear intercept method based on the inverted SE images taken by SEM, as shown in Figure 5-1d and e at magnifications of 2,500x and 6,000x.

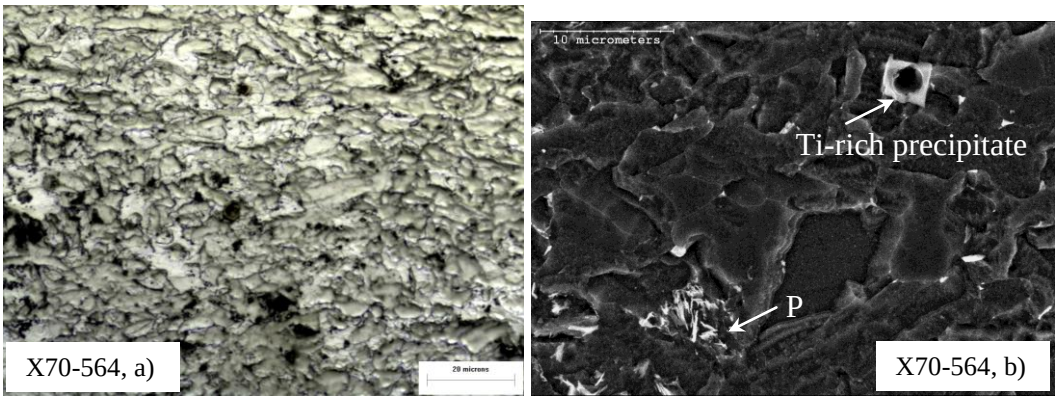

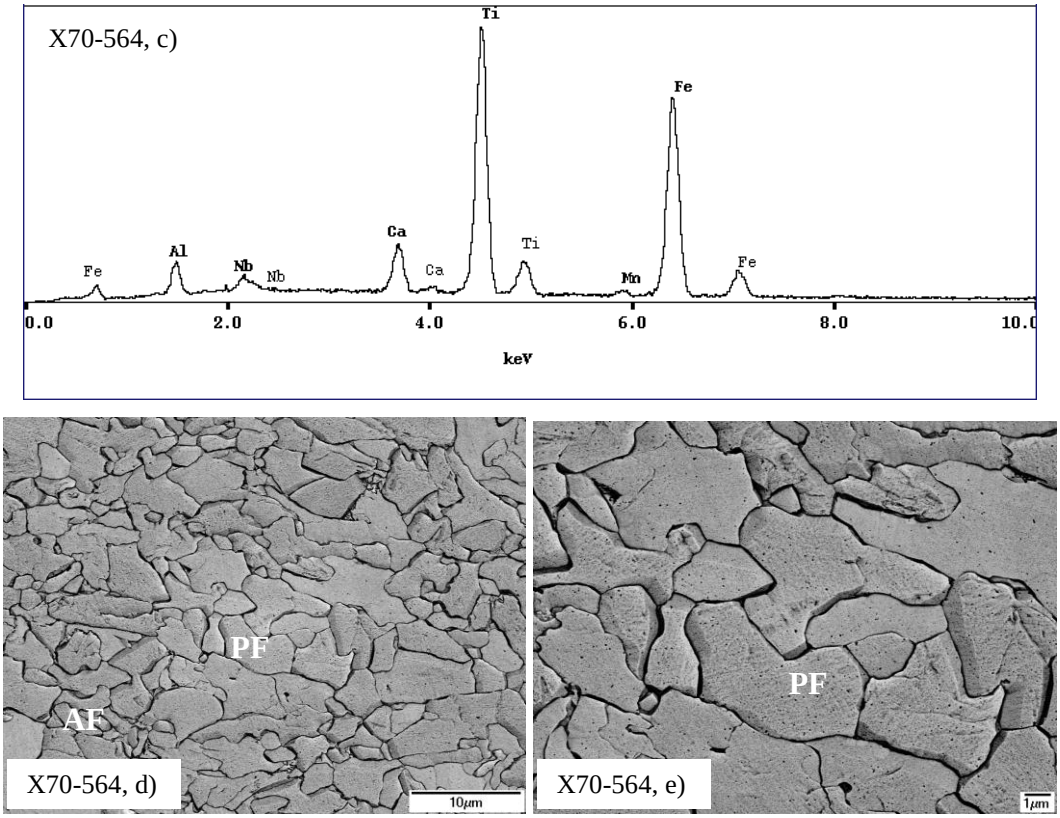

Figure 5-1 Microstructure of X70-564 steel.

a) OM image; b) SEM image showing pearlite-like microstructure, using 20kV;

c) EDX spectrum of the Ti-rich precipitate nucleated on a round inclusion;

d, e) inverted SE-SEM images at different magnifications for grain size measurement, using 5kV.

5-2-2. X80 steels

Although the basic microstructures of the X80 steels are still the same as for the X70 steel, i.e., coarse polygonal ferrite (PF), the microstructures are slightly different from that of the X70-564 steel. For the X80 steels, the amount of acicular (AF) or bainitic ferrite (BF) structure is increased. The microstructure for X80-462 is shown in Figure 5-2. The microstructures for X80-A4B, X80-B4F and X80-A4F are shown in Appendix A.

In Figure 5-2 and those shown in Appendix A, a) is an optical micrograph taken at a magnification of 1000x and b) is an SE-SEM image taken at a magnification of 10,000x. All X80 steels have a fairly uniform structure with a

small amount of a pearlite-like structure in some regions (indicated in b). The grain size was measured by a modified mean linear intercept method based on the inverted SE-SEM images shown in c) and d) at magnifications of 2,500x and 6,000x.

The measured mean linear intercepts (*m.l.i.*) with standard deviation for the X70-564 and X80 steels are shown in Table 5-1. It is clear that the X70-564 has a larger grain size compared to the X80 steels. For all the X80 steels, the grain sizes are fairly similar. The finer microstructure for the X80 steels is expected because there is a higher amount of microalloying contents (Nb, Ti and Mo) in the X80 steels compared to the X70 steel. A richer chemistry shifts the CCT curves to longer times and lower temperatures, leading to more bainitic ferrite content. The ferrite grain size is also effectively refined. Besides the effect of steel chemistry, other factors, such as CR and CT/ICT, also affect the grain microstructure. More discussion is given in Section 7-2. The *m.l.i.* of X80-462 and X80-A4B steels have higher STDEV, indicating the microstructure is less uniform than other steels.

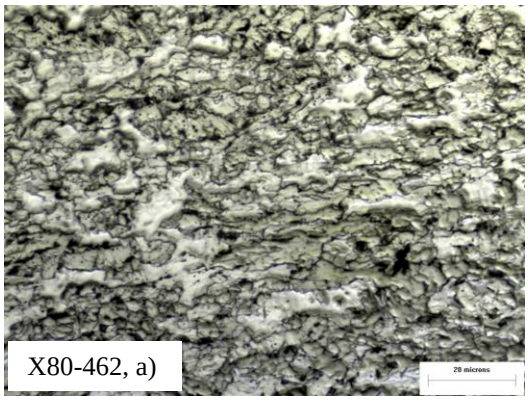

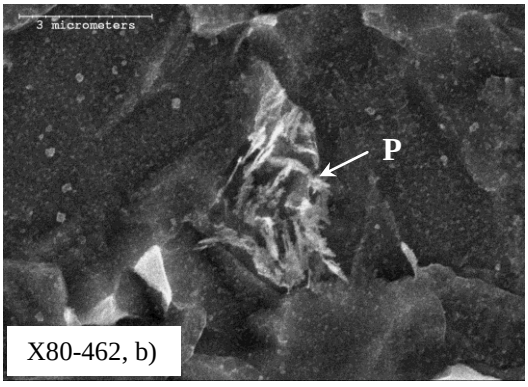

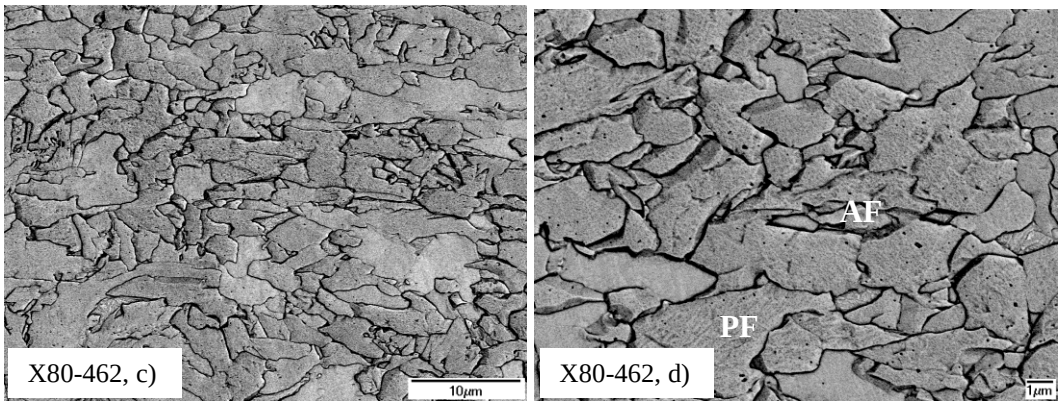

Figure 5-2 Microstructure of X80-462 steel.
a) OM image; b) SEM image showing pearlite-like microstructure, using 20kV; c, d) inverted SE-SEM image at different magnifications for grain size measurement, using 5kV.

Table 5-1 Mean linear intercept (*m.l.i.*) for X70 and X80 steels

Steel	*m.l.i.* (μm)	STDEV (μm)
X70-564	2.89	0.13
X80-462	2.24	0.23
X80-A4B	2.20	0.18
X80-B4F	2.01	0.03
X80-A4F	2.03	0.03

5-3. Overall SEM-EDX analysis of the residues extracted by HCl dissolution

Residues were collected after the ferrite matrix was chemically dissolved using HCl dissolution. One example of an SE-SEM and a BSE-SEM image of the extracted residue from the X70-564 steel is shown in Figure 5-3a and b, respectively. Similar to the results for the Grade100 steel, the majority of the extracted residue is amorphous SiO_2, which is mixed with precipitates. Spherical particles seen in Figure 5-3a correspond to the amorphous SiO_2 phase. White spots seen in Figure 5-3b correspond to precipitates.

The overall chemical composition of the extracted residues was analyzed by EDX spectroscopy in the SEM and representative EDX spectra are shown in Figure 5-4 and Figure 5-5. The spectra correspond to the residues extracted from X70-564 and X80-462. The SEM-EDX spectra from X80-A4B, X80-B4F and

X80-A4F are shown in Appendix A. There are intense or significant peaks for Si, Nb, Mo and Ti. The Ti peak is not obvious for the residue from the X70-564 steel, which is consistent with the ICP result of the supernatant and will be explained in Section 5-5. Most of the Ti is dissolved in the matrix and there is a low extraction yield for Ti in precipitates. Other elements, such as Fe, Cl and O were also detected in the residues. Silicon is from the amorphous phase that formed during the matrix dissolution process. Niobium, Mo and Ti come from the precipitates. Iron and Cl arise from the incomplete removal of Fe ions from the solution. As with the Grade100 steel and explained in Section 4-6-2-2, O is from SiO_2 which is formed during steel dissolution.

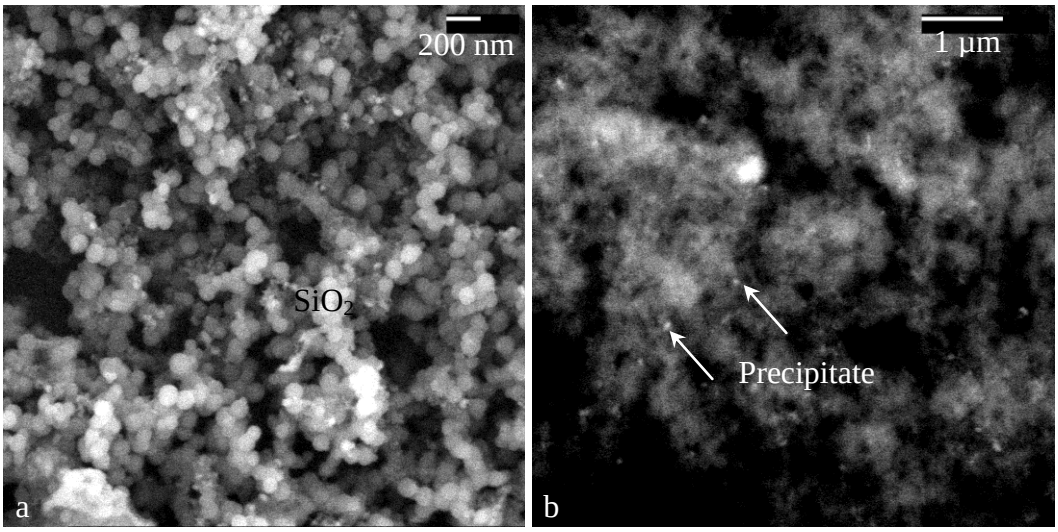

Figure 5-3 SEM image of the residue extracted from X70-564 steel.
a) SE image, showing that SiO_2 (spherical particles) makes up the majority of the residue; b) BSE image, showing precipitates.

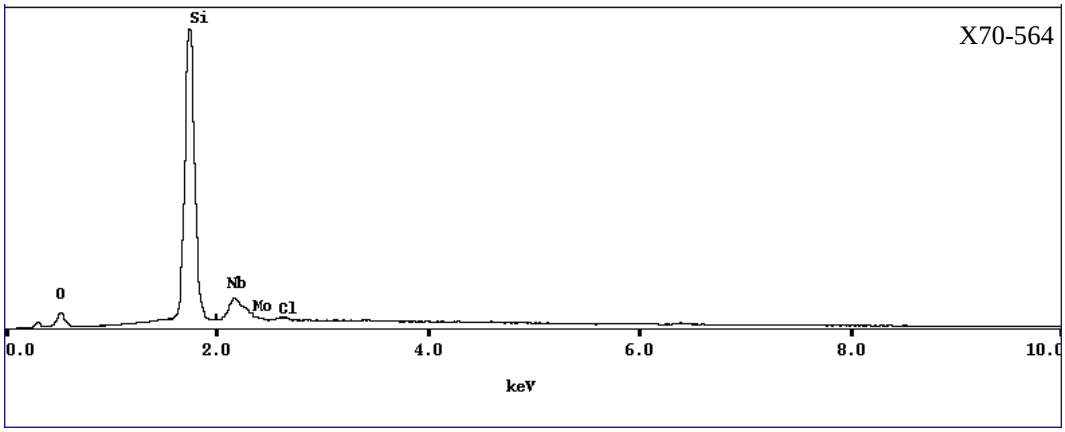

Figure 5-4 SEM-EDX chemical analysis of the residue extracted from X70-564 steel.

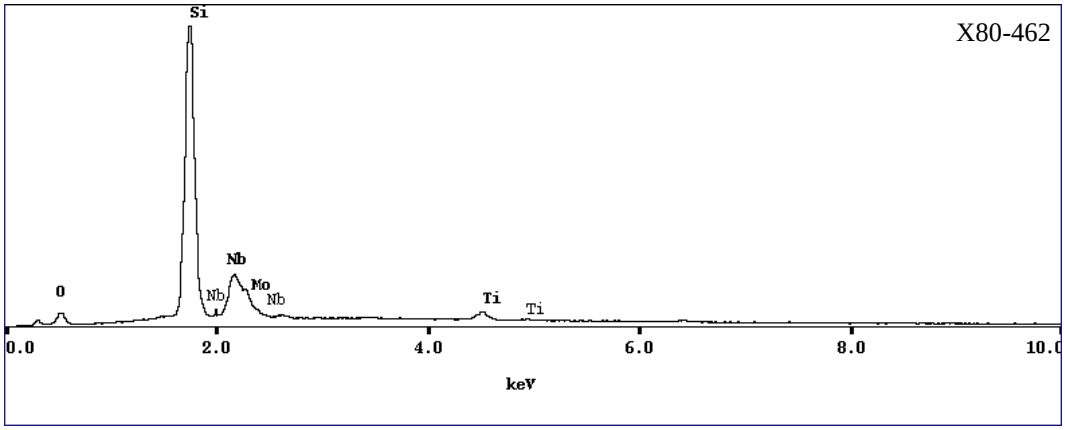

Figure 5-5 SEM-EDX chemical analysis of the residue extracted from X80-462 steel.

It has been mentioned in Chapter 4 that precipitates are categorized into different groups according to their size and chemical composition. This information will serve as a basis for Rietveld refinement to determine the relative abundance of each precipitate phase. In the following sections, precipitates extracted from different steels by carbon replicas will be characterized into different groups by TEM imaging and EDX microanalysis.

5-4. XRD analysis of extracted precipitates

In order to compare precipitate information from different steels with that from the Grade100 steel, XRD patterns from the steels were plotted together with

that from the Grade100 steel. Figure 5-6 shows XRD patterns for residues extracted from X70-564 and Grade100 steel. Because the XRD pattern for residues from X80-A4F steel was obtained using different diffractometer and the collection time is much shorter than other steels (Table 3-4 in Section 3-5), the intensity of the XRD pattern is much lower. Therefore, the XRD patterns for residues from three X80 steels (X80-462, X80-A4B and X80-B4F) were compared with Grade100 steel (Figure 5-7) while X80-A4F was compared with Grade100 steel separately (Figure 5-8). All residues were obtained through HCl dissolution. The XRD patterns confirm that all precipitate phases have a NaCl-type structure and belong to the cubic (NaCl-FCC) crystal system with $Fm\bar{3}m$ space group.

Preliminary analysis of the diffraction pattern for residues from X70-564 steel shows that there is only one crystalline phase present. The same analysis is made for X80-A4B steel. This phase is similar to NbC-based precipitates from Grade100 steel. A different phase was identified in the residues from X80-A4B steel (indicated by triangles in Figure 5-7), and was confirmed to be NaCl. The sample for XRD analysis was contaminated by a small amount of NaCl during sample preparation for XRD scanning. It was not from the original extracted residue; otherwise it would have dissolved in solution. The (111) peak for NaCl, at about 32º 2θ, is obstructed by the broad amorphous peak.

As with the Grade100 steel, preliminary analysis of the diffraction patterns for the other three X80 steels (X80-462, X80-B4F and X80-A4F) showed the presence of two crystalline phases. One set of peaks (indicated by circles in Figure 5-7 and Figure 5-8) represents the smaller NbC-based precipitates and the other set (squares in Figure 5-7 and Figure 5-8) corresponds to the larger TiN-based precipitates. As with the Grade 100 steel, detailed phase analysis required Rietveld refinement, which will be presented in the next section.

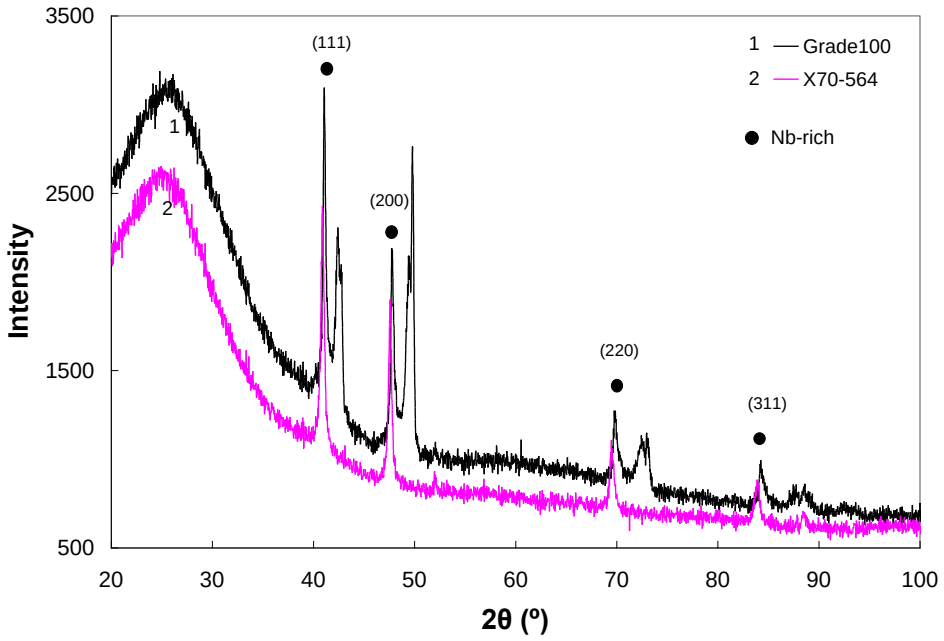

Figure 5-6 XRD patterns for residues extracted from X70-564 and Grade100 steels by chemical dissolution using HCl.

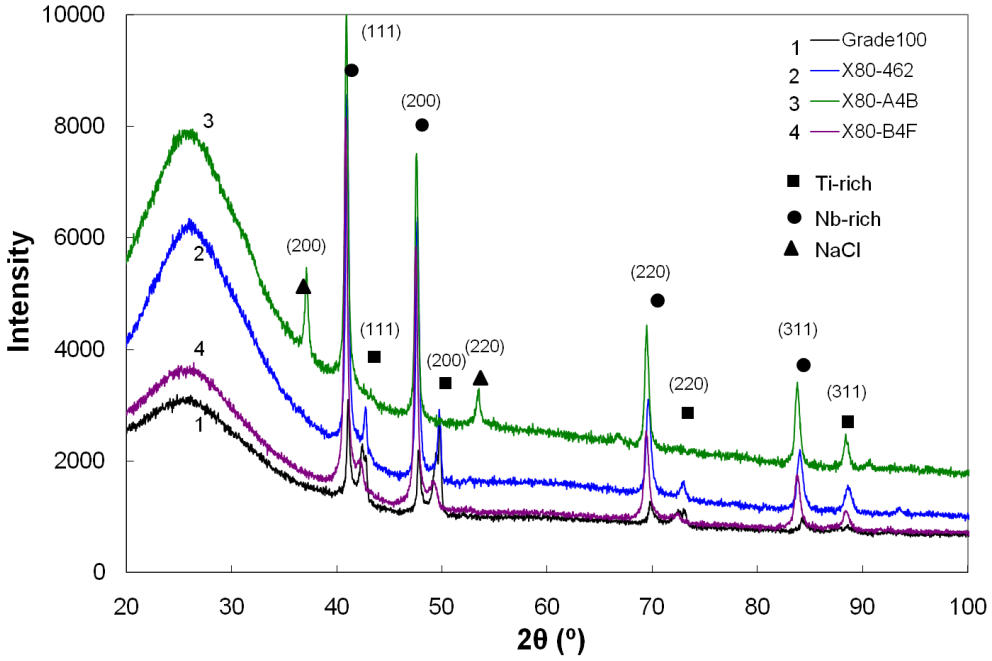

Figure 5-7 XRD pattern for residues extracted from X80 and Grade 100 steels by chemical dissolution uing HCl.

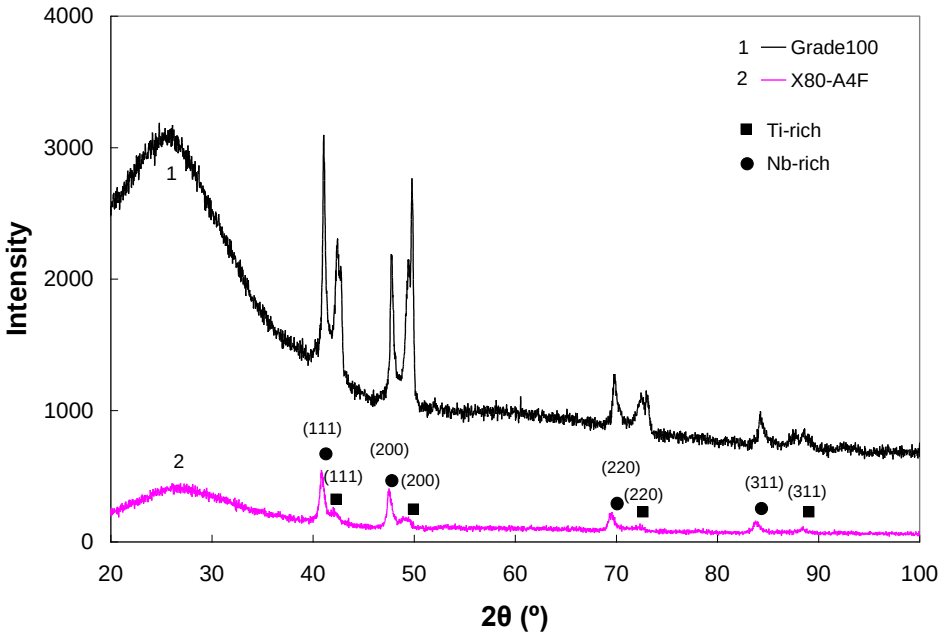

Figure 5-8 XRD pattern for residues extracted from X80-A4F steel by chemical dissolution using HCl.

5-5. ICP analysis of the supernatant

After the precipitates had been extracted from different steels, the supernatant from HCl dissolution was analyzed by ICP. By comparing the chemical composition of the steel with the ICP analysis of the supernatant, the amounts of elements extracted from the steel as part of the residue were obtained, as shown in Table 5-2, Table 5-3, Table 5-4, Table 5-5 and Table 5-6. These correspond to the results from X70-564, X80-462, X80-A4B, X80-B4F and X80-A4F steels, respectively. Again, supernatant chemistry (wt%) is defined as the amount of element in the supernatant per unit mass of steel being dissolved. It is clear that most of the Si in the steel matrix was present in the residue as SiO_2 as explained previously. Most of the Nb in the steel was in precipitate form. There are lower yields for Ti and Mo, especially for Mo, which means that most of the Mo was dissolved in the ferrite matrix. The amount of Nb and Mo in solid solution and precipitate form in the X70 and X80 steels, as well as in Grade100 steel, is shown in Figure 5-9 and Figure 5-10, respectively.

Nano-precipitates (≤10 nm) have been identified in this work in the X70 and X80 steels. They are Nb-rich carbides with significant amounts of Mo. There are some chemistry variations (Nb and Mo) for these nano-precipitates from the different steels. Molybdenum is not obvious in the other types of precipitates for different steels, except for the X70-564 steel. This means that the Mo amount present in precipitate form is only in the nano-precipitates, except for the X70-564 steel; a finding that can be used for determination of the amount of nano-precipitates. This approach will be explained in the next section.

Table 5-2 ICP analysis of the supernatant from X70-564 steel using HCl

Elements	Si	Nb	Ti	Mo
Steel chemistry (wt%)	0.23	0.069	0.023	0.2
Supernatant chemistry (wt%)	0.029	0.013	0.018	0.159
Extraction yield in precipitates	87.2%	81.0%	22.7%	20.3%

Table 5-3 ICP analysis of the supernatant from X80-462 steel using HCl

Elements	Si	Nb	Ti	Mo
Steel chemistry (wt%)	0.27	0.091	0.013	0.297
Supernatant chemistry (wt%)	0.019	0.004	0.007	0.273
Extraction yield in precipitates	93.0%	96.0%	48.0%	8.1%

Table 5-4 ICP analysis of the supernatant from X80-A4B steel using HCl

Elements	Si	Nb	Ti	Mo
Steel chemistry (wt%)	0.283	0.094	0.017	0.305
Supernatant chemistry (wt%)	0.017	0.016	0.002	0.271
Extraction yield in precipitates	93.9%	82.9%	88.3%	11.3%

Table 5-5 ICP analysis of the supernatant from X80-B4F steel using HCl

Elements	Si	Nb	Ti	Mo
Steel chemistry (wt%)	0.128	0.077	0.009	0.299
Supernatant chemistry (wt%)	0.017	0.005	0.003	0.273
Extraction yield in precipitates	86.5%	93.7%	69.7%	8.6%

Table 5-6 ICP analysis of the supernatant from X80-A4F steel using HCl

Elements	Si	Nb	Ti	Mo
Steel chemistry (wt%)	0.115	0.044	0.009	0.404
Supernatant chemistry (wt%)	0.014	0.009	0.004	0.394
Extraction yield in precipitates	87.7%	79.5%	59.2%	2.6%

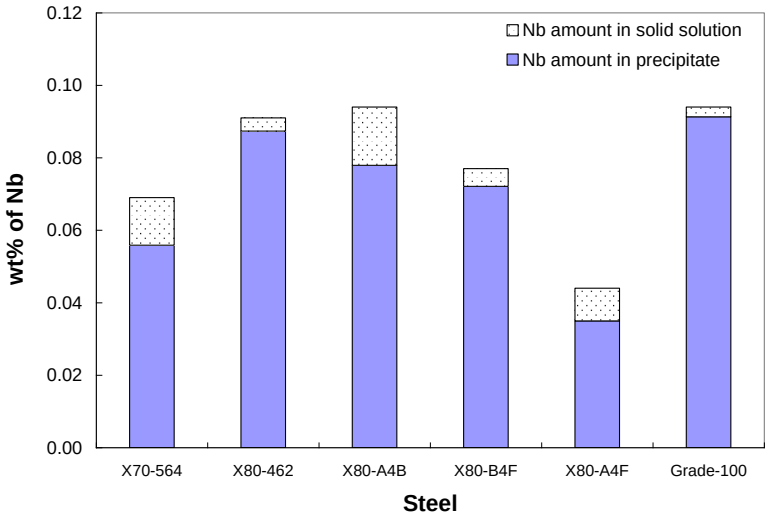

Figure 5-9 Wt% of Nb in solid solution and in precipitates.

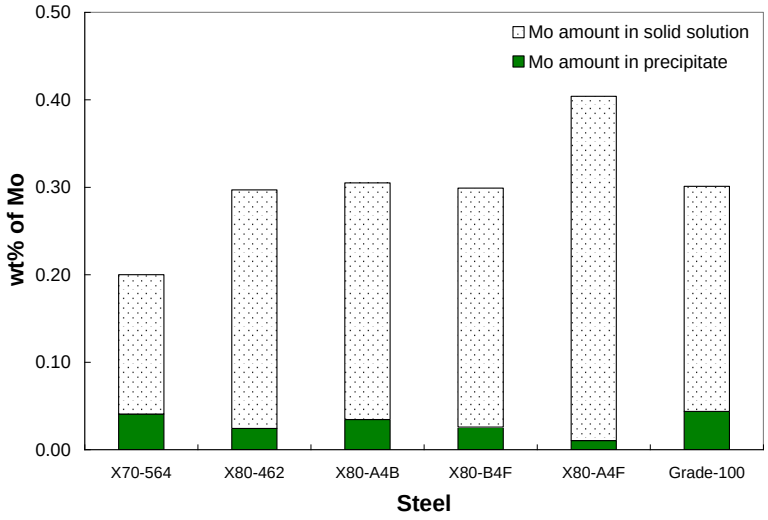

Figure 5-10 Wt% of Mo in solid solution and in precipitates.

5-6. Precipitate characterization

For X70, X80 and X100 steels, more than forty precipitates (>10 nm) were characterized for each steel. The chemistry and size of these precipitates were

analyzed by SEM/TEM-EDX microanalysis and SEM/TEM imaging, respectively. Nano-precipitates (mainly ≤10 nm) were observed in X70-564 and the four X80 steels. For each steel, between 400 and 1000 nano-precipitates (mainly ≤10 nm in size) were counted for the size distribution and chemistry analysis. The precipitate characterization of X70 and the X80 steels will be presented next and the precipitate information for the X100 steels will be presented in Chapter 6.

5-6-1. Precipitates from X80-462 steel

5-6-1-1. Observation by SEM of precipitates dispersed in the steel matrix

Figure 5-11 shows an SE-SEM and two BSE-SEM images of precipitates from X80-462 steel extracted by carbon replicas. Figure 5-11a is taken at 6000x; b and c are taken at 30,000x. It is clear that some precipitates are a few hundred nanometers in size. However, most precipitates are less than 100 nm in size and are visible as white spots.

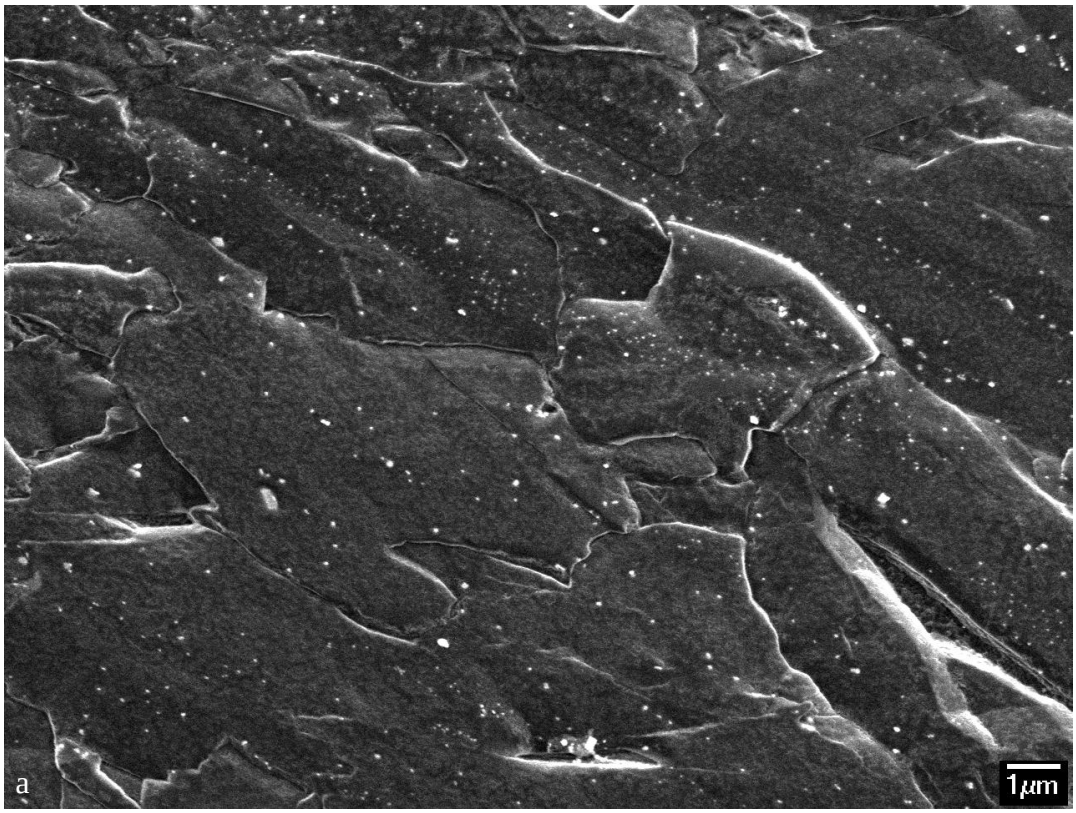

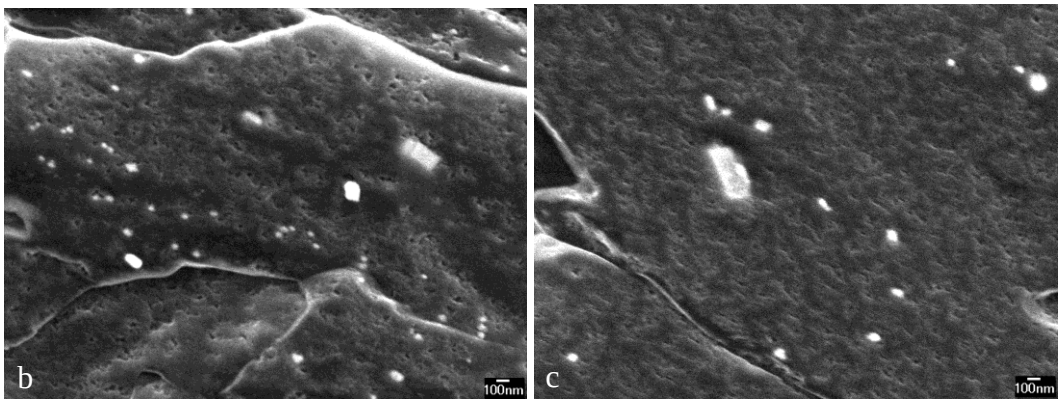

Figure 5-11 SEM images of precipitates from carbon replicas of X80-462 steel. a) SE-SEM image at 6,000x; b, c) BSE-SEM images at 30,000x.

5-6-1-2. Precipitates dispersed in the steel matrix – TEM thin foils

Some TEM BF images from a thin foil TEM sample prepared from X80-462 steel are shown in Figure 5-12. Figure 5-12a shows a Nb-rich precipitate about 100 nm in size. Figure 5-12b shows some fine precipitates aligned in a row, which is indicative of interphase precipitation. They nucleate at the austenite-ferrite phase boundaries during the austenite to ferrite transformation. [57] Figure 5-12c and d are higher magnification images showing some nano-precipitates (≤10 nm) which are dispersed within the ferrite grain as indicated by the circled region in Figure 5-15b. These precipitates were uniformly nucleated within the ferrite. [57]

Figure 5-13 shows two TEM images of dislocations that are pinned by precipitates, as shown by arrows. Fine precipitates have a higher density per unit volume than the coarse ones and can effectively impede dislocation movement.

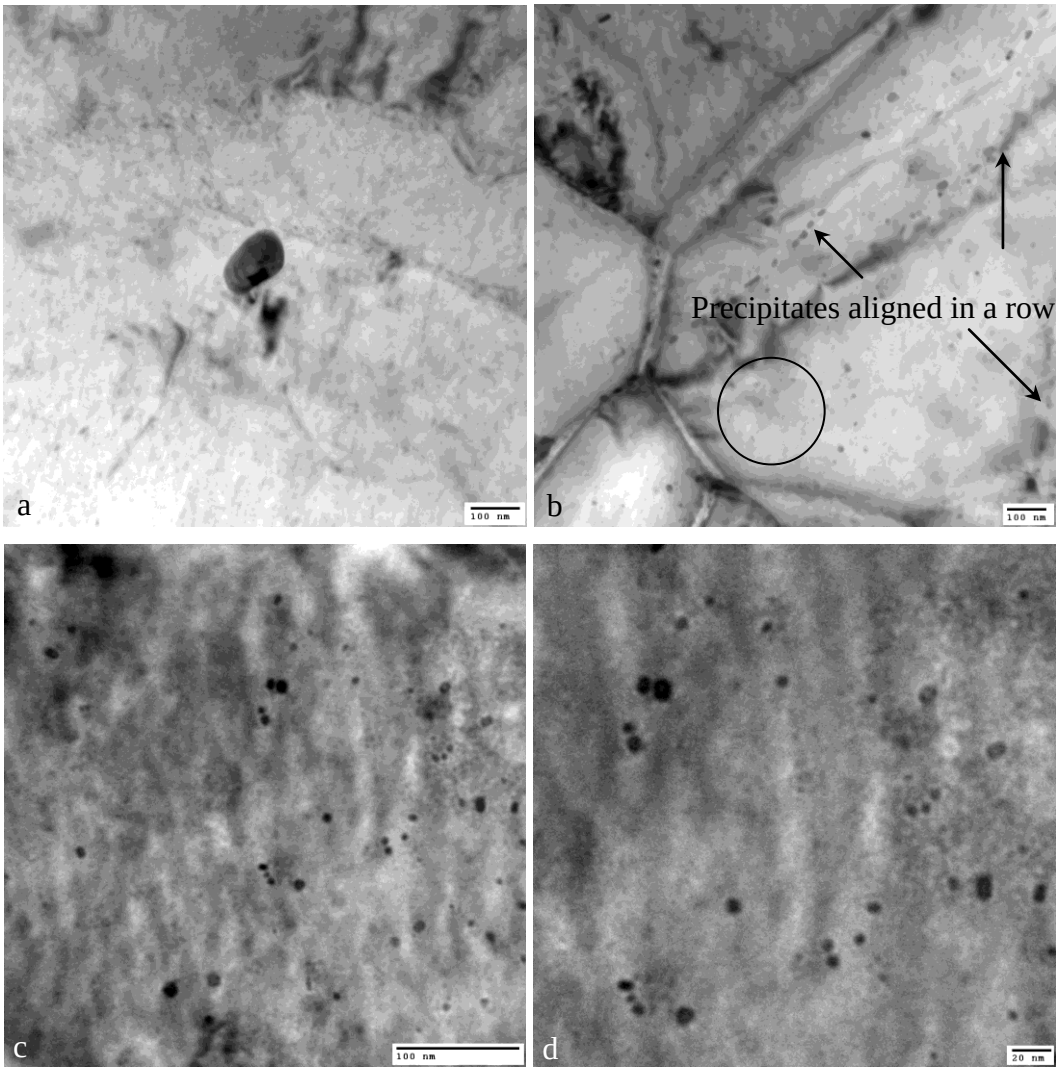

Figure 5-12 TEM BF images of precipitates (a-d) from a thin foil sample of X80-462 steel.

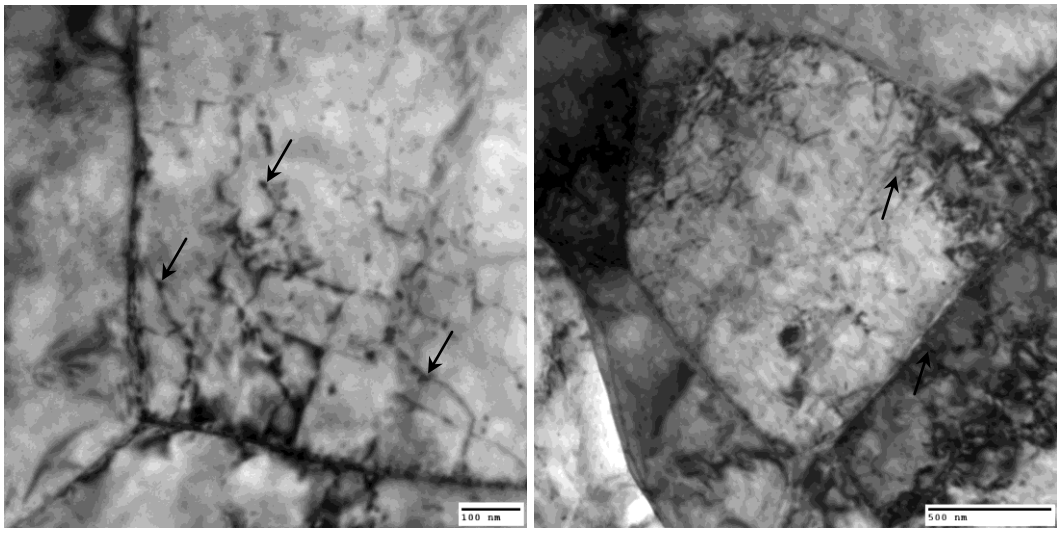

Figure 5-13 TEM BF images of dislocations from a thin foil sample of X80-462 steel.

5-6-1-3. TEM analysis of precipitates (>10 nm) extracted by carbon replicas

Figure 5-14 shows some TEM BF images and corresponding EDX spectra of extracted precipitates via carbon replicas. Figure 5-14a shows a group of epitaxially nucleated precipitates. The corresponding EDX spectra for precipitates 1, 2 and 3 are shown in Figure 5-14b, c and d, respectively. Particle 1 is Ti-rich and forms first; it acts as a nucleation site for the other precipitates. Particle 2 is Ti/Nb-rich and particle 3 is Nb-rich; both form later in the processing. A summary of the composition and approximate sizes of these precipitates is presented in Table 5-7.

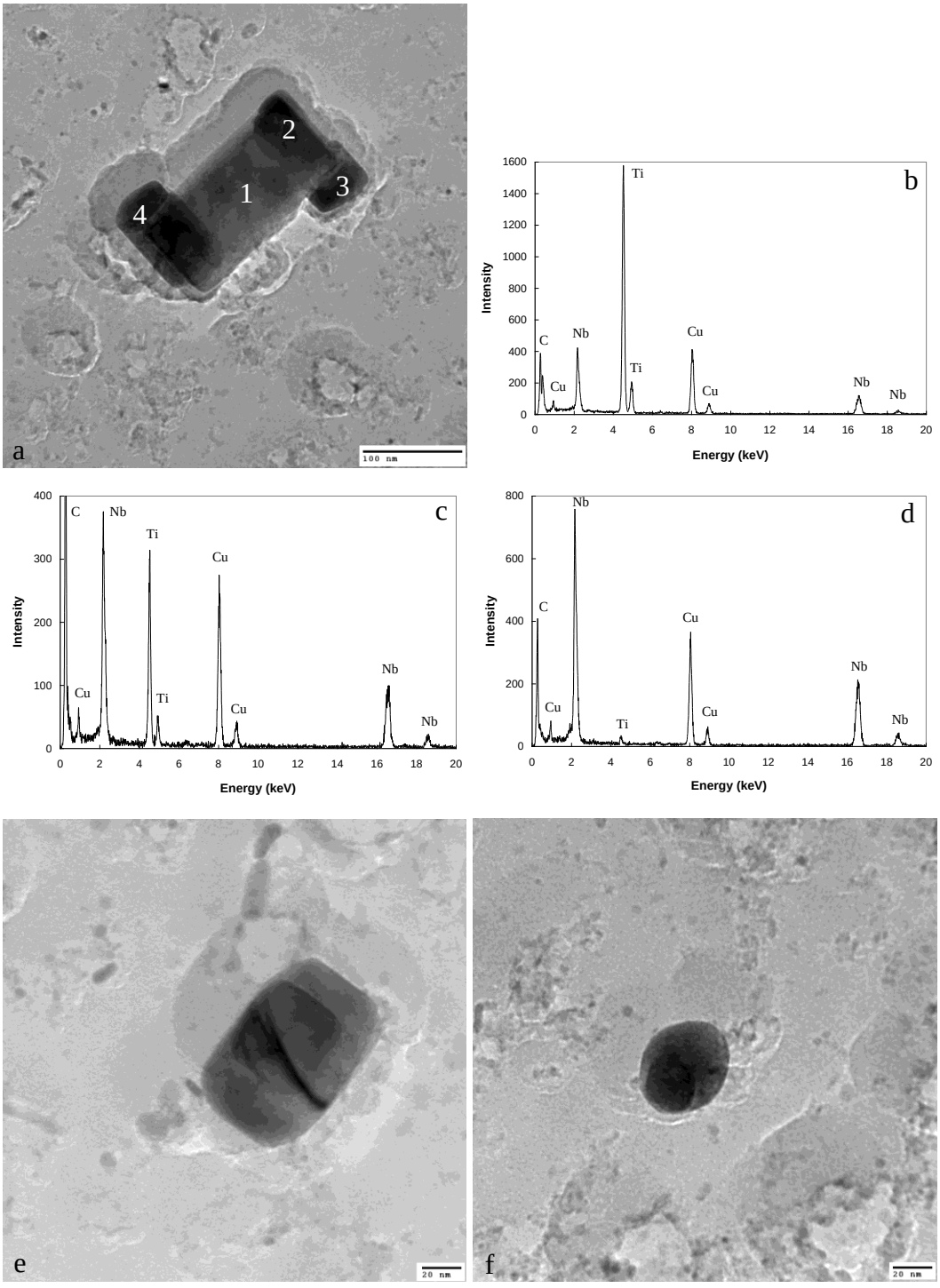

Figure 5-14 TEM BF images and the EDX spectra of precipitates from X80-462 steel.

a, e and f) TEM BF images; b, c and d) EDX of precipitate 1, 2 and 3 in a).

Table 5-7 Chemistry (metallic elements) and size of precipitates (>10 nm) from X80-462 steel extracted by carbon replicas

Image	Position	Chemistry	Largest dimension (nm)	Group
a	1	$Ti_{0.83}Nb_{0.17}$	200	Ti-rich
	2	$Ti_{0.55}Nb_{0.45}$	84	Ti/Nb-rich
	3	$Nb_{0.93}Ti_{0.07}$	55	Nb-rich
	4	$Nb_{0.9}Ti_{0.1}$	90	
e		$Nb_{0.65}Ti_{0.35}$	95	
f		$Nb_{0.92}Ti_{0.08}$	40	

5-6-1-4. Nano-precipitates (most are ≤10 nm in size) extracted by carbon replicas

Figure 5-15 shows the morphology, chemistry and size distribution information for nano-precipitates (≤10 nm) from X80-462 steel via carbon replicas. Figure 5-15a shows an example of a TEM BF image of nano-precipitates. Most of these precipitates are less than 10 nm in size and spherical in shape. Figure 5-15b shows an EDX spectrum from some of the nano-precipitates shown in Figure 5-18a. They are Nb/Mo-rich carbides with the average chemistry shown in Table 5-8.

Figure 5-15c shows another region of nano-precipitates. The inset shows the corresponding SAD pattern from the field of view. Several intermittent rings are visible and correspond to fine precipitates with a NaCl-type crystal structure. Figure 5-15d shows a DF image, taken using part of the {111} and {200} diffraction rings. Following the procedures explained in Section 4-4-2, the size distribution of nano-precipitates was investigated using DF images. Figure 5-15e shows the merged image (inverted contrast) based on the DF images. The relative frequency (n/N) versus diameter of nano-precipitates in the X80-462 steel is shown in Figure 5-15f. The nano-precipitates are generally less than 10 nm in size, with the largest number of precipitates is in the 5-7 nm size range.

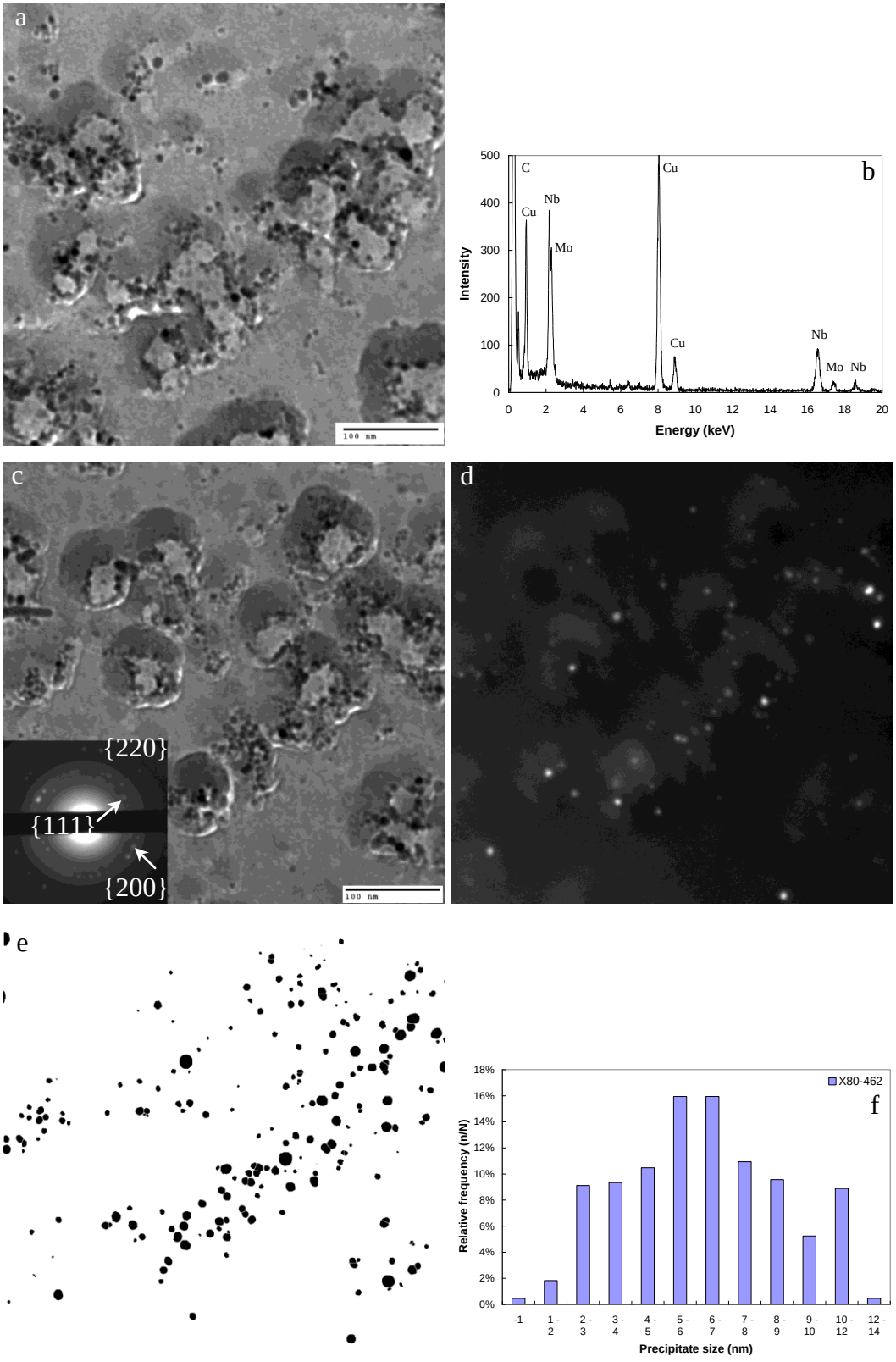

Figure 5-15 Nano-precipitates (≤ 10 nm) from X80-462 steel.

a) TEM BF image of nano-precipitates; b) EDX spectrum from nano-precipitates shown in a; c) TEM BF image of nano-precipitates; d) One TEM DF image of the same area shown in c; e) merged image (inverted contrast) based on DF images, used for size distribution analysis; f) size distribution of nano-precipitates.

From the above results, precipitates from X80-462 steel can be categorized into four groups according to chemistry and size as shown in Table 5-8, i.e., Ti-rich, Ti/Nb-rich, Nb-rich and nano-precipitates (≤10 nm, Nb/Mo-rich). Table 5-8 shows the average composition, composition range (STDEV) and size of the precipitates. Due to the lower Ti content, not many large precipitates were found compared with the Grade100 steel. Ti-rich precipitates with an average composition of $Ti_{0.76}Nb_{0.24,}$ formed at higher rolling temperatures, and are expected to be nitrides. Ti/Nb-rich and Nb-rich precipitates with sizes about 30-60 nm are formed at lower rolling temperatures. They are expected to be carbonitrides. In order to simplify the calculations, it was assumed that they have similar amounts of C and N. Nb/Mo-rich nano-precipitates (≤10 nm) with an average metal composition of $Nb_{0.8}Mo_{0.2}$ are formed at much lower temperatures during or after coiling. They will have mostly carbon based on thermodynamics, but there is likely some nitrogen. They are assumed to be $Nb_{0.8}Mo_{0.2}C$ for simplicity. The precipitate forming temperature for TiN, NbC and NbN under equilibrium conditions will be discussed in Section 5-6-3 and 6-6-3.

Table 5-8 Composition and size range for the different types of precipitates from X80-462 steel

Precipitate chemistry	STDEV of composition in atomic fraction			Size range (nm)
	Ti	Nb	Mo	
$Ti_{0.76}Nb_{0.24}N$	0.05	0.05	N/A	200
$Ti_{0.55}Nb_{0.45}C_{0.5}N_{0.5}$	0.10	0.10	N/A	80-100
$Nb_{0.86}Ti_{0.14}C_{0.5}N_{0.5}$	0.04	0.04	N/A	40-90
$Nb_{0.8}Mo_{0.2}C$	N/A	0.02	0.02	≤10, spherical

5-6-2. Precipitates from X70-564, X80-A4B, X80-B4F and X80-A4F steels

Similar precipitate analysis was carried out for X70-564, X80-A4B, X80-B4F and X80-A4F steels using carbon replicas. Due to the similarities of the experimental methods and precipitate information, all the SEM/TEM images are shown in Appendix A.

Through TEM-EDX microanalysis and TEM-imaging, the average composition, composition range (STDEV) and size of precipitates from X70-564 and other X80 steels were obtained as shown in Table 5-9. According to the chemistry and size, the precipitates can be categorized into four groups for all steels, i.e., Ti-rich, Ti/Nb-rich, Nb-rich and nano-precipitates (≤10 nm, Nb/Mo-rich), but with chemistry variations. For Ti-rich precipitates, they have about 75 at% of Ti and the remaining is mainly Nb. For Ti/Nb-rich precipitates, they have about 50 at% Ti and 50 at% Nb. For Nb-rich precipitates, they have about 85 at% of Nb and the remaining is mainly Ti. The criterion is to keep the STDEV small. However, very few large Ti-rich precipitates (500-3000 nm) were found in these steels compared with the Grade100 steel. For X80-462, X80-B4F and X80-A4F steels, Ti-rich precipitates were observed with sizes about 100-200 nm. They are expected to be nitrides which formed at higher rolling temperatures. For X70-564 and X80-A4B steels, only a few Ti-rich precipitates were detected. For all steels, Ti/Nb-rich and Nb-rich precipitates with sizes about 30-60 nm are formed at lower rolling temperatures and it was assumed that they have the same amount of C and N. A very small amount of Mo was detected in the precipitates from X70-564 steel. Nano-precipitates (mostly ≤10 nm) (with an average composition of $Nb_{0.58}Mo_{0.42}C$ for X70-564 steel, $Nb_{0.68}Mo_{0.32}C$ for X80-A4B steel, $Nb_{0.78}Mo_{0.22}$ for X80-B4F and $Nb_{0.74}Mo_{0.26}$ for X80-A4F steel) are formed at much lower temperatures during or after coiling. They are expected to be carbides. The size and chemistry difference between the various precipitates is due to a variation in the nucleation temperature and nucleation time. Small amounts of Mo were identified in the larger precipitates of the X70 steel. Compared to other precipitates, Mo-carbide has the highest solubility. [43,63] Precipitation of Mo indicates the solubility limit has been reached.

Table 5-9 Classification of precipitates from X70 and X80 steels according to composition and size range

Steel	Precipitate chemistry	STDEV of composition in atomic fraction			Size (nm)
		Ti	Nb	Mo	
X70-564	$Ti_{0.70}Nb_{0.25}Mo_{0.05}N$	0.02	0.03	0.01	60-100
	$Nb_{0.52}Ti_{0.43}Mo_{0.05}C_{0.5}N_{0.5}$	0.13	0.11	0.03	20-40
	$Nb_{0.79}Ti_{0.15}Mo_{0.06}C_{0.5}N_{0.5}$	0.06	0.06	0.03	20-40
	$Nb_{0.58}Mo_{0.42}C$	N/A	0.03	0.03	≤10
X80-462	$Ti_{0.76}Nb_{0.24}N$	0.05	0.05	N/A	100-200
	$Ti_{0.55}Nb_{0.45}C_{0.5}N_{0.5}$	0.10	0.10	N/A	80-100
	$Nb_{0.86}Ti_{0.14}C_{0.5}N_{0.5}$	0.04	0.04	N/A	40-90
	$Nb_{0.8}Mo_{0.2}C$	N/A	0.02	0.02	≤10
X80-A4B	$Ti_{0.74}Nb_{0.26}N$	0.07	0.07	N/A	170-230
	$Ti_{0.52}Nb_{0.48}C_{0.5}N_{0.5}$	0.04	0.04	N/A	60-80
	$Nb_{0.9}Ti_{0.1}C_{0.5}N_{0.5}$	0.06	0.06	N/A	25-70
	$Nb_{0.68}Mo_{0.32}C$	N/A	0.05	0.05	≤10
X80-B4F	$Ti_{0.72}Nb_{0.28}N$	0.03	0.03	N/A	80-100
	$Nb_{0.57}Ti_{0.43}C_{0.5}N_{0.5}$	0.10	0.10	N/A	85-135
	$Nb_{0.92}Ti_{0.08}C_{0.5}N_{0.5}$	0.06	0.06	N/A	40-100
	$Nb_{0.78}Mo_{0.22}C$	N/A	0.06	0.06	≤10
X80-A4F	$Ti_{0.76}Nb_{0.24}N$	0.09	0.09	N/A	100-200
	$Nb_{0.51}Ti_{0.49}C_{0.5}N_{0.5}$	0.10	0.10	N/A	20-30
	$Nb_{0.86}Ti_{0.14}C_{0.5}N_{0.5}$	0.11	0.11	N/A	20-30
	$Nb_{0.74}Mo_{0.26}C$	N/A	0.03	0.03	≤10

5-6-3. Differences in precipitation behaviour between X70, X80 and Grade100 steels

Because of its low solubility, TiN precipitate is expected to precipitate out first during the cooling process compared with other precipitates. The steels have different Ti and N contents, as shown in Table 5-10. Under equilibrium conditions, the TiN precipitation temperature can be calculated based on its solubility product and the Ti and N content in the steel. If there is sufficient Ti and N, TiN will precipitate out in liquid iron first. Therefore, the solubility product equation of TiN in liquid iron (Equation 5-1) was used to calculate the TiN precipitation temperature. Figure 5-16 shows the calculated results for X70, X80

and Grade100 steels. The Ti and N content in the steels were used as the equilibrium concentration of Ti and N respectively. Figure 5-16 indicates that the TiN precipitation temperature in Grade100 steel is the highest, about 1554ºC due to its high Ti content. Under equilibrium conditions, the steel is liquid above 1538ºC. As such, the large TiN precipitates (up to 3 μm in size) observed in Grade100 steel form during or just after casting. For the other steels, TiN precipitation temperatures are all below 1538ºC, which indicates that most Ti-rich precipitates form in the austenite region for X70 and X80 steels. They have much smaller sizes.

Table 5-10 Ti, Nb, Mo, N and C compositions in Grade100, X70 and X80 steels (wt%)

wt%	Grade100	X70-564	X80-462	X80-A4B	X80-B4F	X80-A4F
Ti	0.06	0.023	0.013	0.017	0.009	0.009
Nb	0.094	0.069	0.091	0.094	0.077	0.044
Mo	0.301	0.2	0.297	0.305	0.299	0.404
N	0.011	0.0118	0.0098	0.0058	0.0061	0.0055
C	0.080	0.0398	0.03	0.035	0.052	0.052

$$\log K_{s-TiN}(liquid) = \log[Ti]_e[N]_e = A - C/T = 5.90 - 16586/T \qquad (5\text{-}1)$$

$$\log K_{s-TiN}(\gamma) = \log[Ti]_e[N]_e = A - C/T = 3.82 - 15020/T \qquad (5\text{-}2)$$

Similar calculations were made for NbC, NbN and Mo-C (Mo_2C) precipitates under equilibrium conditions. The Nb, Mo, C and N contents for different steels are shown in Table 5-10. The precipitation temperature for NbC, NbN and Mo_2C are shown in Figure 5-16 as well. The solubility product of NbC, NbN and Mo_2C in austenite can be expressed by the following equations. Under equilibrium conditions, NbC and NbN form in the austenite region for Grade100, X70 and X80 steels. It is expected that Mo_2C forms in the ferrite because the precipitation temperature (between 673ºC and 770ºC for Grade100, X70 and X80 steels) is

lower than the Ar_3 (about 866 ºC), which will be explained in Table 7-2 in Section 7-2-1.

$$\log K_{s-NbC}(\gamma) = \log[Nb]_e[C]_e = A - C/T = 2.06 - 6700/T \quad (5\text{-}3)$$

$$\log K_{s-NbN}(\gamma) = \log[Nb]_e[N]_e = A - C/T = 2.80 - 8500/T \quad (5\text{-}4)$$

$$\log K_{s-Mo_2C}(\gamma) = \log[Mo]^2{}_e[C]_e = A - C/T = 5.00 - 7375/T \quad (5\text{-}5)$$

It should be noted that the above analysis is based on equilibrium conditions. In the real case, the steel system is very complex. There are several factors affecting precipitation, such as segregation, undercooling, processing parameters, rolling schedules, etc. As mentioned in Section 2-2, the processing parameters include reheating temperature, rough rolling temperature, finish rolling temperature, accelerated cooling rate and coiling temperature or interrupted cooing temperature. Rolling schedules include the rolling passes and deformation applied for each pass. Precipitation is also a kinetic process. The above factors all affect precipitation. Therefore, a full understanding of the difference in precipitation behavior is quite challenging. However, the above thermodynamic calculations partially explain the precipitation differences for TiN between Grade100 and X70, X80 steels.

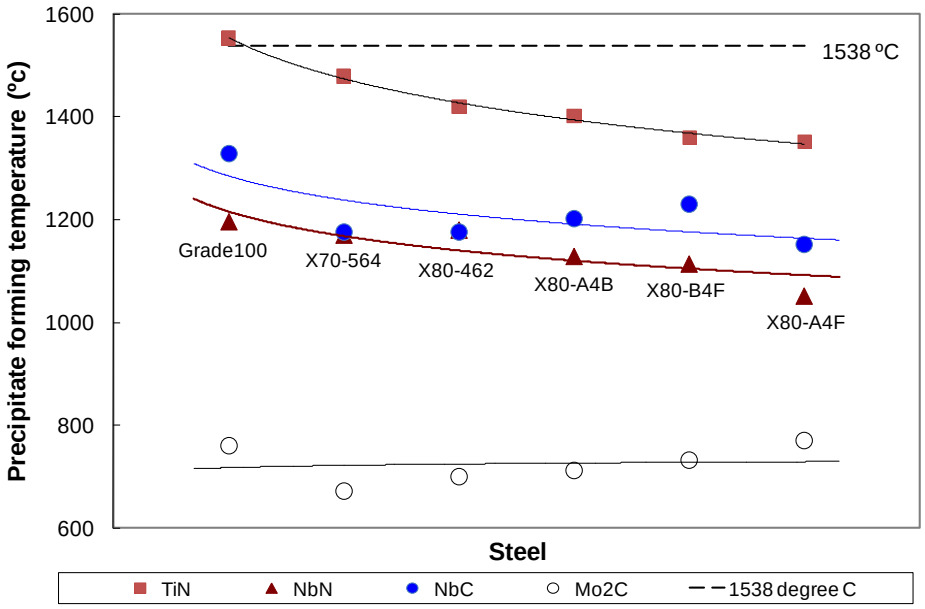

Figure 5-16 Precipitation temperature for TiN, NbN, NbC and Mo_2C under equilibrium conditions.

5-6-4. Comparison of the size distribution of nano-precipitates from different steels

The size distributions for the nano-precipitates (mainly ≤10 nm) in the X70, X80 and Grade100 steels are slightly different and a comparison of the cumulative distributions of nano-precipitates is shown in Figure 5-17. Figure 5-18 shows the effect of normalized CT/ICT temperature on the size (both mode and median) of nano-precipitates. The mode is defined as the precipitate size at the peak position in the relative frequency distribution curve. The median is defined as the precipitate size where half of the distribution is greater than and half is less than, i.e., the size at 50% of y-axis in the cumulative distribution curve. The median of nano-precipitates is slightly larger than that of the mode for the above steels. The nano-precipitates in the X80-A4F steel are the finest of the steels. The nano-precipitates in the X80-462 and X80-A4B steels are slightly larger. The size of nano-precipitates in X80-B4F and Grade100 steels are in between. The difference may be related to the different CT/ICT temperatures. From Gladman, the interphase precipitate size decreases with decreasing CT, as shown in Figure 2-14. [9,12]

The fitting (using a power relationship) of the precipitate size (mode) versus normalized CT/ICT is shown in Figure 5-18. The size of the nano-precipitates only slightly decreases with decreasing CT/ICT for the steels studied here because of the similar CT/ICT values (0.9-1.09 normalized CT/ICT). Precipitate size is related to the growth rate. Higher temperature and longer time available at this temperature promote precipitate growth. Because the nano-precipitate are formed at much lower temperature (after the austenite-to ferrite transformation), the steel is subsequently cooled to room temperature after coiling. Therefore, the precipitate growth is very limited.

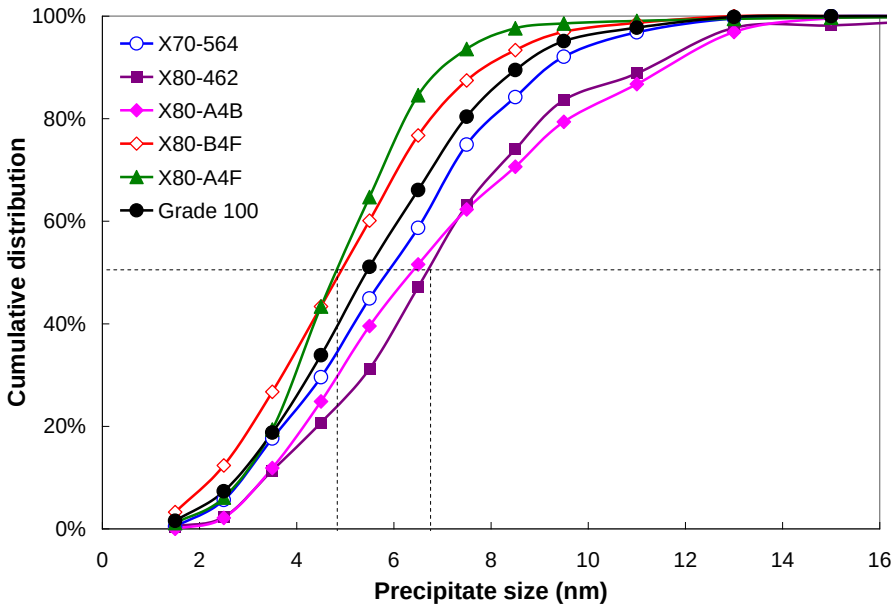

Figure 5-17 Cumulative distribution of nano-precipitates (mostly ≤10 nm) in different steels.

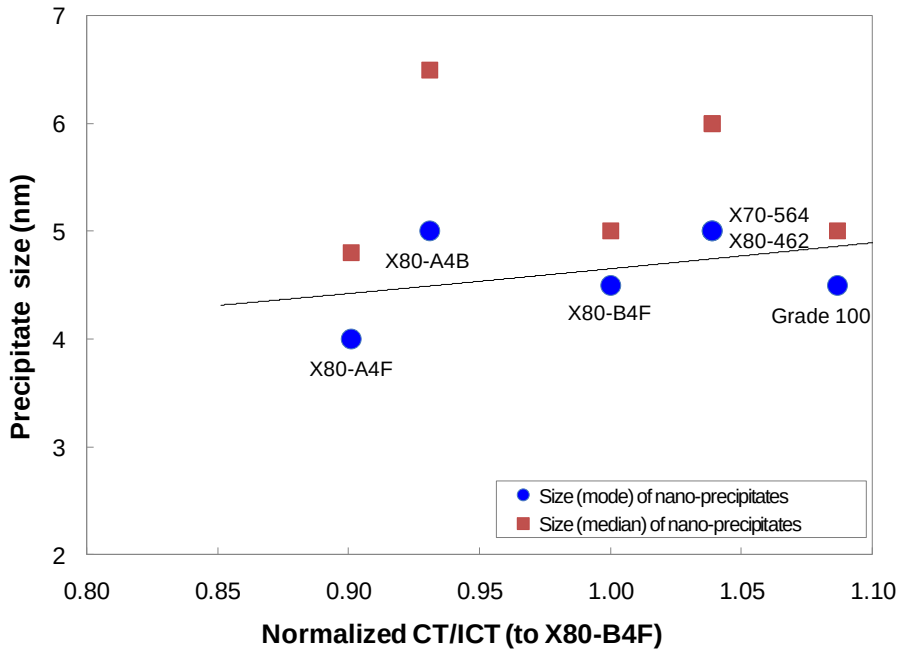

Figure 5-18 Effect of CT/ICT on the sizes (both mode and median) of nano-precipitates (mostly ≤10 nm). Precipitate size (mode) = $2.8e^{0.5\times \text{ (normalized CT/ICT)}}$

5-7. Rietveld refinement of XRD data and determination of the relative abundance of different phases

5-7-1. Rietveld refinement of XRD data

In previous sections, precipitates from different steels were categorized into different groups according to size and chemistry, based on SEM/TEM imaging and EDX microanalysis. This information is used as the basis for XRD pattern profile fitting. Figure 5-19 and Figure 5-20 are the XRD pattern profile fitting for residues from X70-564 and X80-462. The XRD profile fitting results for X80-A4B, X80-B4F and X80-A4F steels are shown in Appendix B.

Different phases, as shown in Table 5-9, are superimposed on the observed diffraction patterns. As explained in Section 4-7-2-1, SiO_2 was used as an internal standard in the refinement because of the strong correlation between the nano-precipitates and the amorphous SiO_2. The resulting residual amorphous content is ascribed to the nano-precipitates (mainly ≤10 nm).

Based on Table 5-9, the overall profile fitting and the difference between the calculated and the observed spectrum for the residue from the X70-564 steel is

shown in Figure 5-19a. The calculated diffraction pattern for $Nb_{0.52}Ti_{0.43}Mo_{0.05}C_{0.5}N_{0.5}$, $Nb_{0.79}Ti_{0.15}Mo_{0.06}C_{0.5}N_{0.5}$ and amorphous SiO_2 is shown in Figure 5-19b, c and d, respectively, as shown by arrows. The tick marks in the bottom of the figures indicate the positions of the above phases. From Chapter 4, it is known that some large and intermediate-sized cuboidal Ti-rich precipitates were observed in the Grade100 steel. The large Ti-rich precipitates are expected to form at high temperatures during or after casting. The intermediate-sized Ti-rich precipitates are formed at higher rolling temperatures. However, large Ti-rich precipitate were not identified in X70-564 steel. This was explained in Section 5-4-3. Although some Ti-rich precipitates, with chemistry $Ti_{0.70}Nb_{0.25}Mo_{0.05}N$, were observed in X70-564 steel using TEM, they were not identified through XRD analysis, probably due to their negligible amounts.

For X80-462 steel, the XRD pattern agrees very well with the TEM observations. In Figure 5-20, the overall profile fitting and the difference between the calculated and the observed patterns are shown in Figure 5-20a. The calculated diffraction patterns for Ti-rich, Ti/Nb-rich, Nb-rich precipitate and amorphous SiO_2 are shown in Figure 5-20b, c, d and e, respectively, as shown by arrows. The tick marks in the bottom of the figures indicate the positions of the above phases. For X80-B4F and X80-A4F steels, the XRD pattern agrees very well with the TEM observations as well.

For different steels, the precipitate chemistry varies for each phase. For the X80-462 steel, the precipitate phases are $Ti_{0.76}Nb_{0.24}N$, $Ti_{0.55}Nb_{0.45}C_{0.5}N_{0.5}$ and $Nb_{0.86}Ti_{0.14}C_{0.5}N_{0.5}$. For the X80-B4F steel, the precipitate phases are $Ti_{0.72}Nb_{0.28}N$, $Nb_{0.57}Ti_{0.43}C_{0.5}N_{0.5}$ and $Nb_{0.92}Ti_{0.08}C_{0.5}N_{0.5}$. For the X80-A4F steel, the precipitate phases are $Ti_{0.75}Nb_{0.25}N$, $Nb_{0.51}Ti_{0.49}C_{0.5}N_{0.5}$ and $Nb_{0.86}Ti_{0.14}C_{0.5}N_{0.5}$.

From the XRD profile fitting, Ti/Nb-rich and Nb-rich precipitates are both identified in the X70-564 and all X80 steels. The chemistry of these two phases varies for different steels. Titanium-rich precipitates are not observed for the residues from the X70-564 and X80-A4B steels in the XRD pattern. This is probably due to the negligible amount. However, this phase (with chemistry

variations) was identified in the XRD pattern for the X80-462, X80-B4F and X80-A4F steels.

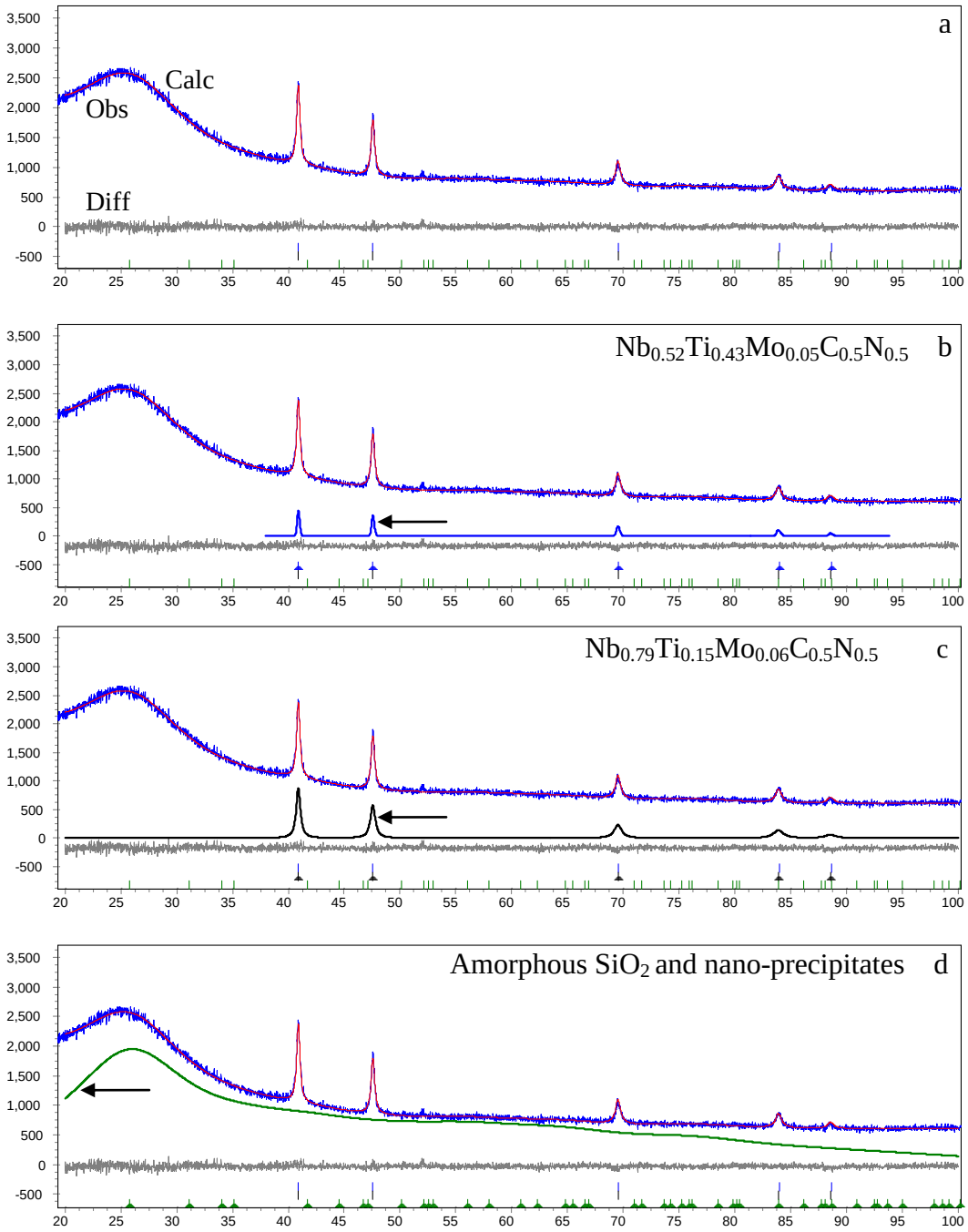

Figure 5-19 Profile fitting of XRD pattern by Rietveld refinement for residue extracted from X70-564 steel by chemical dissolution using HCl.

a) Overall XRD pattern profile fitting;

b) calculated diffraction pattern for $Nb_{0.52}Ti_{0.43}Mo_{0.05}C_{0.5}N_{0.5}$;

c) calculated diffraction pattern for $Nb_{0.79}Ti_{0.15}Mo_{0.06}C_{0.5}N_{0.5}$;

d) calculated diffraction pattern for amorphous SiO_2 and nano-precipitates.

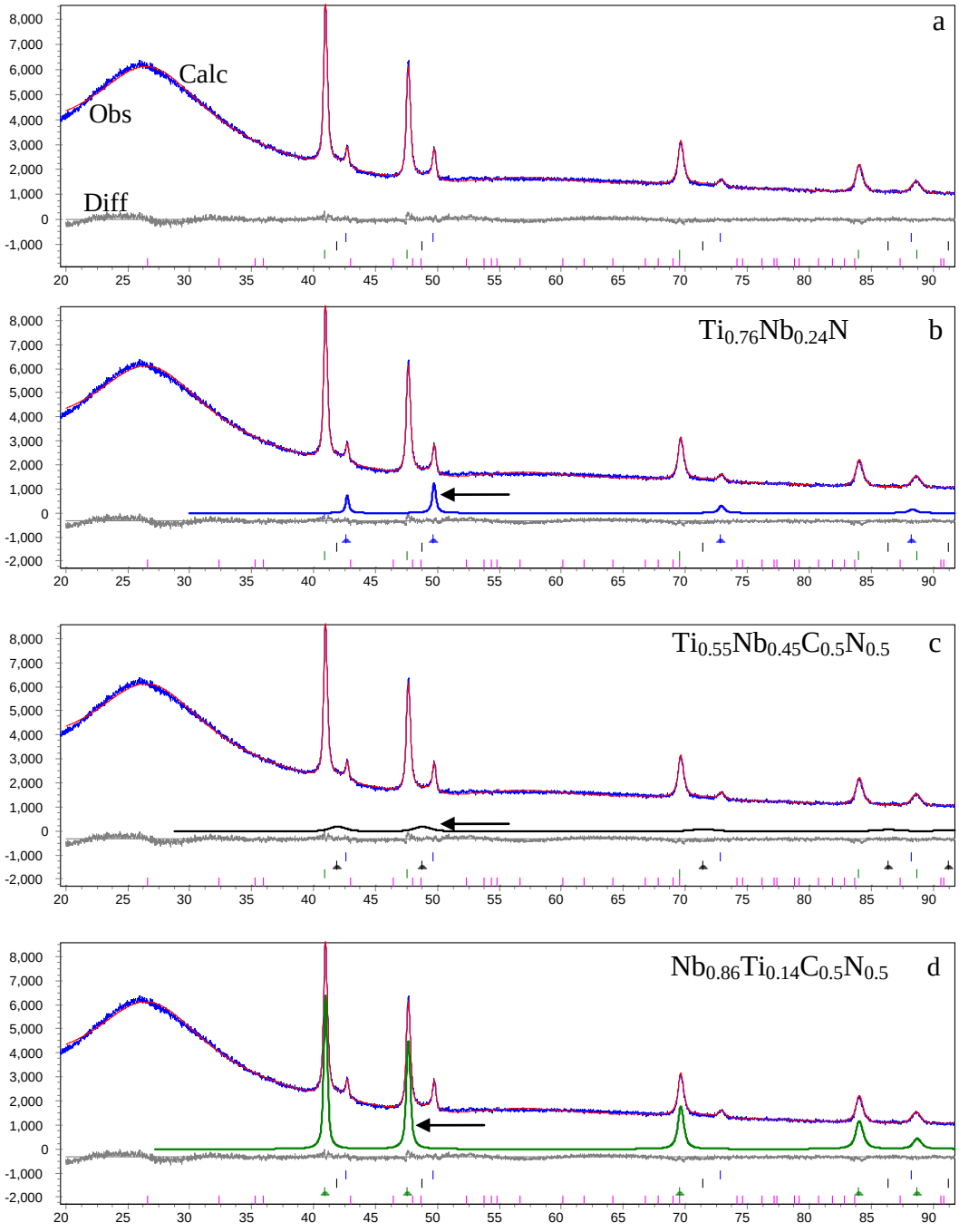

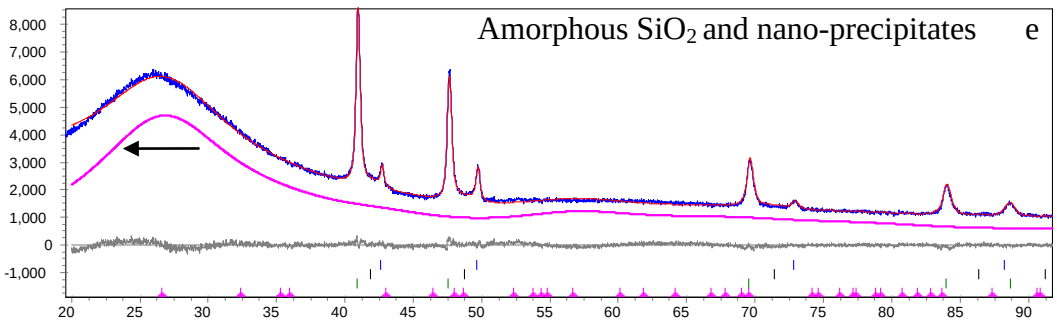

Figure 5-20 Profile fitting of XRD pattern by Rietveld refinement for residue extracted from X80-462 steel by chemical dissolution using HCl.
a) Overall XRD pattern profile fitting; b) calculated diffraction pattern for $Ti_{0.76}Nb_{0.24}N$; c) calculated diffraction pattern for $Ti_{0.55}Nb_{0.45}C_{0.5}N_{0.5;}$ d) calculated diffraction pattern for $Nb_{0.86}Ti_{0.14}C_{0.5}N_{0.5}$; e) calculated diffraction pattern for amorphous SiO_2 and nano-precipitates.

5-7-2. Determination of the relative abundance of different phases

5-7-2-1. Determination of the relative abundance of different phases via Rietveld refinement

From Rietveld refinement, information obtained from precipitates extracted by HCl dissolution is shown in Table 5-11. The table includes the refined lattice parameter and relative abundance of the constituent crystal phases. According to the experimental extraction yield, the wt% of different precipitates compared to the weight of steel was obtained and is shown in Table 5-11 as well.

The lattice parameters of the nano-precipitates from the X70, X80 steels are less accurate than those of other phases. This is because they are determined from the SAD patterns, not from Rietveld refinement. Because of the strong correlation between the nano-precipitates and the amorphous SiO_2, the nano-precipitate phase and amorphous SiO_2 are considered as one phase in the Rietveld refinement. SiO_2 was used as an internal standard in the refinement and the resulting residual amorphous content is ascribed to the nano-precipitates ($\leq$10 nm in size). The lattice parameter does not affect the wt% of the nano-precipitates. It affects the volume fraction and number density, which will be explained in Section 7-4-1.

Table 5-11 Relative abundance (wt%) of the constituent crystal phases for X70 and X80 steels chemically dissolved using HCl dissolution

Steel	Phases	Lattice parameter nm	Relative abundance of precipitates in the extracted residue (wt%)	Experimental extraction yield (wt%)	Wt% compared to the weight of steel being dissolved
X70-564	$Nb_{0.52}Ti_{0.43}Mo_{0.05}C_{0.5}N_{0.5}$	0.4436	0.36%	0.464%	0.002%
	$Nb_{0.79}Ti_{0.15}Mo_{0.06}C_{0.5}N_{0.5}$	0.4437	1.22%		0.006%
	$Nb_{0.58}Mo_{0.42}C$, ≤10 nm	0.440*	19.73%		0.092%
X80-462	$Ti_{0.76}Nb_{0.24}N$	0.4261	1.01%	0.746%	0.008%
	$Ti_{0.55}Nb_{0.45}C_{0.5}N_{0.5}$	0.4336	0.52%		0.004%
	$Nb_{0.86}Ti_{0.14}C_{0.5}N_{0.5}$	0.4434	3.54%		0.026%
	$Nb_{0.8}Mo_{0.2}C$, ≤10 nm	0.444*	15.77%		0.118%
X80-A4B	$Ti_{0.52}Nb_{0.48}C_{0.5}N_{0.5}$	0.4410	0.08%	0.737%	0.001%
	$Nb_{0.9}Ti_{0.1}C_{0.5}N_{0.5}$	0.4450	4.73%		0.035%
	$Nb_{0.68}Mo_{0.32}C$, ≤10 nm	0.442*	14.58%		0.107%
X80-B4F	$Ti_{0.72}Nb_{0.28}N$	0.4302	0.93%	0.390%	0.004%
	$Nb_{0.57}Ti_{0.43}C_{0.5}N_{0.5}$	0.4384	1.37%		0.005%
	$Nb_{0.92}Ti_{0.08}C_{0.5}N_{0.5}$	0.4446	4.72%		0.018%
	$Nb_{0.78}Mo_{0.22}C$, ≤10 nm	0.444*	29.81%		0.116%
X80-A4F	$Ti_{0.75}Nb_{0.25}N$	0.4293	3.92%	0.329%	0.013%
	$Ti_{0.49}Nb_{0.51}C_{0.5}N_{0.5}$	0.4399	3.38%		0.011%
	$Nb_{0.86}Ti_{0.14}C_{0.5}N_{0.5}$	0.4430	4.67%		0.015%
	$Nb_{0.76}Mo_{0.24}C$, ≤10 nm	0.443*	10.59%		0.035%

Note: *: the lattice parameters for nano-precipitates were obtained from the SAD.

5-7-2-2. Determination of the amount of nano-precipitates based on Mo amount

The amount of nano-precipitates (≤10 nm) was also calculated based on the chemistry of the nano-precipitates and the total amount of Mo available for the precipitates. For the X70-564 steel, there was some Mo present in the intermediate-sized precipitates. Most of the Mo is present in the nano-precipitates (≤10 nm), however. For the other steels, the available Mo is only attributed to the nano-precipitates (≤10 nm), as confirmed by TEM-EDX analysis (see Figure 5-15, Figure A-8, Figure A-11, Figure A-14 and Figure A-17). The total amount of Mo available for the precipitates was determined from the amount of Mo in

steel and in the supernatant via ICP analysis and has been presented in Table 5-2, Table 5-3, Table 5-4, Table 5-5 and Table 5-6. Figure 5-21 shows a comparison of the nano-precipitate amount based on Rietveld refinement and the amount of Mo. The amount of nano-precipitates (≤10 nm) determined by the two different methods is quite similar. Grade100 steel has the highest amount of nano-precipitates and X80-A4F steel has the lowest amount of nano-precipitates, which is due to the lower Nb content in the steel.

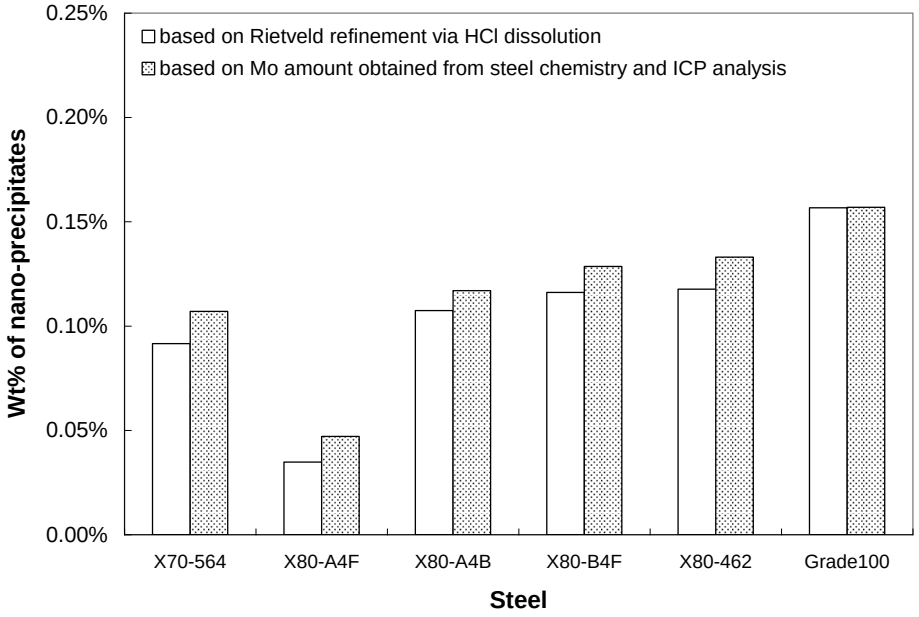

Figure 5-21 Wt% of nano-precipitates (≤10 nm) for X70, X80 and Grade100 steels using different methods.

5-8. Summary

From the microstructural studies of X70 and X80 steels, the main results are summarized as follows.

All X80 steels have similar grain sizes, which are much smaller than that of the X70-564 steel. This is expected because the design principle for the X80 steels is to move the microstructure from a ferritic-pearlitic structure to a ferritic-bainitic structure. Higher amounts of microalloying elements (Nb, Ti and Mo) in the X80 steels shift the CCT curves to longer times and lower temperatures, leading to

more bainitic ferrite content. The ferrite grain size is also effectively refined. Therefore, the strength levels can be increased.

Precipitates from different steels were identified and categorized into different groups according to size and chemistry. Ti/Nb-rich and Nb-rich precipitates were both observed in X70-564 and all X80 steels. The chemistry of these two phases varies for different steels. Titanium-rich precipitates were not observed for the residues from X70-564 and X80-A4B steel via XRD patterns, probably because of their negligible amounts; however, this phase (with chemistry variations) was present in X80-462, X80-B4F and X80-A4F steels.

Nano-precipitates (≤10 nm) were identified as the majority phase in the X70 and X80 steels. They were mainly Nb-Mo carbides, but with chemistry variations.

The amount of nano-precipitates (≤10 nm) determined by Rietveld refinement and Mo-based calculations for the different steels was quite similar. The X80-A4F steel has the lowest amount of nano-precipitates due to the fact that this steel has the lowest Nb content.

Chapter 6: X100 steels

6-1. Introduction

Similar to Chapter 5, the steel microstructure and precipitate information of three X100 steels were studied in this Chapter. The analysis was based on the knowledge developed in Chapter 4. The microstructural features were studied using OM and SEM and are presented in Section 6-2. Grain size was measured based on the SE-SEM images. Precipitates were extracted by matrix dissolution using HCl. Thus, in Section 6-3 and 6-4, the overall chemistry of the extracted precipitates is analyzed by SEM-EDX and then subjected to XRD analysis for phase identification. In Section 6-5, the supernatant is tested using ICP for element concentration analysis. In Section 6-6, precipitate size and chemistry are determined by SEM/TEM imaging and EDX microanalysis, which was used as the basis for Rietveld refinement. In Section 6-7, the relative abundance of each precipitate phase is determined by Rietveld refinement based on XRD data.

The microstructural images of three X100 steels and other representative results from X100-2A steel are shown in the main body of the thesis. This includes SEM/TEM images and EDX spectra of the precipitates and the profile fitting of the XRD pattern. The SEM/TEM images and EDX spectra of the precipitates from X100-2B and X100-3C steels are shown in Appendix A. The profile fitting of the XRD patterns from X100-2B and X100-3C steels are shown in Appendix B.

6-2. Microstructural analysis and grain size measurement

The X100 steels all have a similar microstructure: acicular or bainitic ferrite (BF) with a few dispersed martensite and retained austenite (M/A) islands. [163] A pearlite-like structure was not observed, due to the lower ICT temperatures and faster cooling rates. All X100 steels have fairly uniform microstructures, except the X100-2A steel. In the centerline of the X100-2A steel, the grains have a lower aspect ratio (length/width ratio). The width of this region was about 2 mm, which was evident by visual examination. Figure 6-1 shows the microstructure of the

X100-2A steel in the centerline area. Figure 6-2 shows the area away from the centerline, where the grains are heavily elongated (higher aspect ratio). These effects may be caused by deformation due to leveling effects together with the high cooling rate (35 ºC/s). The microstructures of X100-2B and X100-3C steels are shown in Appendix A. There is no obvious structural difference between the centerline and other areas for these two steels. They both have uniform microstructures and the grains are more equiaxed.

In each figure, a, b) represents OM images with magnifications of 500x and 1,000x. The grain size was measured by a modified mean linear intercept method based on the SE-SEM images shown in b and c at magnifications of 2,500x and 6,000x. The measured mean linear intercepts (*m.l.i.*) with standard deviations for the X100 steels are shown in Table 6-1. It is clear that the grain sizes are fairly similar for the three different steels and the values are effectively refined compared with the X70 and X80 steels. This is expected because the design principle for the X100 steel is a combination of microalloying, higher cooling rates associated with TMCP and low interrupted cooling temperatures (ICT), leading to a microstructure consisting of significant grain refinement of bainite with/without martensite. Therefore, steels with these low carbon microconstituents have higher strength, superior toughness and good weldability.

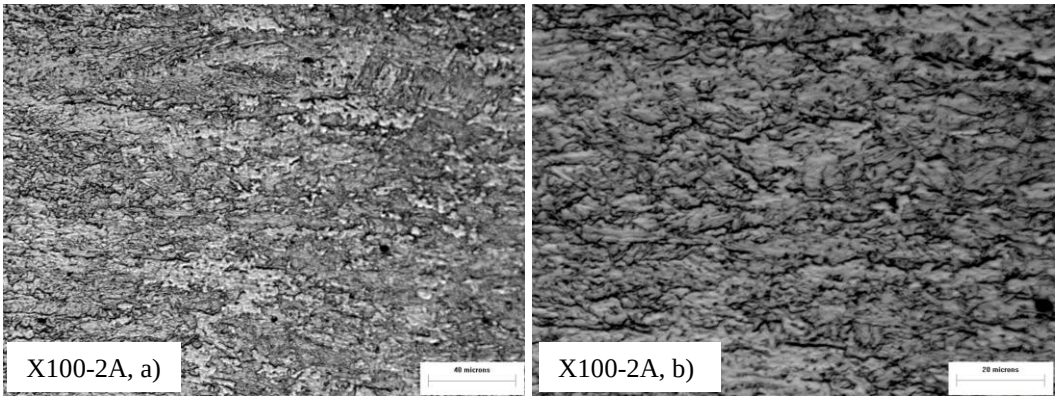

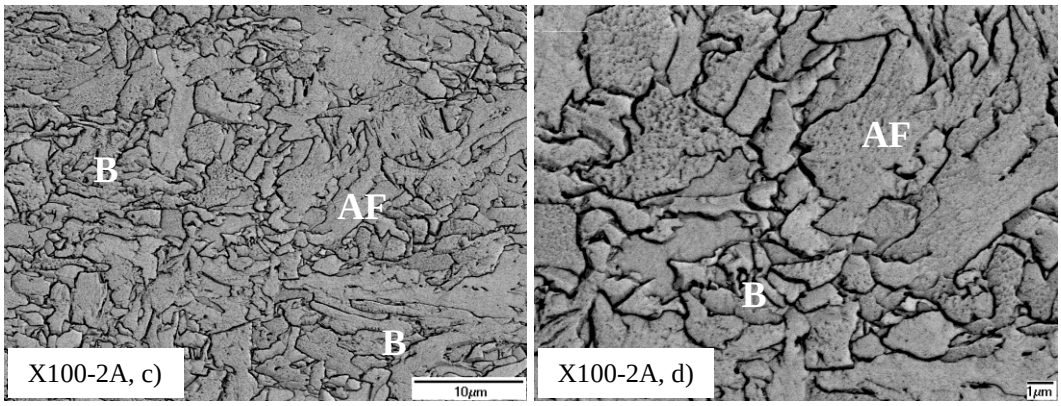

Figure 6-1 Microstructure of X100-2A steel (centerline area): lower length/width ratio. a, b) OM image; c, d) inverted SE-SEM image at different magnifications for grain size measurement, using 5kV.

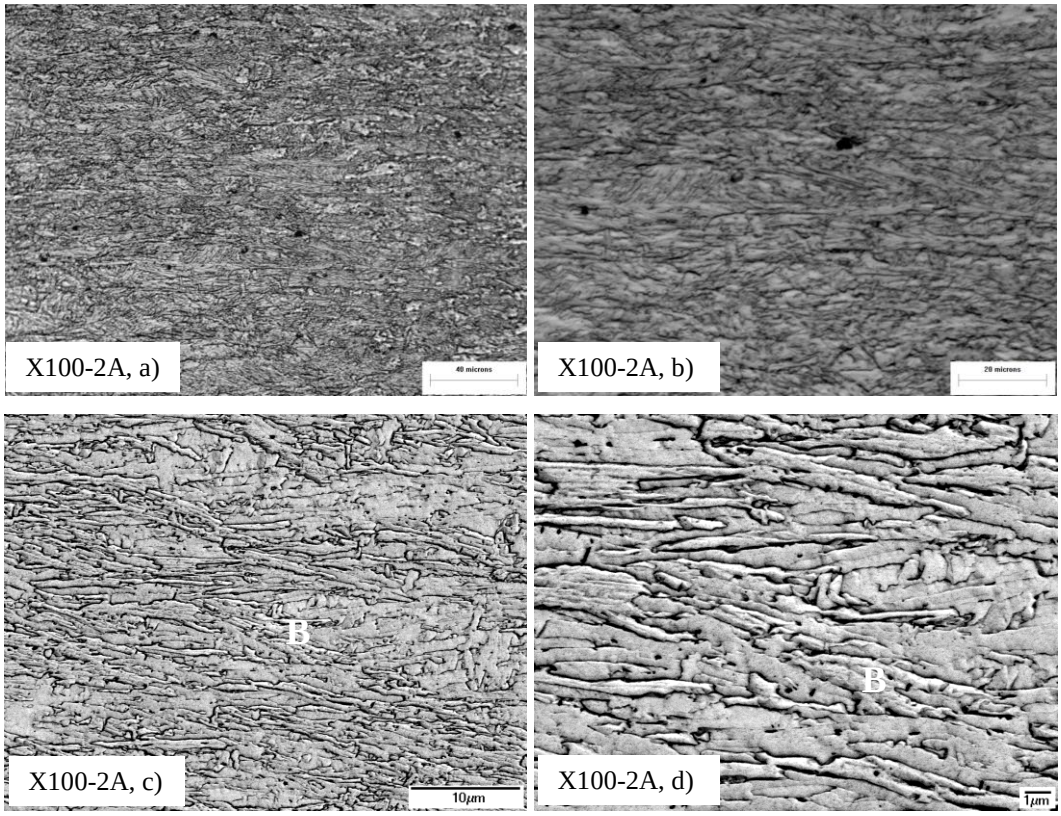

Figure 6-2 Microstructure of X100-2A steel (away from the centerline): elongated grains. a, b) OM image; c, d) inverted SE-SEM image at different magnifications for grain size measurement, using 5kV.

Table 6-1 Mean linear intercept (*m.l.i.*) for X100 steels

Steel	*m.l.i.* (μm)	STDEV (μm)
X100-2A	0.93	0.03
X100-2B	1.03	0.13
X100-3C	1.13	0.04

6-3. Overall SEM-EDX analysis of precipitates extracted by HCl dissolution

Precipitates were collected after the ferrite matrix was chemically dissolved using HCl dissolution. The overall chemical composition of the extracted residues was analyzed by EDX spectroscopy in the SEM. EDX spectrum of precipitates from the X100-2A is shown in Figure 6-3. EDX spectra of precipitates from X100-2B and X100-3C steels are shown in Appendix A. There are intense peaks for Si, Nb and Ti. A small amount of Mo was detected, which was mentioned in the previous section. Other elements, such as Al, Fe, Cl and O, were also detected in the residues. There may be trace amounts of Al inclusions left in the residues. Silicon and O are from the amorphous phase that formed during the matrix dissolution process. Niobium, Mo and Ti come from the precipitates, while Fe and Cl arise from the incomplete removal of Fe ions from the solution.

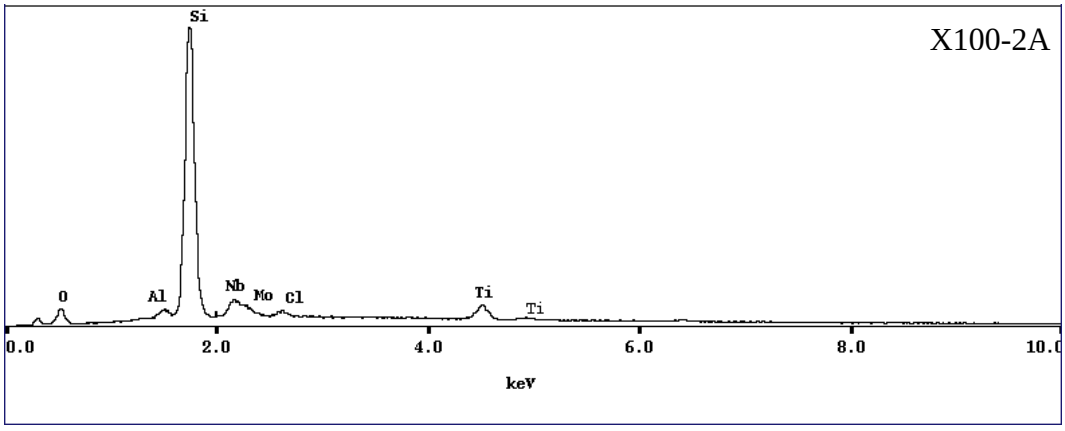

Figure 6-3 SEM-EDX chemical analysis of the residue extracted from X100-2A steel.

6-4. XRD analysis of the extracted residue

Figure 6-4 shows XRD patterns for residues extracted from the X100 steels by HCl dissolution. All precipitate phases have a NaCl-type structure and belong to the cubic (NaCl-FCC) crystal system with $Fm\bar{3}m$ space group. The XRD pattern from the precipitates of X100-3C steel is much weaker compared to the other two steels. The amount of sample for the XRD scan is similar. Therefore, it may be due to the lower collection time. Higher errors may be involved in the Rietveld refinement of X100-3C steel because of the weak peaks.

Preliminary analysis of the diffraction patterns for the residues from X100 steels shows that two crystalline phases are present. This result is similar to that for the Grade100 steel. One set of peaks (indicated by circles in Figure 6-4) represents the NbC-based precipitates and the other set (squares in Figure 6-4) corresponds to the TiN-based precipitates. Similar to the XRD pattern for residues from X80-A4B steel, the XRD samples for X100-2A and X100-3C steels were also contaminated by NaCl. There are two extra peaks (triangles in Figure 6-4) for X100-2A and X100-3C steels, both correspond to the NaCl phase. The one located at about 36º 2θ is the (200) of NaCl. The other one located about 53º 2θ is the (220) of NaCl. The (111) peak of NaCl supposed to show up about 32º 2θ was hidden under the amorphous SiO_2 phase. Detailed phase analysis was done using Rietveld refinement, which is presented in the next section.

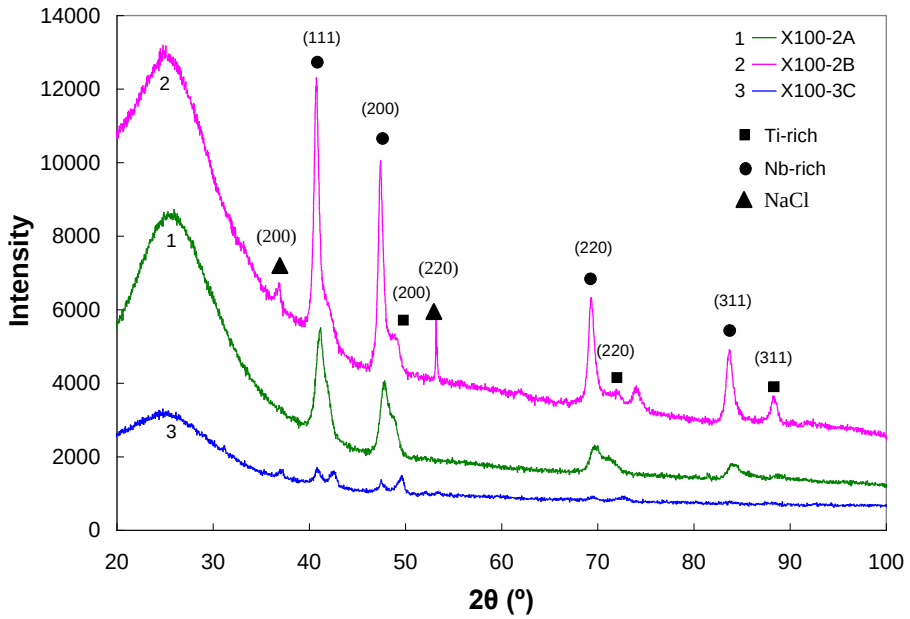

Figure 6-4 XRD patterns for residues extracted from X100 steels by chemical dissolution using HCl.

6-5. ICP analysis of the supernatant

The chemistry of the supernatant was analyzed by ICP. Table 6-2, Table 6-3 and Table 6-4 show the steel chemistry, supernatant chemistry and the extraction yield of Si, Nb, Ti and Mo for the three X100 steels, respectively. Vanadium analysis is also shown in Table 6-3 for X100-2B steel. Similar to the other steels studied in previous chapters (Table 4-2 for Grade100 and Table 5-2 to Table 5-6 for X70, X80 steels), most of the Si in the steel matrix was present in the residue as SiO_2. Most of the Nb in the steel was in precipitate form and it has a higher precipitation yield than Ti. Molybdenum had the lowest yield because most of the Mo exists in solid solution in the steel matrix. Compared with the Mo yield in precipitate form, it is clear that Mo has a lower yield for the X100 steels than the other steels due to the fact that no nano-precipitates (mainly ≤10 nm) were formed. Similarly is that the yield of Nb in residues from X100 steels is lower than that from other steels. Ti yield has no obvious change.

From Table 6-2, Table 6-3 and Table 6-4, the amount of Mo in the supernatant is close to the total Mo content in the steel, especially for X100-2B steel. It

indicates that very small amount of Mo is present in the precipitates. The amount agrees with the precipitate chemistry, which will be introduced in Section 6-6. By TEM-EDX, a small amount of Mo was detected in precipitates from X100-2A and X100-3C steels. However, Mo was not detected in precipitates from X100-2B steel. This indicates that the entire Mo exists in solid solution in the X100-2B steel matrix.

The effect of CT/ICT and FRT on the amount of Nb in precipitate form for all steels is shown in Figure 6-5 and Figure 6-6, respectively. In both figures, the total amount of Nb in steel and the total amount of Nb in precipitate are both shown for the different steels. In Figure 6-5, a linear fitting for the total amount of Nb in precipitate form is shown as well. The amount of Nb in precipitate form increases with increasing CT/ICT. However, there is no obvious relationship between FRT and the amount of Nb in precipitate for different steels. Higher Nb content in the steel enhances Nb precipitation as well.

Figure 6-7 and Figure 6-8 show the effect of CT/ICT and FRT, respectively, on the amount of Mo in precipitate form for all steels. In both figures, the total amount of Mo in steel and the total amount of Mo in precipitate form are both shown for the different steels. In Figure 6-7, curve fitting using an exponential relationship for the total amount of Mo in precipitate form is also shown. The amount of Mo in the precipitates increases with increasing CT/ICT and there is no obvious relationship between FRT and the amount of Mo in precipitate.

From previous sections, nano-precipitates (mainly $\leq$ 10 nm) have been identified in X70, X80 and Grade100 steels. Because of the OR with the ferrite matrix, they form after austenite to ferrite transformation. It is expected that these nano-precipitates are formed at the CT/ICT. Because of the lower formation temperature, these nano-precipitates are assumed to be carbides and mainly composed of Nb and Mo. CT/ICT has a strong effect on the amounts of nano-precipitates, which are also directly related to the amount of Nb and Mo in precipitates. Although X100 steels have much higher amounts of Mo than other steels, the amount of Mo in precipitate form is very low due to the lack of nano-

precipitate formation (Section 6-6) because of the lower CT/ICT. CT/ICT has a stong effect on precipitate nucleation and will be explained in Section 7-4-4.

Table 6-2 ICP analysis of the supernatant from X100-2A steel by HCl matrix dissolution

Elements	Si	Nb	Ti	Mo
Steel chemistry (wt%)	0.11	0.037	0.013	0.41
Supernatant chemistry (wt%)	0.02	0.012	0.007	0.407
Extraction yield in precipitates	81.4%	68.1%	48.2%	0.8%

Table 6-3 ICP analysis of the supernatant from X100-2B steel by HCl matrix dissolution

Elements	Si	Nb	Ti	Mo	V
Steel chemistry (wt%)	0.22	0.047	0.009	0.40	0.07
Supernatant chemistry (wt%)	0.021	0.013	0.004	0.399	0.069
Extraction yield in precipitates	90.4%	73.0%	52.9%	0.4%	2.0%

Table 6-4 ICP analysis of the supernatant from X100-3C steel by HCl matrix dissolution

Elements	Si	Nb	Ti	Mo
Steel chemistry (wt%)	0.33	0.046	0.009	0.40
Supernatant chemistry (wt%)	0.019	0.008	0.001	0.397
Extraction yield in precipitates	94.3%	75.0%	88.2%	0.8%

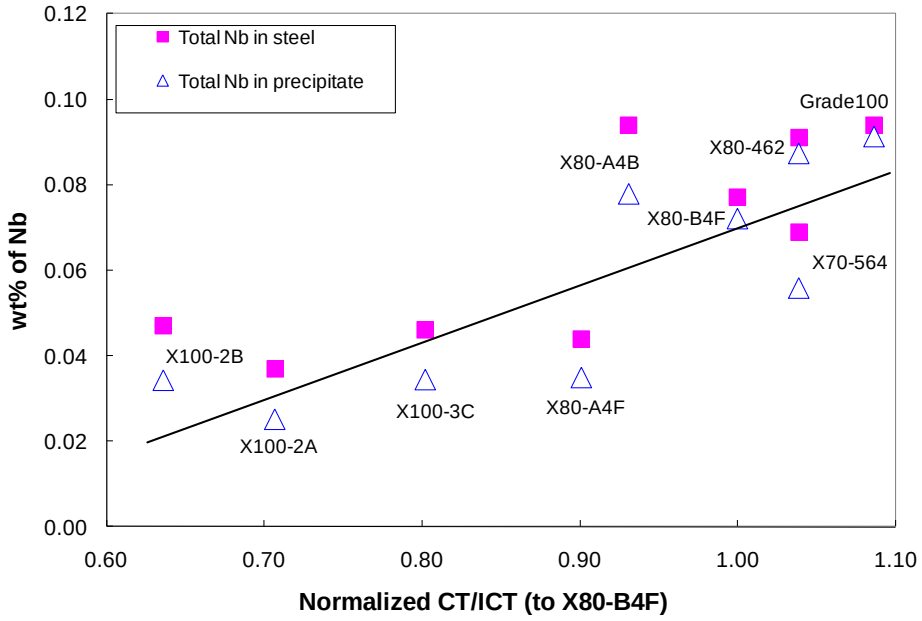

Figure 6-5 Effect of CT/ICT on the wt% of Nb in precipitate form for all steels.

wt%Nb = 0.13×(normalized CT/ICT)-0.06

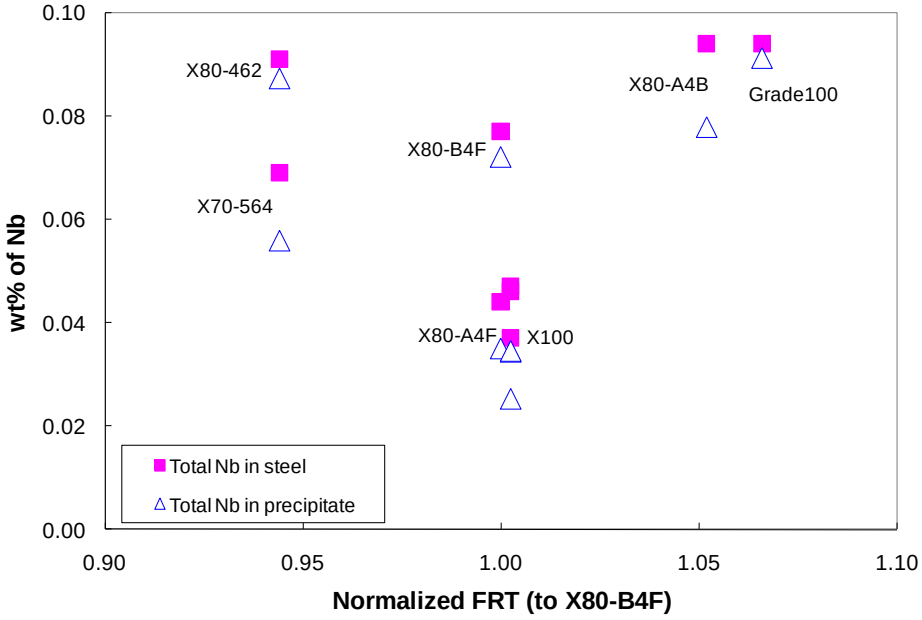

Figure 6-6 Effect of FRT on the wt% of Nb in precipitate form for all steels.

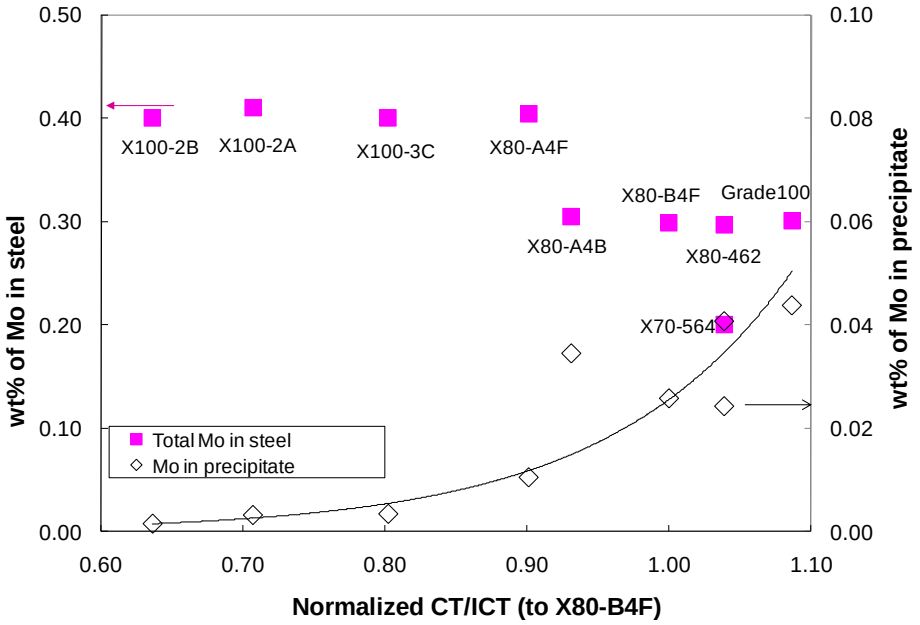

Figure 6-7 Effect of CT/ICT on the wt% of Mo in precipitate form for all steels.

$$wt\%Mo = 1.0E\text{-}5e^{7.8\times(\text{normalized CT/ICT})}$$

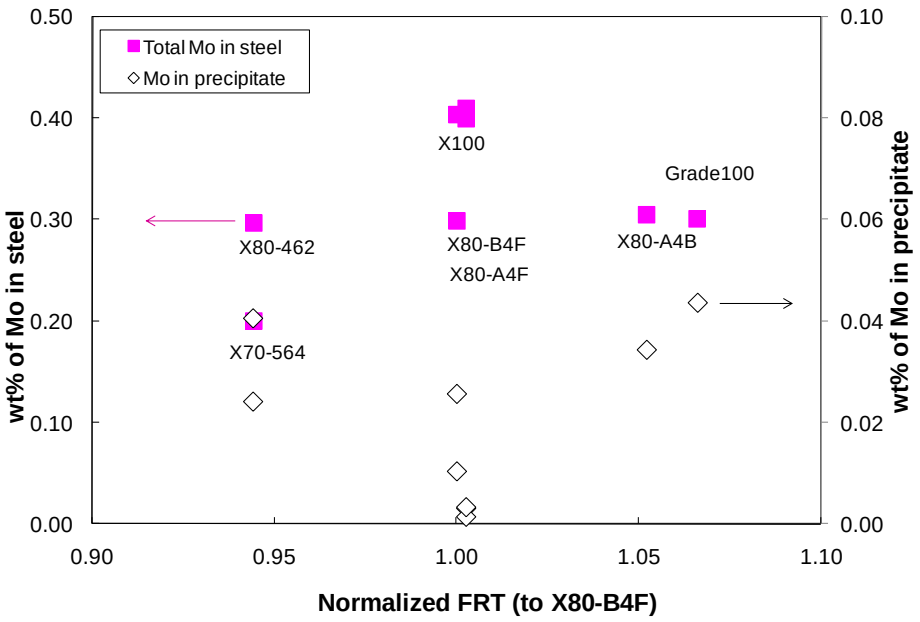

Figure 6-8 Effect of FRT on the wt% of Mo in precipitate form for all steels.

6-6. Precipitate characterization

6-6-1. Precipitates from X100-2A steel

Figure 6-9 shows an SE-SEM image of precipitates extracted by a carbon replica. Bright spots indicate the precipitates. Coarse precipitates 1 and 2 are about 100 nm in size. EDX analysis shows that they are Ti-rich with some Nb. Most of the precipitates are less than 100 nm in size. In the EDX spectra, the C peak is from the carbon replica and Cu peaks are from the sample holder (Cu grid). Because nital solution (mixture of ethanol and HCl) was used in carbon replica preparation, Si-containing inclusions may dissolve in HCl and form Si-O phase with its information shows up in the EDX spectra.

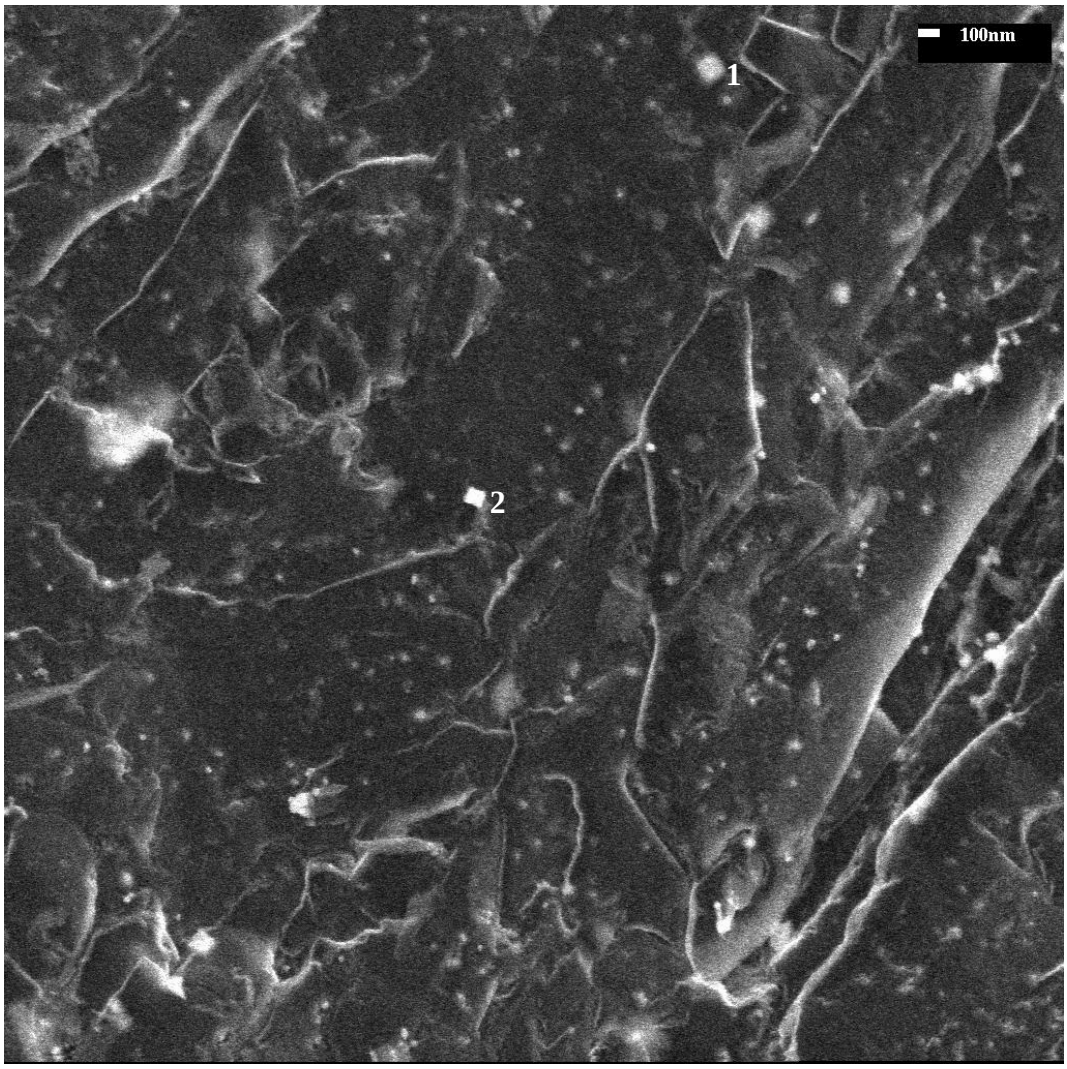

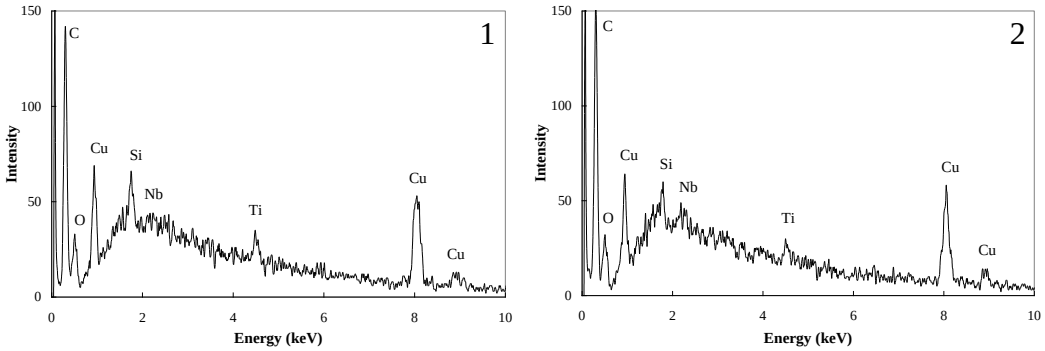

Figure 6-9 SEM image and EDX spectra from precipitates of X100-2A steel.

Due to the fine sizes of the precipitates, TEM was used to characterize precipitate size and chemistry. Figure 6-10 shows several TEM BF images of precipitates, which were extracted by carbon replicas. Figure 6-10e and f are EDX spectra from precipitates 1 and 2 shown in Figure 6-10d. They correspond to Ti-rich and Ti/Nb-rich precipitates, respectively. A summary of the composition and approximate sizes of the precipitates shown in Figure 6-10 is presented in Appendix A. (Table A-1)

The precipitates are categorized into two groups according to chemistry and size as shown in Table 6-5, i.e., Ti-rich and Ti/Nb-rich precipitates. For Ti-rich precipitates, they have about 70 at% of Ti and the remaining is mainly Nb. For Ti/Nb-rich precipitates, they have about 50 at% Ti and 50 at% Nb. The criterion is to keep the STDEV small. Table 6-5 shows the average composition, composition range (STDEV) and size of precipitates. A small amount of Mo was identified in all the precipitates from X100-2A steel. All the precipitate sizes are on the order of 20-40 nm in diameter. It is assumed that C and N compositions are the same for precipitates in X100-2A steel, which will be discussed in Section 6-6-3. Finer precipitates, less than 10 nm in size, were not observed in the X100-2A steel.

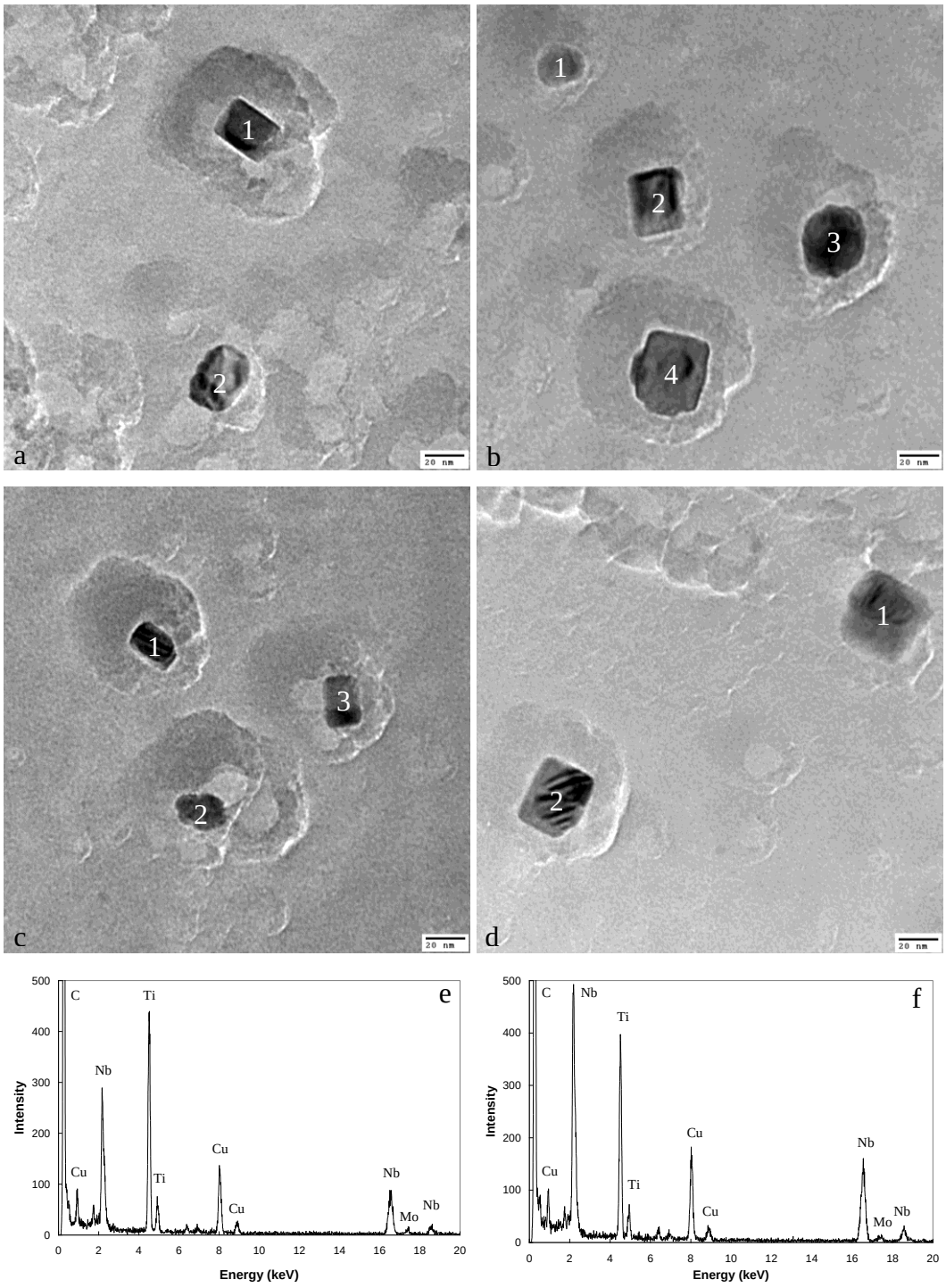

Figure 6-10 TEM BF images and EDX spectra of precipitates extracted from X100-2A steel by carbon replicas.

a, b, c and d) TEM BF images; e, f) EDX of precipitate 1 and 2 in d).

Table 6-5 Classification of precipitates from X100-2A steel according to composition and size range

Precipitate chemistry	STDEV of composition in atomic fraction			Size (nm)
	Ti	Nb	Mo	
$Ti_{0.70}Nb_{0.26}Mo_{0.04}C_{0.5}N_{0.5}$	0.05	0.05	0.02	30-40
$Ti_{0.54}Nb_{0.41}Mo_{0.05}C_{0.5}N_{0.5}$	0.04	0.04	0.02	20-30

6-6-2. Precipitates from X100-2B and X100-3C steels

The SEM/TEM images for precipitates from X100-2B and X100-3C steels are shown in Appendix A.

For X100-2B steel, the precipitates are categorized into three groups according to chemistry and size as shown in Table 6-6, i.e., Ti-rich, Ti/Nb-rich and Nb-rich precipitates. Table 6-6 shows the average composition, composition range (STDEV) and size of the precipitates. Due to the higher V content in this steel relative to the other two X100 steels, small amount of V was identified in all precipitates in X100-2B steel. However, Mo was not identified in precipitates from X100-2B steel, which agrees with the ICP results (Table 6-3 in Section 6-5). All precipitates were about 30-80 nm in diameter. Finer precipitates less than 10 nm were not observed in the X100-2B steel.

For X100-3C steel, the precipitates are categorized into two groups according to chemistry and size as shown in Table 6-6, i.e., Ti/Nb-rich and Nb-rich precipitates. Table 6-6 shows the average composition, composition range (STDEV) and size of the precipitates. All precipitates are about 20-40 nm in size. Similar to X100-2A steel, it is assumed that C and N compositions are the same for precipitates in X100-2B and X100-3C steels, which will be discussed in Section 6-6-3. Finer precipitates, less than 10 nm in size, were not observed in X100-3C steel.

Table 6-6 Classification of precipitates from X100-2B and X100-3C steels according to composition and size range

Steel	Precipitate chemistry	STDEV of composition in atomic fraction				Size (nm)
		Ti	Nb	Mo	V	
X100-2B	$Ti_{0.66}Nb_{0.29}V_{0.05}C_{0.5}N_{0.5}$	0.07	0.06	N/A	0.01	40-80
	$Nb_{0.53}Ti_{0.42}V_{0.05}C_{0.5}N_{0.5}$	0.1	0.11	N/A	0.02	30-50
	$Nb_{0.85}Ti_{0.13}V_{0.02}C_{0.5}N_{0.5}$	0.06	0.07	N/A	0.01	40-55
X100-3C	$Ti_{0.50}Nb_{0.47}Mo_{0.03}C_{0.5}N_{0.5}$	0.06	0.06	0.01	N/A	20-40
	$Nb_{0.67}Ti_{0.3}Mo_{0.03}C_{0.5}N_{0.5}$	0.07	0.08	0.01	N/A	20-30

6-6-3. Precipitates forming temperatures under equalibrium conditions for X100 steels

As mentioned previously, nano-precipitates (≤10nm) were not identified in X100 steels. The precipitates from X100 steels all have smaller sizes (mainly 30-40nm). Under equilibrium conditions, the precipitation temperatures of TiN, NbC NbN and Mo_2C precipitates in X100 steels were calculated based on the precipitate solubility products and steel chemistry as shown in Table 6-7. Precipitate solubility products are shown in the following equations. Figure 6-11 shows the precipitation temperatures of TiN, NbC, NbN and Mo_2C for all steels studied in this thesis. Under equilibrium conditions, TiN, NbC and NbN form in the austenite region for three X100 steels. No large Ti-rich precipitates were identified in X100 steels and all precipitates have smaller sizes compared to those precipitates with similar chemistries from other steels. Therefore, precipitates from X100 steels are expected to be Ti, Nb carbonitrides. In order to simplify the calculations, it is assumed that C and N compositions are the same for precipitates in three X100 steels.

It is expected that Mo_2C forms in the ferrite because the precipitation temperature (between 753ºC and 783ºC for X100 steels) is lower than the Ar_3 (about 866 ºC), which will be explained in Table 7-2 in Section 7-2-1.

Table 6-7 Ti, Nb, Mo, N and C compositions in X100 steels (wt%)

wt%	X100-2A	X100-2B	X100-3C
Ti	0.013	0.009	0.009
Nb	0.037	0.047	0.046
Mo	0.41	0.4	0.4
N	0.005	0.0059	0.0063
C	0.039	0.065	0.064

$$\log K_{s-TiN}(liquid) = \log[Ti]_e[N]_e = A - B/T = 5.90 - 16586/T \quad (5\text{-}1)$$

$$\log K_{s-TiN}(\gamma) = \log[Ti]_e[N]_e = A - B/T = 3.82 - 15020/T \quad (5\text{-}2)$$

$$\log K_{s-NbC}(\gamma) = \log[Nb]_e[C]_e = A - B/T = 2.06 - 6700/T \quad (5\text{-}3)$$

$$\log K_{s-NbN}(\gamma) = \log[Nb]_e[N]_e = A - B/T = 2.80 - 8500/T \quad (5\text{-}4)$$

$$\log K_{s-Mo_2C}(\gamma) = \log[Mo]^2{}_e[C]_e = A - B/T = 5.00 - 7375/T \quad (5\text{-}5)$$

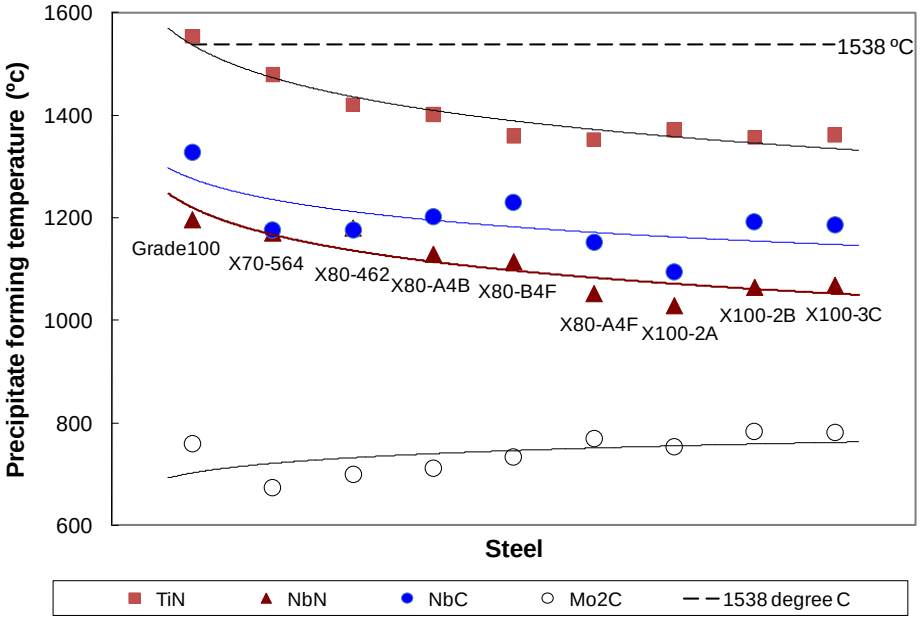

Figure 6-11 Precipitation temperature for TiN, NbN, NbC and Mo_2C in all steels under equilibrium conditions.

6-7. Rietveld refinement of the XRD data and determination of the relative abundance of different phases

6-7-1. Rietveld refinement of the XRD data

Based on the precipitate chemistry from TEM-EDX microanalysis, detailed phase analysis was done using Rietveld refinement. Figure 6-12 shows the overall profile fitting and the difference between the calculated and observed patterns for residues from the X100-2A steel. Figure 6-12a shows the overall XRD pattern profile fitting. The calculated diffraction patterns for $Ti_{0.70}Nb_{0.26}Mo_{0.04}C_{0.5}N_{0.5}$, $Ti_{0.54}Nb_{0.41}Mo_{0.05}C_{0.5}N_{0.5}$ and amorphous SiO_2 are shown in Figure 6-12b, c and d, respectively, as shown by arrows. The tick marks in the bottom of the figures indicate the positions of the above phases. The XRD pattern profile fitting for X100-2B and X100-3C steels is shown in Appendix B.

From previous chapters, nano-precipitates (≤10 nm) were observed in the Grade100, X70 and X80 steels. As explained in Section 4-7-2-1, there is a strong correlation between the nano-precipitates and the amorphous SiO_2. SiO_2 was used as an internal standard in the refinement and the resulting residual amorphous content was ascribed to the nano-precipitates (≤10 nm). For the X100 steels, the resulting residual amorphous content is close to zero after Rietveld refinement. However, for other steels, the resulting residual amorphous content, which corresponds to the nano-precipitates, is between 10-30wt% using HCl dissolution. (Table 4-11 for Grade100 and Table 5-11 for X70 and X80 steels) This indicates that no nano-precipitates (≤10 nm) are present in the three X100 steels, which is in agreement with the TEM analysis.

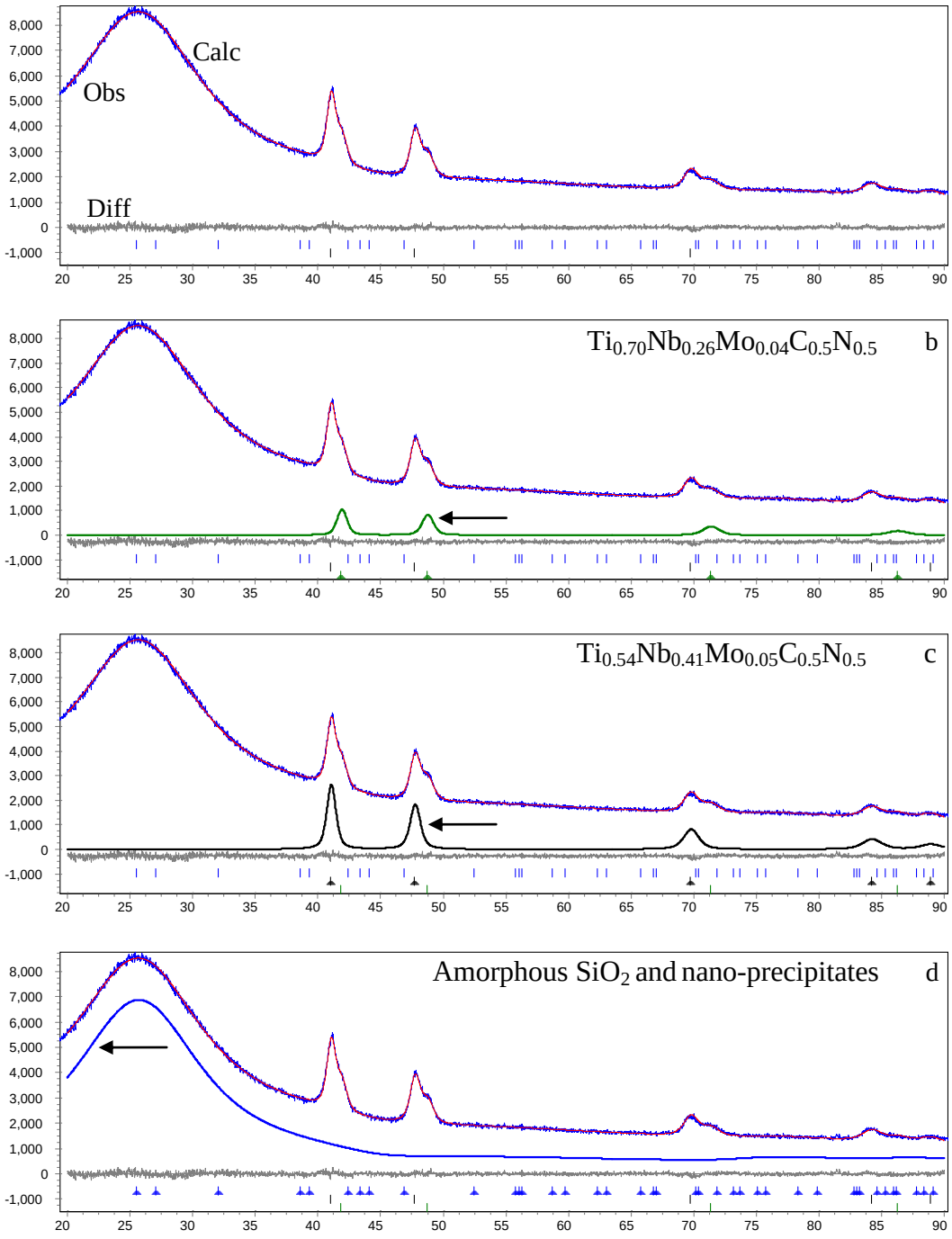

Figure 6-12 Profile fitting of XRD pattern by Rietveld refinement for residue extracted from X100-2A steel by chemical dissolution using HCl.

a) Overall XRD pattern profile fitting;

b) calculated diffraction pattern for $Ti_{0.70}Nb_{0.26}Mo_{0.04}C_{0.5}N_{0.5}$;

c) calculated diffraction pattern for $Ti_{0.54}Nb_{0.41}Mo_{0.05}C_{0.5}N_{0.5}$;

d) calculated diffraction pattern for amorphous SiO_2 and nano-precipitates.

6-7-2. Determination of the relative abundance of different phases

The precipitate information from three X00 steels using Rietveld refinement via HCl dissolution is shown in Table 6-8. The table includes the refined lattice parameter and relative abundance of the constituent crystal phases. According to the experimental extraction yield, the wt% of different precipitates compared to the weight of steel can be obtained and are shown in Table 6-8 as well.

Table 6-8 The relative abundance (wt%) of the constituent crystal phases for X100 steels chemically dissolved using HCl dissolution

Steel	Phases	Lattice parameter nm	Relative abundance of precipitates in the extracted residue (wt%)	Experimental extraction yield wt%	Wt% compared to the weight of steel being dissolved
X100 -2A	$Ti_{0.70}Nb_{0.26}Mo_{0.04}C_{0.5}N_{0.5}$	0.4339	2.85%	0.288%	0.008%
	$Ti_{0.54}Nb_{0.41}Mo_{0.05}C_{0.5}N_{0.5}$	0.4425	13.13%		0.038%
X100 -2B	$Ti_{0.66}Nb_{0.29}V_{0.05}C_{0.5}N_{0.5}$	0.4317	3.46%	0.523%	0.018%
	$Nb_{0.53}Ti_{0.42}V_{0.05}C_{0.5}N_{0.5}$	0.4431	3.00%		0.016%
	$Nb_{0.85}Ti_{0.13}V_{0.02}C$	0.4447	3.96%		0.021%
X100 -3C	$Ti_{0.5}Nb_{0.47}Mo_{0.03}C_{0.5}N_{0.5}$	0.4254	2.50%	0.746%	0.019%
	$Nb_{0.67}Ti_{0.3}Mo_{0.03}C_{0.5}N_{0.5}$	0.4415	3.17%		0.024%

6-8. Summary

From the microstructural studies of the X100 steels, the main results are summarized as follows.

The X100 steels have similar microstructures and the grain sizes are effectively refined compared with the X70 and X80 steels. This is expected because the design principle for the X100 steels is a combination of microalloying, higher cooling rates associated with TMCP and low ICT, leading to a microstructure consisting of significant grain refinement of the bainite with/without martensite. Therefore, steels with these low carbon microconstituents should have higher strength, superior toughness and good weldability compared with the X70 and X80 steels.

Precipitates from the different steels were identified and categorized into different groups according to size and chemistry. Most precipitates in the X100 steels were about 20-60 nm in size. Finer precipitates (≤10 nm) were not observed, due to the lower interrupted cooling temperature.

Small amount of Mo was detected in the precipitates from X100-2A and X100-3C steels. In X100-2A steel, small amount of B is added. It effectively increases steel hardenability and promotes the formation of bainite. Together with the highest cooling rate, some Mo precipitates out from the solid solution into the precipitates.

In X100-2B steel, it has higher amount of V. V was detected in the precipiates, which is similar to the Grade100 steel. Mo was not identified in precipitates from this steel.

Temperature has a stong effect on precipitate nucleation. The amount of Nb and Mo in precipitate form increases with increasing CT/ICT. Higher Nb content in steel enhances Nb precipitation.

Chapter 7: Discussion

7-1. Introduction

In the previous chapters, Grade100, X70, X80 and X100 steels were characterized individually in terms of grain microstructure and precipitates. In this chapter, the effect of steel chemistry, CR and CT/ICT on the grain microstructure and steel mechanical properties is discussed. The volume fraction of the nano-precipitates (average size ≤10 nm) is determined based on the weight fractions obtained from Rietveld refinement. The effect of microalloying content, FRT and CT/ICT on the amount of nano-precipitates is also discussed. The dependence of precipitate nucleation rate on temperature is investigated as well. Different strengthening components, including grain size effect, precipitation and solid solution strengthening are quantified. Finally, the different strengthening components are combined. Comparison is made to the experimental yield strengths of the steels.

7-2. Grain microstructure and the effect of steel chemistry, CR and CT/ICT on microstructure and mechanical properties

The CR and CT/ICT are very important processing parameters. They have strong influences on the final microstructure and mechanical properties of steels as well as steel chemistries. Figure 7-1 shows the measured mean linear intercept (*m.l.i.*) for all the steels studied. The grain size generally decreases with increasing steel grade, an effect which is directly related to the steel chemistry, CR and CT/ICT and will be explained in the following.

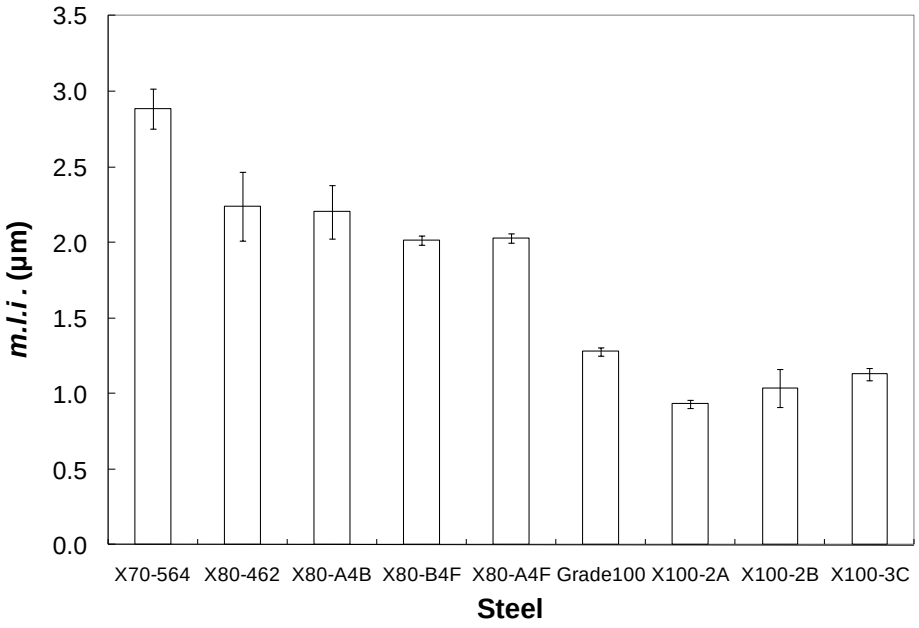

Figure 7-1 Summary of mean linear intercept (*m.l.i.*) measurements.

7-2-1. Effect of steel chemistry on grain microstructure

The primary aim of adding alloying elements to steels is to increase the hardenability, that is, to delay the time required for austenite decomposition into ferrite, pearlite or bainite. [164] Manganese, Mo, Ni and Cr, which are frequently added to modify the steel microstructure, are substantially dissolved in the austenite and ferrite. In addition to Mn, Mo, Ni and Cr, other elements (such as Nb, Ti and V) also have certain effects on steel microstructure. As mentioned in Section 2-1-4, Nb, Ti and V retard austenite recrystallization and lower the austenite to ferrite transformation temperature, leading to grain size refinement. However, the amounts of Nb, Ti and V are relatively small compared with Mn, Mo, Ni and Cr. Their main effects on grain microstructure are in forming carbides, nitrides and carbonitrides, resulting in grain refinement and precipitation strengthneing.

Manganese, Mo, Ni and Cr all have strong effects on steel hardenability. [165] For hardenability improvement, B is the most beneficial element, followed by Mn, Mo, Cr and Ni. Table 7-1 shows the hardenability multiplying factors for the alloying elements. [165] They shift the ferrite and pearlite curves of the CCT

diagram to the right. Under the same CR conditions, the formation of polygonal ferrite is suppressed. Finer lower-temperature transformation products, such as acicular/bainitic ferrite structures, are promoted, leading to grain refinement. [12]

Table 7-1 Alloy multiplying factors for calculating hardenability [165]

Alloy	Alloy multiplying factors	wt% alloy
B	$f_B = 17.23B^{0.268}$	B< 0.002 wt%
Mn	$f_{Mn} = 3.46Mn+1$	0< Mn <1.2 wt%
	$f_{Mn} = 5.125Mn-1$	1.2 wt%< Mn <2.0 wt%
Mo	$f_{Mo} = 3.09Mo+1$	Mo <1.0 wt%
Cr	$f_{Cr} = 2.18Cr+1$	Cr <2.0 wt%
Ni	$f_{Ni} = 0.40Ni+1$	Ni <2.0 wt%

It is known that Mn, Ni, as well as Cu are all austenite stabilizers, so that their presence decreases the austenite to ferrite transformation temperature. However, Mo, Cr and Si are all ferrite stabilizers which helps move the austenite to ferrite transformation temperature upwards. [16,164] Due to the strong effect on hardenability, Mo and Cr shift the ferrite and pearlite curves of the CCT diagram to the right (longer times). Therefore, the formation of polygonal ferrite is suppressed. The austenite to ferrite transformation temperature decreases with increasing levels of Cr. As for the bainite transformation, most alloys depress the bainite transformation temperature. [166]

The A_1 and A_3 temperature upon cooling (Ar_1, Ar_3) and the bainite start temperature (B_s) under slow cooling conditions can be estimated by equation (7-1), (7-2) and (7-3), respectively. [150,63] Ar_1, Ar_3 and B_s are all composition related. Both Ar_1 and Ar_3 decrease with increasing levels of Mn and Ni while increase with increasing Si content. For the steels studied in current thesis, the estimated Ar_1, Ar_3 and B_s are shown in Table 7-2. Although these steels have different chemistry, the estimated Ar_1, Ar_3 and B_s for different steels are virtually the same.

$$Ar_1(^{o}\mathrm{C}) = 723 - 25\%\mathrm{Mn} - 30\%\mathrm{Ni} + 25\%\mathrm{Si} + 30\%\mathrm{Al} + 25\%\mathrm{Mo} + 50\%\mathrm{V} \quad (7\text{-}1)$$

$$Ar_3(^{o}\mathrm{C}) = 868 - 396\%\mathrm{C} - 68.1\%\mathrm{Mn} - 36.1\%\mathrm{Ni} - 20.7\%\mathrm{Cu} - 24.8\%\mathrm{Cr} + 24.6\%\mathrm{Si} \quad (7\text{-}2)$$

$$B_s(^{o}\mathrm{C}) = 830 - 270\%\mathrm{C} - 90\%\mathrm{Mn} - 37\%\mathrm{Ni} - 70\%\mathrm{Cr} - 83\%\mathrm{Mo} \quad (7\text{-}3)$$

Table 7-2 Ar_1, Ar_3 and B_s for all steels (ºC)

Steel	X70-564	Grade100	X80				X100		
			462	A4B	B4F	A4F	2A	2B	3C
Ar_1	689.3	687.5	692.3	689.0	681.4	679.9	677.2	682.9	683.0
Ar_3	866.7	866.3	866.7	866.6	866.5	866.4	866.4	866.3	866.3
B_s	828.2	827.7	828.1	828.0	828.0	827.7	827.6	827.5	827.5

Figure 7-2 shows the effect of Mn, Mo, Ni and Cr on the mean linear intercept (*m.l.i.*) of the microalloyed steels. The linear fitting and empirical equations for each element is shown as well. It is clear that with increasing levels of these elements in the steel, the grain size decreases. Yield strength and toughness are improved accordingly.

From Table 3-1, X100 steels have a higher amount of Mo, Ni and Cr than X70 and X80 steels. Due to these element contributions, it is expected that X100 steels will have much finer grain sizes than X70 and X80 steels, which agrees with the grain size measurement. The Mo, Ni and Cr levels of Grade100 steel are between those for the X70, X80 and X100 steels. As such, it is expected that the grain size of Grade100 steel will also be between the values for X100 steels and the other steels.

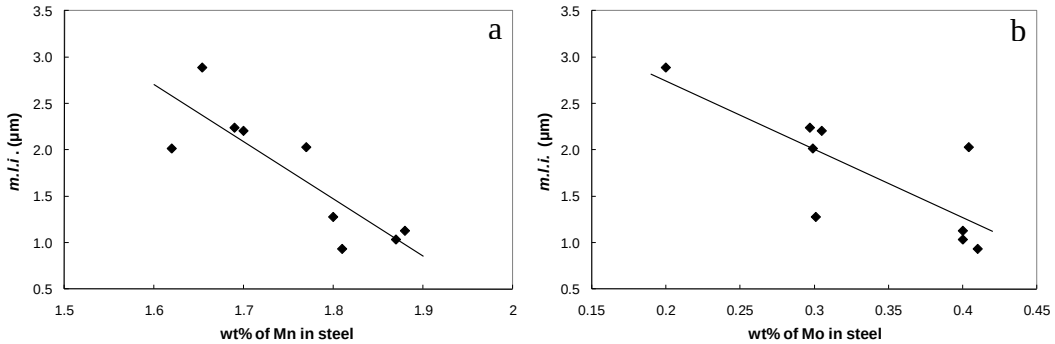

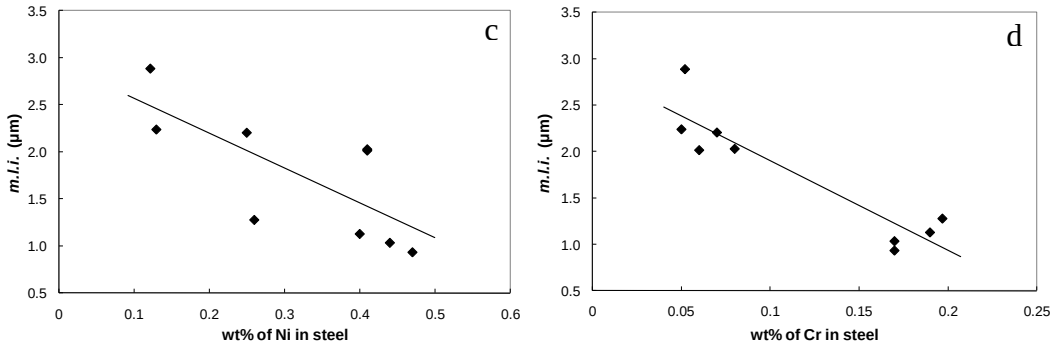

Figure 7-2 Effect of steel chemistry on mean linear intercept (*m.l.i.*) of steels.
a) *m.l.i.* = -6.1 × (%Mn) +12.5; b) *m.l.i.* = -7.4 × (%Mo) +4.2;
c) *m.l.i.* = -3.7 × (%Ni) +2.9; d) *m.l.i.* = -9.7 × (%Cr) +2.9.

7-2-2. Effect of CR on grain microstructure and mechanical properties

In TMCP, accelerated cooling is used after finish rolling. Cooling rate has a direct influence on steel microstructure evolution, which can be seen from the CCT diagrams (Figure 2-11, Figure 3-1, Figure 3-2 and Figure 3-3) and confirmed by microstructure investigations. Figure 7-3 shows the effect of CR on the *m.l.i.* of the steels, which indicates that the grain size decreases with an increase in steel grade. The main microstructures for X70, X80 and X100 steels are PF+AF, AF+BF and BF, respectively. A higher CR helps avoid the F + P nose, leading to a finer microstructure with a ferrite and bainite mixture or even a fully bainitic microstructure. If the CR is even higher, such as in X100 steels, ferrite nucleation becomes rate determining. Therefore ferrite nucleation is inhibited, resulting in finer, low-temperature transformation products such as bainite or even martenite. Higher CR can also suppress the austenite to ferrite transformation temperature and increase the ferrite nucleation rate.

Because only the intended CR values are available for X70, X80 and Grade100 steels, and they are same, there is no point to discussing the effect of CR on the *m.l.i.* for these steels. However, there is a significant change in grain size for these steels. For X100 steels, there is a significant change in CR between X100-3C and the other two steels (X100-2A and X100-2B), but their grain sizes are almost the same. It indicates that steel microstructure evolution and/or other

factors (e.g., steel composition, CT/ICT, rolling conditions, etc.) are more important for steel grain size.

The relationship between the yield strength and CR is shown in Figure 7-4.The fitting is not good because of the effect of CR on grain size is not obvious as mentioned above.

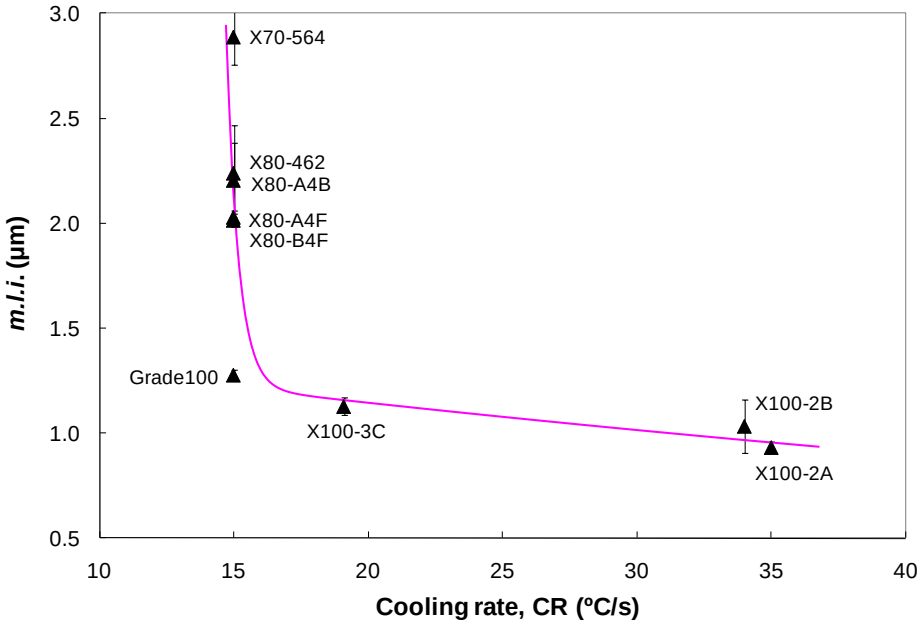

Figure 7-3 Effect of CR on mean linear intercept of steels.

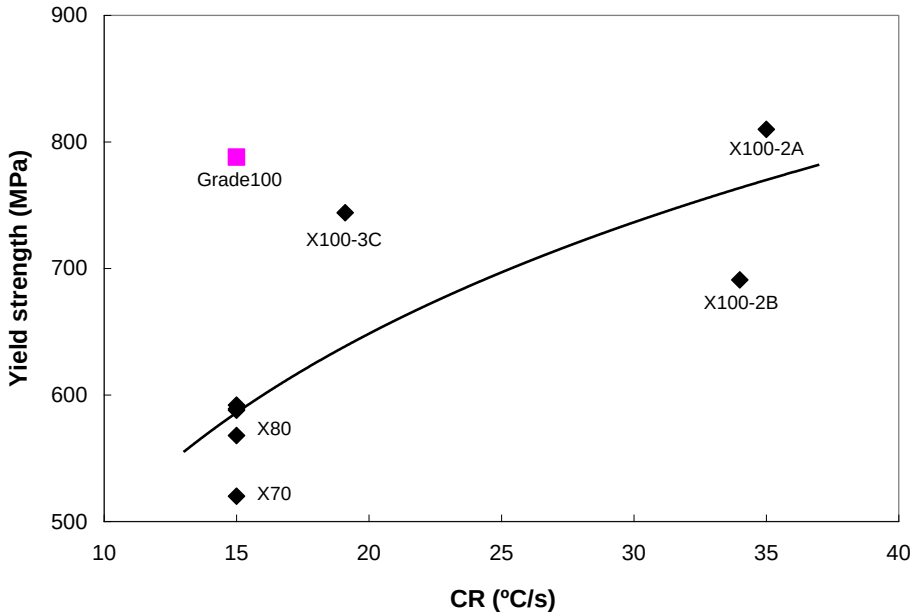

Figure 7-4 Effect of CR on yield strength.

7-2-3. Effect of CT/ICT on grain microstructure and mechanical properties

CT/ICT can affect the grain microstructure as well. Figure 7-5 shows the effect of CT/ICT on the *m.l.i.* of steels. The linear fitting is shown as well, although Grade100 is not included. The strengthening mechanism for Grade100 steel is different from other steels because it is a structural steel with higher amounts of carbon and other alloying elements. However, other steels are intended for production of pipelines. The grain size decreases with decreasing CT/ICT which is consistent with the literature. [9,12] This effect is related to the nucleation and grain growth during the austenite to ferrite transformation. During cooling, phase transformation is generally shifted to a lower temperature, which is called undercooling. If the steel is cooled quickly, the undercooling depends on the CT/ICT. A lower CT/ICT causes a higher degree of undercooling. Greater undercooling below Ar_1 enhances the driving force for the austenite to ferrite transformation, resulting in an increase in the ferrite nucleation rate. As the temperature decreases, the ferrite growth rate is reduced because grain growth is directly related to the diffusion process. If other processing parameters are the same, the ferrite nucleation rate increases and grain growth rate decreases at low CT/ICT, resulting in a finer ferrite grain size. This means that a lower CT/ICT helps refine grains. However, CT should not be too low or undesirable low-temperature products such as martensite will form.

Figure 7-6 shows the effect of CT/ICT on the yield strength of steels. The linear fitting is shown as well. In Figure 7-6, data from Grade100 is not included in the fitting because it is an outlier, which may due to the structural steel feature and having a more complex composition. It is clear that yield strength improves with decreasing CT/ICT due to the grain refinement effect.

From the above analysis, a combination of high CR and low CT/ICT in microalloyed steels helps to produce a fully fine bainitic microstructure, making higher strength steels (X100) possible.

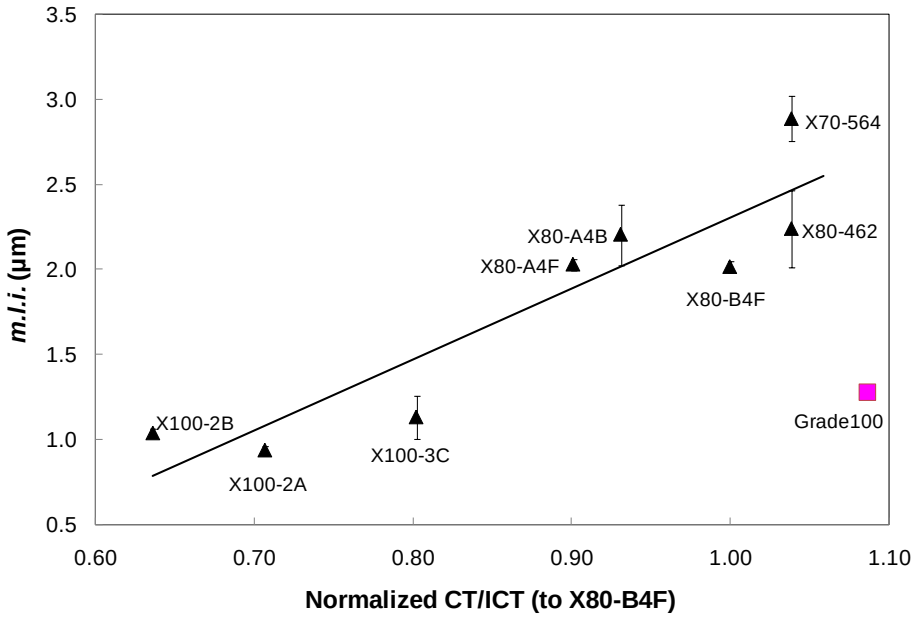

Figure 7-5 Effect of CT/ICT on mean linear intercept of steels.

m.l.i. = 4.2 × (normalized CT/ICT) -1.9

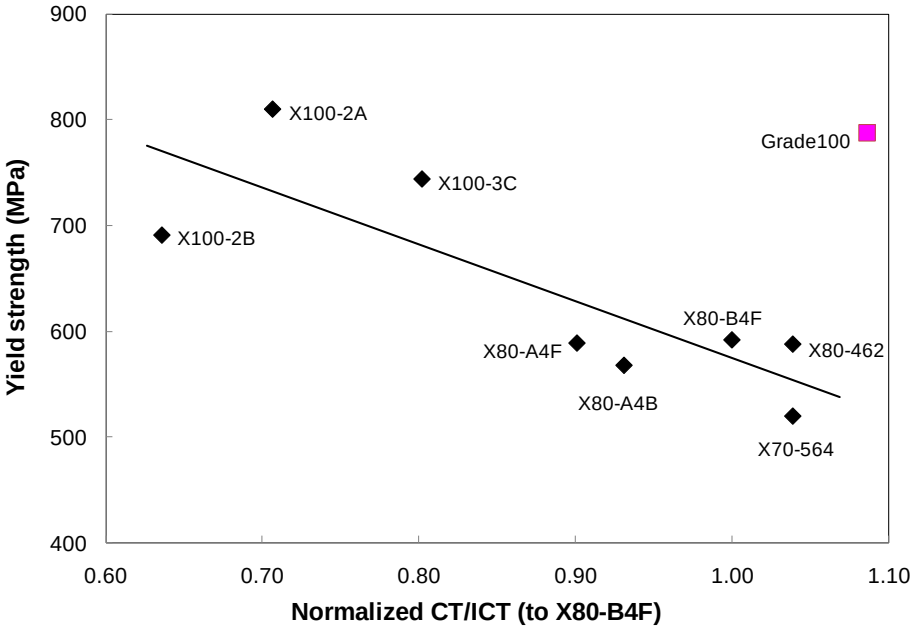

Figure 7-6 Effect of CT/ICT on yield strength.

Yield strength = -537.0 × (normalized CT/ICT) +1111.3

7-3. Mass balance

There are two ways to calculate the amounts of Nb, Ti and Mo that are present in the precipitate, i.e., Rietveld refinement and ICP analysis of the supernatant,

with the procedures shown in Figure 7-7. From Rietveld refinement (Section 4-7, 5-7 and 6-7), the relative abundance of different phases in the precipitate is obtained. Based on precipitate chemistries, the total amount of microalloying elements present in precipitates can be calculated. From ICP analysis of the supernatant (Section 4-5, 5-5 and 6-5), the total amount of microalloying elements dissolved in the ferrite matrix can be obtained. By comparison with the total amount of element in the steel, the remaining microalloying elements contribute to precipitates. Therefore, a comparison can be made for the mass balance of Nb, Ti and Mo obtained from the above two ways. Table 7-3 shows the mass balance of Nb, Ti and Mo based on Rietveld refinement and ICP analysis of the supernatant. For Rietveld refinement and ICP analysis, ICP method is more believable to analyze the total amount of microalloying elements present in precipitates. ICP analyzes the supernatant directly. However, Rietveld refinement involves more experimental procedures, such as precipitate chemistry determination through SEM/TEM-EDX, XRD scan of the extracted precipitates as well as XRD profile fitting. More error sources will be involved. But Rietveld refinement can provide the relative abundance of different precipitate phases and therefore the amount of nano-precipitates is available, which is most important for precipitation strengthening quantification. From Table 7-3, the mass balance of Nb, Mo and V seems acceptable for Rietveld refinement method and ICP analysis. However Ti is not good. The error sources will be discussed shortly in this section.

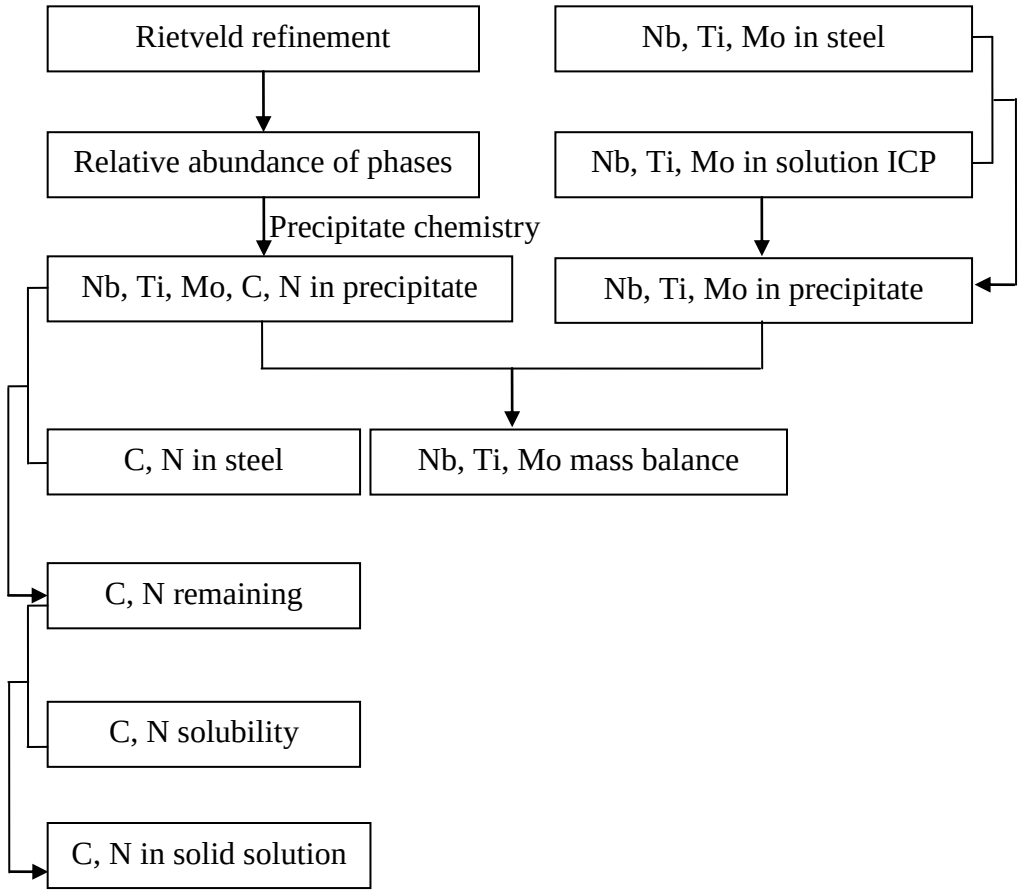

Figure 7-7 Diagram for mass balance calculations of microalloying elements as well as C and N.

The total amount of C and N tied up in the precipitates can be calculated based on the amount of Nb, Ti and Mo obtained from Rietveld refinement and also the C, N composition in the precipitate. The total wt% of C and N in the steel, the amount tied up in the precipitate and their remaining contents are shown in Table 7-3.

As mentioned in Chapter 2, both C and N have very limited solubilities in ferrite at room temperature, with a maximum of 0.005wt% for C [16] and 0.01wt% for N at 590 ºC. Because the solubility of N is higher than that of C, the solubility of N in ferrite is assumed to be 0.01wt% at room temperature in the current thesis.

From Table 7-3, it was found that some of the N contributes to precipitation and the remaining N (the total N content minus the amount of N tied up in the precipitate) is within its solubility range in ferrite for all steels except X70-564 steel. Therefore, a N solubility 0.01wt% is used for contribution to the solid solution for X70-564 steel. For other steels, the remaining N content is in solid solution, contributing to solid solution strengthening.

From Table 7-3, the remaining C content far exceeds its solubility for all steels studied here. If supersaturation is not considered, the remaining C will precipitate out forming Fe_3C. Although Ti, Nb and Mo are strong carbide formers compared with Fe, Fe_3C can still form because of two reasons. First, the above microalloying elements are within their solubility ranges. Second, the availability of Fe is high due to the amount of Fe present. Therefore, for all steels, 0.005wt% is the amount of C that contributes to solid solution for C. It should be mentioned that the C and N content in the precipitates are assumed values based on the different solubilities of carbides, nitrides and carbonitrides. For example, the largest precipitates form at high temperature during or just after casting. They are Ti-rich with a small amount of Nb. They are assumed to be Ti(Nb)N. However, some C may exist. This assumption does not change the solid solution strengthening because the solid solution strengthening coefficients for C and N are the same. It will be explained in Section 7-5-2.

Table 7-3 Mass balance - wt% of elements in steels and in precipitate

Steel		Grade100	X70-564	X80-462	X80-A4B	X80-B4F	X80-A4F	X100-2A	X100-2B	X100-3C
wt%Nb	Total Nb[1]	0.094	0.069	0.091	0.094	0.077	0.044	0.037	0.047	0.046
	Nb in ppt[2]	0.104	0.052	0.108	0.093	0.096	0.045	0.020	0.0323	0.0260
	Nb by ICP[3]	0.091	0.0559	0.087	0.078	0.072	0.035	0.025	0.0343	0.0345
	Difference	-14.0%	7.8%	-24.0%	-19.6%	-32.4%	-29.9%	19.6%	5.8%	24.6%
wt%Mo	Total Mo[1]	0.301	0.2	0.297	0.305	0.299	0.404	0.41	0.4	0.4
	Mo in ppt[2]	0.0439	0.035	0.021	0.031	0.027	0.008	0.0026	N/A	0.0014
	Mo by ICP[3]	0.0437	0.041	0.024	0.034	0.026	0.010	0.0031	N/A	0.0032
	Difference	0.5%	13.3%	11.5%	9.5%	-6.8%	22.1%	14.1%	N/A	55.9%
wt%V	Total V[1]	0.047	0.001	0.002	0.003	0.002	0.003	0.003	0.07	0.003
	V in ppt[2]	0.003	N/A	N/A	N/A	N/A	N/A	N/A	0.0013	N/A
	V by ICP[3]	0.002	N/A	N/A	N/A	N/A	N/A	N/A	0.0014	N/A
	Difference	-7.7%	N/A	N/A	N/A	N/A	N/A	N/A	4.7%	N/A
wt%Ti	Total Ti[1]	0.06	0.023	0.013	0.017	0.009	0.009	0.013	0.009	0.009
	Ti in ppt[2]	0.045	0.0008	0.007	0.002	0.004	0.0105	0.016	0.0048	0.009
	Ti by ICP[3]	0.046	0.0052	0.0062	0.015	0.0063	0.0054	0.006	0.0127	0.008
	Difference	1.6%	84.6%	-9.2%	87.8%	42.0%	-93.5%	-150%	-167%	-16.3%
wt%C	Total C[1]	0.08	0.0398	0.03	0.035	0.052	0.052	0.039	0.065	0.064
	C in ppt[2]	0.0219	0.011	0.0153	0.0143	0.0147	0.0057	0.0034	0.0051	0.003
	Remaining	0.0581	0.0288	0.0147	0.0207	0.0373	0.0463	0.0356	0.0599	0.061
	Solubility	0.005 [16]								
wt%N	Total N[1]	0.011	0.0118	0.0098	0.0058	0.0061	0.0055	0.0050	0.0059	0.0063
	N in ppt[2]	0.0052	0.0005	0.0036	0.0025	0.0024	0.0045	0.004	0.003	0.0034
	Remaining	0.0058	0.0113	0.0062	0.0033	0.0037	0.001	0.001	0.0029	0.0029
	Solubility	0.01								

Note:

ppt: precipitate;

[1]: Total wt% of element in steel;

[2]: Total wt% of element in precipitate form obtained from Rietveld refinement;

[3]: Total wt% of element in precipitate form obtained from ICP analysis;

Difference: (element content from ICP-element content from Rietveld refinement) divided by element content from ICP.

As mentioned previously, there are a variety of sources for the errors to occur for the mass balance discrepancy between Rietveld refinement and ICP analysis. For the ICP analysis, there are two error sources involved with the accuracy of the analysis.

1) The accuracy of steel chemistry. The steels are industry products and the chemistries are supplied by the steel company. Error exists due to the chemistry homogeneity in the whole strip.
2) ICP analysis. Although ICP has a very low detection limit, interference is a potential source of error for ICP analysis. Dilution of the solution and multi-point calibration for each element are used to minimize this error.

For the Rietveld refinement, some error sources exist due to the complicated experimental procedures.

1) The reported Ti amounts in steels are much lower than that of Nb and Mo; higher error is expected due to the complicated experimental procedures.
2) Matrix dissolution was used for precipitate extraction; errors may exist during experimental operations. For example, residues are separated with the supernatant by centrifuging, collected from the centrifuge tubes, dried and weighed. Each process has error.
3) Precipitate chemistries are analyzed using SEM/TEM-EDX, which has a detection limit with a typical value of 0.1wt%. [152] Assuming thin-foil criterion, quantification was done using a standardless approach. Therefore, the Cliff-Lorimer equation (presented in Section 3-6-1) is used to determine the wt% of each element. Compared to the standard approach, a primary source of error due to poor counting statistics is involved because the absorption and fluorescence of X-rays within the specimen are ignored in the correction procedure for thin specimens. [151]
4) The extracted residues were analyzed by X-ray diffraction. It has a detection limit, which is dependent on the phase concentration and the counts produced from this phase. The volume fraction of Ti-rich nitrides is small compared with the nano-precipitates. Ti-rich nitrides may not be detected if the content is below the XRD detection limit. For example, a

single Ti-rich precipitate was observed in X70-564 and X80-A4B steels by TEM. However, this phase was not identified in the XRD pattern, probably due to the detection limit of XRD technique.

5) Errors are involved in the profile fitting via Rietveld refinement as well. Nano-precipitates have the largest volume fraction compared with other phases. However, the nano-precipitates have a strong correlation with the amorphous SiO_2 phase. The amount of nano-precipitates is not determined directly from the Rietveld refinement. SiO_2 was used as an internal standard in the refinement and the resulting residual amorphous content was ascribed to the nano-precipitates (≤10 nm). The procedure explanation was made in Section 4-7-2-1.

The above sources of error explain the discrepancy between the Rietveld refinement and ICP analysis. The error in the Rietveld refinement using SiO_2 as an internal standard is a concern. A specimen with similar phase composions and known SiO_2 content should be used as a standard to validate this technique.

7-4. Effect of microalloying content, CR, FRT and CT/ICT on the amount of nano-precipitates (≤10 nm)

7-4-1. Volume fraction and number density determination of nano-precipitates

The nano-precipitates (≤10 nm) have a NaCl-type structure. From the precipitate chemistry, the density of the precipitates can be expressed mathematically as follows: [62]

$$\rho_{ppt} = \frac{nA_{ppt}}{VN_A} \tag{7-4}$$

$\rho_{ppt:}$ density of the nano-precipitate;

$n:$ number of formula units in the unit cell (n = 4);

$A_{ppt:}$ molecular weight of the precipitate;

$V:$ volume of the unit cell ($V = a^3$, a is the lattice parameter of nano-precipitates);

$N_{A:}$ Avogadro's number (6.023×10^{23} atoms/mol).

The molecular weight A_{ppt} can be calculated from the following equation, using $Nb_{0.58}(Mo)_{0.42}C$ as an example. This is the composition of the nano-precipitates in the X70-564 steel.

$$A_{ppt} = A_{Nb} \times 0.58 + A_{Mo} \times 0.42 + A_C \quad (7\text{-}5)$$

A_{ppt}: molecular weight of the precipitate;

$A_{Nb:}$ atomic weight of Nb;

$A_{Mo:}$ atomic weight of Mo;

$A_{C:}$ atomic weight of C.

The volume fraction of the nano-precipitates (≤10 nm) can be calculated as:

$$Vol_{ppt} = \frac{1\mu m^3 \times \rho_{Fe} \times wt\%_{ppt}}{\rho_{ppt}} \quad (7\text{-}6)$$

Vol_{ppt}: total volume of nano-precipitates in 1 μm^3 of steel (volume fraction of nano-precipitates);

ρ_{Fe}: density of Fe, approximately 7.87 g/cm^3; [62,152]

$wt\%_{ppt}$: wt% of the nano-precipitates.

Assuming the nano-precipitates (≤10 nm) are spherical with radius r, the volume of a single precipitate can be expressed as:

$$Vol_{single} = \frac{4\pi r^3}{3} \quad (7\text{-}7)$$

The number density of the nano-precipitates in 1 μm^3 of steel can be calculated based on the total volume of the nano-precipitates and the volume of a single precipitate, which can be expressed as:

$$\#density = \frac{Vol_{ppt}}{Vol_{single}} \quad (7\text{-}8)$$

$Vol_{ppt:}$ total volume of nano-precipitates in 1 μm^3 of steel;

$Vol_{single:}$ volume of a single nano-precipitate;

$r:$ radius of nano-precipitates (≤10 nm) with the largest number distribution by DF imaging.

The weight fraction and volume fraction of the nano-precipitates (≤10 nm) for different steels is shown in Table 7-4. According to the diameter of the nano-precipitates with the largest number distribution, the number density is shown in Table 7-4 as well. Comparison of the amount of nano-precipitates can be clearly seen in Figure 7-8. The precipitates were all extracted by HCl dissolution. It is clear that the Grade100 steel, X70 and X80 steels all have nano-precipitates. Grade100 has the highest amount of nano-precipitates; X80-A4F has the lowest amount. However, no nano-precipitates were detected in the X100 steels. Grade100, X70 and X80 steels all had similar processing histories. The amount of nano-precipitates is directly related to the amount of microalloying elements and the CT/ICT. The lack of nano-precipitates for X100 steels is due to the lower ICT temperature, which will be discussed in the following section.

Table 7-4 Weight fraction, volume fraction and number density of nano-precipitates (mainly ≤10 nm) in steels

Steel	Nano-preciptates (≤10 nm)			
	Weight fraction (Wt %)	Volume fraction (Vol %)	Diameter with the largest number distribution (nm)	Number density (# per μm^3)
Grade100	0.157	0.166	4.5	34770
X70-564	0.092	0.087	5	13299
X80-462	0.118	0.116	5	17671
X80-A4B	0.107	0.104	5	15862
X80-B4F	0.116	0.114	4.5	23911
X80-A4F	0.035	0.034	4	10121
X100-2A	0	0	-	0
X100-2B	0	0	-	0
X100-3C	0	0	-	0

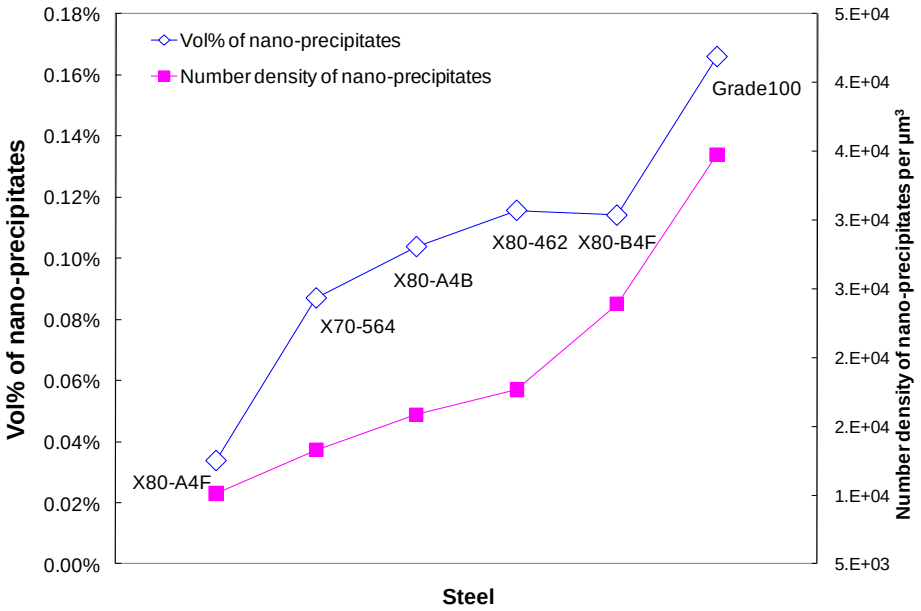

Figure 7-8 Volume fraction and number density of nano-precipitates (≤10 nm) per μm^3 in steels (HCl dissolution).

7-4-2. Effect of microalloying elements on the amount of nano-precipitates (≤10 nm)

Grade100, X70 and X80 steels all have similar processing histories. The amount of nano-precipitates is related to the amount of microalloying elements. Niobium and Mo, especially Nb, are the main microalloying elements contributing to the nano-precipitates (≤10 nm). The effect of Nb on the amount of nano-precipitates in the different grades of steels is shown in Figure 7-9. Curve fitting using an exponential function is shown as well, although the data from X100 steels are not included due to the lack of nano-precipitates. For similar processing conditions, higher Nb content appears to increase precipitation, leading to a higher volume fraction and number density of nano-precipitates. The effect of total Nb and Mo content on the amount of nano-precipitates is shown in Figure 7-10. Grade100 steel has a much higher microalloying content (Nb+Mo) and some Ti and V contribute to nano-precipitates for the Grade100 steel as well. This may account for the significantly higher nano-precipitate content in the Grade100 steel. The amount of C and N tied up in precipitates was also calculated based on the amount of Nb, Ti and Mo; this will be explained in Section 7-4-2. The results

show that, besides contributing to precipitation, there is additional C and N remaining. The additional C and N dissolve in the ferrite matrix if the amounts are within their solubility range. A supersaturated solid solution could result if the solubility limit of C and N is exceeded. If there is a significant amount of C remaining, Fe_3C will form.

In X100 steels, the Nb content is much lower compared to other steels (see in Figure 7-9). The Mo content and the (Nb+Mo) content is much higher in X100 steels than other steels (see Figure 7-10). However, nano-precipitates (≤10 nm) have not been observed in X100 steels. It is directly related to the different processing histories and will be explained in the following section.

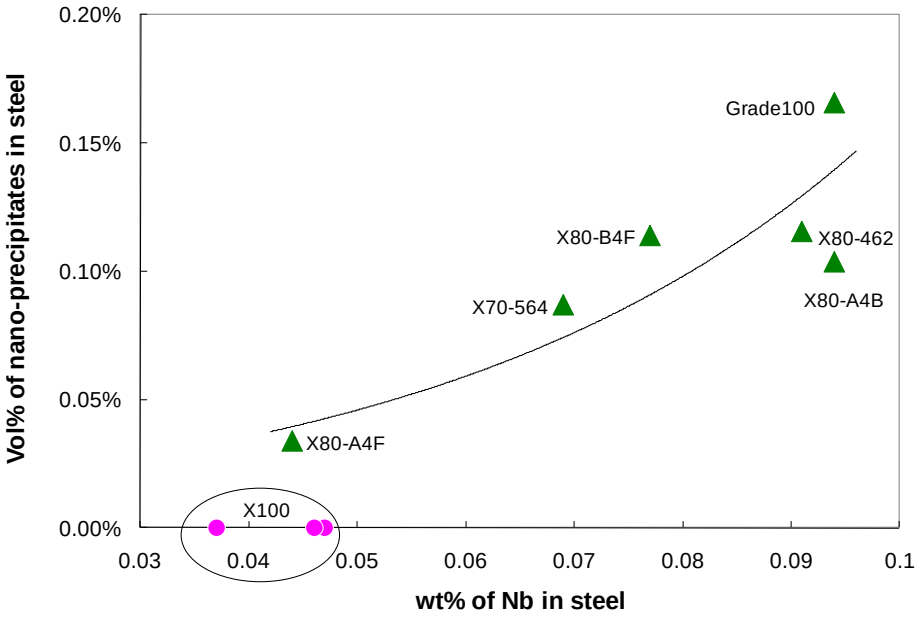

Figure 7-9 Effect of Nb content on the amount of nano-precipitates (≤10 nm).

Vol% = 1.3E-4$e^{25.3\times(wt\%Nb)}$, (Nb content range is 0.044 wt% - 0.094 wt%)

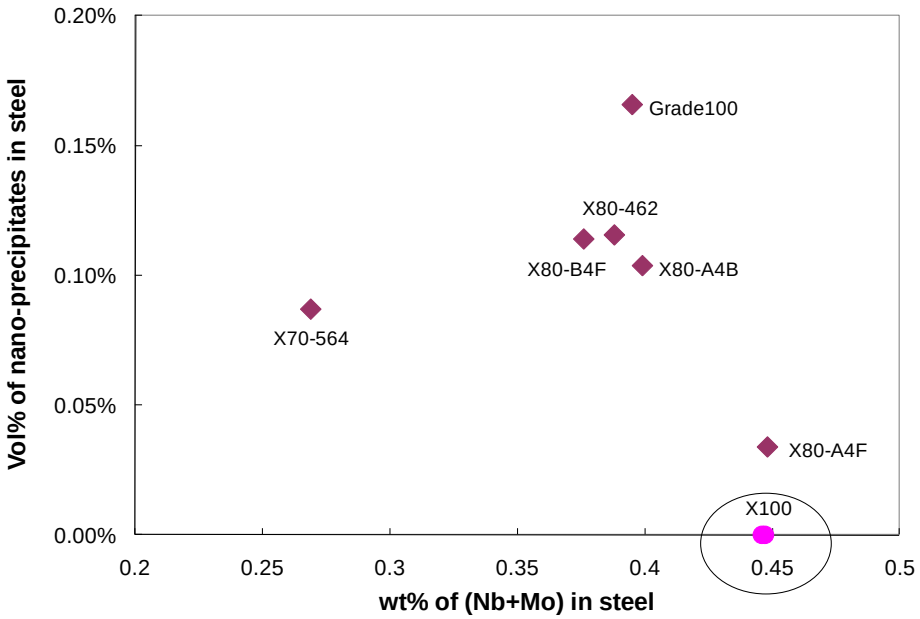

Figure 7-10 Effect of microalloying content (Nb+Mo) on the amount of nano-precipitates (≤10 nm).

7-4-3. Effects of CR, FRT and CT/ICT on the nano-precipitates (≤10 nm)

For the steels studied here, the effect of FRT and CT/ICT on the volume fraction of nano-precipitates (mainly ≤10 nm) is shown in Figure 7-11 and Figure 7-12, respectively. No obvious relationship was found between FRT and the amount of precipitates. This is likely due to the fact that most nano-precipitates are formed at lower temperatures, i.e., during or after coiling. However, CT/ICT has a strong effect on nano-precipitate formation. The relationship between CT/ICT and the volume fraction of the nano-precipitates for X70, X80 and Grade100 steels is fitted with a linear relationship as shown in Figure 7-12. It indicates that the amount of precipitates increases with increasing CT/ICT. It also appears that there is a critical CT/ICT, about 0.8, below which no nucleation of nano-precipitates occurs. The ICT of X100-2A and X100-2B steels are lower than this critical temperature and the ICT of X100-3C steel is just above this critical temperature. It explains why there is lack of nano-precipitates in X100 steels. The effect of temperature on the nano-precipitate nucleation rate will be discussed in Section 7-4-4.

At the same CR condition, lower CT/ICT leads to higher undercooling and higher supersaturation of the solute. Thus a larger driving force is obtained, which enhances precipitation. However nucleation is a kinetic process. There is insufficient thermal energy at lower CT/ICT, which hinders the precipitate nucleation process. At higher CT/ICT, there is a higher species diffusivity and atomic impingement rate, which enhances the nucleation process. However, the driving force is lower and the critical nucleus sizes are larger, which inhibits the number of nuclei present at high temperature. These two competitive processes lead to a maximum nucleation rate at an intermediate temperature for the nucleation of precipitates.

CR can affect the precipitation behavior of nano-precipitates as well. If CT/ICT is fixed, a faster CR leads to a higher degree of undercooling and higher supersaturation of the solute (for example Nb) for subsequent precipitation in ferrite. Thus a larger driving force and higher precipitate nucleation rate can be obtained for precipitation to occur. However, faster cooling of the skelp after the austenite-ferrite transformation may be translated into lower CT/ICT values, leading to a lower precipitate nucleation rate.

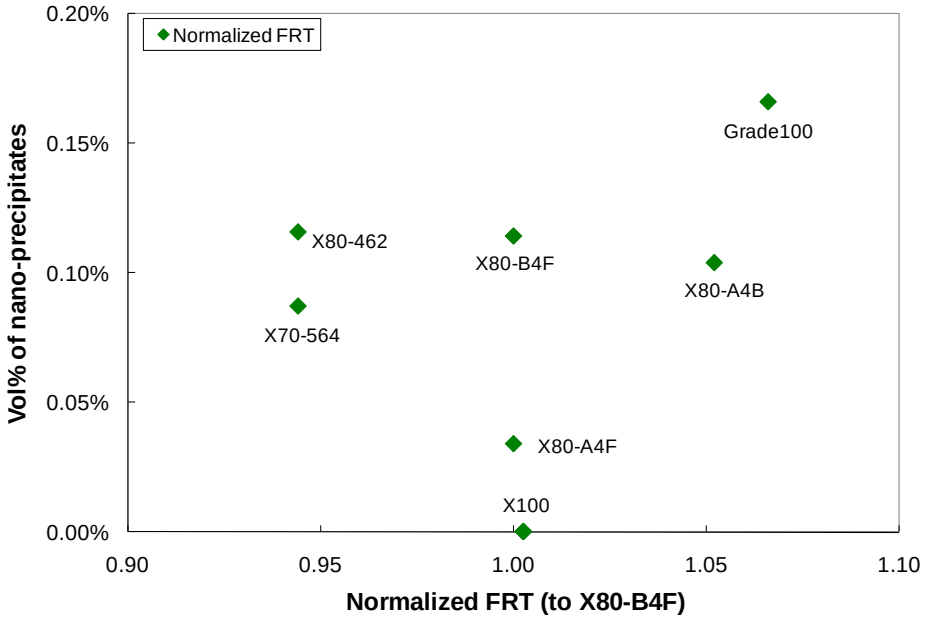

Figure 7-11 Volume fraction of nano-precipitates (≤10 nm) as a function of the FRT.

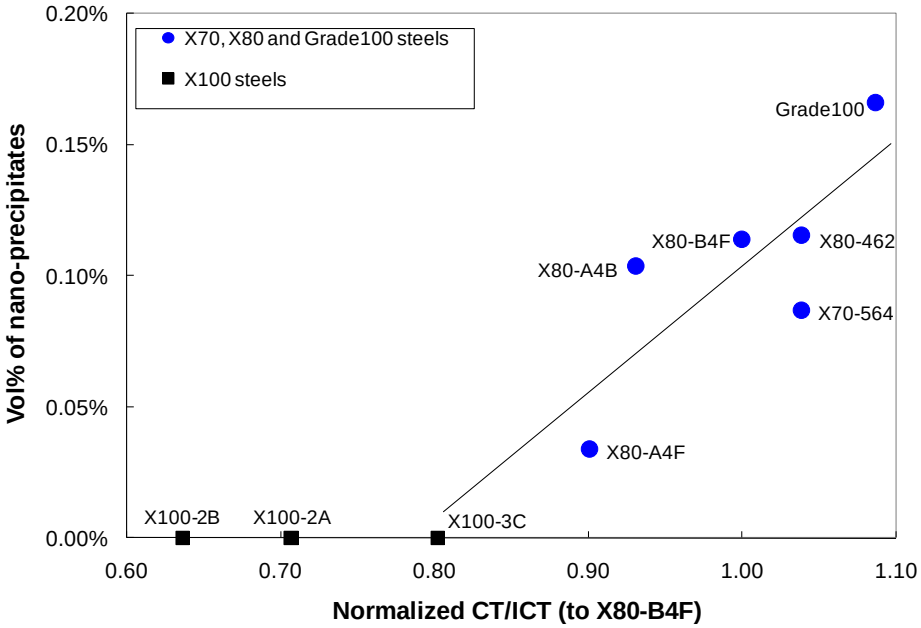

Figure 7-12 Effect of CT/ICT on the volume fraction of nano-precipitates (mainly ≤10 nm).

$Vol\% = 0.005 \times (\text{normalized CT/ICT}) - 0.004$

7-4-4. Nano-precipitate nucleation rate

A list of parameters, used in this section, and their values are defined here. These terms will be used in the nucleation rate calculations in the following section. The precipitates were assumed to be spherical in shape. From previous sections, the nano-precipitates are Nb-rich carbides. In order to simplify the problem, only Fe, Nb and C are considered in the nucleation system (Fe-Nb-C system). Therefore, the nano-precipitates are considered to be NbC. The precipitate nucleation rate is calculated based on the work by Dutta [167] in the following section.

a_0: lattice parameter of NbC, 4.4698×10^{-10} m;

a_{Fe}: lattice parameter of ferrite matrix, 2.8664×10^{-10} m;

A_C: atomic weight of C, 12.011 amu;

A_{Fe}: atomic weight of Fe, 55.85 amu;

A_{Nb}: atomic weight of Nb, 92.91 amu;

A_{NbC}: molecular weight of NbC, 104.921 amu;

b:	magnitude of burgers vector, 2.5×10^{-10} m; [12]
$[C]_{e:}$	wt% of C dissolved the ferrite under equilibrium condition;
C_{NbC}:	wt% of C present as NbC;
C_T:	wt% of C in the alloy;
D:	diffusion coefficient for Nb in ferrite at a given temperature;
$D_0(\alpha)$:	temperature-independent pre-exponential factor for Nb pipe diffusion in ferrite, 1.27×10^{-2} m^2/s; [33]
dN/dt:	nucleation rate of NbC in ferrite;
$f\rho$:	dislocation density factor, used to obtain the best fit between the experiments and predictions, $f\rho$ = 2.24; [167]
G:	shear modulus, 80.3 GPa; [12]
ΔG:	Overall change in free energy (nucleation activation energy), J;
$\Delta G_{dislocation}$:	dislocation core energy over the precipitate radius, (energy stored in the dislocation core), J;
ΔG_{volume}:	volume energy term in nucleation energy, J
$\Delta G_{surface}$:	surface energy term in nucleation energy, J
ΔG_{strain}:	misfit strain energy term in nucleation energy, J
ΔG_{ε}:	misfit strain energy per unit volume of the phase formed, J/m^3
ΔG_v:	chemical driving force for nucleation, i.e., free energy difference between the product and reactant phases, J/m^3;
ΔG^*:	critical free energy for nucleation, J;
K:	work hardening coefficient;
M':	Taylor factor, a measure of plastic deformation in crystal plasticity and a function of the lattice orientation [168], M'=3 for BCC and FCC materials; [12]
n':	work hardening index;
N:	number of precipitates per unit volume;

N_0: number of sites per unit volume for homogeneous or heterogeneous nucleation;

$N_{0\text{-}hom}$: number of sites per unit volume for homogeneous nucleation;

$N_{0\text{-}het}$: number of sites per unit volume for heterogeneous nucleation;

$[Nb]_{e:}$ wt% of Nb dissolved the ferrite under equilibrium conditions;

(NbC): wt% of NbC separated from the ferrite matrix;

Nb_{NbC}: wt% of Nb present as NbC;

Nb_T: wt% of Nb in the alloy;

Q(α): activation energy for Nb pipe diffusion in ferrite, 224000 J/mol.K; pipe diffusion is assumed because of the low ICT/CT and large dislocation densities; [33]

r: radius of spherical precipitate embryo;

R_g: universal gas constant, 8.314 J/mol.K;

R_c: critical nucleation radius;

T: temperature in Kelvin;

V_m: molar volume of NbC to precipitate, 1.34×10^{-5} m^3/mol;

X_C: instantaneous concentration of C in mol fraction;

X_C^e: equilibrium concentration of C in mol fraction at the specified temperature;

X_{Nb}: instantaneous concentration of Nb in mol fraction;

X_{Nb}^e: equilibrium concentration of Nb in mol fraction at the specified temperature; X_C^e and X_{Nb}^e can be determined from the solubility constants;

Z': Zeldovich factor, Z' is assumed to be 0.05; [167]

α: constant, 0.15; [167]

β': atomic impingement rate;

γ: surface energy of the precipitate per unit area, 0.5 J/m^2; [167]

ε:	true plastic strain;
δ:	zone misfit due to lattice parameter difference;
ρ:	dislocation density at the beginning of precipitation, m^{-2};
σ_{fl}:	flow strength, MPa;
σ_{ys}:	yield strength, MPa;
σ_{UT}:	ultimate tensile strength, MPa;
τ':	incubation time; small compared to the nucleation time and can be neglected. [167]

7-4-4-1. Precipitate formation following the stoichiometric ratio

In the microalloyed carbides and nitrides studied here, the elements always react in proportion to their relative atomic weight, which is known as the stoichiometric ratio. Using NbC as an example, Nb and C will always react in the ratio of their atomic weights A_{Nb} and A_C to form NbC, as shown in Figure 7-13. [12] This is an example using Grade100 steel. In this figure, point P shows the Nb and C alloy compositions as point P_4 and P_1, respectively. The lower line represents the stoichiometric ratio of Nb-C. This line is shifted upwards to intersect with point P. The intersection with the solubility curve gives the equilibrium concentration of Nb and C in the ICT in ferrite, indicated by points P_3 and P_2, respectively. This stoichiometric ratio relationship is also valid for precipitates formed in austenite.

$$[\mathrm{Nb}] + [\mathrm{C}] \leftrightarrow (\mathrm{NbC})$$

$$1 \text{ mole Nb} + 1 \text{ mole C} \leftrightarrow 1 \text{ mole NbC}$$

$$A_{Nb} + A_C \leftrightarrow A_{NbC}$$

This leads to

$$\frac{Nb_T - [\mathrm{Nb}]_e}{C_T - [\mathrm{C}]_e} = \frac{A_{Nb}}{A_C} \tag{7-9}$$

$$\frac{P_4 - P_3}{P_1 - P_2} = \frac{A_{Nb}}{A_C} \tag{7-10}$$

Therefore, the equilibrium concentrations of microalloying elements in ferrite can be determined from the solubility diagram. [12]

$$\begin{aligned} K_s &= [Nb]_e[C]_e \\ &= (Nb_T - Nb_{NbC})(C_T - C_{NbC}) \\ &= (Nb_T - Nb_{NbC})(C_T - Nb_{NbC} \cdot A_C / A_{Nb}) \end{aligned} \tag{7-11}$$

or

$$A_C (Nb_{NbC})^2 / A_{Nb} - (C_T + Nb_T \cdot A_C / A_{Nb})(Nb_{NbC}) + (Nb_T \cdot C_T - K_s) = 0 \tag{7-12}$$

The solution of the above quadratic equation is given by:

$$\mathrm{Nb}_{\mathrm{NbC}} = \frac{(C_T + Nb_T \times \frac{A_C}{A_{Nb}}) - \sqrt{(\mathrm{C}_T + \mathrm{Nb}_T \times \frac{A_C}{A_{Nb}})^2 - 4 \times \frac{A_C}{A_{Nb}} \times (\mathrm{C}_T \times Nb_T - \mathrm{K}_s)}}{2 \times \frac{A_C}{A_{Nb}}} \tag{7-13}$$

$$C_{NbC} = Nb_{NbC} \times \frac{A_C}{A_{Nb}} \tag{7-14}$$

The amount of microalloying elements dissolved in the matrix (equivalent concentrations) can then be determined as follows:

$$[\mathrm{Nb}]_e = \mathrm{Nb}_T - \mathrm{Nb}_{\mathrm{NbC}} \tag{7-15}$$

$$[\mathrm{C}]_e = \mathrm{C}_T - \mathrm{C}_{\mathrm{NbC}} \tag{7-16}$$

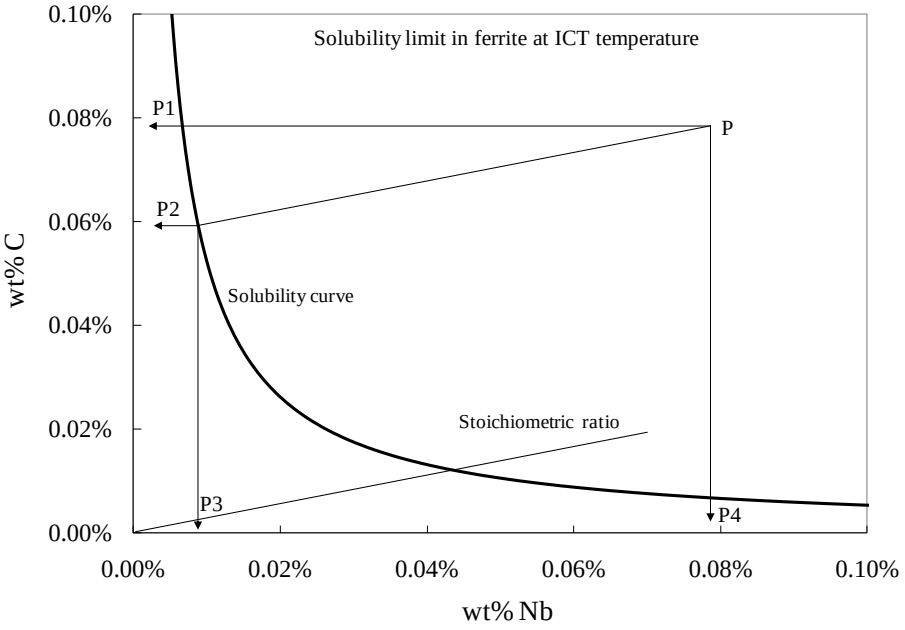

Figure 7-13 Solubility diagram, for Grade 100 steel at ICT temperature, showing the stoichiometric ratio between Nb and C in ferrite.

7-4-4-2. Free energy for precipitate nucleation

7-4-4-2-1. Free energy for homogeneous nucleation

Precipitate nucleation free energy can be determined based on classical nucleation theory. For homogeneous nucleation, the overall change in free energy ΔG for a spherical embryo of radius *r* is: [169]

$$\Delta G = \Delta G_{volume} + \Delta G_{surface} + \Delta G_{strain} = \frac{4}{3}\pi r^3 \Delta G_v + 4\pi r^2 \gamma + \frac{4}{3}\pi r^3 \Delta G_\varepsilon \qquad (7\text{-}17)$$

There are three terms in equation (7-17). The first term ($\Delta G_{volume} = \frac{4}{3}\pi r^3 \Delta G_v$) is the volume energy term that represents the energy associated with the formation of a precipitate of a given volume. The driving force ΔG_v, also called the chemical free energy arising from the chemical supersaturation of the solutes, is given in equation (7-18). It is always negative if precipitation is feasible, i.e., $X_{Nb}X_C > X^e_{Nb}X^e_C$ if precipitation occurs.

$$\Delta G_v = -\frac{R_g T}{V_m} \ln\left(\frac{X_{Nb}X_C}{X^e_{Nb}X^e_C}\right) \qquad (7\text{-}18)$$

The second term ($\Delta G_{surface} = 4\pi r^2 \gamma$) in equation (7-17) represents the surface energy of the forming precipitate. It is also referred to as the interfacial free energy to create the precipitate/matrix interface. It is always positive.

The third term ($\Delta G_{strain} = \frac{4}{3}\pi r^3 \Delta G_\varepsilon$) is the misfit strain energy. There will be strain in the ferrite matrix due to the difference in volume occupied by the precipitate compared with the matrix. It is always positive. ΔG_ε is a function of δ (zone misfit due to lattice parameter differences). Ferrite has BCC structure and there are two Fe atoms in one unit cell. Nano-precipitates have NaCl-FCC structure and there are 4 Nb atoms and 4 C atoms in one unit cell. The C atoms occupy the interstitial positions. Therefore, the lattice parameter for nano-precipitates is normalized in the zone misfit and the misfit strain energy can be expressed in equation (7-19).

$$\Delta G_{strain} = \frac{4}{3}\pi r^3 \Delta G_\varepsilon = \frac{4}{3}\pi r^3 (4G\delta^2) = \frac{16}{3}\pi r^3 G\left(\frac{\frac{a_0}{2} - a_{Fe}}{a_{Fe}}\right)^2 \qquad (7\text{-}19)$$

Figure 7-14 shows the free energy changes with the nucleation of a spherical nucleus of radius *r*. The volume free energy (ΔG_{volume}) is negative, which reduces the free energy, while the surface ($\Delta G_{surface}$) and strain energy (ΔG_{strain}) are positive. The resultant free energy change increases to a maximum at a critical value of R_c. ΔG^* is the critical free energy for the formation of a critical nucleus R_c.

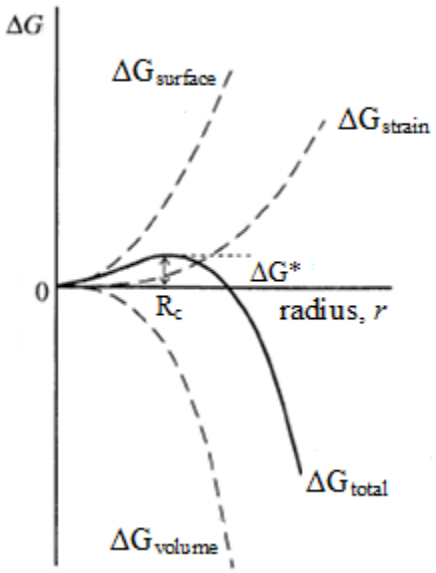

Figure 7-14 The free energy changes with the nucleation of a spherical nucleus of radius *r*.

Differentiation of equation (7-17) with respect to *r* and letting $\frac{\partial(\Delta G)}{\partial r} = 0$ gives

$$\frac{\partial(\Delta G)}{\partial r} = 4\pi r^2(\Delta G_v + \Delta G_\varepsilon) + 8\pi r\gamma = 0 \qquad (7\text{-}20)$$

Therefore, the critical nucleus size R_c for homogeneous nucleation can be solved from equation (7-20) and given as

$$R_c = \frac{-2\gamma}{(\Delta G_v + \Delta G_\varepsilon)} \qquad (7\text{-}21)$$

Therefore, the critical nucleation energy ΔG^* for homogeneous nucleation is shown in equation (7-22).

$$\Delta G^* = \frac{4}{3}\pi R_c^3(\Delta G_v + \Delta G_\varepsilon) + 4\pi R_c^2\gamma$$
$$= \frac{4}{3}\pi\left(\frac{-2\gamma}{\Delta G_v + \Delta G_\varepsilon}\right)^3(\Delta G_v + \Delta G_\varepsilon) + 4\pi\left(\frac{-2\gamma}{\Delta G_v + \Delta G_\varepsilon}\right)^2\gamma \qquad (7\text{-}22)$$
$$= \frac{16}{3}\frac{\pi\gamma^3}{\left(\Delta G_v + 4G\left(\frac{\frac{a_0}{2} - a_{Fe}}{a_{Fe}}\right)^2\right)^2}$$

7-4-4-2-2. Free energy for heterogeneous nucleation at dislocations

For nucleation at dislocations, the overall change in free energy ΔG for a spherical nucleus of radius r is:

$$\Delta G = \frac{4}{3}\pi r^3\Delta G_v + 4\pi r^2\gamma + \frac{4}{3}\pi r^3\Delta G_\varepsilon + \Delta G_{dislocation} \qquad (7\text{-}23)$$

Similar to the terms in equation (7-17), the first term ($\frac{4}{3}\pi r^3\Delta G_v$), the second term ($4\pi r^2\gamma$) and the third term ($\frac{4}{3}\pi r^3\Delta G_\varepsilon$) in equation (7-23) represent the free energy associated with the formation of a precipitate of a given volume, the surface energy of the precipitate and the misfit strain energy, respectively.

$\Delta G_{dislocation}$ in equation (7-23) is the dislocation core energy over the radius of the nucleating precipitate and is given as:

$$\Delta G_{dislocation} = -0.4Gb^2r \qquad (7\text{-}24)$$

Therefore, equation (7-23) becomes to equation (7-25).

$$\Delta G = \frac{4}{3}\pi r^3\Delta G_v + 4\pi r^2\gamma + \frac{4}{3}\pi r^3\Delta G_\varepsilon - 0.4Gb^2r \qquad (7\text{-}25)$$

Differentiation of equation (7-25) with respect to *r* and setting $\frac{\partial(\Delta G)}{\partial r} = 0$ gives

$$\frac{\partial(\Delta G)}{\partial r} = 4\pi r^2(\Delta G_v + \Delta G_\varepsilon) + 8\pi r\gamma - 0.4Gb^2 = 0 \qquad (7\text{-}26)$$

The critical nucleus size R_c can be solved from the following quadratic equation.

$$R_c = \frac{-8\pi\gamma + \sqrt{(8\pi\gamma)^2 - 4\times 4\pi(\Delta G_v + \Delta G_\varepsilon)(-0.4Gb^2)}}{2\times 4\pi(\Delta G_v + \Delta G_\varepsilon)}$$

$$= \frac{-\pi\gamma + \sqrt{(\pi\gamma)^2 + 0.1\pi Gb^2(\Delta G_v + \Delta G_\varepsilon)}}{\pi(\Delta G_v + \Delta G_\varepsilon)} \qquad (7\text{-}27)$$

Therefore, the critical nucleation energy ΔG^* for heterogeneous nucleation at dislocations is shown in equation (7-28).

$$\Delta G^* = \frac{4}{3}\pi R_c^3(\Delta G_v + \Delta G_\varepsilon) + 4\pi R_c^2\gamma - 0.4Gb^2R_c$$

$$= \frac{4}{3}\pi\left(\frac{-\pi\gamma + \sqrt{(\pi\gamma)^2 + 0.1\pi Gb^2(\Delta G_v + \Delta G_\varepsilon)}}{\pi(\Delta G_v + \Delta G_\varepsilon)}\right)^3(\Delta G_v + \Delta G_\varepsilon)$$
$$+ 4\pi\left(\frac{-\pi\gamma + \sqrt{(\pi\gamma)^2 + 0.1\pi Gb^2(\Delta G_v + \Delta G_\varepsilon)}}{\pi(\Delta G_v + \Delta G_\varepsilon)}\right)^2\gamma$$
$$- 0.4Gb^2\left(\frac{-\pi\gamma + \sqrt{(\pi\gamma)^2 + 0.1\pi Gb^2(\Delta G_v + \Delta G_\varepsilon)}}{\pi(\Delta G_v + \Delta G_\varepsilon)}\right) \qquad (7\text{-}28)$$

7-4-4-3. Precipitate nucleation rate

The precipitate nucleation rate can be expressed by equation (7-29):

$$dN/dt = N_0 Z'\beta'\exp(-\frac{\Delta G^*}{R_g T})\exp(-\frac{\tau'}{t}) \qquad (7\text{-}29)$$

The incubation time, τ', is quite small compared to the nucleation time and is assumed to be zero in this calculation. [167] Therefore, equation (7-29) is simplified as equation (7-30):

$$dN/dt = N_0 Z'\beta'\exp(-\frac{\Delta G^*}{R_g T}) \qquad (7\text{-}30)$$

For homogeneous nucleation, $N_{0\text{-}hom}$ *is* the number of lattice sites per unit volume of steel. It can be calculated for ferrite as:

$$N_{0-\hom} = 2/a_{Fe}{}^3 = 2/(0.28664\times 10^{-9})^3 = 8.49\times 10^{28}\ /\mathrm{m}^3 \qquad (7\text{-}31)$$

For heterogeneous nucleation, N_0 can be estimated as:

$$N_{0-het} = 0.5\rho^{1.5} \tag{7-32}$$

The dislocation density ρ can be calculated as

$$\rho = \left(\frac{\sigma_{fl} - \sigma_{ys}}{M'\alpha Gb} f_{\rho} \right)^2 \tag{7-33}$$

The flow strength, σ_{fl}, can be determined from equation (7-34) or (7-35). Equation (7-35) is typically used to estimate the flow strength of engineering materials, and is used here. [170]

$$\sigma_{fl} = K\varepsilon^{n'} \tag{7-34}$$

$$\sigma_{fl} = 0.5(\sigma_{ys} + \sigma_{UT}) \tag{7-35}$$

The atomic impingement rate β' can be expressed by equation (7-36), where the diffusion coefficient of Nb is used because C diffuses much faster, so Nb diffusion will be rate controlling. Because of the high dislocation density in these steels and the low CT/ICT (<0.5 of the absolute melting temperature of the steel), pipe diffusion is assumed to be predominant. The diffusion coefficient of Nb can be estimated from equation (7-37).

$$\beta' = \frac{4\pi R_c^2 DX_{Nb}}{a_{Fe}^4} \tag{7-36}$$

$$D = D_0 \exp(-\frac{Q}{R_g T}) \tag{7-37}$$

7-4-4-4. Critical nucleation energy for nano-precipitate for X70, X80 and Grade100 steels

7-4-4-4-1. Critical free energy determination from classical nucleation theory

The critical nucleation free energy ΔG* can be determined from classical nucleation theory. For homogeneous nucleation, ΔG* can be calculated from equation (7-22), where the chemical driving force per unit volume (ΔG_v) and the misfit strain energy per unit volume (ΔG_ε) need to be known. They can be determined from equations (7-18) and (7-19), respectively. In order to determine ΔG_v, the initial concentrations of Nb and C in ferrite are determined, as shown in Table 7-5. The Nb concentrations were obtained from the amount of Nb in the

nano-precipitates plus the Nb in the supernatant. This represents the amount of Nb dissolved in ferrite after precipitation of all the precipitates with the exception of the finest ones (nano-precipitates). The latter was determined from ICP analysis of the supernatant. The initial concentrations of C in ferrite were determined from the total C content in the steel minus the amount that reacted with Nb according to the stoichiometric ratio of Nb-C. The equilibrium concentrations of Nb and C in ferrite are shown in Table 7-6. They were determined from equations (7-9) to (7-16) as well as the solubility products at the coiling temperatures for the different steels. The solubility equation for NbC in ferrite is shown in equation (7-38) [12], from which the solubility product K_s can be obtained, and was used to determine the equilibrium concentrations of Nb and C in ferrite at their coiling or interrupted cooling temperatures. Equations (7-39) and (7-40) show the conversion from wt% to mole fractions for the initial Nb and C concentrations, respectively. The equilibrium mole fractions for Nb and C were obtained similarly.

$$\log K_s(\alpha) = \log[Nb]_e[C]_e = A - C/T = 3.9 - 9930/T \tag{7-38}$$

$$X_{Nb} = \frac{\dfrac{\text{wt\% Nb}}{\text{A}_{\text{Nb}}}}{\dfrac{\text{wt\% Nb}}{\text{A}_{\text{Nb}}} + \dfrac{\text{wt\% C}}{\text{A}_{\text{C}}} + \dfrac{(100 - \text{wt\% Nb - wt\% C})}{\text{A}_{\text{Fe}}}} \tag{7-39}$$

$$X_C = \frac{\dfrac{\text{wt\% C}}{\text{A}_{\text{C}}}}{\dfrac{\text{wt\% Nb}}{\text{A}_{\text{Nb}}} + \dfrac{\text{wt\% C}}{\text{A}_{\text{C}}} + \dfrac{(100 - \text{wt\% Nb - wt\% C})}{\text{A}_{\text{Fe}}}} \tag{7-40}$$

Table 7-5 Initial concentrations of Nb and C in ferrite before nano-precipitates formation for different steels

Steel	wt% Nb	wt% C	X_{Nb}	X_C
X70-564	0.059	0.039	3.57×10^{-4}	1.83×10^{-3}
X80-462	0.087	0.028	5.22×10^{-4}	1.31×10^{-3}
X80-A4B	0.080	0.033	4.81×10^{-4}	1.53×10^{-3}
X80-B4F	0.077	0.051	4.62×10^{-4}	2.35×10^{-3}
X80-A4F	0.032	0.050	1.91×10^{-4}	2.33×10^{-3}
Grade100	0.076	0.078	4.55×10^{-4}	3.61×10^{-3}

Table 7-6 Equilibrium concentrations of Nb and C in ferrite at the coiling or interrupted cooling temperatures for different steels

Steel	$[Nb]_e$	$[C]_e$	X_{Nb}^e	X_C^e
X70-564	7.36×10^{-7}	0.032	4.42×10^{-9}	1.47×10^{-3}
X80-462	1.38×10^{-6}	0.017	8.29×10^{-9}	7.84×10^{-4}
X80-A4B	1.36×10^{-7}	0.023	8.19×10^{-10}	1.05×10^{-3}
X80-B4F	2.85×10^{-7}	0.041	1.71×10^{-9}	1.89×10^{-3}
X80-A4F	3.58×10^{-8}	0.046	2.15×10^{-10}	2.14×10^{-3}
Grade100	7.66×10^{-7}	0.068	4.60×10^{-9}	3.16×10^{-3}

ΔG_v is about -6.5×10^9 J/m^3 for the X70-564, X80 and Grade100 steels, while ΔG_ε is about 1.6×10^{10} J/m^3 for all the steels. Clearly, the strain energy is larger in magnitude than the available driving force, so no homogeneous nucleation would be expected.

For heterogeneous nucleation, the critical nucleus size and the critical nucleation energy of NbC in ferrite for heterogeneous nucleation are calculated from equations (7-23) to (7-28) and the data are shown in Table 7-7. The critical nucleus size is quite small, about 0.09 nm, which means that the nucleus is about 1/20 the volume of a NbC unit cell. The critical nucleation energy ΔG^* is about 45 kJ/mol for all the steels at their CT/ICT temperatures.

Table 7-7 Number of nucleation sites, dislocation density and critical free energy for heterogeneous nucleation

Steel	Normalized CT/ICT	ΔG_v (kJ/m^3)	ΔG_ε (kJ/ m^3)	Rc (nm)	ΔG^* (kJ/mol)
X70-564	1.04	-6.15×10^9	1.56×10^{10}	0.09	44.90
X80-462	1.04	-6.18×10^9		0.09	44.94
X80-A4B	0.93	-6.78×10^9		0.09	46.08
X80-B4F	1.00	-6.62×10^9		0.09	45.77
X80-A4F	0.90	-6.70×10^9		0.09	45.91
Grade100	1.09	-6.41×10^9		0.09	45.38

In the above section, the critical nucleation free energy ΔG* of NbC was determined from classical nucleation theory under Fe-Nb-C system using equation 7-28. In the real condition, certain amounts of Mo replace some of Nb atoms (refer to Table 4-10, Table 4-11 and Table 5-9) and show up in the nano-precipitates. In Grade100 steel, the composition of the nano-precipitates is more complex, i.e., $Nb_{0.48}Mo_{0.28}Ti_{0.21}V_{0.03}C$. From equation 7-28, there are four terms in ΔG*. They are $(\frac{4}{3}\pi r^3\Delta G_v)$, $(4\pi r^2\gamma)$, $(\frac{4}{3}\pi r^3\Delta G_\varepsilon)$ and $\Delta G_{dislocation}$. The terms, $(4\pi r^2\gamma)$ and $\Delta G_{dislocation}$ are the same whether Mo is considered or not. The term $(\frac{4}{3}\pi r^3\Delta G_\varepsilon)$ exhibits almost no change since the lattice parameter of NbC is very close to that of Nb(Mo)C. Thus, $(\frac{4}{3}\pi r^3\Delta G_v)$ is the only parameter that could appreciably change. ΔG_v is expressed by equation 7-18 and it is related to the equilibrium concentrations of all the elements in the nano-precipitates. The equilibrium concentrations of these elements can be calculated from the solubility product. However, the solubility product for these complex precipitates is lacking in the literature. If it is assumed that the nano-precipitates have the same solubility as NbC, the deviation of ΔG_v (and thus ΔG*) for the complex carbides will be given by the change in the molar volume of the nano-precipitates (V_m) in the ΔG_v equation (equation 7-18). Thus ΔG* for the complex carbide for Grade100 steel

will be about 1.3% higher than it is for simple NbC. A similar value can be shown for the X70 and X80 steels in Table 7-8.

Table 7-8 Critical free energy for nano-precipitates nucleation in X70, X80 and Grade 100 steels

Steel	Nano-precipitates	Vm (m^3/mol)	ΔG_v (kJ/m^3)	ΔG^* (kJ/mol)	% change
X70-564	$Nb_{0.58}Mo_{0.42}C$	1.28×10^{-5}	-6.46×10^{9}	45.47	1.3%
X80-462	$Nb_{0.8}Mo_{0.2}C$	1.32×10^{-5}	-6.27×10^{9}	45.11	0.4%
X80-A4B	$Nb_{0.68}Mo_{0.32}C$	1.30×10^{-5}	-6.99×10^{9}	46.49	0.9%
X80-B4F	$Nb_{0.78}Mo_{0.22}C$	1.32×10^{-5}	-6.72×10^{9}	45.97	0.4%
X80-A4F	$Nb_{0.74}Mo_{0.26}C$	1.31×10^{-5}	-6.85×10^{9}	46.21	0.7%
Grade100	$Nb_{0.48}Mo_{0.28}Ti_{0.21}V_{0.03}C$	1.28×10^{-5}	-6.73×10^{9}	45.99	1.3%

7-4-4-4-2. Critical free energy determination from experimental results

The critical nucleation energy can be back-calculated using precipitate volume fractions determined experimentally.

Nucleation rates for X70, X80 and Grade100 nano-precipitates were calculated based on the experimental results and Rietveld refinement. Table 7-9 shows the precipitate nucleation rates (*dN/dt*) for different steels. The precipitate sizes and volume fractions of the nano-precipitates in Table 7-9 were determined from TEM and Rietveld refinement, respectively. A nucleation time of one hour, based on reference [171], and spherical precipitates were assumed. The precipitate nucleation rate was estimated according to equation (7-41). The other calculations in Table 7-9 will be presented in the following paragraphs. A comparison of nucleation rates for different steels is shown in Figure 7-15. The nucleation rate increases with increasing CT/ICT temperature for the steels in the current study. This may explain the lack of nano-precipitates in the X100 steels because of their low ICT (about or less than 450 ºC).

Assuming the nano-precipitates (≤10 nm) are spherical with radius *r*, the volume of one nano-precipitate can be calculated as

$$Vol_{single} = \frac{4\pi r^3}{3} = \frac{4\pi\left(\frac{X}{2}\right)^3}{3} \quad (7\text{-}7)$$

r: radius of nano-precipitates (≤10 nm) with the largest number distribution obtained by TEM DF imaging;

X: diameter of nano-precipitates with the largest number distribution (nm).

The total volume of the nano-precipitates (Vol_{ppt}) in 1 unit volume of steel was determined from the experimental extractions and Rietveld refinement and is defined as the volume fraction. Therefore, the number of precipitates per m^3 of steel can be calculated as

$$\#density = \frac{Vol_{ppt}}{Vol_{single}} \quad (7\text{-}8)$$

Vol_{single} in equation (7-8) is the volume of one nano-precipitate determined by equation (7-7). If the nucleation time is assumed to be 1 hour, the nucleation rate dN/dt can be obtained.

$$dN/dt = \frac{\#density}{3600s} \quad (7\text{-}41)$$

If the nano-precipitates are evenly distributed in the ferrite matrix, the precipitate spacing (L) can be estimated. Assuming that the precipitates are uniformly distributed in the ferrite, the average matrix volume containing one precipitate can be calculated by taking the inverse of the number of precipitates per m^3. Assuming this volume is cubic, the distance between precipitates is the length of the side of the cube holding one precipitate. The precipitate spacings for different steels are shown in Table 7-9; these values agree reasonably well with TEM observations (Figure 4-20, Figure 4-21 and Figure 5-12).

$$L = \left(\frac{Vol_{single}}{Vol_{ppt}}\right)^{\frac{1}{3}} \quad (7\text{-}42)$$

Table 7-9 Nucleation rate (dN/dt) calculations for different steels

Steel	X70-564	X80				Grade100
		462	A4B	B4F	A4F	
X (nm)	5	5	5	4.5	4	4.5
Vol_{single} (m^3)	6.54×10^{-26}	6.54×10^{-26}	6.54×10^{-26}	4.77×10^{-26}	3.35×10^{-26}	4.77E-26
Vol_{ppt}	0.087%	0.116%	0.104%	0.114%	0.035%	0.166%
# density	1.33×10^{22}	1.77×10^{22}	1.59×10^{22}	2.39×10^{22}	1.04×10^{22}	3.48E+22
Nucleation time (s)	3600					
dN/dt (number/(m^3.s))	3.69×10^{18}	4.91×10^{18}	4.41×10^{18}	6.64×10^{18}	2.88×10^{18}	9.66×10^{18}
L (nm)	42	38	40	35	46	31

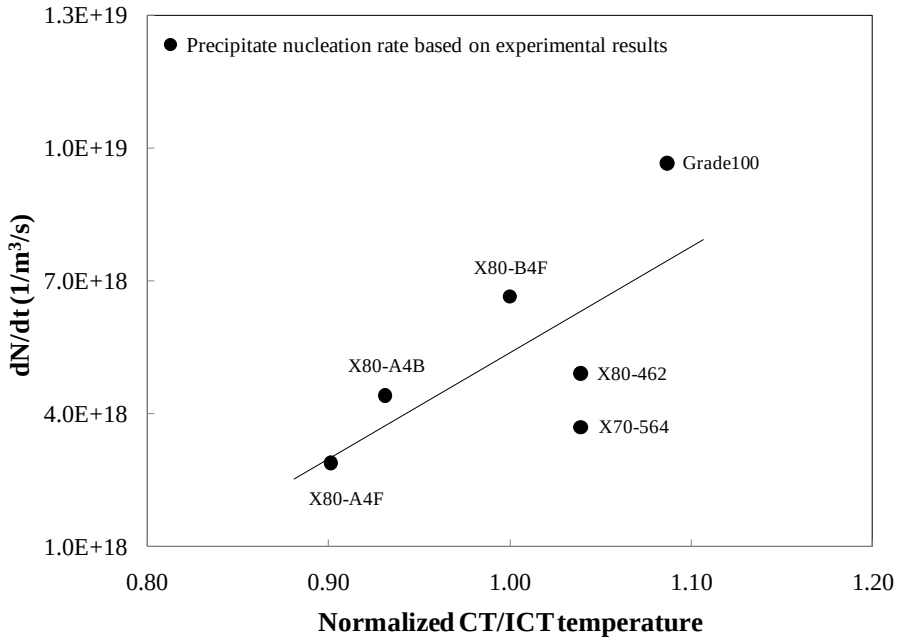

Figure 7-15 Precipitate nucleation rate (dN/dt) for different steels.

As mentioned previously, the precipitate nucleation rate can be expressed by equation (7-30):

$$dN/dt = N_0 Z' \beta' \exp(-\frac{\Delta G^*}{R_g T}) \tag{7-30}$$

If ln (dN/dt) is plotted against 1/T, the above equation becomes

$$\ln(dN/dt) = -\frac{\Delta G^*}{R_g T} + \ln(N_0 Z' \beta') \tag{7-43}$$

The critical nucleation energy can be estimated from the slope of the above plot (ln (dN/dt) against 1/T) according to equation (7-44).

$$\Delta G^* = -R_g \times (slope) \tag{7-44}$$

Figure 7-16 shows the relationship between ln (*dN/dt*) and 1/T from experimental results for X70, X80 and Grade100 steels. The data was fit to a linear equation in order to determine a critical nucleation energy. The fit was not particularly good (square of the correlation coefficient R^2 = 0.5), but the data provided an estimate of the critical nucleation energy.

$$\ln(dN/dt) = -5222.3/T+49.3 \tag{7-45}$$

The average critical nucleation energy ΔG* is estimated as

$$-R_g \times (-5222.3) = -8.314 \times (-5222.3) = 43.4 \text{ kJ/mol}$$

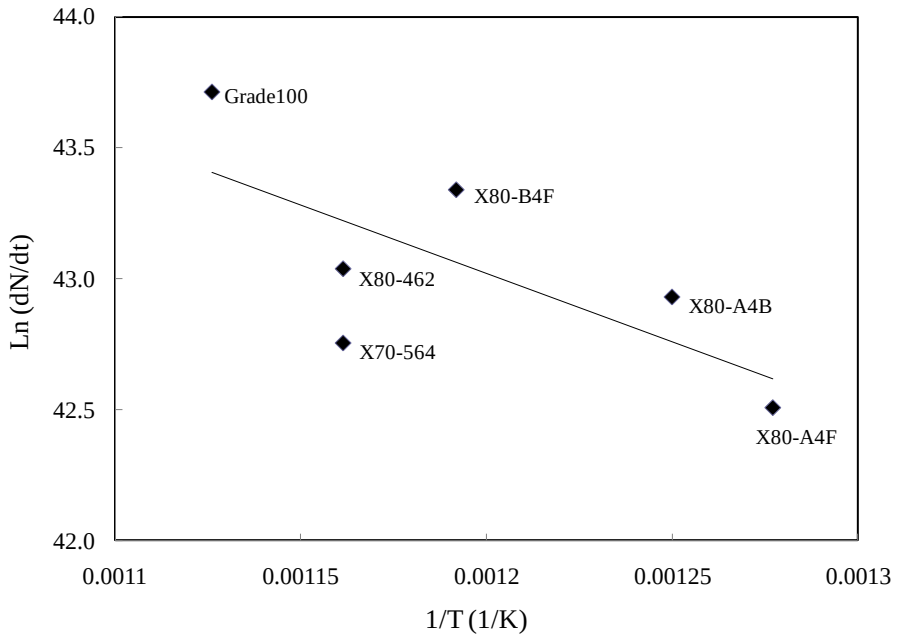

Figure 7-16 Critical free energy calculated from experimental nucleation rates. $\ln(dN/dt) = -5222.3/T+49.3$; $R^2 = 0.5$.

The experimentally determined average critical nucleation energy (43.4 kJ/mol from equation (7-44)) was compared with the calculated values for heterogeneous nucleation in the previous section (Table 7-7). The agreement is quite good and indicates that nucleation likely occurs heterogeneously on dislocations. In addition, the above activation energy is in the same order of

magnitude as that being reported for precipitate nucleation at dislocations in Al alloys (between 15 - 25 kJ/mol). [172]

7-5. Superposition of strengthening mechanisms

7-5-1. Strengthening component due to grain refinement

Based on the grain sizes of the steels, Figure 7-17 shows the relationship between the yield strength and the inverse square root of mean linear intercept, i.e. $(m.l.i.)^{-1/2}$. There is reasonable agreement with the Hall-Petch equation. Grade100 and X100-2B appear to be outliers compared with the other steels. Grade100 is a structural steel with higher C levels and other alloying elements. The strengthening mechanism is a little different from other steels, i.e., it has a higher precipitation strengthening effect and this will be discussed in Section 7-5-3. For X100-2B steel, the errors may be related to the grain size measurement. As grains are refined (X100 steels have pretty close grain size and are finer than other steels), it is difficult to determine the number of grains, which is directly related to *m.l.i.*

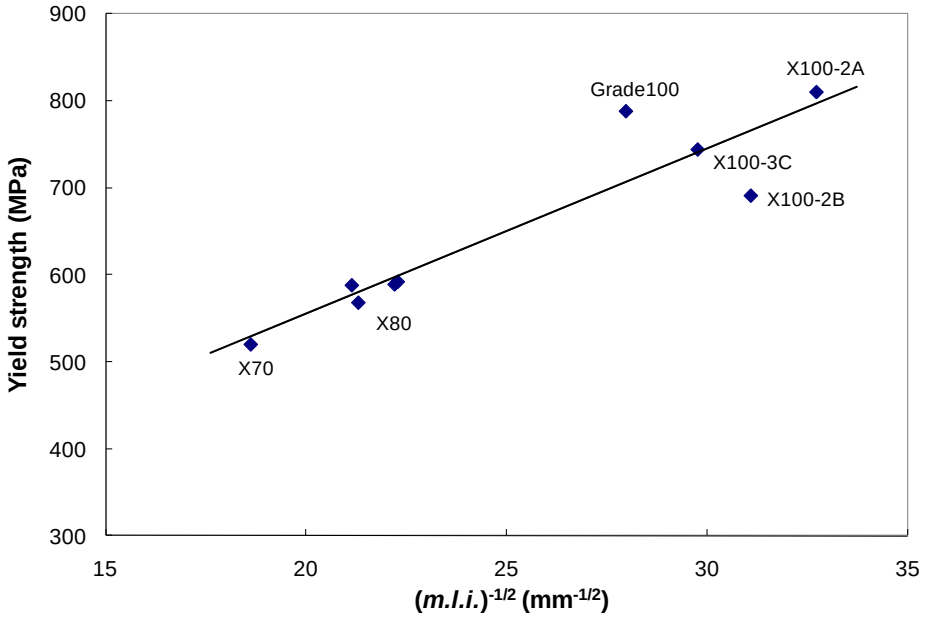

Figure 7-17 Relationship between yield strength and mean linear intercept for steels studied.

Yield strength = 19.0× $(m.l.i.)^{-1/2}$+175.1

The strengthening contribution due to grain size was calculated according to equation (2-7). Table 7-10 presents the value for k_y' used in the above calculation and the grain size strengthening component for all steels. From Table 7-10, the grain size strengthening component is between 336.9 and 592.4 MPa for the steels studied. X70-564 steel has the largest grain size and the lowest grain size strengthening effect. Alternatively, the X100 steels have the smallest grain sizes and they have the strongest grain size strengthening effects. It should be noted that grain refinement is good for both yield strength and toughness. Grain refinement is the only strengthening mechanism that does not decrease toughness.

$$\sigma_{gb} = k_y d^{-1/2} = k_y'(m.l.i.)^{-1/2} \quad (2\text{-}7)$$

σ_{gb}: grain boundary strengthening;

k_y: strengthening coefficient when grain size (d) is used;

k_y': strengthening coefficient when mean linear intercept (*m.l.i.*) is used.

Table 7-10 Grain size strengthening in steels

Steel	k_y' (MPa.mm$^{1/2}$)	*m.l.i.* (μm)	Grain size strengthening (σ_{gb}) (MPa)
Grade100	17.5-19.2 [63]	2.18	506.4
X70-564		2.89	336.9
X80-462		2.24	382.6
X80-A4B		2.20	385.5
X80-B4F		2.01	403.3
X80-A4F		2.03	401.9
X100-2A		0.93	592.4
X100-2B		1.03	562.8
X100-3C		1.13	538.8

If precipitation strengthening is not considered, the relationship between $\sigma_i + \sigma_{ss} + \sigma_{gb}$ and $(m.l.i.)^{-1/2}$, is shown in Figure 7-18. It agrees very well with the Hall-Petch equation. The slope of the fitting line is 17.1 MPa.mm$^{1/2}$. The individual

strengthening components (σ_i and σ_{ss}) and the superposition of different strengthening mechanisms will be discussed in the following sections.

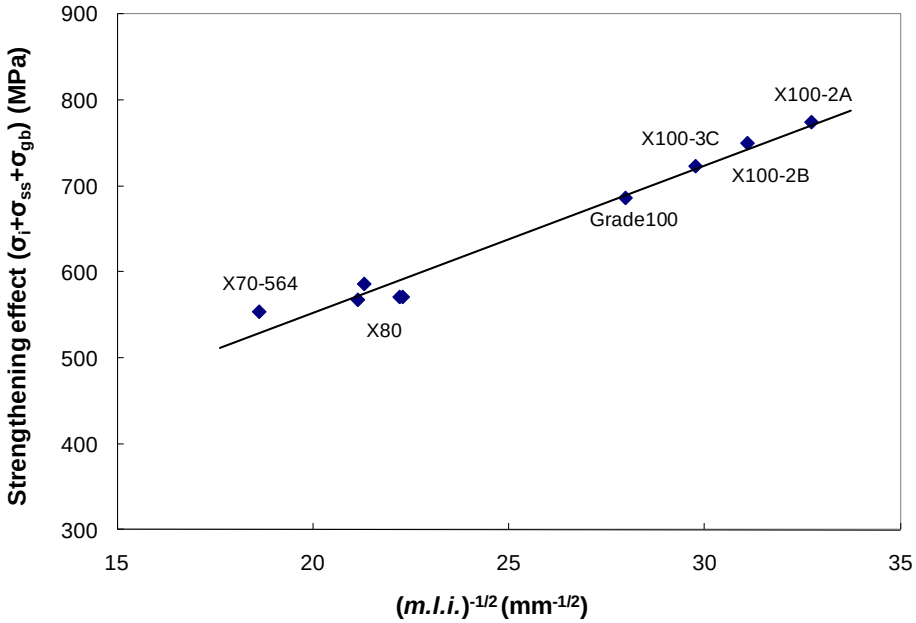

Figure 7-18 Relationship between strengthening effect ($\sigma_i+\sigma_{gb}+\sigma_{ss}$) and mean linear intercept for steels studied.

$$\sigma_i+\sigma_{ss}+\sigma_{gb} = 17.1\times (m.l.i.)^{-1/2}+210.6$$

7-5-2. Strengthening component due to solid solution strengthening

The concentrations of the elements present in the supernatant correspond to those dissolved in solid solution in the ferrite. They were analyzed by ICP analysis and include Si, Mn, Cu, Mo, Ni, Cr, Ti and Nb. Based on the solubilities of C and N, 0.005wt% of C [16] and 0.01wt% of N contribute to solid solution strengthening. Here, supersaturation, especially for C, is not considered. However, supersaturation is a possiblility to occur. Therefore, the following calculation about solid solution strengthening is a lower bound solution.

Table 7-11 shows the solid strengthening coefficients and the wt% of each element in solution. [65,63,68,69,70] The solid solution strengthening was determined according to equation (2-9) with the results shown in Table 7-11 as

well for all steels. The solid solution strengthening component is between 115 and 163 MPa for the steels being studied.

$$\sigma_{ss} = \sum k_i C_i \tag{2-9}$$

Table 7-11 Solid solution strengthening in steels

Solute		C	N	Si	Mn	Cu	Mo	Ni	Cr	Ti	Nb
k_i (MPa)		5082	5082	83	31.5	39	11	0	-31	80	2400
Grade 100	Wt% [1]	0.005	0.0058	0.021	1.541	0.4	0.257	0.259	0.177	0.014	0.003
	σ_{ss} (MPa)	125.7									
X70-564	Wt% [1]	0.005	0.01	0.029	1.341	0.229	0.159	0.116	0.048	0.018	0.013
	σ_{ss} (MPa)	163.0									
X80-462	Wt% [1]	0.005	0.0062	0.019	1.635	0.27	0.273	0.13	0.05	0.007	0.004
	σ_{ss} (MPa)	131.2									
X80-A4B	Wt% [1]	0.005	0.0033	0.017	1.595	0.34	0.271	0.25	0.07	0.002	0.016
	σ_{ss} (MPa)	146.7									
X80-B4F	Wt% [1]	0.005	0.0037	0.017	1.563	0.15	0.273	0.41	0.06	0.003	0.005
	σ_{ss} (MPa)	113.8									
X80-A4F	Wt% [1]	0.005	0.001	0.014	1.704	0.15	0.394	0.41	0.08	0.004	0.009
	σ_{ss} (MPa)	115.2									
X100-2A	Wt% [1]	0.005	0.001	0.02	1.726	0.326	0.407	0.47	0.161	0.007	0.012
	σ_{ss} (MPa)	127.6									
X100-2B	Wt% [1]	0.005	0.0029	0.021	1.728	0.16	0.399	0.439	0.158	0.004	0.013
	σ_{ss} (MPa)	132.8									
X100-3C	Wt% [1]	0.005	0.0029	0.019	1.762	0.15	0.397	0.4	0.163	0.001	0.012
	σ_{ss} (MPa)	130.1									

Note:

[1]: Wt% of element in solid solution.

7-5-3. Strengthening component due to precipitation effects

Precipitation strengthening is calculated according to equation (2-22), which is based on Orowan looping. Orowan looping usually occurs for precipitates a few nanometers in size. However, direct evidence of the Orowan looping is lacking due to difficulties in observing such fine precipitates. [12] Table 7-12 shows the precipitation strengthening contribution for all the steels studied. For X70, X80 and Grade100 steels, nano-precipitates (mainly ≤10 nm) were identified. The

volume fraction and the nano-precipitate diameter with the largest number distribution were used in the calculations. For the X70, X80 and Grade100 steels, precipitation strengthening due to these nano-precipitates is between 90 and 195 MPa. The Grade100 steel has the highest volume fraction of nano-precipitates; therefore, it has the highest precipitation strengthening effect. Alternatively, X80-A4F has the lowest value of precipitation strengthening. There is no precipitation strengthening effect due to nano-precipitates (≤10 nm) in X100 steels because of the lack of nano-precipitates.

$$\sigma_{ppt} = \left(\frac{10.8 f_v^{1/2}}{X} \right) \ln \left(\frac{X}{6.125 \times 10^{-4}} \right) \tag{2-22}$$

Table 7-12 Precipitation strengthening in steels due to nano-precipitates (≤10 nm)

Steel	Volume fraction (f_v), vol %	Diameter with the largest number distribution (nm)	Precipitation strengthening (σ_{ppt}) (MPa)
Grade100	0.166	4.5	195.0
X70-564	0.087	5	133.8
X80-462	0.116	5	154.2
X80-A4B	0.104	5	146.1
X80-B4F	0.114	4.5	161.7
X80-A4F	0.034	4	93.3
X100-2A	0	-	-
X100-2B	0	-	-
X100-3C	0	-	-

In addition to the nano-precipitates (mainly ≤10 nm), precipitates larger than 10 nm were also identified in the above steels. According to the volume fraction and size of these precipitates, (Table 4-9 and Table 4-11 for Grade100 steel, Table 5-9 and Table 5-11 for X70 and X80 steels, Table 6-5, Table 6-6 and Table 6-8 for X100 steels) precipitation strengthening (for particles larger than 10 nm and less than 50 nm) can also be calculated using equation (2-22), as shown in Table 7-13. For X70, X80 and Grade100 steels, nano-precipitates (mainly ≤10 nm) contribute to precipitation strengthening. For X100 steels, the precipitation strengthening contribution is much less compared to other strengthening

mechanisms. Table 7-13 also indicates that the potential effect of the 2nd smallest precipitates (10-50 nm) was not significant.

Based on the data in Table 7-10, Table 7-11 and Table 7-12, the strengthening contribution due to the different mechanisms are summarized in Table 7-13. The lattice friction stress of iron (σ_i) is included as well. [12] Superposition of the different strengthening mechanisms and comparison with the measured values will be explained in the next section.

Table 7-13 Strengthening contributions from different mechanisms in steels - 4 contributions

Steels	Strengthening contribution (MPa)						Actual yield strength (MPa)
	σ_i	σ_{ss}	σ_{gb}	σ_{ppt}			
				≤10 nm	10-50 nm	total	
Grade100	54	125.7	506.4	195.0	0	195.0	788
X70-564	54	163.0	336.9	133.8	17.0	150.8	520
X80-462	54	131.2	382.6	154.2	0	154.2	588
X80-A4B	54	146.7	385.5	146.1	0	146.1	568
X80-B4F	54	113.8	403.3	161.7	0	161.7	592
X80-A4F	54	115.2	401.9	93.3	33.8	127.1	589
X100-2A	54	127.6	592.4	0	39.1	39.1	810
X100-2B	54	132.8	562.8	0	31.3	31.3	691
X100-3C	54	130.1	538.8	0	39.2	39.2	744

7-5-4. Superposition of strengthening mechanisms

7-5-4-1. Superposition of strengthening mechanisms based on σ_i, σ_{ss}, σ_{gb} and σ_{ppt}

The individual strengthening contributions were determined for different steels in previous sections. The superposition of different strengthening contributions needs to be compared with the actual yield strength of the steels.

If a linear model is used, the effect of individual strengthening contributions from Peierls-Nabarro barriers, grain boundary strengthening, solid solution

strengthening and precipitation strengthening are combined and quantitatively estimated according to equation (2-24). [12]

$$\sigma_{ys}(MPa) = \sigma_i + \sigma_{gb} + \sigma_{ss} + \sigma_{ppt} = \sigma_i + k_y\, d^{-1/2} + \sum k_i C_i + \sum \left(\frac{10.8 f_v^{1/2}}{X} \right) \ln \left(\frac{X}{6.125 \times 10^{-4}} \right)$$

(2-24)

Due to the mutual interaction between grain refinement and precipitation strengthening in microalloyed steel systems, [81] a combination of a root mean square and a linear summation model is used as an alternative. The effect of individual strengthening contributions can be quantitatively estimated by the following equation.

$$\sigma_{ys}(MPa) = \sigma_i + \sigma_{ss} + (\sigma_{gb}^2 + \sigma_{ppt}^2)^{1/2} \qquad (7\text{-}46)$$

Table 7-14 shows the superposition effect using the two models, where the four different strengthening components are considered. Figure 7-19 shows the fitting effect. The experimental yield strength of all the steels sits on a 45 degree line, indicated by circles. Square points in Figure 7-19 correspond to the yield strength calculated using the linear model. Triangular points correspond to the yield strength calculated using the combination of a root mean square and a linear summation model. It is clear that the yield strength fitting via the combination of root mean square and linear summations is better than that via linear fitting.

If the individual strengthening components are normalized according to the yield strength of the steel, the strengthening contribution of the four different strengthening mechanisms are shown in Figure 7-20. The figure indicates that strengthening due to grain size refinement plays a major role for all steels being investigated.

Table 7-14 Strengthening contributions from different mechanisms in steels - 4 contributions

Steels	Strengthening contribution (MPa)				Linear summation (MPa)	Superposition using equation 7-46 (MPa)	Actual yield strength (MPa)
	σ_i	σ_{ss}	σ_{gb}	σ_{ppt}			
Grade100	54	125.7	506.4	195.0	881.0	722.2	788
X70-564	54	163.0	336.9	150.8	704.8	586.2	520
X80-462	54	131.2	382.6	154.2	722.0	597.7	588
X80-A4B	54	146.7	385.5	146.1	732.3	613.0	568
X80-B4F	54	113.8	403.3	161.7	732.8	602.3	592
X80-A4F	54	115.2	401.9	127.1	698.2	590.7	589
X100-2A	54	127.6	592.4	39.1	813.0	775.3	810
X100-2B	54	132.8	562.8	31.3	780.9	750.5	691
X100-3C	54	130.1	538.8	39.2	762.0	724.3	744

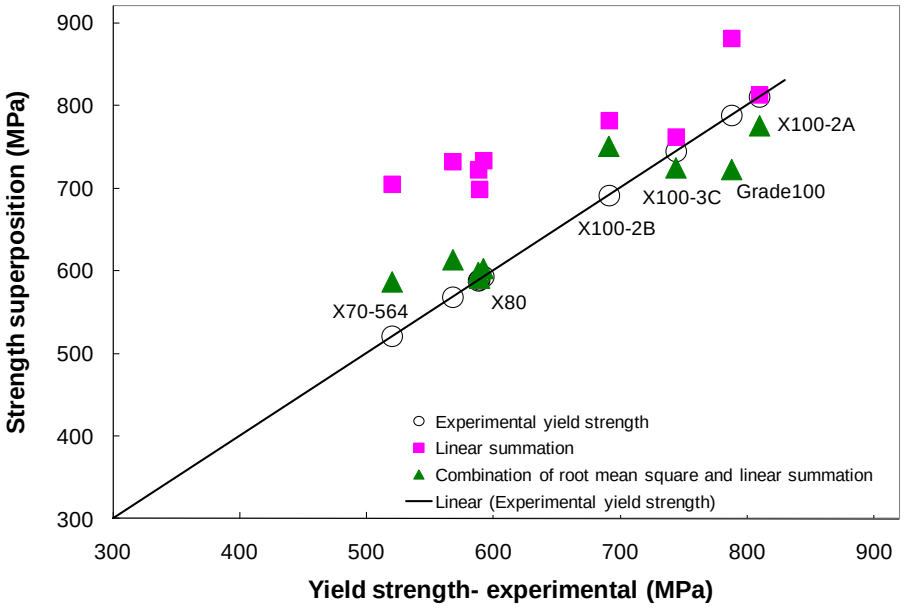

Figure 7-19 Superposition of different strengthening components using equation 7-46 (4 contributions).

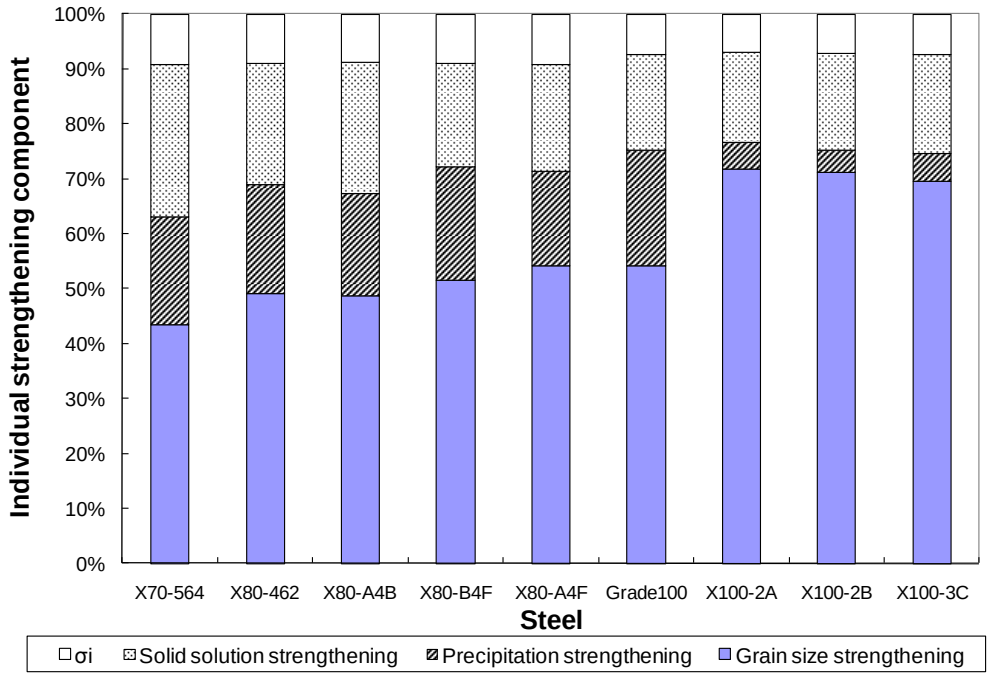

Figure 7-20 Individual strengthening components - 4 contributions.

7-5-4-2. Superposition of strengthening mechanisms based on σ_i, σ_{ss}, σ_{gb}, σ_{ppt} and $\sigma_{dislocation}$

It was mentioned in Section 2-3-4 that dislocation strengthening does not have a significant contribution to strengthening in hot-rolled or normalized microalloyed steels because cold deformation is not commonly used in these steels. [12] Therefore, dislocation strengthening is not included in these steels. However, dislocations may contribute to strengthening in other ways. Dislocation strengthening is achieved by an increase in dislocation density and a change in dislocation arrangement. [12] The dislocations may mutually tangle with each other, hinder dislocation motion and increase the strength. Forest dislocation strengthening is generally calculated as follows. [75,76] The average dislocation density is about 4×10^{13} m^{-2} for X80 steels. [173] Since X70 and Grade100 steels have similar processing histories compared to X80 steels, 4×10^{13} m^{-2} is also used as the average dislocation density for X70 and Grade100 steels. For X100 steels, the average dislocation density is about 2×10^{14} m^{-2}. [173] These numbers agree

fairly well with typical dislocation densities (10^{13} - 10^{14} m^{-2}) reported in the literature for modern low-alloy steels. [174,175]

$$\sigma_{dis} = \alpha M' G b \rho^{1/2} \tag{2-23}$$

σ_{dis}: strengthening contribution due to dislocations;

α: dimensionless coefficient with a value of 0.38 when the stress is calculated in kg/mm^2; [63]

M': Taylor factor, $M' = 3$; [12]

G: shear modulus of the steel, 80.3 GPa; [12]

b: magnitude of Burgers vector, 2.5×10^{-10} m; [12]

ρ: dislocation density, $\rho = 4\times10^{13}$ m^{-2} for X70, X80 and Grade100 steels, $\rho = 5\times10^{14}$ m^{-2} for X100 steels.

Based on Table 7-13 and equation (2-23), the strengthening contributions due to the five different mechanisms are summarized in Table 7-15. It is clear that the contribution due to dislocation strengthening is very small compared to the other strengthening contributions. This result agrees very well with the literature. [12] If linear superposition is used, the strengthening effect can be quantitatively estimated according to equation (7-47). If a combination of a root mean square and a linear summation model is used, the effect of individual strengthening contributions can be quantitatively estimated by equation (7-48).

Table 7-15 Strengthening contributions from different mechanisms in steels - 5 contributions

Steels	Strengthening contribution (MPa)					Linear summation (MPa)	Superposition using equation 7-48 (MPa)	Yield strength (MPa)
	σ_i	σ_{ss}	σ_{gb}	σ_{ppt}	σ_{dis}			
Grade100	54	125.7	506.4	195.0	14.8	895.7	722.4	788
X70-564	54	163.0	336.9	150.8	14.8	719.5	586.5	520
X80-462	54	131.2	382.6	154.2	14.8	736.8	598.0	588
X80-A4B	54	146.7	385.5	146.1	14.8	747.1	613.2	568
X80-B4F	54	113.8	403.3	161.7	14.8	747.5	602.5	592
X80-A4F	54	115.2	401.9	127.1	14.8	713.0	590.9	589
X100-2A	54	127.6	592.4	39.1	33.0	846.1	776.2	810
X100-2B	54	132.8	562.8	31.3	33.0	813.9	751.4	691
X100-3C	54	130.1	538.8	39.2	33.0	795.1	725.3	744

$$\sigma_{ys}(MPa) = \sigma_i + \sigma_{gb} + \sigma_{ss} + \sigma_{ppt} + \sigma_{dis}$$
$$= \sigma_i + k_y\, d^{-1/2} + \sum k_i C_i + \sum \left(\frac{10.8 f_v^{1/2}}{X} \right) \ln \left(\frac{X}{6.125 \times 10^{-4}} \right) + \alpha M' G b \rho^{1/2} \quad (7\text{-}47)$$

$$\sigma_{ys}(MPa) = \sigma_i + \sigma_{ss} + (\sigma_{gb}^2 + \sigma_{ppt}^2 + \sigma_{dis}^2)^{1/2} \quad (7\text{-}48)$$

Figure 7-21 shows the fitting effect using the above two models, where five different strengthening components are considered. The experimental yield strength of all the steels still sits on a 45 degree line, indicated by circles. Square points in Figure 7-21 correspond to the yield strength calculated using the linear model. Triangular points correspond to the yield strength calculated using the combination of a root mean square and a linear summation model. It is clear that the yield strength fitting via the combination of root mean square and linear summations is better than that via linear fitting.

If the individual strengthening components are normalized according to the yield strength of the steel, the strengthening contribution of the different strengthening mechanisms is shown in Figure 7-22. This figure indicates that

strengthening due to grain size refinement plays a major role and dislocation strengthening has the least contribution for all steels being investigated. For X70, X80 and Grade100 steels, there is a significant precipitation strengthening contribution, mainly due to the existence of nano-precipitates (mainly ≤10 nm). However, due to the lack of nano-precipitates, there is a lower precipitation strengthening contribution for X100 steels compared with other steels.

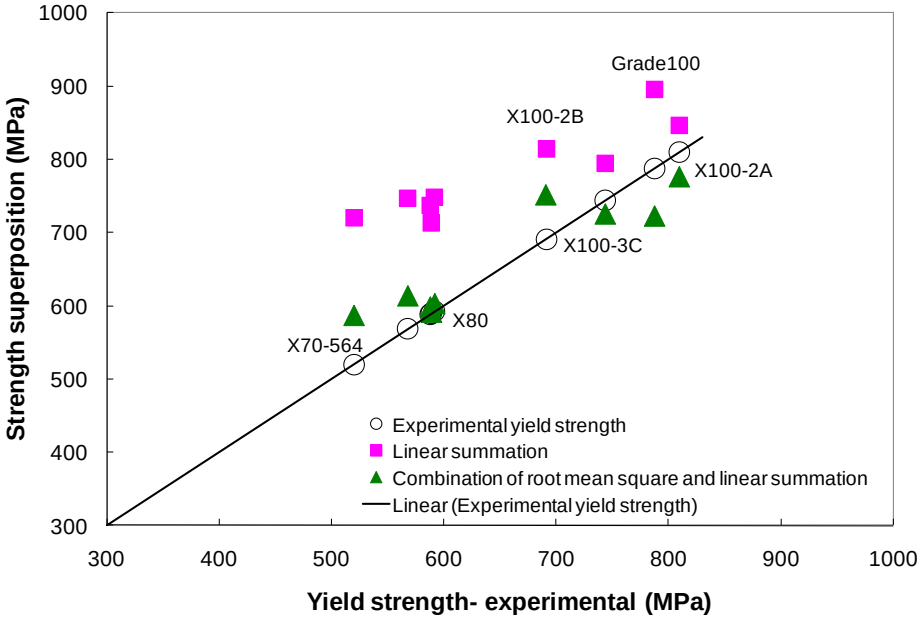

Figure 7-21 Superposition of different strengthening components using equation 7-48 (5 contributions).

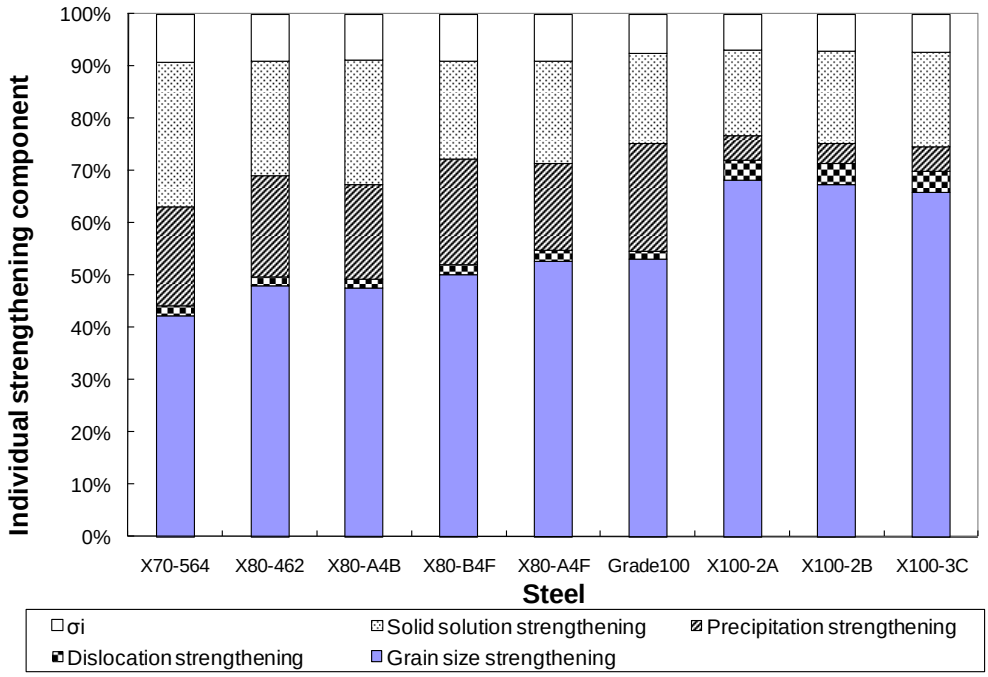

Figure 7-22 Individual strengthening components - 5 contributions.

7-5-4-3. Coherency strengthening

One thing needs to be noted that in current thesis, precipitation strengthening in microalloyed steels is based on Orowan looping. In Orowan looping mechanism, the nature of the interface between the particles and the matrix is not differentiated. This means that coherent or incoherent precipitates do not show differences in precipitation strengthening for an Orowan looping mechanism. In addition, coherency strain is not considered in an Orowan looping mechanism. Coherency strain is considered as a strengthening mechanism when particles are sheared. [176] Coherency strain strengthening due to nano-precipitates can be estimated using equation (7-49), which is an approximate expression for the increase in resolved shear stress during early stages of precipitation. Ferrite has BCC structure and there are two Fe atoms in one unit cell. Nano-precipitates have NaCl-FCC structure and there are 4 Nb atoms and 4 C atoms in one unit cell. The C atoms occupy the interstitial positions. Therefore, the lattice parameter for nano-precipitates is normalized in the constraint misfit and the coherency strengthening is given in equation (7-50).

$$\tau_{coh}(MPa) \cong 7 \times |\delta|^{3/2} G\left(\frac{rf_v}{b}\right)^{1/2} \cong 7 \times \left|\frac{a_p - a_{Fe}}{a_{Fe}}\right|^{3/2} G\left(\frac{rf_v}{b}\right)^{1/2} \quad (7\text{-}49)$$

$$\tau_{coh}(MPa) \cong 7 \times \left|\frac{\frac{a_p}{2} - a_{Fe}}{a_{Fe}}\right|^{3/2} G\left(\frac{rf_v}{b}\right)^{1/2} \quad (7\text{-}50)$$

δ: zone misfit due to lattice parameter difference;

a_p: lattice parameter of nano-precipitates, NbC precipitate is considered as an example, 0.44698 nm;

a_{Fe}: lattice parameter of Fe matrix, 0.28664 nm;

G: shear modulus of the steel, 80.3 GPa [12];

r: precipitate radius, r = 2.5 nm is used as an example;

f_v: volume fraction of precipitate, f_v = 0.00166 (Grade100) is used an example;

b: magnitude of Burgers vector, 2.5×10^{-10} m. [12]

Using the above parameters, the calculated shear stress is about 7490 MPa. Also, considering that the normal stress is about 3 times (Taylor factor) the value of the shear stress, the calculated yield stress would be about 22,467 MPa. However, the yield strength of the steel is less than 800 MPa, which indicates that the nano-precipitates are not sheared. As such, an Orowan looping mechanism is valid. In microalloyed steels, the nano-precipitates are very hard and therefore undeformable. Because of the strong bonding and fine sizes of the precipitates, extensive dislocation bowing is commonly seen. [12] In addition, creation of matrix/particle interfacial areas will have significant effects if cutting occurs on the precipitates, especially for nano-precipitates with high surface area to volume ratio.

7-6. Summary

Grain size decreases with increasing grade of steel and the yield strength follows a Hall-Petch type behaviour. Alloying elements, such as Mn, Ni, Mo and Cr, help to increase the steel hardenability. Therefore, the bainite-like transformation is promoted, leading to strength and toughness improvement. CR and CT/ICT have strong effects on microstructure evolution and grain refinement as well. Higher CR and lower CT/ICT promote low temperature transformation products (acicular ferrite/bainite), leading to grain refinement and corresponding strength and toughness improvement.

The volume fraction of nano-precipitates (≤10 nm) can be determined based on their weight fraction obtained from Rietveld refinement of XRD data.

X70, X80 and Grade100 steels have similar processing histories and they all have nano-precipitates (≤10 nm in size). Higher microalloying content in the steel increases precipitation, leading to a higher volume fraction and number density of nano-precipitates. CT/ICT has a direct effect on the nucleation of nano-precipitates and affects the amount of nano-precipitates.

For all steels studied here, grain boundary effects have a major contribution to strengthening. However, dislocation strengthening has the lowest contribution for all steels investigated. Yield strength fitting via a combination of root mean square and linear summation is better than a linear fitting because of the synergy between grain size, precipitation and dislocation effects. For X70, X80 and Grade100 steels, there is a significant precipitation strengthening contribution, mainly due to the existence of nano-precipitates (≤10nm).

Chapter 8: Conclusions, achievements and future work

The main focus of this research work was to characterize the microstructure features of a series of microalloyed steels. It includes the grain microstructure and precipitate characterization. Steel chemistry and processing histories have strong effect on both microstructure evolution and precipitation behaviors. The strengthening mechanisms were obtained based on the above studies. This final chapter gives the full conclusions of this research work. The novelty and achievements, evaluation of the experimental techniques and the suggestions for future work are included as well.

8-1. Conclusions

The matrix dissolution method can be successfully used to quantify precipitates in microalloyed steels and can provide valuable quantitative information based on samples that are more representative of the steel strip than the only microscopy methods. Matrix dissolution technique was validated by carbon replicas because they can give consistent results on precipitate chemistry and size.

Rietveld refinement of XRD patterns can be successfully used to identify and determine the relative abundance of different precipitate phases, making it possible to determine the volume fraction of nano-precipitates ($\leq$10 nm) in microalloyed steels.

Grain size decreases with increasing grade of steel and the yield strength follows Hall-Petch type behaviour. Steel chemistry, such as Mn, Ni, Mo and Cr, helps to increase the steel hardenability. Therefore, the bainite-like transformation is promoted, leading to strength and toughness improvement. CR and CT/ICT have strong effects on microstructure evolution and grain refinement as well. Higher CR and lower CT/ICT promote low temperature transformation products (acicular ferrite/bainite), leading to grain refinement, strength and toughness improvement.

Microalloying content and CT/ICT have strong effect on precipitation behaviour. Under similar processing conditions, increasing microalloying content results in a higher precipitation driving force, leading to a higher yield of nano-precipitates (mostly are ≤10 nm). CT/ICT has a direct effect on the precipitate nucleation and affects the amount of nano-precipitates.

Nano-precipitates (≤10 nm) have been observed in X70, X80 and Grade100 steels. These nano-precipitates are mostly less than 10 nm in size and spherical in shape. They are mainly Nb-Mo carbides, but with chemistry variations. For X100 steels, no nano-precipitates (≤10 nm) were observed. The lack of fine precipitates is due to the low ICT temperature.

Different strengthening mechanisms contribute to the high strength of microalloyed steels, of which grain refinement plays a major contribution for the steels being studied. Grain refinement is the only strengthening mechanism that improves both strength and toughness.

8-2. Novelty and achievements

Most of the published work about precipitate is focused on the morphology, size and the orientation relationship with the austenite or ferrite matrix. Because of the challenges related to precipitate quantification, not too much work has been done in this area, especially nano-precipitates (≤10 nm) quantification. However, precipitate quantification is a critical problem in order to fully understand the strengthening mechanisms. Knowledge of the microstructure development in TMCP and understanding the strengthening mechanisms are very important for optimizing the rolling schedules with the aim of improving steel mechanical properties. Therefore, it is necesary to systematically correlate the effect of steel chemistry and processing parameters on microstructure evolution and precipitation formation and also connect with steel mechanical properties.

In order to achieve this goal, a novel method, matrix dissolution combined with XRD, was developed to characterize precipitates with different sizes and various chemistries, especially their volume fraction determination. The effects of steel chemistry and TMCP parameters on steel microstructure and nano-precipitates were

studied. The strengthening mechanisms of the microalloyed pipeline steels were successfully abtained. It establishes important guidelines in steel processing.

8-3. Evaluation of the experimental techniques in current research

In this research work, precipitate quantification in a series of microalloyed steels was achieved using matrix dissolution and several microscopy and diffraction techniques. The strengthening mechanisms for these microalloyed steels were quantified. Furthermore, microstructure evolution, precipitate formation and steel mechanical properties were systematically correlated to the steel chemistry and processing parameters.

From an industrial or practical point of view, knowledge of microstructure development and understanding of the strengthening mechanisms are valuable for improving steel mechanical properties. However, each characterization technique has its limitations. Several techniques need to be combined to achieve the goal. For example, TEM has good resolution and it is good for characterizing precipitate composition and size distribution. From TEM analysis, precipitates can be categorized into different groups, which serve as input information for Rietveld refinement. However, TEM is not good for precipitate quantification mainly because of the small sample size.

Relatively large volumes of material can be analyzed using matrix dissolution techniques, so that statistically significant quantities of precipitates of different sizes are collected. Rietveld refinement of the XRD patterns from the extracted precipitates can be used to quantify the relative amounts of the precipitates. However, Rietveld refinement is a profile fitting tool. It cannot be used to generate correct data without correct input information. TEM has to be used, which is time consuming.

Therefore, the techniques used in this research work are good research tools. Collaboration between university and industry provides the opportunity to succeed in quantifying precipitation effects.

8-4. Future work

A complete microstructural characterization of a material is complicated. It includes morphological characterization, composition analysis, phase identification, crystallographic orientation, size distribution and phase concentration determination, etc. Although steel is widely used in industry; it is not a simple material at all because of the heterogeneity in the microstructure. [177] Steel has very complex composition. It consists of multiple grains with specific sizes, shapes. Different phases, such as ferrite, pearlite, acicular ferrite, bainite, martensite and retained austenite, can be present in the steel. Non-metallic inclusions (micron scale) and precipitates (from micron scale down to a few nanometers) can be present as well. The mechanical properties of steel are closely related to the microstructure, which is strongly affected by steel processing parameters. Due to the microstructure complexity, a combination of different techniques is needed to achieve a full investigation.

8-4-1. Laboratory steels

Commercial steels have very complex compositions and the processing parameters can not be accurately controlled through the whole strip. It means the steel may not be homogeneous and the TMCP may not be the same in all regions during steel making. Precipitation is a very complex process, due to the fact that it takes place inside a two phase matrix (austenite and ferrite) and the matrix itself is continuously evolving. There are many factors affecting the precipitation of nano-precipitates, such as processing temperature, strain and steel chemistry. It is, therefore, challenging to study the precipitation of nano-precipitates by using commercial steels with complex chemistries. Therefore, laboratory steels with simple chemistry and accurate processing parameters can be used. Examination of precipitate at different stages will provide more information on precipitation formation

8-4-2. Other matrix extraction mothods

Other matrix extraction methods, which can eliminate amouphous SiO_2 phase and with high extraction yield, are worth trying. It can reduce the signal/noise ratio, providing more accurate quantification information via Rietveld refinement of XRD pattern.

8-4-3. Electron Energy Loss Spectroscopy (EELS)

In microalloyed steels, precipitates consist of Ti, Nb and/or V carbonitrides. Conventional SEM/TEM-EDX microanalysis can not accurately determine the amount of elements with low atomic numbers. EELS can be used to quantitative determine the C and N contents in precipitates. [178,179]

8-4-4. Atom Probe Field-ion Microscopy (APFIM)

The field-ion microscope and the time-of flight mass spectrometer are the two basic sections in the atom probe. High resolution images are obtained from the field-ion microscope and the chemistry information is obtained from the time-of flight mass spectrometer. [180] The image is formed by the ionization of atoms from the specimen. In APFIM, three dimensional morphology of specimen microstructure can be determined by recording a series of images after removal of surface layers using field evaporation. [180] Alloying elements can be mapped out in three dimensions with almost atomic resolution. [181] In APFIM, chemistry of specimen can be accurately determined, including light elements such as C and N. Therefore, APFIM tecnnique has major advantages in nano-precipitate investigation. The chemistry can be accurately determined on a single particle down to 1 nm diameter. [180,182] However, the specimen used in APTIM is sharp needle-shaped; the volume of material analyzed is much smaller than that in TEM. Sample preparation used for APFIM is also complex. This technique is also time-consuming and only a small volume is analyzed at each measurement.

8-4-5. Study of the supersaturated interstitials in the steel

Carbon and N have strong solid solution strengthening effect due to their large solid solution strengthening coefficients. In this thesis, the equilibrium solubility was used to calculate their solid solution strengthening contribution. However, supersaturated C and N may be present due to the fast cooling during steel making process. Therefore, in order to accurately determine the solid solution strengthening contribution, the total free C and N should be determined.

There are a variety of methods to detect interstitial atoms. Amongst different physical techniques, internal friction measurement with a torsional pendulum method and electrical resistivity measurement have been very successful. [7,64,183] The internal friction measurement is based on the fact that the damping capacity of a specimen under externally imposed vibrations varies with the interstitial atom sites within the metal lattice and can produce an abnormal rise and fall, i.e. the internal friction peak. The position of the internal friction peak is characteristic of the type of the interstitial element in solid solution as well as its diffution rate. The height and width of the peak indicate the amount and distribution of the interstitial elements respectively. This technique makes it possible to measure the solubility and diffusion coefficient of the interstitial element. The electrical resistivity measurement measures the resistivity at very low temperatures (near absolute zero) and its temperature dependence. From the measurement, the interstitial impurity content can be obtained. [64]

8-4-6. Validation the Rietveld refinement using standards

As mentioned previously, the error in the Rietveld refinement using SiO_2 as an internal standard to determine the relative abundance of nano-precipitates is a concern. A specimen with similar phase composions and known SiO_2 content should be used as a standard to validate this technique.

8-4-7. Study of Cu precipitate strengthening

Lots of studies have been carried out on Cu precipitate strengthening in the 1960s. [184] Because C and N are not needed to form Cu precipitates, Cu

precipitation is widely used in interstitial free (IF) steels. It has been reported that age hardening due to Cu precipitates occurs between 450 and 600 ºC. The solubility product of Cu can be expressed in the following equation. [185]

$$\log K_s = \log[Cu]_e = 4.435 - 4499/T \quad (8\text{-}1)$$

$[Cu]_e$: wt% of Cu dissolved in the ferrite under equilibrium condition.

In the microalloyed steels studied in current research, the Cu content is between 0.15-0.42 wt%. The solubility limit of Cu has been highly reached at room temperature with this Cu content. Therefore Cu precipitates are expected to occur in these steels. In order to fully understand the strengthening mechanisms, it is necessary to study Cu precipitation in microalloyed pipeline steels. Due to the complex chemical composition of microalloyed steels, other precipitates such as Ti, Nb, and/or V carbonitride exist, making it more complicated.

References

[1] J. Y. Koo, M. J. Luton, N. V. Bangaru and R. A. Petkovic, "Metallurgy design of ultra high-strength steels for gas pipelines", International Journal of Offshore and Polar Engineering, Vol. 14, 2004, p. 2-10.

[2] A. J. DeArdo, "The metallurgy of high strength linepipe steels", in *Pipelines for the 21th Century*, Metallurgical Society of CIM (MetSoc), Montreal, Quebec, Canada, 2005, p. 85-100.

[3] M. K. Graf, H. -G. Hillenbrand and P. A. Peters, "Accelerated cooling of plate for high strength large diameter pipe", in *Proceedings of a Symposium: Accelerated Cooling of Steel*, The Metallurgical Society of AIME, Pittsburgh, PA, USA, 1986, p. 165-180.

[4] R. W. K. Honeycombe and H. K. D. H. Bhadeshia, Steels Microstructure and Properties, Elsevier Ltd, 2006.

[5] H. Asahi, E. Tsuru, Y. Terada, M. Murata, H. Miyazaki and N. Anukawa, "Development and properties of ultra high-strength UOE pipeline", in *Proceedings of the 5th International Pipeline Conference (IPC2004)*, ASME International, Calgary, AB, Canada, 2004, Vol. 2, p. 1733-1742.

[6] V. B. Ginzburg, Steel- Rolling Technology Theory and Practice, Marcel Dekker Inc., New York and Basel, USA, 1989.

[7] F. G. Wilson and T. Gladman, "Aluminum nitride in steel", International Materials Reviews, Vol. 33, no. 5, 1988, p. 211-286.

[8] R. Lagneborg, T. Siwecki, S. Zajac and B. Hutchinson, "The role of vanadium in microalloyed steel", Scandinavian Journal of Metallurgy, Vol. 28, no. 5, 1999, p. 186-241.

[9] V. B. Ginzburg, Metallurgical Design of Flat Rolled Steels, Marcel Dekker Inc., New York, USA, 2005.

[10] E. L. Brown and A. J. DeArdo, "Aluminum nitride precipitation in C-Mn-Si and microalloyed steels", in *Proceedings of the International Conference on the Thermomechanical Processing of Microalloyed Austenite*, Edited by A. J. DeArdo, G. A. Ratz and P. J. Wray, AIME, 1982, p. 319-341.

[11] T. Kikutake, Y. Tokunaga, H. Nakao, K. Ito and S. Takaishi, "Effect of Al and N on the toughness of heavy section steel plates", The Iron and Steel Institute of Japan (ISIJ), Vol. 74, 1988, p. 847-854.

[12] T. Gladman, The Physical Metallurgy of Microalloyed Steels, The Institute of Materials, London, UK, 1997.

[13] C. J. Heckmann, D. Ormston, F. Grimpe, H. -G. Hillenbrand and J.-P. Jasen, "Development of low carbon Nb-Ti-B microalloyed steels for high

strength large diameter linepipe", Ironmaking and Steelmaking, Vol. 32, no. 4, 2005, p. 337-341.

[14] L. E. Collins, M. J. Godden and J. D. Boyd, "Microstructures of linepipe steels", Canadian Metallurgical Quarterly, Vol. 22, no. 2, 1983, p. 169-179.

[15] Ya. E. Gol'dshrein and A. L. Starikova, "Effects of boron, molybdenum, and titanium on brittleness induced by tempering of structural steels", Metal Science and Heat Treatment, Vol. 5, no 5, 1963, p. 250-256.

[16] M. Kutz, Handbook of Materials Selection, John Wiley & Sons, Inc., New York, USA, 2002, p. 44.

[17] T. Taira, K. Matsumoto, Y. Kobayashi, K. Takeshige and I. Kozasu, "Development of super-tough acicular ferrite steel for line pipe-optimization of carbon and niobium content in low-carbon steel", in *Conference Proceedings of International Conference on Technology and Applications of HSLA Steels*, ASM, 1984, p. 723-731.

[18] R. L. Brockenbrough, "Properties of structural steels and effects of steelmaking and fabrication", Structural Steel Designer's Handbook, MaGraw-Hill, 3rd edition, 1999, 1.23.

[19] W. Huang, "Thermodynamic properties of the Fe-Mn-V-C system", Metallurgical Transactions A, Vol. 22 A, no. 9, 1991, p. 1911-1920.

[20] Z. Tang and W. Stumpf, "The role of molybdenum additions and prior deformation on acicular ferrite formation in microalloyed Nb–Ti low-carbon line-pipe steels", Materials Characterization, Vol. 59, 2008, p. 717-728.

[21] R. Uemori, R. Chijiiwa, H. Tamehiro and H. Morikawa, "AP-FIM study on the effect of Mo additions on microstructure in Ti-Nb steel", Applied Surface Science, Vol. 76/77, 1994, p. 255-260.

[22] P. J. P. Bordignon, "Applications of Niobium as a microalloying element in steel", SEAISI Quarterly (South East Asia Iron and Steel Institute Quarterly), Vol. 15, no. 2, 1986, p. 55-68.

[23] S. S. Hansen, "Microalloyed plate and bar products: Production technology", in *Fundamentals of Microalloying Forging Steels: Proceedings of an International Symposium* sponsored by the Ferrous Metallurgy Committee of the Metallurgical Society held in Golden, Colorado, Edited by G. Krauss and S. J. K. Banerji, The Metallurgical Society of AIME, 1987, p.155-174.

[24] E. Kashif, K. Asakura, T. Koseki and K. Shibata, "Effects of boron, niobium and titanium on grain growth in ultra high purity 18%Cr ferritic stainless steel", ISIJ International, Vol. 44, no. 9, 2004, p. 1568-1575.

[25] J. J. Jonas and M. G. Akben, "Retardation of austenite recrystallization by solute: a critical appraisal", Metals Forum, Vol. 3-4, 1981, p. 92-101.

[26] N. Maruyama, R. Uemori and M. Sugiyama, "The role of niobium in the retardation of the early stage of austenite recovery in hot-deformed steels", Materials Science and Engineering, Vol. A259, 1998, p. 2-7.

[27] A. Abdollah-Zedeh and D.P. Dunne, "Effect of Nb on recrystallization after hot deformation in austenitic Fe-Ni-C", ISIJ International, Vol. 43, no. 8, 2003, p. 1213-1218.

[28] T. Gladman, I. D. Mcivor and F. B. Pickering, "Effect of carbide and nitride particles on the recrystallization of ferrite", Journal of the Iron and Steel Institute, Vol. 5, 1971, p. 380-390.

[29] A. T. Davenport, L. C. Brossard and R. E. Miner, "Precipitation in microalloyed high-strength low-alloy steels", Journal of Metals, Vol. 6, 1975, p. 21-27.

[30] D. Bai, M. A. Cooke, J. Asante and J. Dorricott. "Process for making high strength micro-alloy steel", United States Patent, Patent No.: US 6,682,613 B2, Jan. 27, 2004.

[31] L. E. Collins, " Processing of niobium-containing steels by Steckel mill rolling" *Niobium Science and Technology: Proceedings of the International Symposium Niobium 2001*, TMS-AIME and Niobium 2001 Limited, Bridgeville, PA, USA, 2001, p. 527-542.

[32] A. J. DeArdo, "Metallurgical basis for thermomechanical processing of microalloyed steels", Ironmaking and Steelmaking, Vol. 28, no. 2, 2001, p. 138-144.

[33] A. J. DeArdo, "Niobium in modern steels", International Materials Review, Vol. 48, no. 6, 2003, p. 371-402.

[34] G. E. Totten, X. Lin and F. Kiyoshi, Handbook of Mechanical Alloy Design, Marcel Dekker Inc., New York, USA, 2004.

[35] Y. H. Bae, S. H. Hong, J. S. Lee, J. -K Choi and W. -Y. Choo, "Effect of prior austenite microstructure on austenite/ferrite transformation of fine grained high strength low alloy steel", Materials Science Forum, Vol. 426-432, 2003, p. 1583-1588.

[36] F. B. Pickering, "High-Strength Low-Alloy Steels - A Decade of Progress" in *Microalloying 75 - Proceedings of an International Symposium on High-strength Low-alloy Steels*, Union Carbide Corp., New York, 1977, p. 9-31.

[37] H. J. Jun, J. S. Kang, D. H. Seo, K. B. Kang and C. G. Park, "Effects of deformation and boron on microstructure and continuous cooling transformation in low carbon HSLA steels", Materials Science and Engineering A, Vol. 422, 2006, p. 157-162.

[38] G. Krauss and S. W. Thompson, “Ferritic microstructures in continuously cooled low- and untralow-carbon steel”, ISIJ International, Vol. 35, no. 8, 1995, p. 937-945.

[39] N. K. Balliger and R. W. K. Honeycombe, “The effect of nitrogen on precipitation and transformation kinetics in vanadium steels”, Metallurgical and Materials Transactions A, Vol. 11A, 1980, p. 421-429.

[40] E. E. Fletcher, High-Strength, Low-Alloy Steels: Status, Selection, and Physical Metallurgy, Metals and Ceramics Information Center, Battelle Press, 1979.

[41] J. Kunze, “Solubility of titanium nitride in delta iron”, Steel Research, Vol. 62, no. 10, 1991, p. 430-432.

[42] K. A. Taylor, “Solubility products for titanium-, vanadium-, and niobium-carbide in ferrite,” Scripta Metallurgica et Materialia, Vol. 32, no. 1, 1995, p. 7-12.

[43] K. E. Easterling, Introduction to the Physical Metallurgy of Welding, Butterworth-Heinemann Ltd, Oxford, UK, 1992, p. 139.

[44] C. Wagner, Thermodynamics of alloys, Addison-Wesley Co., Reading, Mass, 1952.

[45] J. Kunze, “Solubility product of titanium nitride in γ-iron”, Metal Science, Vol. 16, no. 4, 1982, p. 217-218.

[46] K. Inoue, I. Ohnuma, H. Ohtani, K. Ishida and T. Nishizawa, “Solubility product of TiN in austenite”, ISIJ International, Vol. 38, no. 9, 1998, p. 991-997.

[47] M. Chen, “Phase analysis of titanium in steel and some aspects on its application”, Journal of Iron and Steel Research, Vol. 4, no. 1, 1992, p. 87-92.

[48] L. F. S. Dumitrescu and M. Hillert, “Reassessment of the solubility of TiC and TiN in Fe”, ISIJ International, Vol. 39, no. 1, 1999, p. 84-90.

[49] H. Ohtani and M. Hillert, “A thermodynamic assessment of Ti-N system”, CALPHAD: computer coupling of phase diagrams and thermochemistry, Vol. 14, no. 3, 1990, p. 289-306.

[50] H. Ohtani and M. Hillert, “A thermodynamic assessment of Fe-N-Ti system”, CALPHAD: computer coupling of phase diagrams and thermochemistry, Vol. 15, no. 1, 1991, p. 41-52.

[51] K. Inoue, N. Ishikawa, I. Ohnuma, H. Ohtani and K. Ishida, “Calculation of phase equilibria between austenite and (Nb, Ti, V)(C, N) in microalloyed steels”, ISIJ International, Vol. 41, no. 2, 2001, p. 175-182.

[52] S. Zajac and B. Jansson, "Thermodynamics of the Fe-Nb-C-N system and the solubility of niobium carbonitrides in austenite", Metallurgical and Materials Transactions B, Vol. 29B, 1998, p. 163-176.

[53] T. Siwecki and S. Zajac, "Recrystallization controlled rolling and accelerated cooling of Ti-V- (Nb)-N microalloyed steels", in *32nd Mechanical Working and Steel Processing*, Iron and Steel Society, Vol. XXVIII, 1991, p. 441-451.

[54] S. Zajac, T. Siwecki and M. Korchynsky, "Importance of nitrogen for precipitation phenomena in Vanadium-microalloyed steels", in *International Symposium on Low-Carbon Steels for the 90's*, TMS, 1993, p. 139-149.

[55] W. Roberts, "Prediction of microstructure development during recrystallization hot rolling of Ti-V steels", in *Conference Proceedings of International Conference on Technology and Applications of HSLA Steels,* ASM, Philadelphia, PA, USA, 1983, p. 67-84.

[56] T. Siwechi, A. Sandberg and W. Roberts, "Processing characteristics and properties of Ti-V-N steels", in *Conference Proceedings of International Conference on Technology and Applications of HSLA Steels,* ASM, Philadelphia, PA, USA, 1983, p. 619-634.

[57] S. Zajac, T. Siwecki, W. B. Hutchinson and R. Lagneborg, "Strengthening mechanisms in vanadium microalloyed steels intended for long products", ISIJ International, Vol. 38, no. 10, 1998, p.1130-1139.

[58] S. Zajac, "Ferrite grain refinement and precipitation strengthening in V-microalloyed steel", in *43rd Mechanical Working and Steel Processing Conference proceedings*, Iron and Steel Society of AIME, 2001, p. 497-508.

[59] N. Shams, "Carbonitride precipitates in HSLA", Journal of Metals, Vol. 38, no 5, 1986, p. 31-33.

[60] International Center for Diffraction Data (ICDD) database, pdf charts.

[61] S. M. Wolf, "Properties and applications of dispersion-strengthened metal", Journal of Metals, Vol. 19, no. 6, 1967, p. 22-28.

[62] W. D. Callister, Materials Science and Engineering: An Introduction, 5th Edition, John Wiley & Sons Inc., 2000.

[63] K. Poorhaydari-Anaraki, PhD thesis, Microstructure and property examination of the weld HAZ in Grade 100 microalloyed steel, University of Alberta, Canada, 2005.

[64] H. J. Goldschmidt, Interstitial Alloys, Plenum Press, New York, USA, 1967.

[65] D. T. Llewellyn and R. C. Hudd, Steels: Metallurgy & Applications, Reed Educational and Professional Publishing Ltd, 1998.

[66] Z. Cui, Metallurgy and Heat Treatment, Mechanical Industry Press, China, 1988.

[67] A. S. Argon, Strengthening Mechanisms in Crystal Plasticity, Oxford University Press Inc., New York, USA, 2008.

[68] J. Heslop and N. J. Petch, "Dislocation locking and fracture in α-iron", Philosophical Magazine, Vol. 2, no. 17, 1957, P. 649-658.

[69] F. B. Pickering and T. Gladman, "Metallurgical developments in carbon steels", Iron and Steel Institute, Special report No. 81, 1963, p. 10.

[70] P. Buessler, P. Maugis and O. Bouaziz, "Integrated process-metallurgy modelling: example of precipitation during coil cooling", in *44th Mechanical Working and Steel Processing Conference Proceedings: 8th International Rolling Conference and International Symposium on Zinc-coated Steels*, Iron and Steel Society of AIME, 2002, p. 1105-1116.

[71] A. J. Ardell, "Precipitation hardening", Metallurgical Transactions A, Vol. 16A, 1985, p. 2131-2165.

[72] M. F. Ashby and D. R. H. Jones, "Strengthening methods, and plasticity of polycrystals", Engineering Materials: An introduction to their properties and applications, Vol. 1, Pergamon Press, Oxford, UK, 1980.

[73] E. Orowan, in *Symposium on Internal Stresses in Metals and Alloys*, Session III Discussion, Institute of Metals, London, UK, 1948, p. 451-453.

[74] D. R. Askeland and P. P. Phule, The Science and Engineering of Materials, Bill Stenquist, 5th edition, 2006.

[75] T. N. Baker, "Determination of the friction stress from microstructural measurement", Yield, Flow and Fracture of polycrystals, Applied Science Publishers, London, UK, 1983, p. 235-273.

[76] W. Soboyejo, Mechanical Properties of Engineered Materials, Marcel Dekker, Inc., New York, USA, 2003, 8.4.

[77] M. Kirk and M. E. Natishan, Predictive Material Modeling: Combining Fundamental Physics Understanding, Computational Methods and Empirically Observed Behavior, ASTM International, 2003, p. 13-14.

[78] D. Chandrasekaran, Doctoral Dissertation, Grain Size and Solid Solution Strengthening in Metals, Royal Institute of Technology, Sweden, 2003.

[79] J. C. Williams and A. W. Thompson, "Strengthening of metals and alloys", in *Metallurgical Treatises*, USA-China Bilateral Conference, The Metallurgical Society of AIME, Edited by J. K. Tien and J. F. Elliott, Nov. 13-22, 1981, Beijing, China, p. 487-504.

[80] J. Li, F. Sun and W. Xu, "On the evaluation of yield strength for microalloyed steels", Scripta Metallurgica et Materialia, Vol. 24, no. 7, 1990, p. 1393-1398.

[81] E. Nembach, "Synergetic effects in the superposition of strengthening mechanisms", Acta Metallurgica et Materialia, Vol. 40, no. 12, 1992, p. 3325-3330.

[82] S. Akhlaghi and D.G. Ivey, "Precipitation behavior of Grade100 structural steel", Canadian Metallurgical Quarterly, Vol. 41, no. 1, 2002, p. 111-119.

[83] J. Zrnik, T. Kvackaj, D. Sripinproach and P. Sricharoenchai, "Influence of plastic deformation conditions on structure evolution in Nb-Ti microalloyed steels", Journal of Materials Processing Technology, Vol. 133, no. 1-2, 2003, p. 236-242.

[84] A. J. DeArdo, M. Hua, C. I. Garcia and V. Thillou, "Precipitation hardening of ferrite in commercially processed niobium-bearing HSLA steels", in *Conference Proceedings of MS&T 2004*, TMS, 2004, p. 3-20.

[85] J. D. Embury, "Strengthening by dislocation substructures", Strengthening Methods in Crystals, Edited by A. Kelly and R. B. Nicholson, John Wiley & Sons, Inc., New York, USA, 1971, p. 331-402.

[86] F. H. D. Torre, R. Lapovok, P. F. Thomson, J. D. Sandlin, C. H. J. Davies and E. V. Pereloma, "On the influence of the misorientation of grains, grain size and boundary volume on the strength and ductility of ultrafine grained Cu", in *Symposium Proceedings of Materials Research Society*, MRS, 2004, Vol. 821, Paper #: P9.10.

[87] E. Nembach, Particle Strengthening of Metals and Alloys, John Wiley & Sons, Inc., New York, USA, 1997.

[88] U. F. Kocks, A. S. Argon and M. F. Ashby, Thermodynamics and Kinetics of Slip, Pergamon Press Ltd., Oxford, UK, 1975.

[89] J. C. Huang and A. J. Ardell, "Addition rules and the contribution of δ' precipitates to strengthening of aged Al-Ti-Cu alloys", Acta metallurgica, Vol. 36, no. 11, 1988, p. 2995-3006.

[90] C. Schlesier and E. Nembach, "Strengthening of aluminium-lithium alloys by long-range ordered δ'-precipitates", Acta Metallurgica et Materialia, Vol. 43, no. 11, 1995, p. 3983-3990.

[91] L. M. Brown and R. K. Ham, "Dislocation-particle interactions", Strengthening Methods in Crystals, Edited by A. Kelly and R. B. Nicholson, John Wiley & Sons, Inc., New York, USA, 1971, p. 9-135.

[92] T. J. Koppenaal, "Microstrain yield stress in neutron-irradiated copper single crystals", Journal of Applied Physics, Vol. 35, no. 9, 1964, p. 2750-2753.

[93] T. J. Koppenaal, D. Kuhlmann-Wilsdorf, "The effect of prestressing on the strength of neutron-irradiated copper single crystals" Applied Physics Letters, Vol. 4, no. 3, 1964, p. 59-61.

[94] V. Cihal and J. Jezek, "Some observations on the nature of precipitating phases in 18/9/Nb steels", Journal of Iron and Steel Institute. Vol. 202, 1964, p. 124-127.

[95] A. Koreeda and K. Shimizu, "Dislocations in cementite", Philosophical Magazine, 1968, Vol. 17, part 2, p.1083-1086.

[96] C. Dasarathy and R. C. Hudd, "An example of secondary recrystallization induced by aluminum nitride precipitation", Acta Metallurgica, Vol. 15, part. 2, 1967, p. 1665-1671.

[97] R. H. Packwood and K. M. Pickwick, "A new extraction replica techniques for inclusion analysis in the microscope", Metallography, Vol. 4, 1971, p. 365-369.

[98] U. Lagerpusch, B. Anczykowski and E. Nembach, "Comparison of atomic force microscopy and transmission electron microscopy of second-phase particles", Philosophical Magazine A, Vol. 81, no. 11, 2001, p. 2613-2628.

[99] B. Fruhstorfer, V. Mohles, R. Reichelt and E. Nembach, "Quantitative characterization of second-phase particles by atomic force microscopy and scanning electron microscopy", Philosophical Magazine A, Vol. 82, no. 13, 2002, p. 2575-2589.

[100] H. Abrams, "An analytical method applicable to the preshadowed extraction replica technique", Metallography, Vol. 4, 1971, p. 565-568.

[101] R. J. Seher and G. N. Maniar, "Analytical-preshadowed extraction replica technique", Metallography, Vol. 5, no. 5, 1972, p. 409-414.

[102] P. Staron, B. Jamnig, H. Leitner R. Ebner and H. Clemens, "Small-angle neutron scattering analysis of the precipitation behaviour in a maraging steel", Journal of Applied Crystallography, Vol. 36, 2003, p. 415-419.

[103] F. Perrard, A. Deschamps, P. Donnadieu and P. Maugis, "Characterization and modeling on NbC heterogeneous precipitation in model IF steels", in *Conference Proceedings of MS&T 2004*, TMS, 2004, p. 31-37.

[104] S. Dawson, N. D. G. Mountford, I. D. Sommerville and A. McLean, "The evaluation of metal cleanliness in the steel industry", Part IV, Preferential dissolution techniques, Iron and Steelmaker, Vol. 15, no. 10, 1988, p. 54-55.

[105] S. Read, R. K. Gibbs and B. A. Parker, "Extraction and characterization of precipitates formed in a niobium HSLA steel", Materials Forum, Vol. 14, 1990, p. 304-307.

[106] S. Hinotani, J. Endo, T. Takayama, N. Mizui and Y. Inokuma, "Isolation and determination of sulfides in Ti-bearing ultra low carbon steels", The Iron and Steel Institute of Japan (ISIJ International), Vol. 34 (1), 1994, p. 17-23.

[107] K. Segawa, "Recent development on the isolation of inclusions (precipitates) in steel", The Iron and Steel Institute of Japan (ISIJ International), Vol. 52, 1966, p. 967-980.

[108] S. Kanazawa, A. Nakashima, K. Okamoto, K. Tanabe and S. Nakazawa, "On the behavior of precipitates in the Nb-Mo heat-treated high strength steel having 80 Kg/mm^2 tensile strength", Transactions of the Japan Institute of Metals, Vol. 8, no. 2, 1967, p. 113-119.

[109] W. R. Bandi, "Second phases in steel", Science, New Series, Vol. 196, no. 4286, 1977, p. 136-142.

[110] "Standard test method for acid-insolute content of copper and iron powders", ASTM designation: E194-99, Pennsylvania: American Society for Testing Materials-ASTM; 1990, p. 1-2.

[111] M. Fernandes, N. Cheung and A. Garcia, "Investigation of nonmetallic inclusions in continuously cast carbon steel by dissolution of the ferrite matrix", Materials Characterization, Vol. 48, 2002, p. 255-261.

[112] T. Mori and K. Fujita, "Behaviour of niobium carbides and nitrides in steel", Journal of the Iron and Steel Institute of Japan, Vol. 50, 1964, p. 911-917.

[113] H. Brunckova and S. Niznik, "Chemical isolation of precipitates in IF steels", Chemistry, Vol. 47, no. 6, 1993, p. 346-350.

[114] Physical constants of inorganic compounds, CRC Handbook of Chemistry and Physics, Binghamton, N.Y.: Knovel, c2004.

[115] R. G. Smerko and D. A. Flinchbaugh, "Recent progress in the chemical extraction of nonmetallic inclusions in steel----techniques and applications", Journal of Metals, Vol. 20, 1968, p. 43-51.

[116] Y. Yoshida and Y. Funahashi, "On the extraction and size distribution determination of large nonmetallic inclusions in steel by slime method," Transactions of the Iron and Steel Institute of Japan, Vol. 16, no. 11, 1976, p. 628-636.

[117] J. E. Garside, T. E. Rooney and J. J. J. Belli, "The alcoholic-iodine method for the extraction of inclusions from steel", Journal of the Iron and Steel Institute, Vol. 185, 1957, p. 95-103.

[118] H. F. Beeghly, "Determination of aluminum nitride nitrogen in steel", Analytical Chemistry, Vol. 21, no. 12, 1949, p. 1513-1519.

[119] Y. Ishiguro, T. Murayama, A. Chino, K. Sato, Y. Shima, A. Kido and M. Morita, "A precise quantitative analysis of precipitates in Ti-bearing interstitial-free steel", in *39th Mechanical Working and Steel Processing Conference*, Iron and Steel Society of AIME, 1998, p. 255-264.

[120] Y. Okura, "Separation and determination of oxide inclusions in plain carbon steel with a methanolic bromine solution", 1st Report, Bulletin of the Japan Institute of Metals (Nippon Kinzoku Gakkaishi), Vol. 24, no. 4, 1960, p. 237-241.

[121] Y. Okura, "Separation and determination of oxide inclusions in plain carbon steel with a methanolic bromine solution", 3rd Report, Bulletin of the Japan Institute of Metals (Nippon Kinzoku Gakkaishi), Vol. 24, no. 5, 1960, p. 289-293.

[122] O. Kammori, I. Taguchi and K. Sato, "Infrared spectroscopic identification of trace amounts of boron nitride in the residues extracted from steel", Transactions of the Japan Institute of Metals, Vol. 12, no, 2, 1971, p. 125-129.

[123] Y. Yoshida, Y. Funahashi and Y. Kamino, "The determination of boron nitride in steel by means of electrolytic extraction-infrared spectroscopy", Journal of the Iron and Steel Institute of Japan (Tetsu-to-Hagane), Vol. 64, no. 5, 1978, p. 640-649.

[124] H. Brunckova and F. Kovac, "Chemical and electrochemical isolation of AlN and MnS precipitates from Fe-3% Si steels", Chemistry, Vol. 49, no. 3, 1995, p. 115-121.

[125] C. M. Garzon, A. Toro and A. P. Tschiptschin, "Microstructure and chemical characterization of high temperature nitrided 12%Cr stainless steels", Transactions of the Indian Institute of Metals, Vol. 55, no. 4, 2002, p. 255-263.

[126] J. F. Brown, W. D. Clark and A. Parker, "The extraction of minor phases from austenitic steel", Metallurgia, Vol. 56, no. 333, 1957, p. 215-223.

[127] R. Stickler and G. Weidlich, "Microstructure and intergranular corrosion of Inconel-600 and Incoloy-800 tubes", Praktische Metallographie (Prakt. Metallogr.), Vol. 20, no. 4, 1983, p. 174-193.

[128] H. Hughes, "Potentiostatic techniques in constitutional examination of alloy steels", Journal of the Iron and Steel Institute, Vol. 204, 1966, p. 804-810.

[129] Y. Yoshida, Y. Funahashi, KI. Kamino and Y. Kamino, "Determination of nonmetallic inclusions in steel at Kawasaki Steel Corp", Kawasaki Steel Giho, Vol.12, no. 4, 1980, p. 653-664.

[130] Y. Yoshida, Y. Funahashi and Y. Kamino, "State analysis of Ca in steel by electrochemical separation technique", Journal of the Iron and Steel Institute of Japan, Vol. 68, no. 1, 1982, p. 162-171.

[131] C. J. Cron, J. H. Payer and R. W. Staehle, "Dissolution behavior of Fe-Fe_3 structures as a function of pH, potential, and anion - An electron microscopic study", Corrosion, Vol. 27, 1971, p. 1-25.

[132] Y. Kikuta, T. Araki, A. Ohkubo and M. Yoneda, "Metallurgical study on the HAZ embrittlement of high strength steel (Report 1) - Application of the quantitative chemical analysis for the precipitates to steel and its welds", Transactions of the Japan Welding Society, Vol. 10, no. 2, 1979, p. 41-46.

[133] S. Alperine, P. Josso, A. Walder, JH. Davidson and P. Heritier, "Evaluation of the inclusion content in clean nickel-based superalloys", in *Conference Proceedings: High Temperature Materials for Power Engineering 1990*, Kluwer Academic Publishers, 1990, p. 1653-1663.

[134] Y. Okada, J. Endo and T. Nakayama, "Identification of the precipitates in maraging steels by non-aqueous electrolyte extraction method", Journal of the Iron and Steel Institute of Japan (Tetsu-to-Hagane), Vol. 69, no. 6, 1983, p. 703-710.

[135] Y. Yoshida and Y. Funahashi, "On the extraction of large inclusions in steel by slime method and classification according to the size", Journal of the Iron and Steel Institute of Japan (Tetsu-to-Hagane), Vol. 61, no. 10, 1975, p. 2489-2500.

[136] R. A. Stevens and D. Lonsdale, "Isolation, identification and quantification by X-ray diffraction of carbide phases in $2\frac{1}{4}$Cr-1 Mo steel", Journal of Materials Science, Vol. 20, 1985, p. 3631-3638.

[137] G. R. Evers, H. H. Smith and D. J. Michel, "An investigation of second phases in alloy 718 using electrolytic extraction techniques", Metallography, Vol. 11, 1978, p. 441-457.

[138] D. F. Paulonis, J. M. Oblak and D. S. Duvall, "Precipitation in nickel-base alloy 718", ASM Transactions Quarterly**,** Vol. 62, 1969, p. 611-622.

[139] A. Chino and H. Iwata, "Quantitative analysis of gamma prime phase in nickel base superalloys", Journal of the Iron and Steel Institute of Japan (Tetsu-to-Hagane), Vol. 77, no. 11, 1991, p. 2014-2020.

[140] H. M. Rietveld, "Line profiles of neutron powder-diffraction peaks for structure refinement", Acta Crystallographica**,** Vol. 22, 1967, p. 151-152.

[141] H. M. Rietveld, "A profile refinement method for nuclear and magnetic structures", Journal of Applied Crystallography, Vol. 2, 1969, p. 65-71.

[142] G. Will, Powder Diffraction: the Rietveld Method and the Two-stage Method to Determine and Refine Crystal Structures from Powder Diffraction Data, Berlin; New York: Springer, c2006.

[143] V. K. Pecharsky and P. Y. Zavalij, Fundamentals of Powder Diffraction and Structural Characterization of Materials, Boston: Kluwer Academic Publisher, 2003.

[144] R. J. Hill and C. J. Howard, "Quantitative phase analysis from neutron powder diffraction data using the Rietveld method", Journal of Applied Crystallography, Vol. 20, 1987, p. 467-474.

[145] K. Koyanagi, "X-ray diffraction apparatus and method", United States Patent, Patent No.: US 6,516,047 B2, Feb. 4, 2003.

[146] A. Coelho, Topas Academic, Technical Reference.

[147] B. D. Cullity, Elements of X-ray Diffraction, Addison-Weseley Publishing Company Inc., 2nd Edition, 1978.

[148] A. C. Larson and R. B. Von Dreele, General Structure Analysis System (GSAS), Los Alamos National Laboratory Report LAUR 86-748 (2004).

[149] Internal information, IPSCO, Regina, Saskatchewan, Canada.

[150] B. M. Patchett, The Metals Blue Book Welding Filler Metals, CASTI Publishing Inc. and Americal Welding Society, Edmonton, AB, Canada, 1998.

[151] D. B. Williams and C. B. Carter, Transmission Electron Microscopy: a Textbook for Materials Science, New York: Plenum Press, c1996.

[152] J. Goldstein, D. Newbury, D. Joy, C. Lyman, P. Echlin, E. Lifshin, L. Sawyer and J. Michael, Scanning Electron Microscopy and X-Ray Microscopy, Kluwer Academic/Plenum Publishers, New York, USA, 3rd Edition, 2003, p. 371-372.

[153] Z. Chen, M. H. Loretto, R. C. Cochrane, "Nature of large precipitates in titanium-containing HSLA steels", Materials Science and Technology, Vol. 3, 1987, p. 836-844.

[154] M. Beres, T. E. Weirich, K. Hulka and J. Mayer, "TEM investigations of fine niobium precipitates in HSLA steel", Steel Research International, Vol. 75, no. 11, 2004, p. 753-758.

[155] R. G. Baker and J. Nutting, "The tempering of a Cr-Mo-V-W and a Mo-V steel", in *Precipitation Processes in Steels*, The Iron and Steel Institute Special Report No. 64, London, UK, 1959, p. 1-22.

[156] Q. Sha, G. Li, L. Qiao and P. Yan, "Effect of cooling rate and coiling temperature on precipitate in ferrite of a Nb-V-Ti microalloyed strip steel", Journal of Iron and Steel Research, International**,** Vol. 14, Issue 5, Supplement 1, 2007, p. 316-319.

[157] H. -J. Kestenbach, “Dispersion hardening by niobium carbonitride precipitation in ferrite”, Materials Science and Technology, Vol. 13, 1997, p. 731-739.

[158] R. M. Brito and H. -J. Kestenbach, “On the dispersion hardening potential of interphase precipitation in micro-alloyed niobium steel”, Journal of Materials Science, Vol. 16, 1981, p. 1257-1263.

[159] M. Charleux, W. J. Poole, M. Militzer and A. Deschamps, “Precipitation behavior and its effect on strengthening of an HSLA-Nb/Ti steel”, Metallurgical and Materials Transactions A, Vol. 32A, 2001, p. 1635-1647.

[160] K. Miyata, T. Omura, T. Kushida and Y. Komizo, “Coarsening kinetics of multicomponent MC-type carbides in high-strength low-alloy steels”, Metallurgical and Materials Transactions A, 2003, Vol, 34A, p. 1565-1573.

[161] A. L. Patterson, "The Scherrer formula for x-ray particle size determination", Physical Review, Vol. 56, Issue 10, 1939, p. 978-982, American Physical Society.

[162] U. Sharma, MSc thesis, Microstructural characterization of microalloyed linepipe steels, University of Alberta, Canada, 2001.

[163] D. Bai, L. Collins, F. Hamad, X. Chen and R. Klein, “Microstructure and mechanical properties of high strength linepipe steels”, Materials Science and Technology (MS&T) 2007, p. 355-366.

[164] D. A. Porter, K. E. Easterling and M. Y. Sherif, Phase Transformations in Metals and Alloys, Third Edition, CRC Press, 2009.

[165] J. Datsko, Materials Selection for Design and Manufacturing: Theory and Practice, CRC Press, 1997.

[166] George E. Totten, Lin Xie, Kiyoshi Funatani, Handbook of mechanical alloy design, New York: Marcel Dekker, c2004, p. 221-224.

[167] B. Dutta, E. J. Palmiere and C. M. Sellars, “Modelling the kinetics of strain induced precipitation in Nb microalloyed steels”, Acta Materialia, Vol. 49, 2001, p. 785-794.

[168] C. P. Przybyla, B. L. Adams amd M. P. Miles, “Methodology for determining the variance of the Taylor factor: application in Fe-3%Si”, Journal of Engineering Materials and Technology, Vol. 129, 2007, p. 82-93.

[169] A. Putnis, Introduction to Mineral Sciences, Cambridge Univerisity Press, New York, 1992.

[170] C. E. Jaske, CorLAS™ User Manual: Computer program for corrosion-life assessment of piping and pressure vessels, Version 1.0, CC Technologies, 3-2.

[171] A. Saboonchi and S. Hassanpour, "Heat transfer analysis of hot-rolled coils in multi-stack storing", Journal of Materials Processing Technology, Vol. 182, 2007, p. 101-106.

[172] M. A. Mahmoud, A. F. Abd El-Rehim, A. M. Abd El-Khalek, A. H. Ashry, G. Graiss , "Study of precipitates formation in Al-4.5Wt%Cu and Al-4.5Wt%Cu-0.1Wt%In alloys using creep measurements and positron annihilation technique", Crystal Research and Technology, Vol. 40, no. 7, 2005, p. 665-671.

[173] X. Li, J. B. Wiskel, H. Henein, D. G. Ivey and O. Omotoso, "Characterization of microstructure in high strength microlloyed steels using quantitative x-ray diffraction", in *Porceedings of the 7th International Pipeline Conference*, Calgary, AB, Canada, 2008, ASME, Paper# IPC2008-64643.

[174] S. Yu. Nastich, Yu. D. Morozov, B. F. Zin'ko, V. L. Kornilov, S. V. Denisov and E. A. Kudryakov, "Production of high-weldability steel for large-diameter pipe", Metallurgist, Vol. 50, no. 1-2, 2006, p. 54-60.

[175] J. R. Yang and H. K. D. H. Bhadeshia, "The dislocation density of acicular ferrite in steel welds", Welding Research Supplement, 1990, p. 305s-307s.

[176] T. H. Courtney, Mechanical Behavior of Materials, McGraw-Hill Higher Education, 2nd Edition, 2000.

[177] H. Dillen, C. Xhoffer, H. Storms and L. Kestens, "Application of microbeam techniques in the steel industry", Mikrochimica Acta, Vol. 132, 2000, p. 323-335.

[178] P. Maugis, S. Lanteri, D. Ravaine, P. Barges, M. Goune, Y. Bi, M. Lambergts and T. Siwecki, Development of methods for the characterisation and modeling of precipitation in steels: final report, 2004, European Commission.

[179] T. Epicier, "Transmission electron microscopy and nano-precipitation", Advanced Engineering Materials, Vol. 8, no. 12, 2006, p. 1197-1201.

[180] M. G. Burke and M. K. Miller, "Comparison of TEM and APFIM in microstructural characterization and interpretation: an overview", Journal of Electron Microscopy Technique, Vol. 8, 1988, p. 201-210.

[181] M. Leisch, "Three-dimensional nanoscale analysis in physical metallurgy", Vacuum, Vol. 67, 2002, p. 435-442.

[182] K. Stiller and M. Hattestrand, "Nanoscale precipitation in a maraging steel studied by APFIM", Microscopy and Microanalysis, Vol. 10, 2004, p. 341-348.

[183] V. Massardier, V. Guetaz, J. Merlin and M. Soler, "Kinetic and microstructural study of aluminum nitride precipitation in a low carbon aluminum-killed steel", Materials Science and Engineering, Vol. A355, 2003, p. 299-310.

[184] T. Senuma, "Present status of and future prospects for precipitation research in the steel industry", ISIJ International, Vol. 42, no. 1, 2002, p. 1-12.

[185] M. Militzer, A. Deschamps, S. Dilney and D. Meade, "Effect of Cu on microstructure in low-carbon steels", in *41st Mechanical Working and Steel Processing Conference Proceedings*, Iron and Steel Society of AIME, 1999, p. 735-742.

Appendix A: SEM/TEM analysis

A-1. Introduction

In this Appendix, the following information is contained. It includes the microstructure of the steel matrix, SEM/TEM images and EDX spectra of precipitates from different steels.

A-2. SEM/TEM analysis of X80 steels

The microstructure of X80-A4B, X80-B4F and X80-A4F steels is shown in Figure A-1, Figure A-2 and Figure A-3, respectively. The overall SEM-EDX spectrum of the residues from the above steels is shown in Figure A-4, Figure A-5 and Figure A-6, respectively.

TEM BF images and EDX spectra of precipitates from X70-564 steel are shown in Figure A-7 and Figure A-8. Similar SEM/TEM images and spectra of precipitates from other steels are also shown, i.e., Figure A-9, Figure A-10 and Figure A-11 for X80-A4B steel, Figure A-12, Figure A-13 and Figure A-14 for X80-B4F steel, Figure A-15, Figure A-16 and Figure A-17 for X80-A4F steel,

Figure A-7 and Figure A-8 show precipitates from X70-564 steel. Figure A-7 shows some TEM BF images and the corresponding EDX spectra of the extracted precipitates (>10 nm). Figure A-8 shows the morphology, chemistry and size distribution of nano-precipitates (most are ≤10 nm). These nano-precipitates are spherical in shape. Although most of them are less than 10 nm, the largest number of precipitates is in the 4-7 nm size range. Compared with Grade100 steel (Figure 4-11), the nano-precipitates are sparsely distributed in the steel matrix, having a much lower density in the X70-564 steel. TEM-EDX indicates that the nano-precipitates are Nb/Mo-rich with an average composition of $Nb_{0.58}Mo_{0.42}$. Although there is C present in the precipitates, the large C peak in the EDX spectra arises primarily from the carbon replica. The Cu peaks are an artifact arising from the Cu support grid. The Fe peak arises when some of the steel matrix is extracted by the carbon film during sample preparation.

Figure A-9 to Figure A-11 show precipitates from X80-A4B steel. Figure A-9 shows one SE-SEM image. It is clear that most precipitates are less than 100 nm in size and are visible as white spots. Figure A-10 shows several TEM BF images and the corresponding EDX spectra of the extracted precipitates (>10 nm). Figure A-11 shows the morphology, chemistry and size distribution of nano-precipitates (≤10 nm). The largest number of nano-precipitates is in the 4-5 nm size range. Nano-precipitates from X80-A4B steel are Nb/Mo-rich with an average composition of $Nb_{0.68}Mo_{0.32}$.

Figure A-12 to Figure A-14 show precipitates from X80-B4F steel. Figure A-12 shows one BSE-SEM image. Most precipitates are less than 100 nm in size and are visible as white spots. Figure A-13 shows several TEM BF images and the corresponding EDX spectra from the precipitates (>10 nm). Figure A-14 shows the morphology, chemistry and size distribution of nano-precipitates (≤10nm). The largest number of these nano-precipitates is in the 3-6 nm size range. Nano-precipitates from X80-B4F steel are Nb/Mo-rich with an average composition of $Nb_{0.78}Mo_{0.22}$.

Figure A-15 to Figure A-17 show precipitates from X80-A4F steel. Figure A-15 shows some TEM BF images of extracted precipitates (>10 nm). Figure A-16 shows two examples of TEM BF images of nano-precipitates (≤10 nm). In most regions, nano-precipitates are sparsely dispersed in the ferrite matrix, making it difficult to collect enough signals from these precipitates. Figure A-17 shows a region with a cluster of nano-precipitates. The largest number of nano-precipitates in X80-A4F steel is in the 3-4 nm size range. Nano-precipitates from X80-A4F steel are Nb/Mo-rich with an average composition of $Nb_{0.74}Mo_{0.26}$.

In Figure A-10 and Figure A-15, a Ti-rich precipitate has grown together with a MnS inclusion. They were observed in X80-A4B and X80-A4F steels, respectively. The solubility product of MnS in austenite and TiN in the liquid and austenite can be expressed by the following equations. [1,2]

---

[1] T. Gladman, The Physical Metallurgy of Microalloyed Steels, The Institute of Materials, London, UK, 1997.

$$\log K_{s-MnS}(\gamma) = \log[Mn]_e[S]_e = A - C/T = 5.02 - 11625/T \quad \text{(A-1)}$$

$$\log K_{s-TiN}(liquid) = \log[Ti]_e[N]_e = A - C/T = 5.90 - 16586/T \quad \text{(5-1)}$$

$$\log K_{s-TiN}(\gamma) = \log[Ti]_e[N]_e = A - C/T = 3.82 - 15020/T \quad \text{(5-2)}$$

It was assumed that the S content is 0.001wt% for both steels. Under equilibrium conditions, according to the steel chemistry, TiN was formed at 1646ºC using equation (5-2) for X80-A4B steel. The precipitation temperature of MnS is 1219ºC. Therefore, it is expected that TiN precipitates out first and MnS nucleates on the preexisting TiN precipitate for the X80-A4B steel.

Using the same equations, the precipitation temperature for MnS is 1223ºC for X80-A4F steel. However, the precipitation temperature for TiN is 974ºC. Therefore it is expected that MnS precipitates out first and TiN nucleates on the preexisting MnS inclusion for X80-A4B steel.

A-3. SEM/TEM analysis of X100 steels

The microstructure of X100-2B and X100-3C steels is shown in Figure A-18 and Figure A-19, respectively. The overall SEM-EDX spectrum of the residues from the above steels is shown in Figure A-20 and Figure A-21, respectively.

Figure A-22 and Figure A-23 show inclusion and precipitates from X100-2B steel. Figure A-22 shows two SEM images of precipitates that were extracted by carbon replicas. Figure A-22a is an SE-SEM image and Figure A-22b is a BSE-SEM image. The images were taken from the same position. Particles 1 and 2 are both inclusions containing S, Al, Si and some Fe with the corresponding EDX spectra shown in Figure A-22c and d. Other fine bright spots are precipitates. Figure A-23 shows several TEM BF images of precipitates, which were extracted by carbon replicas. Figure A-23d, e and f are EDX spectra from precipitates 1, 2

---

[2] Y. Kang, H. Yu, K. Wang, J. Fu and D. Liu, "Study of microstructure evolution and strengthening mechanism of low carbon steel produced by CPS line", Iron and Steel, Vol. 38, no. 8, 2003, p. 20-26.

and 3 in Figure A-23c. They correspond to Ti-rich, Ti/Nb-rich and Nb-rich precipitates, respectively.

Figure A-24 and Figure A-25 show inclusion and precipitates from X100-3C steel. Figure A-24 shows a BSE-SEM image of precipitates that were extracted by a carbon replica. Particle 1 is an inclusion containing S, Mn, Al, Si and some Fe. Other fine bright spots are precipitates. Figure A-25 shows several TEM BF images of precipitates, which were extracted by carbon replicas. Figure A-25c and d are EDX spectra from precipitates 3 and 4 in Figure A-25b. They correspond to Ti/Nb-rich and Nb-rich precipitates, respectively.

It should be noted that large Si peak shows up in some of the TEM-EDX spectra of precipitates. These precipitates were obtained from carbon replicas. During carbon replica preparation, nital was used to dissolve some of the steel matrix and then precipitates were extracted. Some Si-containing inclusions were dissolved by nital (composed of HCl and ethanol) and forming Si-O phase. Si-O phase was picked up on the carbon replicas with the information shows up in the EDX spectra.

The compositions and approximate sizes of specific precipitates extracted by carbon replicas from X100-2A, X100-2B and X100-3C steels are shown in Table A-1, Table A-2 and Table A-3, respectively.

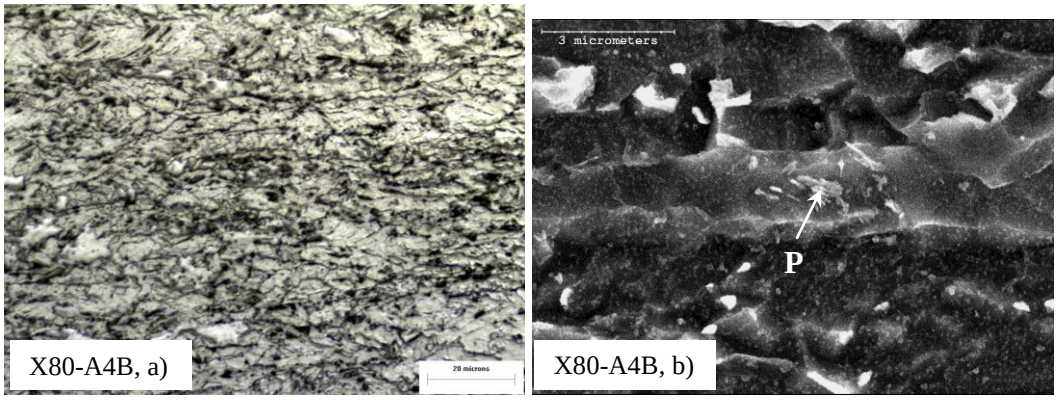

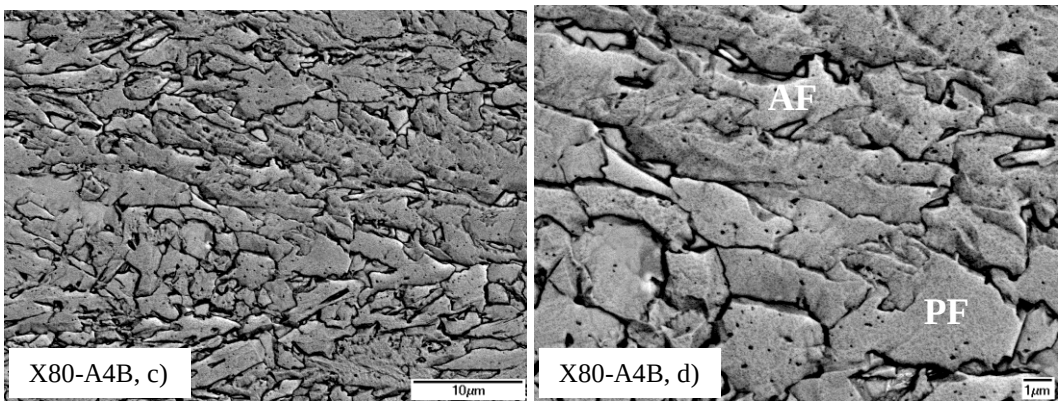

Figure A-1 Microstructure of X80-A4B steel.

a) OM image; b) SEM image showing pearlite-like microstructure, using 20kV; c, d) inverted SE-SEM image at different magnifications for grain size measurement, using 5kV.

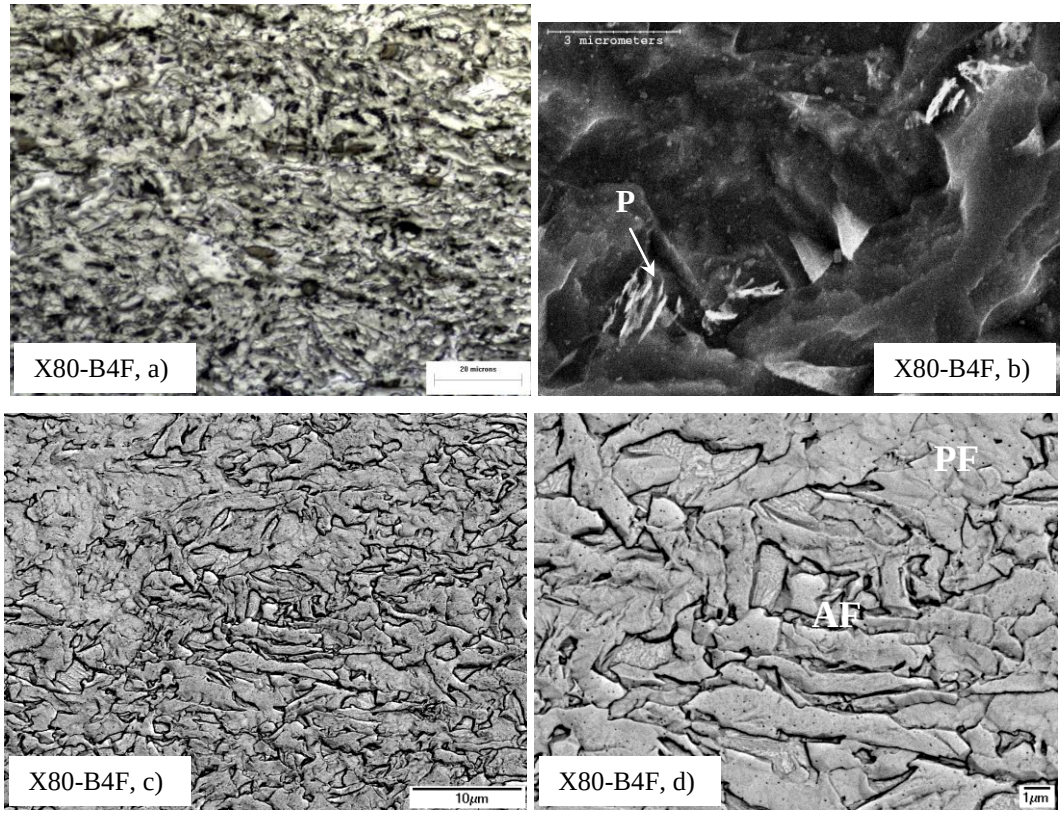

Figure A-2 Microstructure of X80-B4F steel.

a) OM image; b) SEM image showing pearlite-like microstructure, using 20kV; c, d) inverted SE-SEM image at different magnifications for grain size measurement, using 5kV.

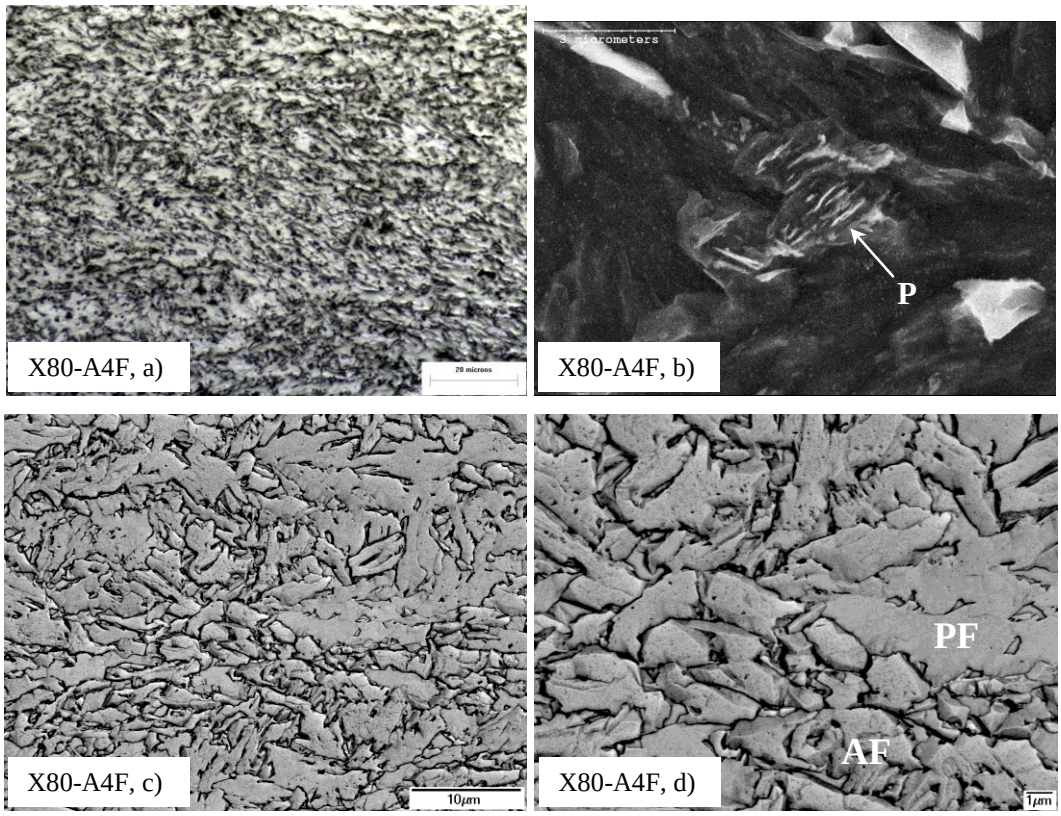

Figure A-3 Microstructure of X80-A4F steel.

a) OM image; b) SEM image showing pearlite-like microstructure, using 20kV; c, d) inverted SE-SEM image at different magnifications for grain size measurement, using 5kV.

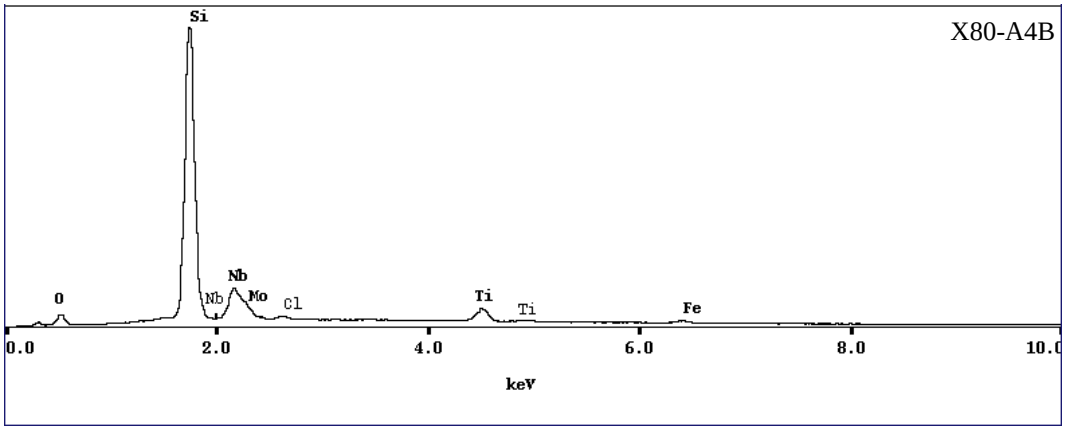

Figure A-4 SEM-EDX chemical analysis of the residue extracted from X80-A4B steel.

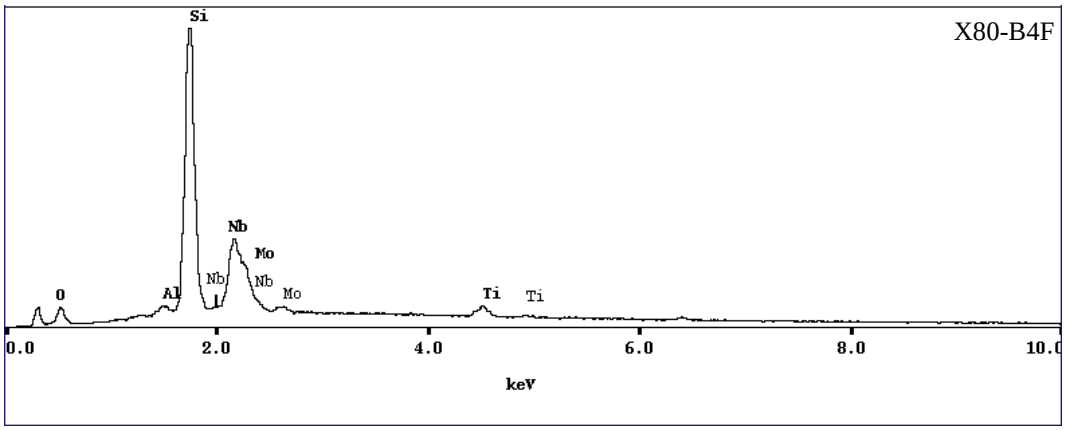

Figure A-5 SEM-EDX chemical analysis of the residue extracted from X80-B4F steel.

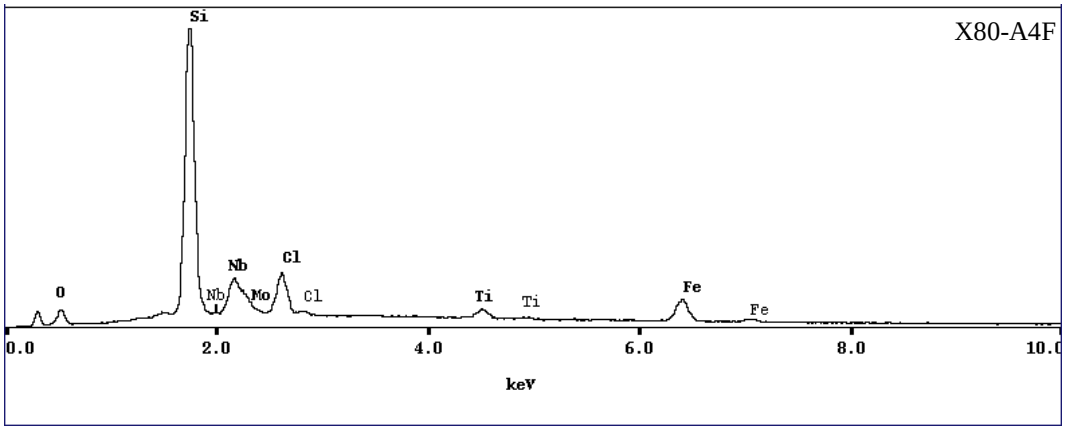

Figure A-6 SEM-EDX chemical analysis of the residue extracted from X80-A4F steel.

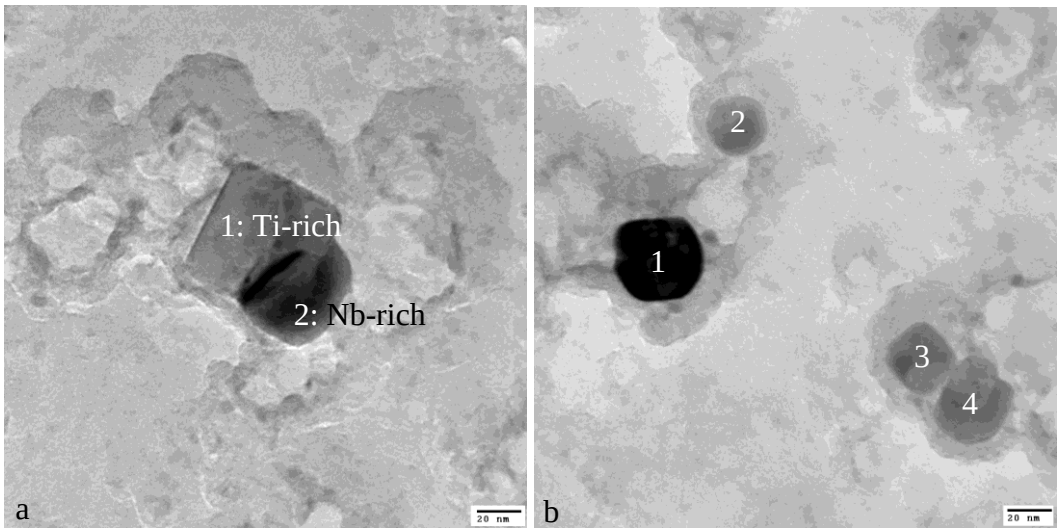

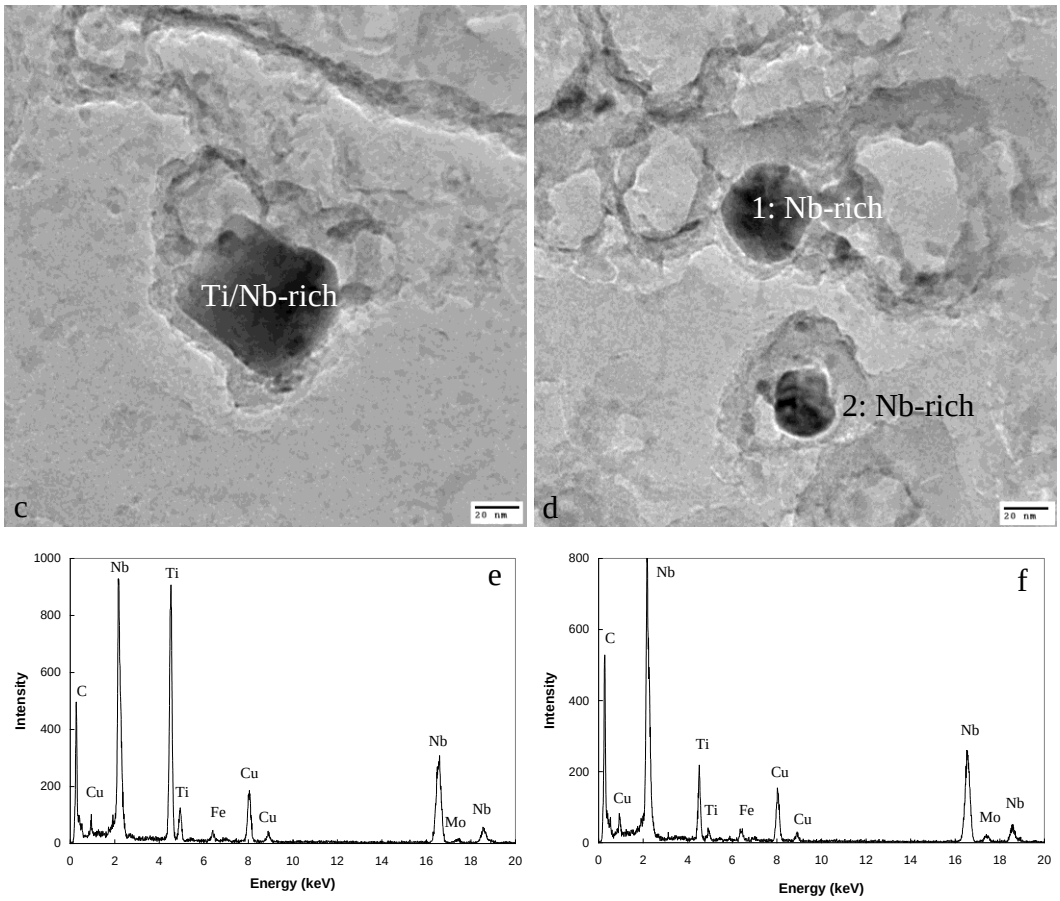

Figure A-7 TEM BF images and EDX spectra of precipitates (>10 nm) from X70-564 steel extracted by carbon replicas.

a-d) TEM BF images; four particles in b are all Nb-rich; e) EDX spectrum of precipitate (Ti/Nb-rich) in c; f) EDX spectrum of particle 1 (Nb-rich) in d.

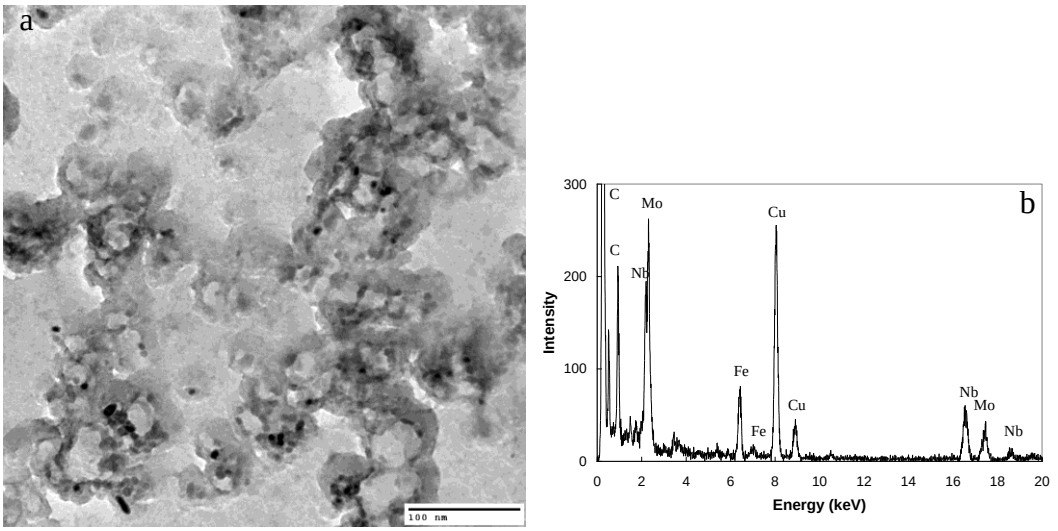

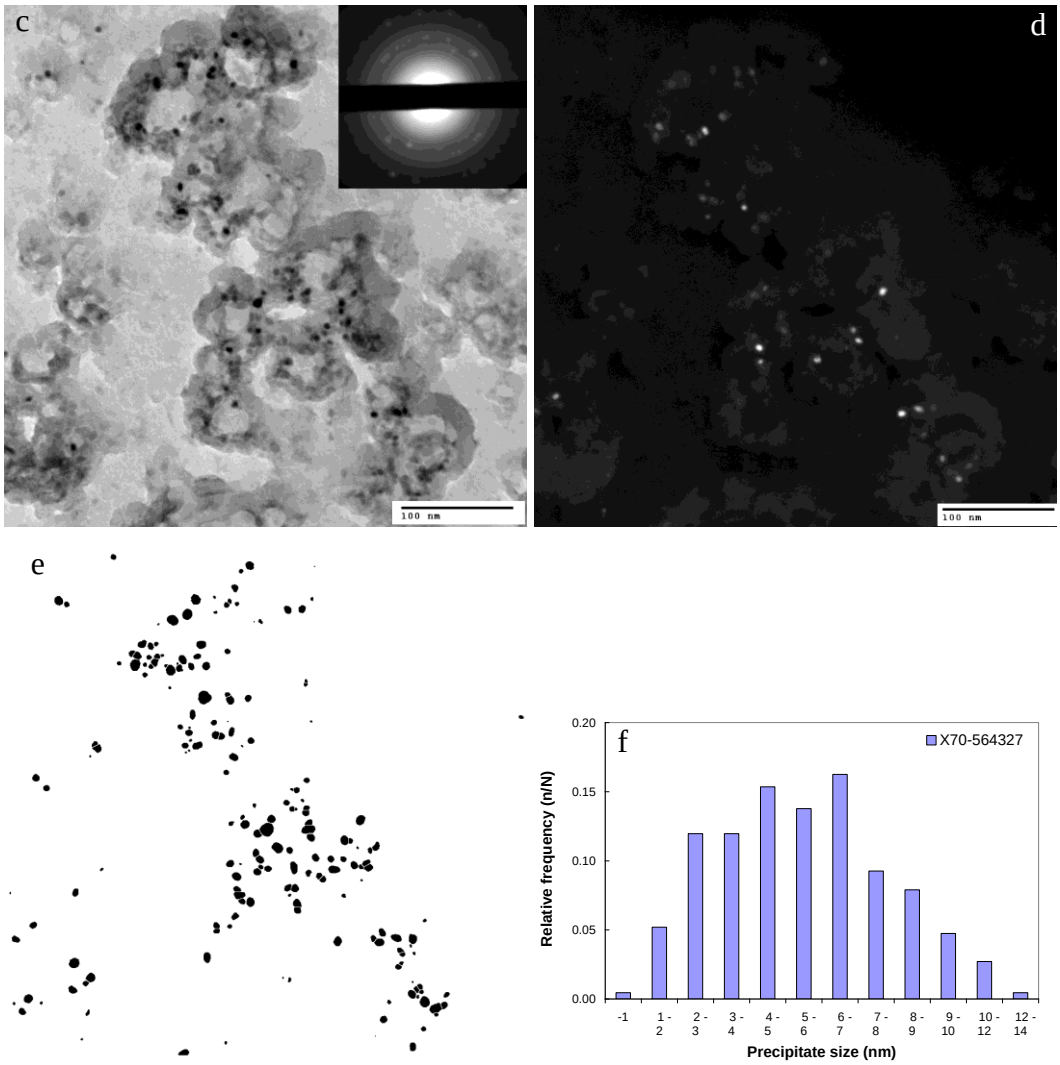

Figure A-8 Nano-precipitates (≤ 10 nm) from X70-564 steel.

a) TEM BF image of nano-precipitates; b) EDX spectrum from nano-precipitates shown in a; c) TEM BF image of nano-precipitates. The inset in c shows the corresponding SAD pattern from the field of view, indicating fine precipitates have a NaCl-type crystal structure; d) one TEM DF image, taken using part of the {111} and {200} diffraction rings, of the same area shown in c. e) merged image (inverted contrasted) based on DF images, used for size distribution analysis; f) size distribution of nano-precipitates.

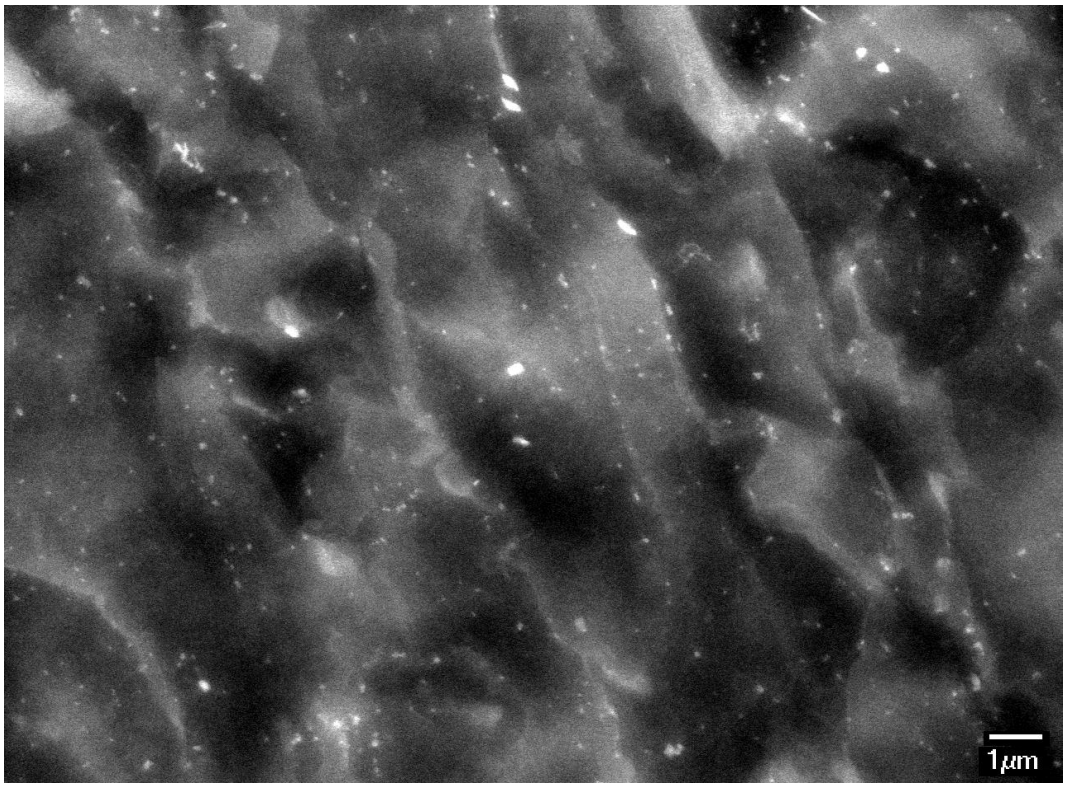

Figure A-9 SE-SEM image of precipitates from X80-A4B steel.

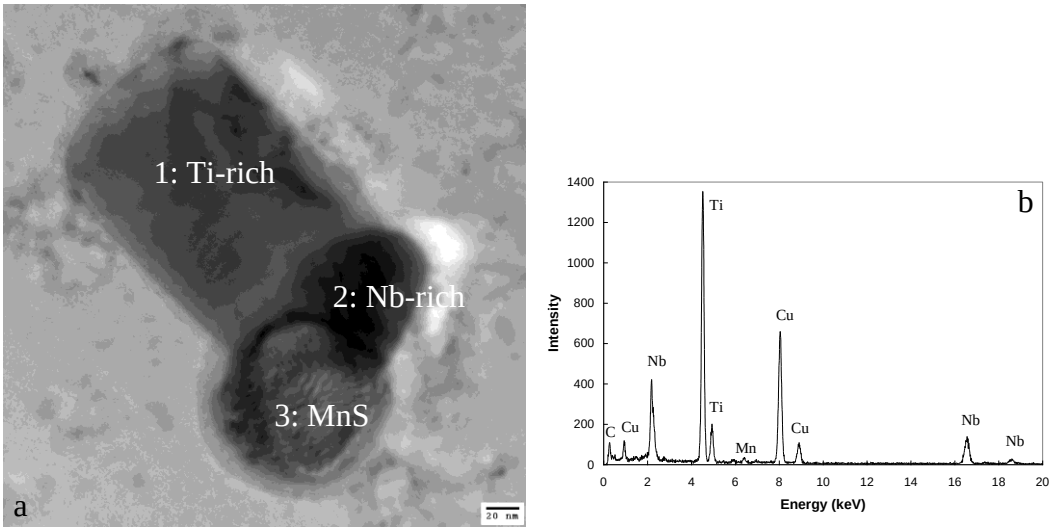

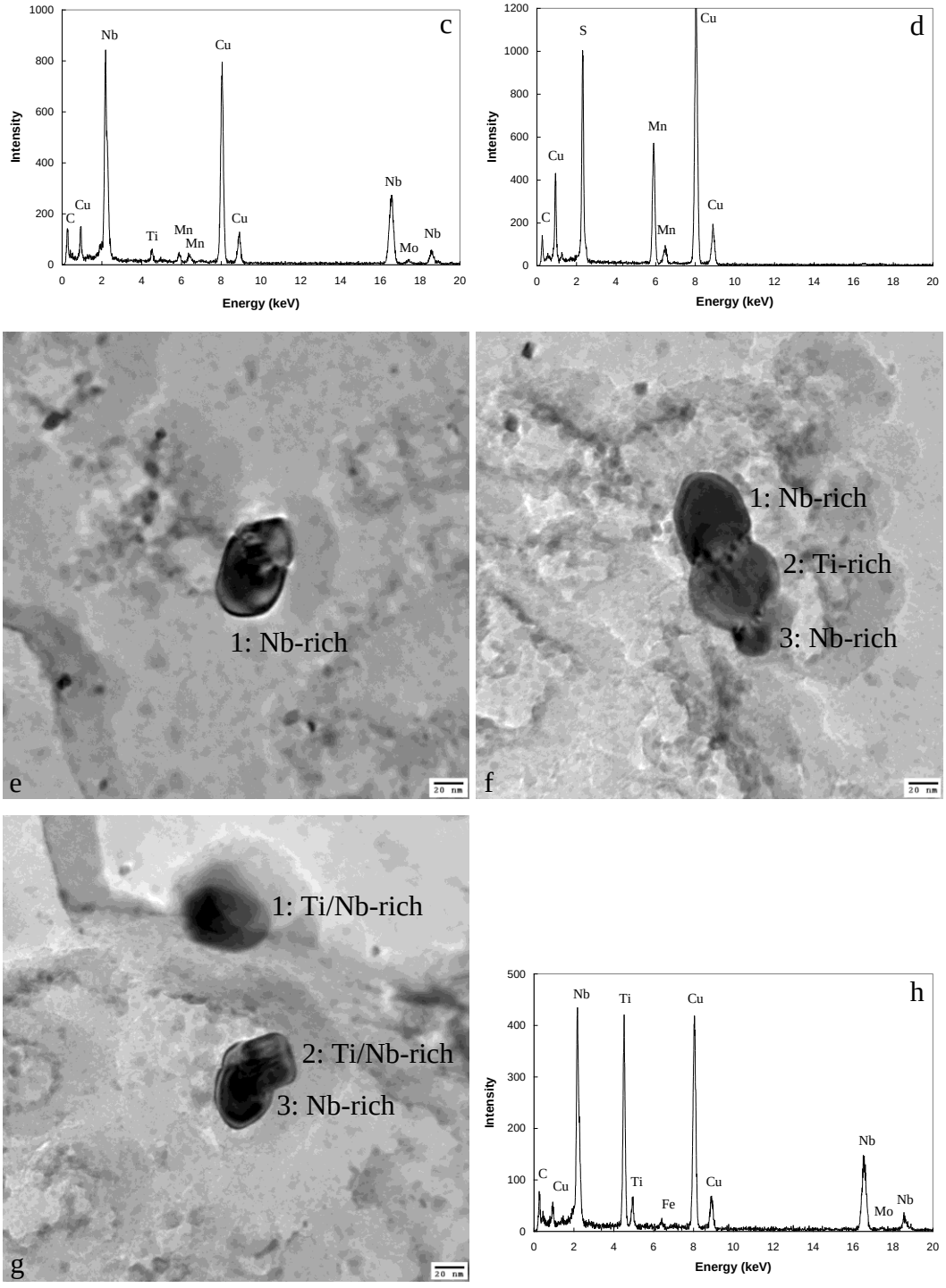

Figure A-10 TEM BF images and EDX spectra of precipitates (>10nm) from X80-A4B steel.

a) A round MnS inclusion and a Nb-rich precipitate nucleate on a Ti-rich precipitate. The rounded inclusion indicates the efficiency of inclusion shape control by additions of Ca, minimum amounts of Zr or Ce; [3]
b-d) EDX spectrum from particle 1 (Ti-rich), 2 (Nb-rich) and 3 (MnS inclusion) in a; e-g) Nb-rich and Ti/Nb-rich precipitates;
h) EDX spectrum from particle 1(Ti/Nb-rich) in g.

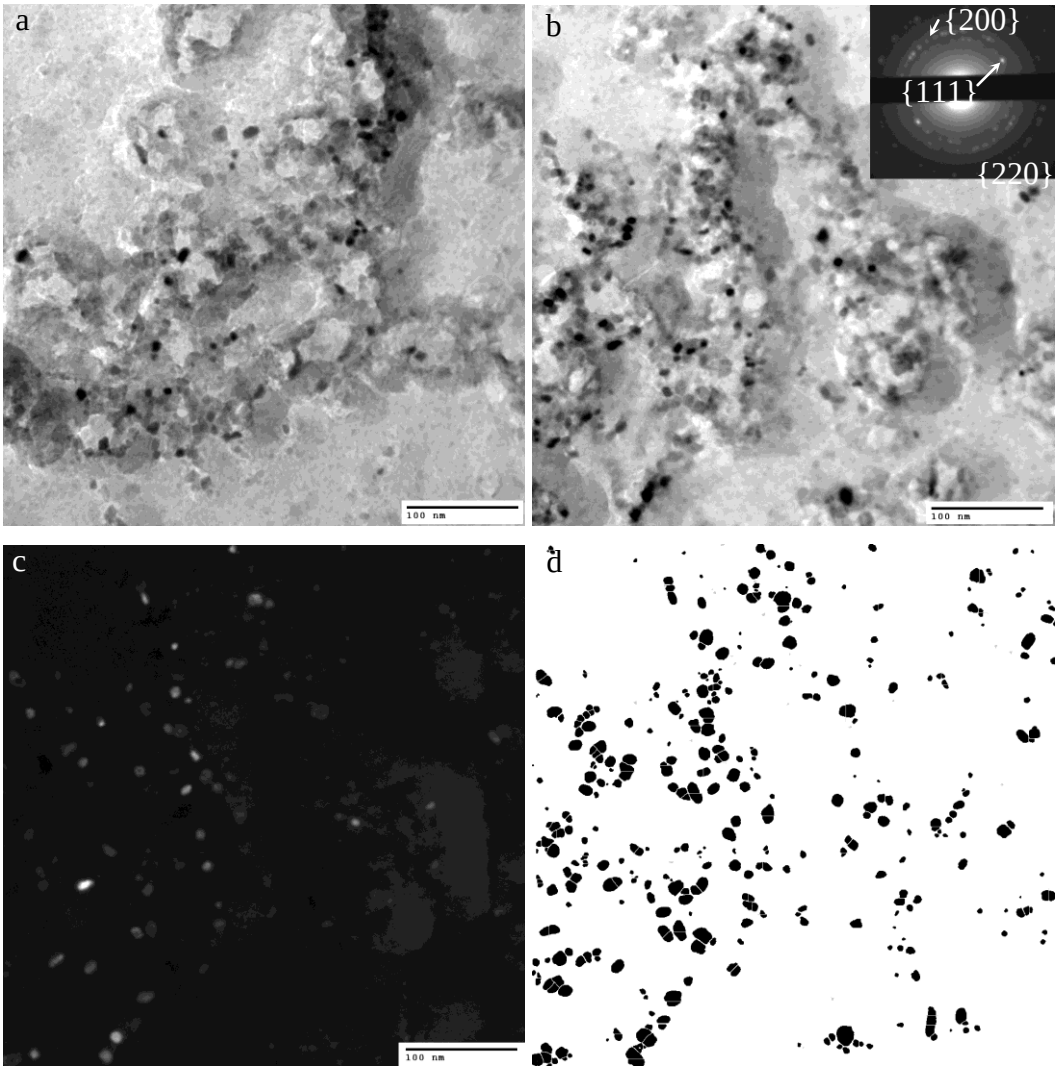

[3] F. B. Pickering, Physical Metallurgy and the Design of Steels, Applied Science Publishers Ltd, London, UK, 1978, p. 81-85.

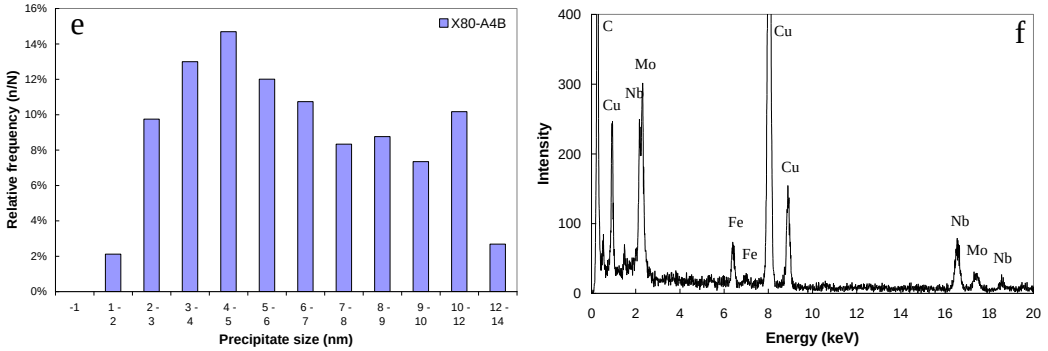

Figure A-11 TEM BF images of nano-precipitates (≤ 10 nm) from X80-A4B steel from a carbon replica.

a, b) TEM BF image of nano-precipitates. The inset in b shows the corresponding SAD pattern from the field of view, indicating fine precipitates have a NaCl-type crystal structure; c) TEM DF image, taken using part of the {111} and {200} diffraction rings, of the same area shown in b; d) merged image (inverted contrast) based on DF images, used for size distribution analysis; e) size distribution of nano-precipitates; f) EDX of nano-precipitates shown in b.

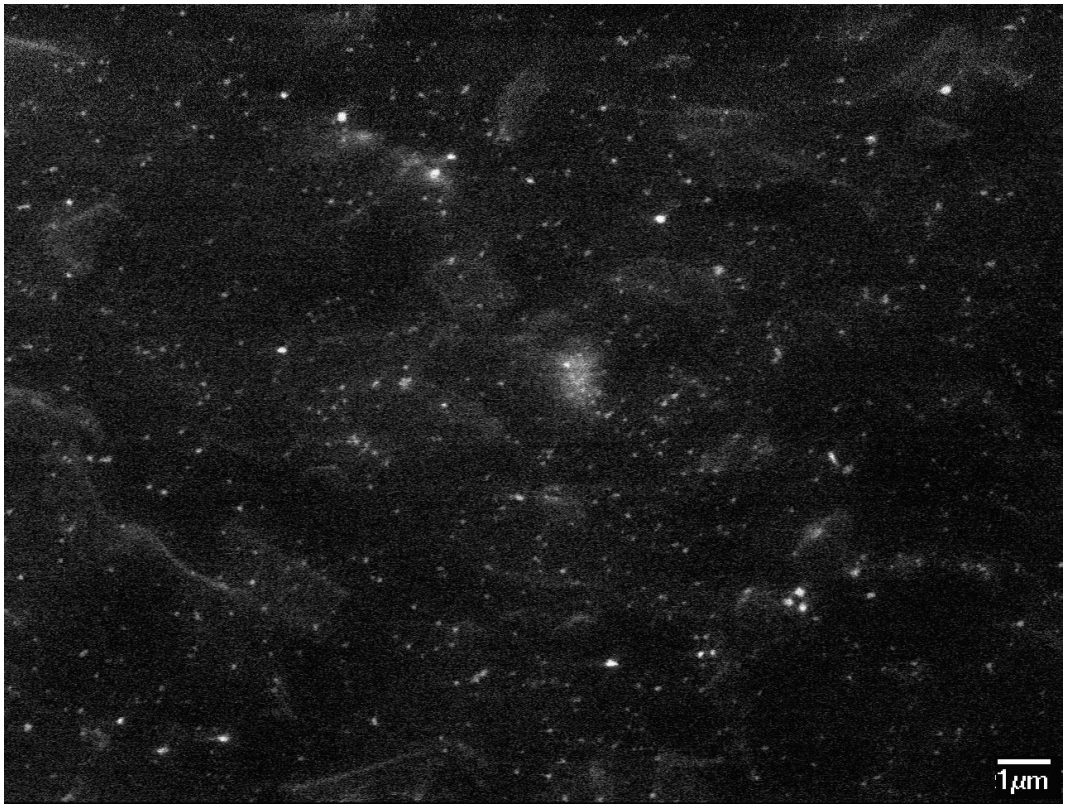

Figure A-12 BSE-SEM image of precipitates from X80-B4F steel.

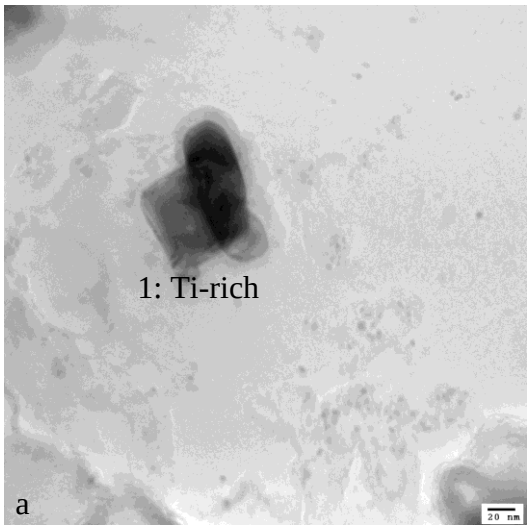
1: Ti-rich
a
20 nm

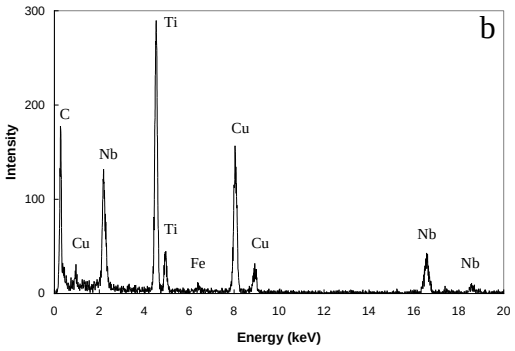
b
Intensity
Energy (keV)
C
Cu
Nb
Ti
Fe
Cu
Cu
Nb
Nb
0
100
200
300
0
2
4
6
8
10
12
14
16
18
20

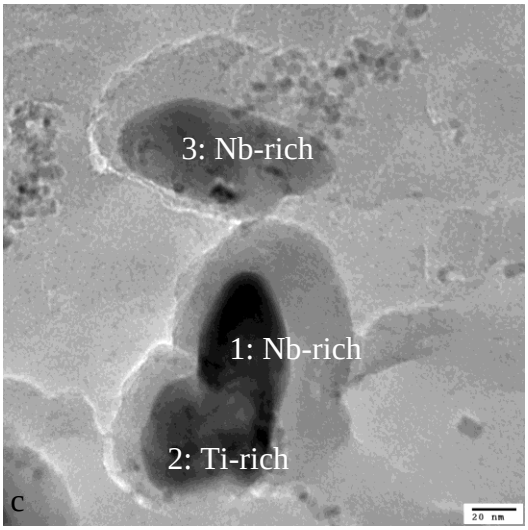
3: Nb-rich
1: Nb-rich
2: Ti-rich
c
20 nm

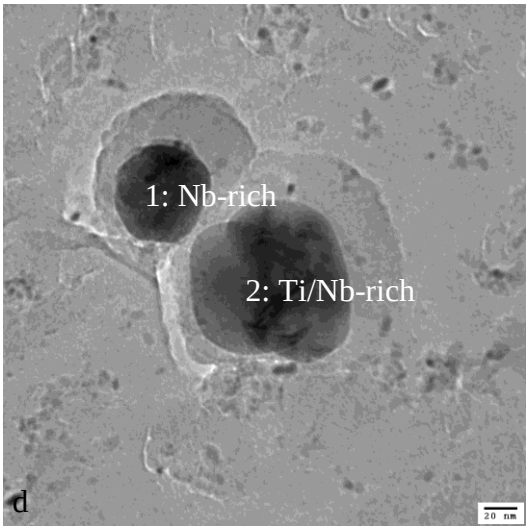
1: Nb-rich
2: Ti/Nb-rich
d
20 nm

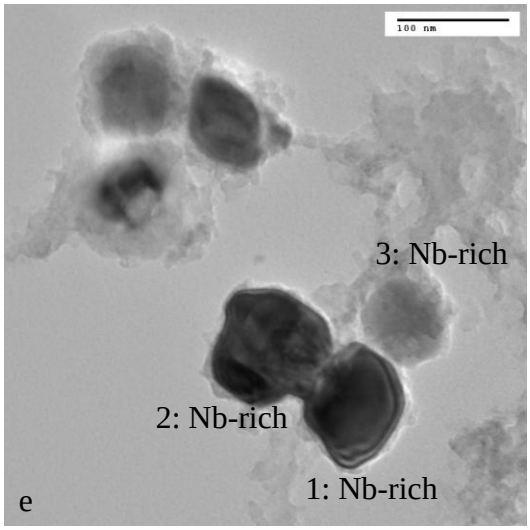
100 nm
3: Nb-rich
2: Nb-rich
1: Nb-rich
e

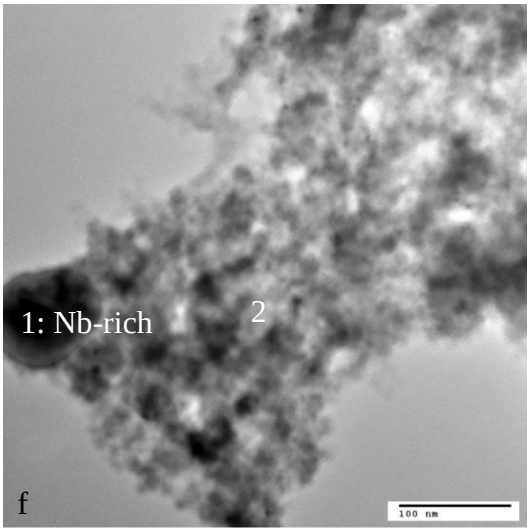
1: Nb-rich
2
f
100 nm

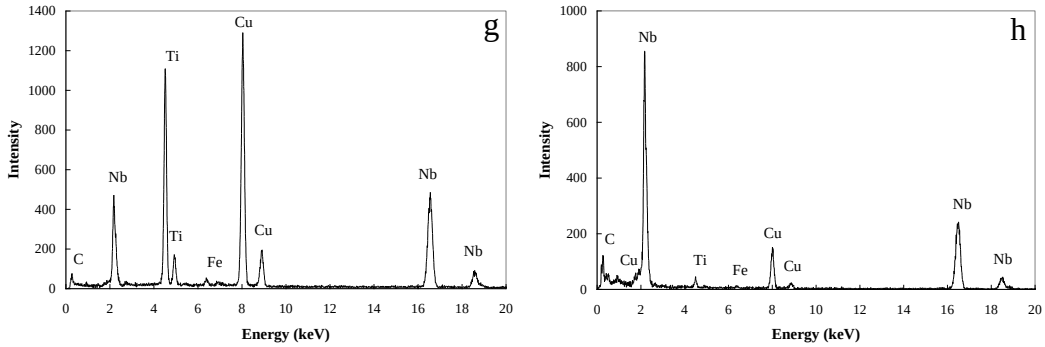

Figure A-13 TEM BF images and the EDX spectra of precipitates from X80-B4F steel. a, b) Ti-rich precipitate and the corresponding EDX; c, d) precipitates extracted by carbon replicas; e, f) precipitates extracted by HCl dissolution; g) EDX spectrum from particle 2 (Ti/Nb-rich) shown in d; h) EDX spectrum from particle 1(Nb-rich) shown in e.

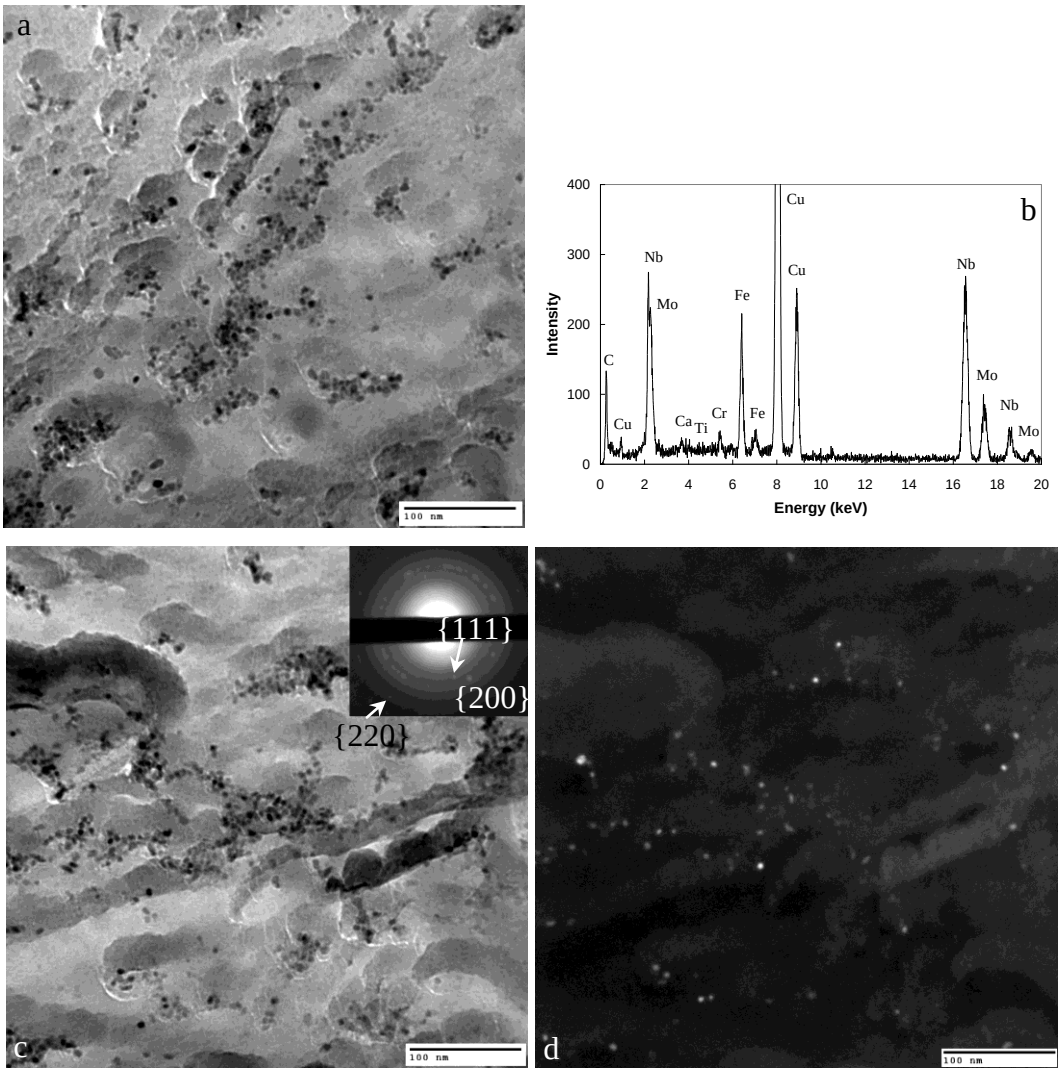

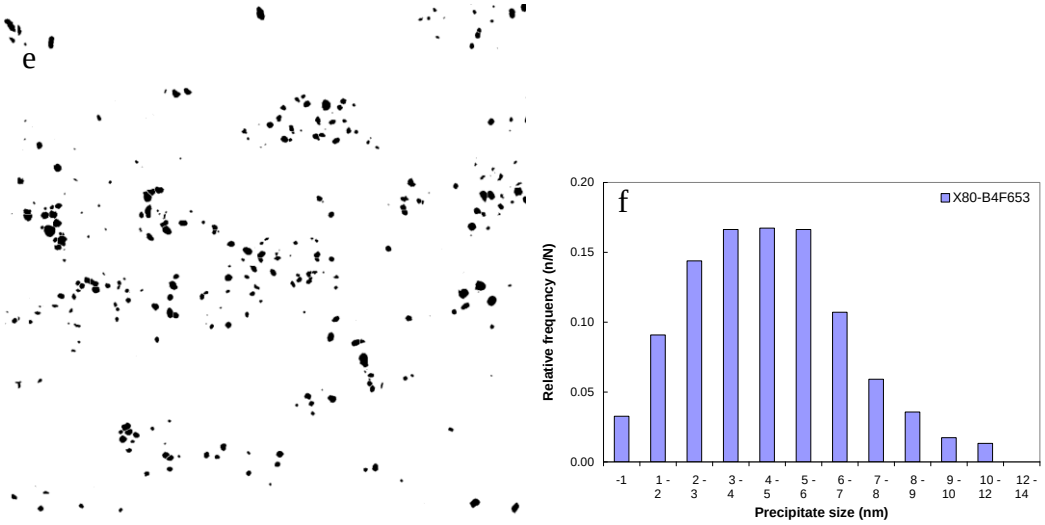

Figure A-14 Nano-precipitates (≤10 nm) from X80-B4F steel.
a) TEM BF image of nano-precipites; b) EDX of nano-precipitates shown in a; c) TEM BF image of nano-precipites. The inset in c shows the corresponding SAD pattern from the field of view, indicating fine precipitates have a NaCl-type crystal structure; d) TEM DF image, taken using part of the {111} and {200} diffraction rings, of the same area shown c; e) merged image (inverted contrast) based on DF images, used for size distribution analysis; f) size distribution of nano-precipiatates.

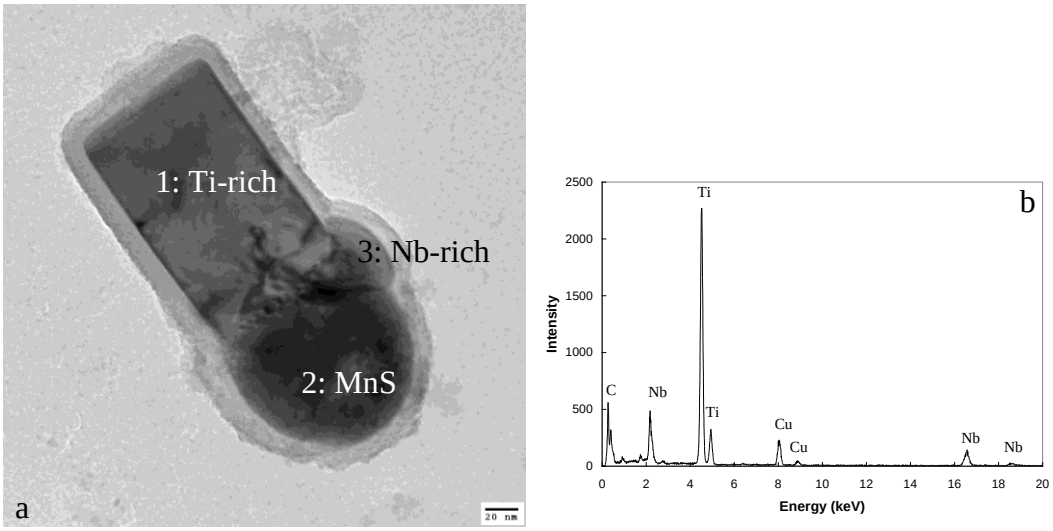

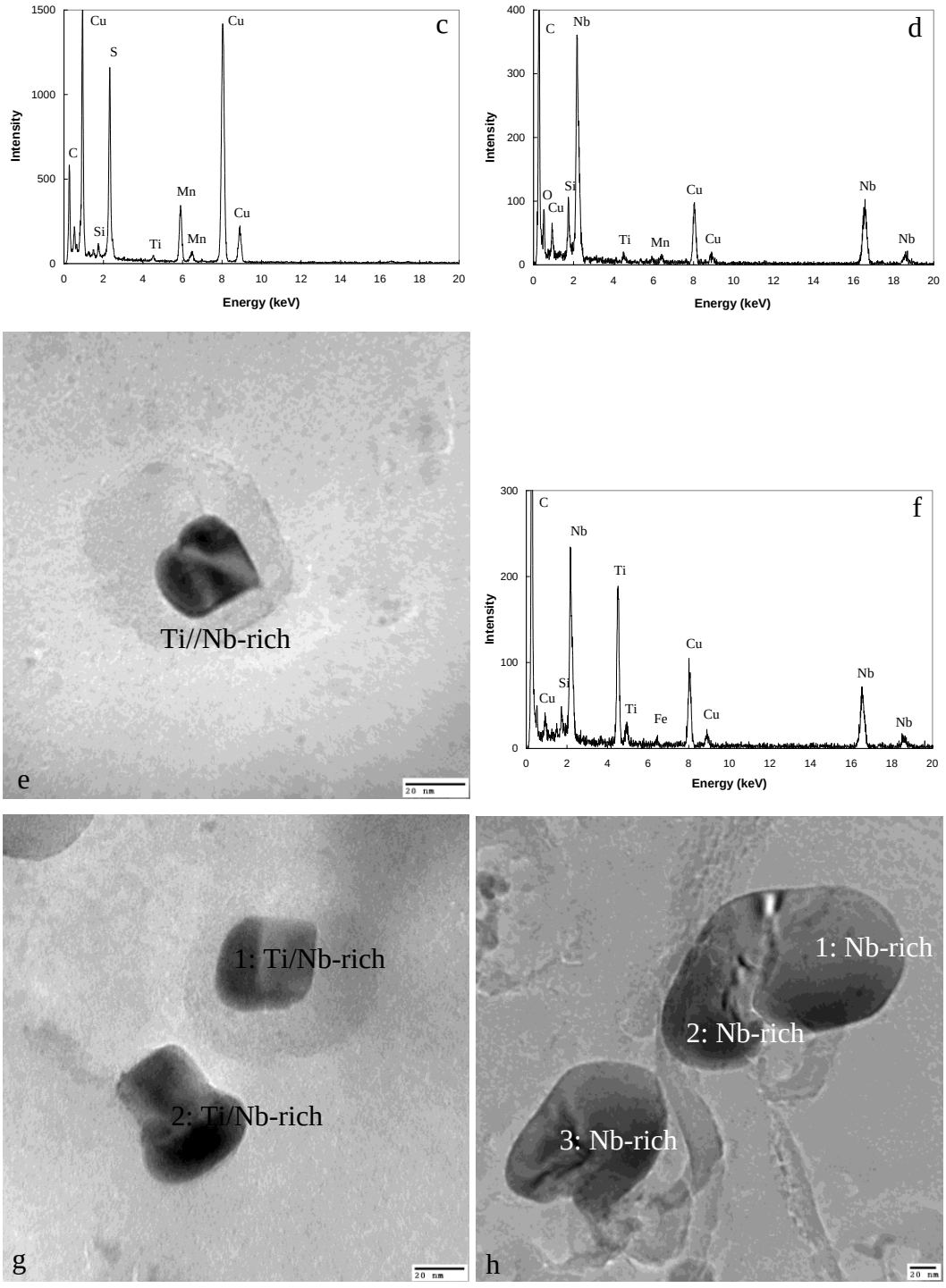

Figure A-15 TEM BF images and the corresponding EDX spactra of precipitates from X80-A4F steel.

a) One Ti-rich precipitate nucleates on a MnS inclusion and a Nb-rich precipitate nucleates on the Ti-rich precipitate. Round MnS inclusion indicates the efficiency of inclusion shape control; b-d) EDX spectra corresponding to particles 1 (Ti-

rich), 2 (Nb-rich) and 3 (MnS inclusion) in a; e, f) Ti/Nb-rich precipitates and the corresponding EDX spectrum. g) Ti/Nb-rich precipitates; h) Nb-rich precipitates.

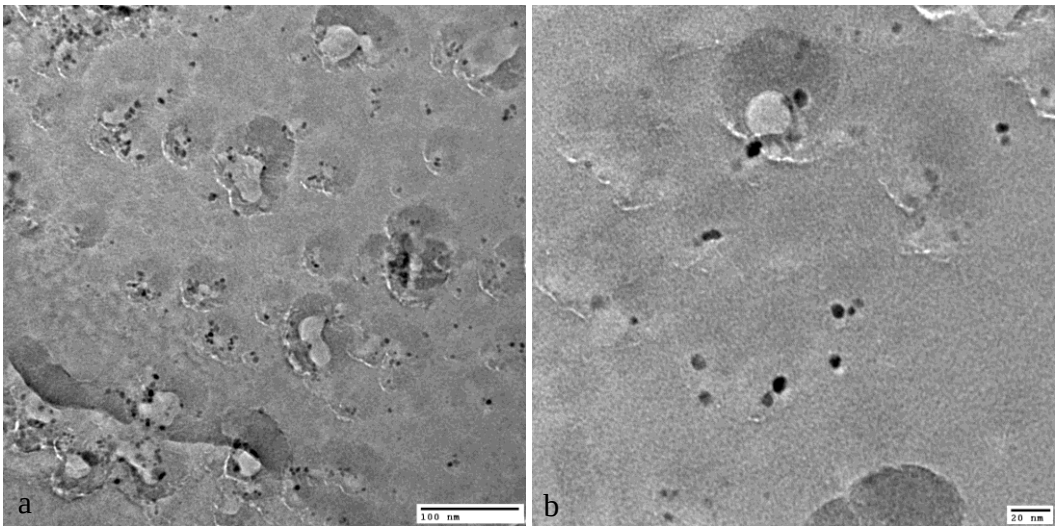

Figure A-16 TEM BF images of nano-precipitates (≤10 nm) sparsely distributed in the X80-A4F steel matrix, making it difficult to collect enough signals from these precipitates.

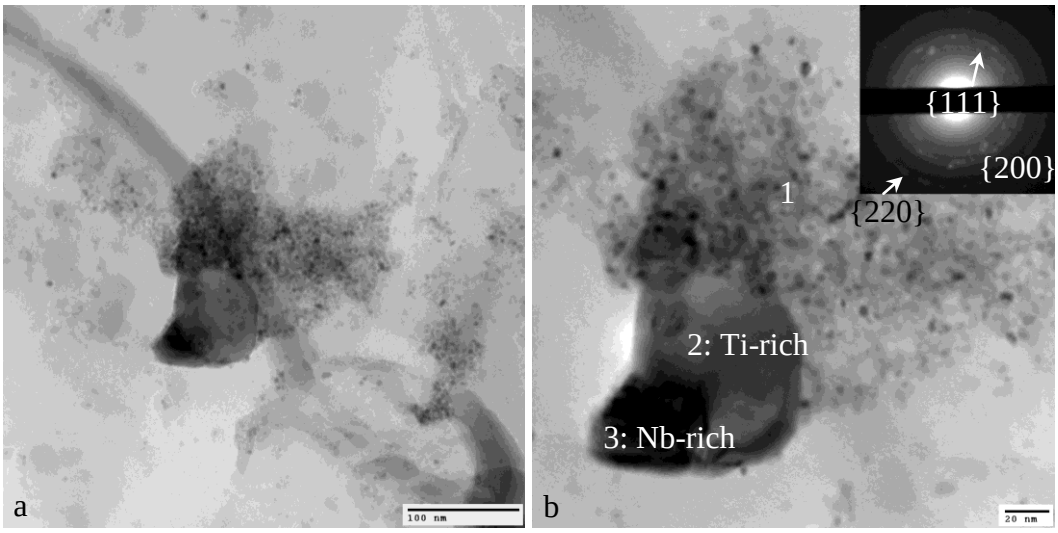

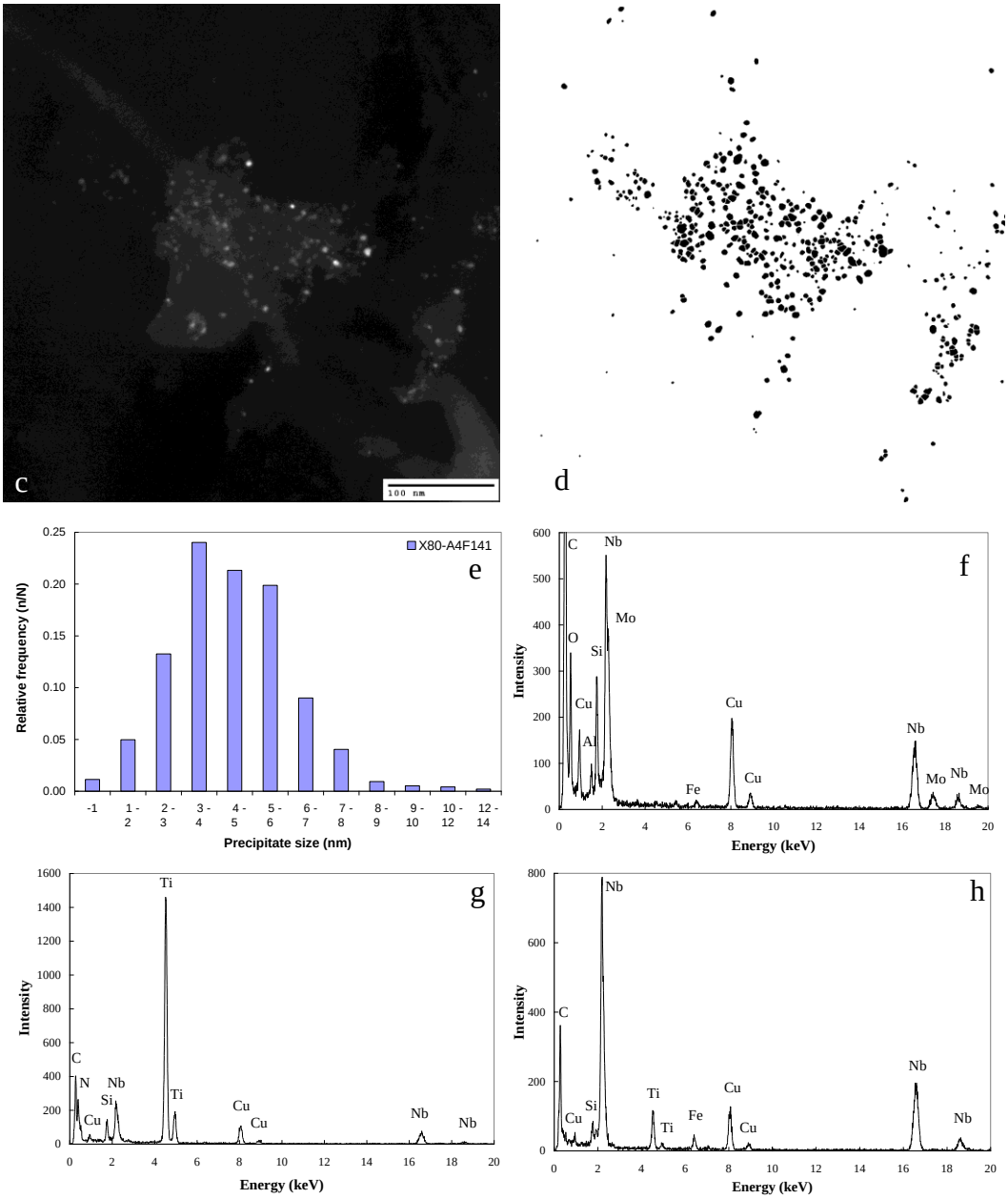

Figure A-17 Nano-precipitates (≤10 nm) from X80-A4F steel.

a) TEM BF image, showing a cluster of nano-precipitates; b) TEM BF image (high magnification); the inset shows the corresponding SAD pattern from the field of view, indicating fine precipitates have a NaCl-type crystal structure; c) One of the TEM DF images, taken using part of the {111} and {200} diffraction rings, of the same area shown in a; d) merged image (inverted contrast) based on DF images, used for size distribution analysis; e) size distribution of nano-

precipitates; f) EDX of nano-precipitates shown in b; g) EDX of precipitate 2 (Ti-rich) shown in b; h) EDX of precipitate 3(Nb-rich) shown in b.

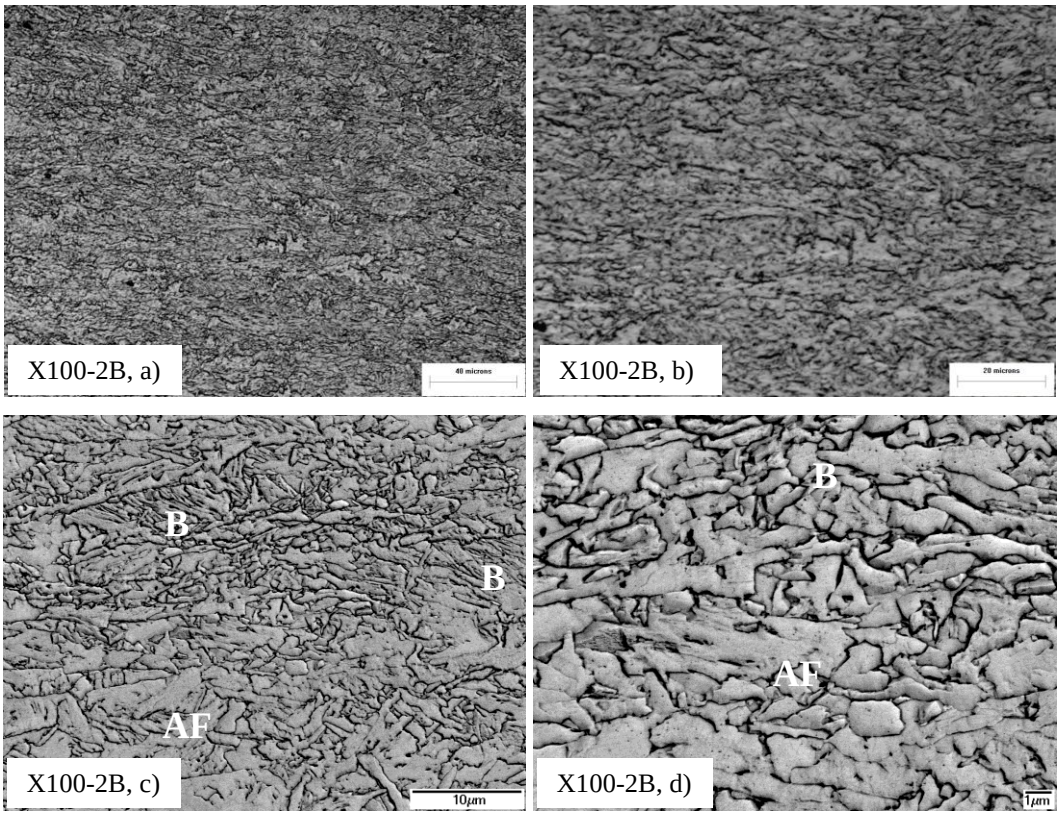

Figure A-18 Microstructure of X100-2B steel.
a, b) OM image; c, d) inverted SE-SEM image at different magnifications for grain size measurement, using 5kV.

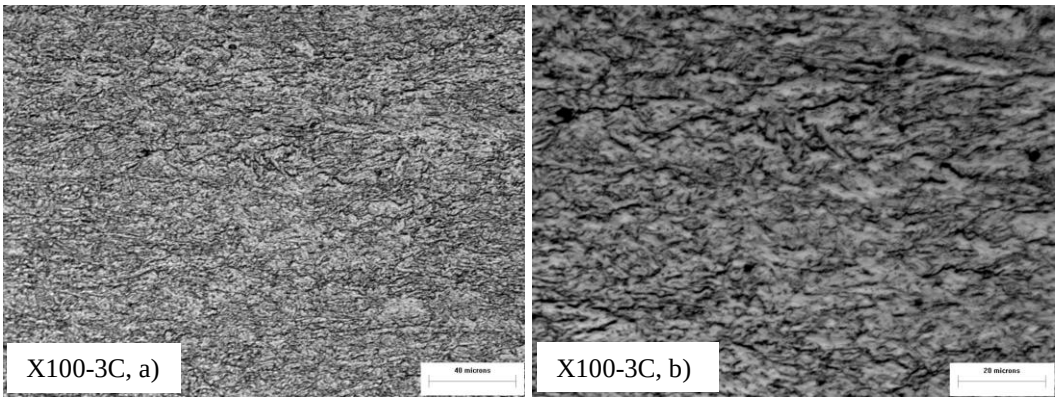

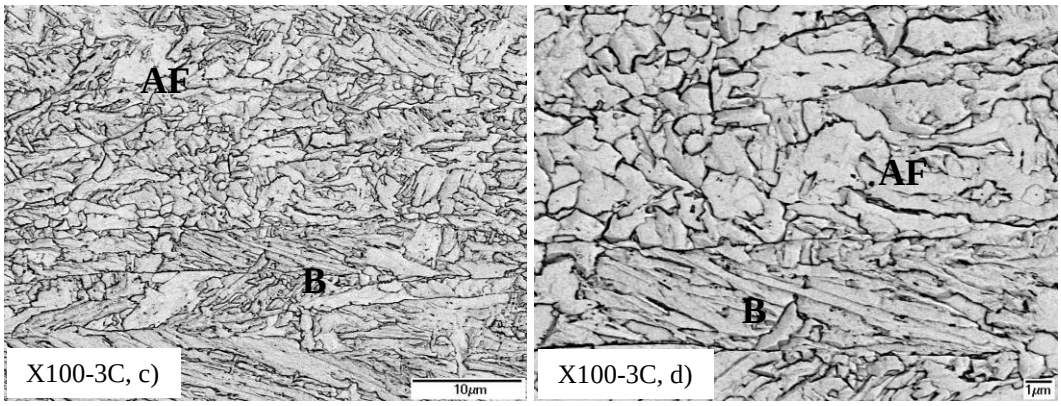

Figure A-19 Microstructure of X100-3C steel.

a, b) OM image; c, d) inverted SE-SEM image at different magnifications for grain size measurement, using 5kV.

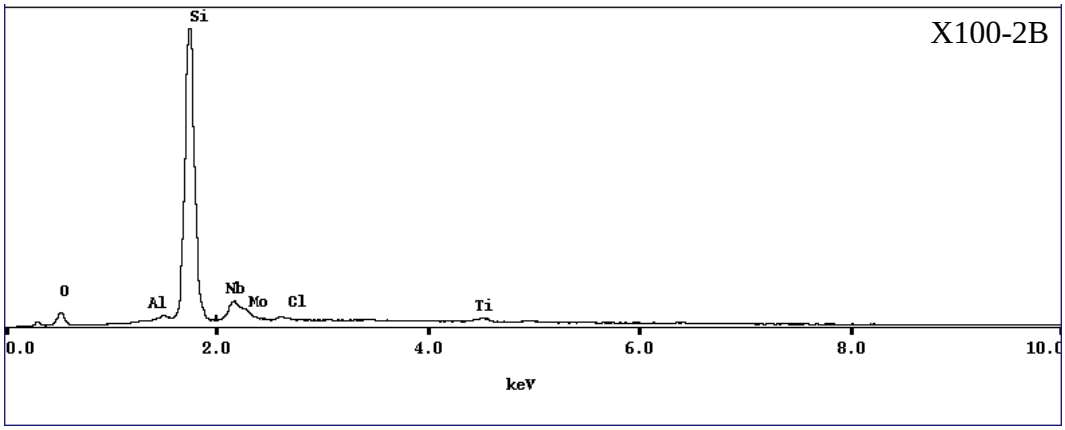

Figure A-20 SEM-EDX chemical analysis of the residue extracted from X100-2B steel.

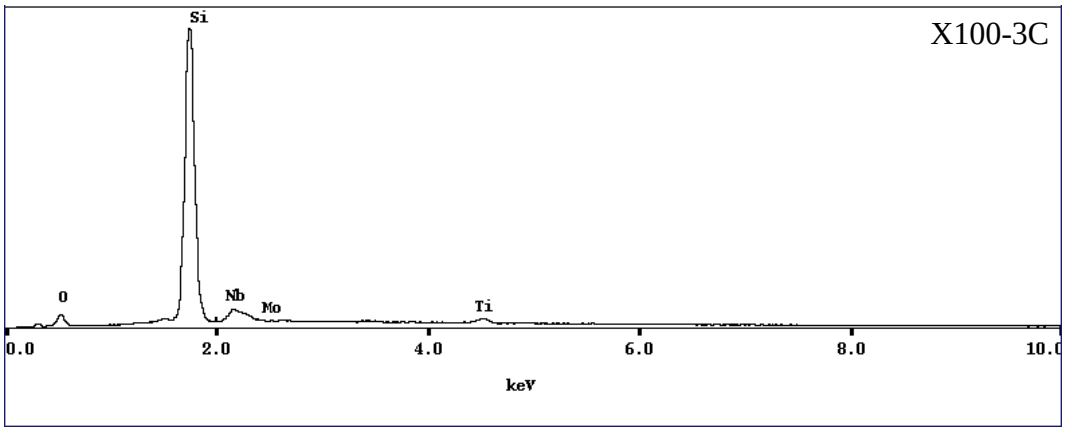

Figure A-21 SEM-EDX chemical analysis of the residue extracted from X100-3C steel.

Table A-1 Chemistry (metallic elements) and size of precipitates from X100-2A steel extracted by carbon replicas

Image	Position	Chemistry	Size (nm)	Group
a	1	$Ti_{0.66}Nb_{0.29}Mo_{0.05}$	30	Ti-rich
	2	$Ti_{0.59}Nb_{0.37}Mo_{0.04}$	32	Ti/Nb-rich
b	1	$Ti_{0.71}Nb_{0.24}Mo_{0.05}$	24	Ti-rich
	2	$Ti_{0.74}Nb_{0.22}Mo_{0.04}$	30	
	3	$Ti_{0.80}Nb_{0.17}Mo_{0.03}$	30	
	4	$Ti_{0.70}Nb_{0.27}Mo_{0.03}$	40	
c	1	$Ti_{0.59}Nb_{0.34}Mo_{0.07}$	25	Ti/Nb-rich
	2	$Ti_{0.53}Nb_{0.43}Mo_{0.04}$	25	
	3	$Ti_{0.59}Nb_{0.39}Mo_{0.02}$	25	
d	1	$Ti_{0.73}Nb_{0.24}Mo_{0.03}$	40	Ti-rich
	2	$Ti_{0.58}Nb_{0.38}Mo_{0.04}$	35	Ti/Nb-rich

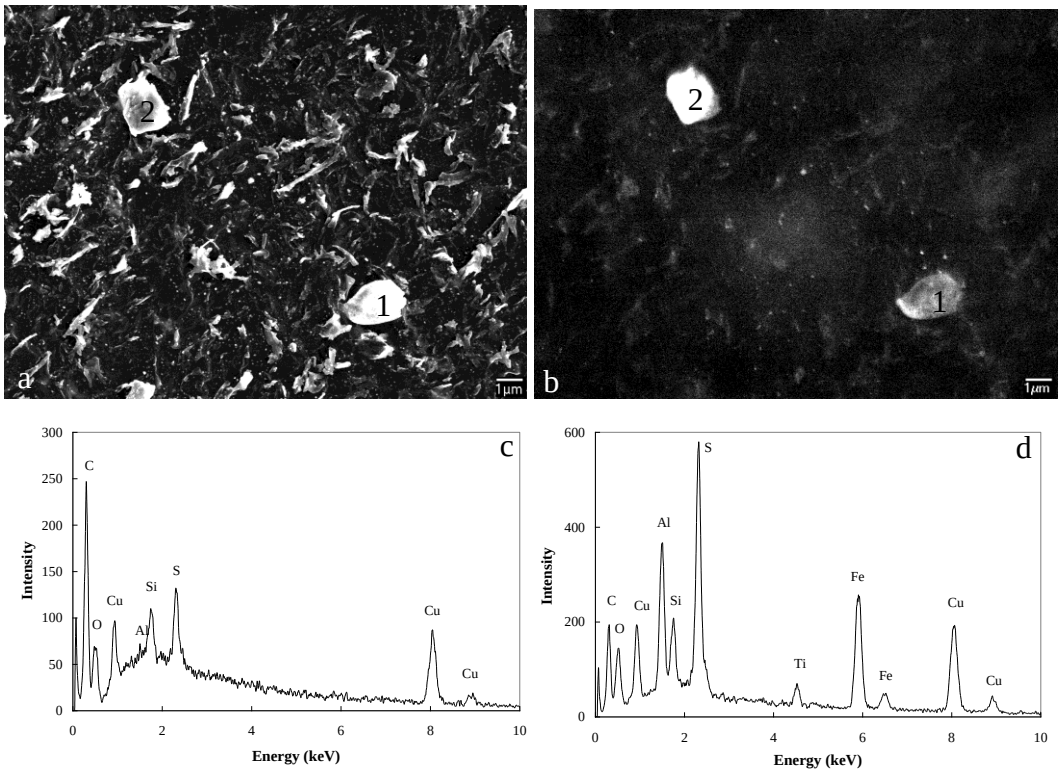

Figure A-22 SEM images and EDX spectra of inclusions and precipitates from X100-2B steel. a) SE-SEM image; b) BSE-SEM image; c) EDX spectrum from particle 1; d) EDX spectrum from particle 2.

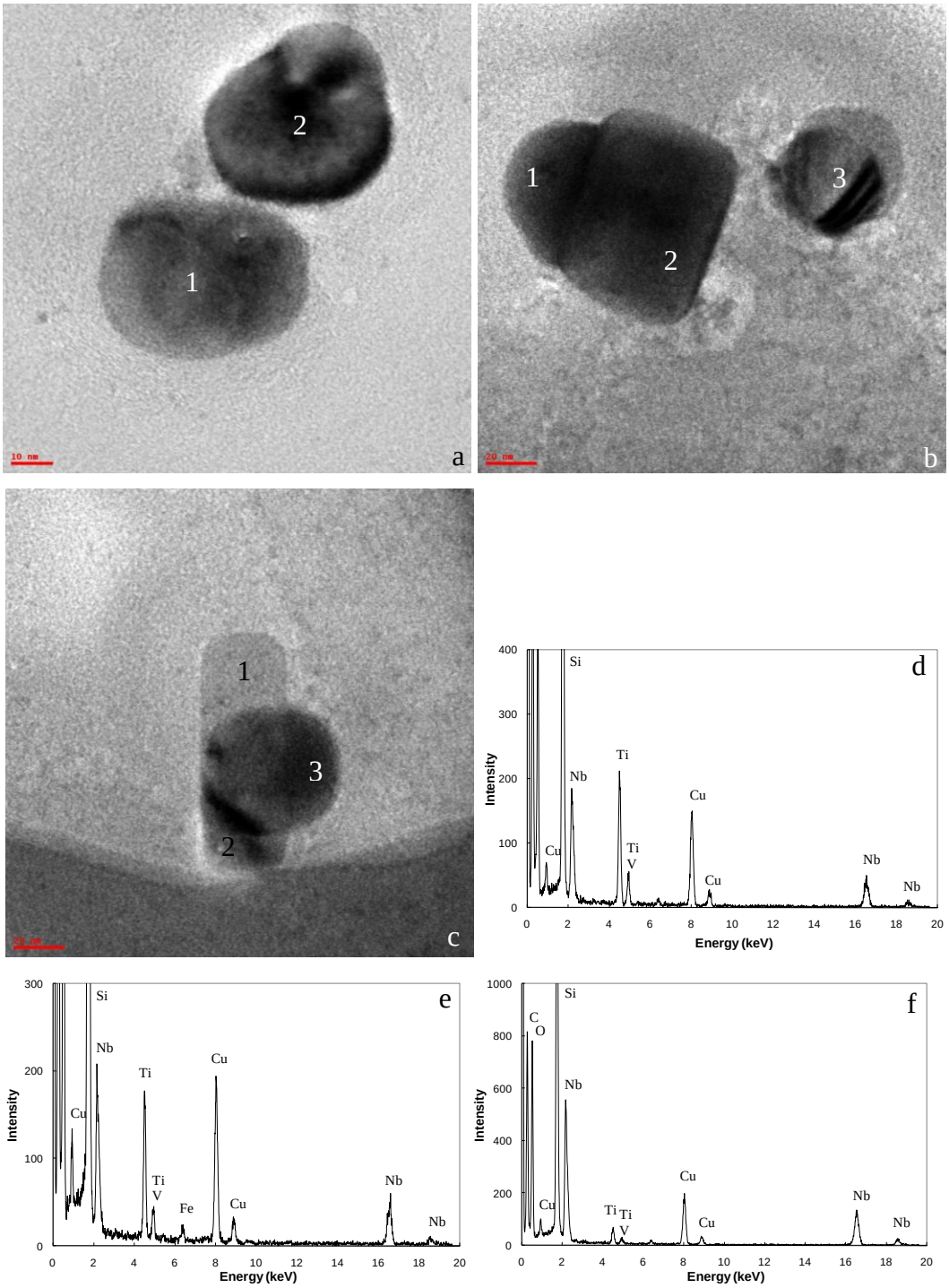

Figure A-23 TEM BF images and EDX spectra of precipitates extracted from X100-2B steel by carbon replicas.

Table A-2 Chemistry (metallic elements) and size of precipitates from X100-2B steel extracted by carbon replicas

Image	Position	Chemistry	Size (nm)	Group
a	1	$Nb_{0.58}Ti_{0.35}V_{0.06}$	50	Ti/Nb-rich
	2	$Nb_{0.89}Ti_{0.09}V_{0.02}$	45	Nb-rich
b	1	$Nb_{0.79}Ti_{0.18}V_{0.03}$	55	
	2	$Ti_{0.78}Nb_{0.18}V_{0.04}$	77	Ti-rich
	3	$Ti_{0.72}Nb_{0.23}V_{0.05}$	40	
c	1	$Ti_{0.62}Nb_{0.32}V_{0.06}$	33	
	2	$Ti_{0.55}Nb_{0.40}V_{0.05}$	30	Ti/Nb-rich
	3	$Nb_{0.83}Ti_{0.14}V_{0.02}$	50	Nb-rich

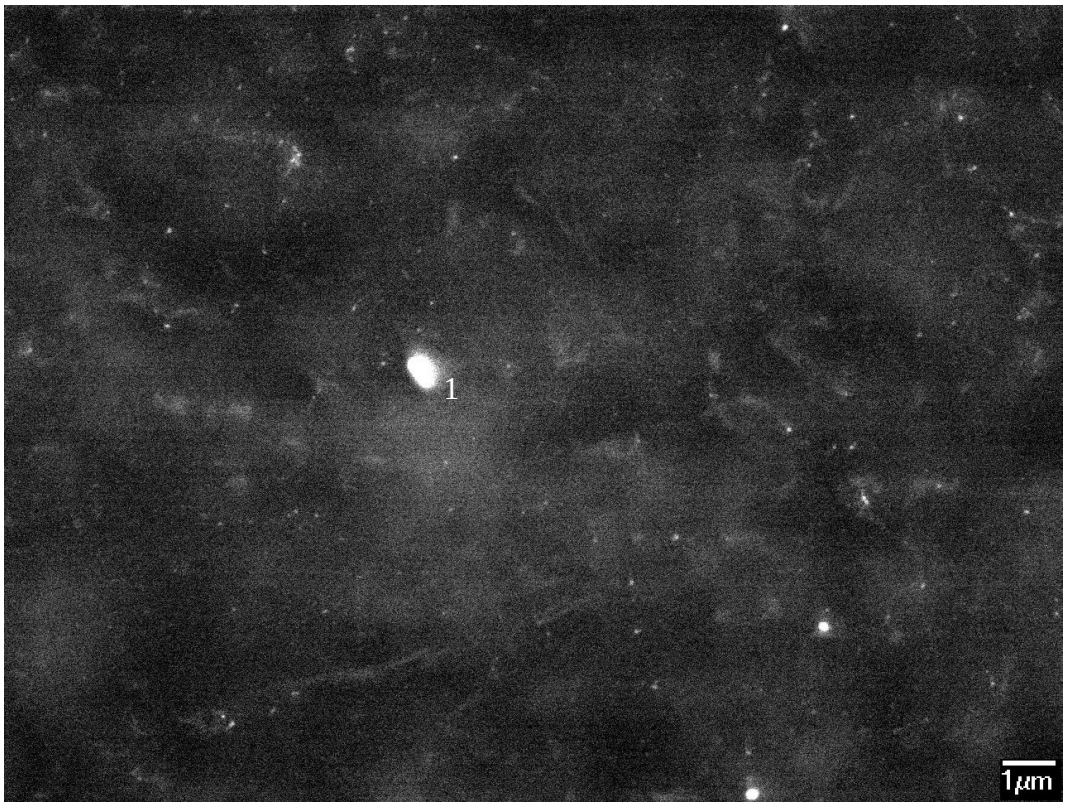

Figure A-24 BSE-SEM image of an inclusion and precipitates from X100-3C steel.

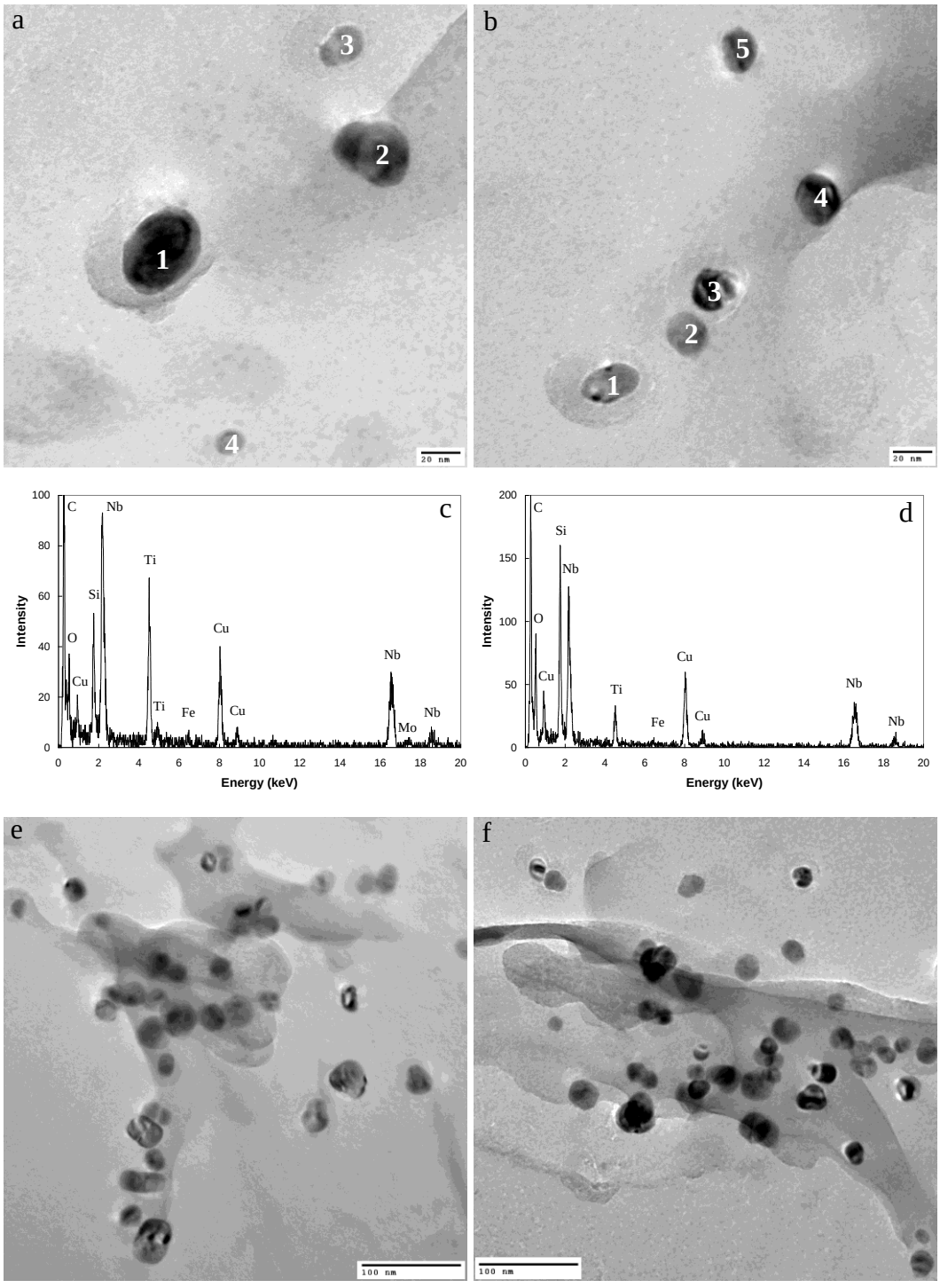

Figure A-25 TEM BF images and EDX specta of precipitates from X100-3C steel extracted by carbon replicas.

Table A-3 Chemistry (metallic elements) and size of precipitates from X100-3C steel extracted by carbon replicas

Image	Position	Chemistry	Size (nm)	Group
a	1	$Nb_{0.62}Ti_{0.38}$	47	Nb-rich
	2	$Nb_{0.61}Ti_{0.36}Mo_{0.03}$	40	
	3	$Nb_{0.64}Ti_{0.36}$	23	
	4	$Nb_{0.58}Ti_{0.42}$	13	Ti/Nb-rich
b	1	$Nb_{0.52}Ti_{0.48}$	30	
	2	$Nb_{0.69}Ti_{0.31}$	20	Nb-rich
	3	$Ti_{0.47}Nb_{0.48}Mo_{0.05}$	22	Ti/Nb-rich
	4	$Nb_{0.73}Ti_{0.27}$	26	Nb-rich
	5	$Nb_{0.59}Ti_{0.37}Mo_{0.04}$	20	
e		$Nb_{0.69}Ti_{0.25}Mo_{0.05}$	20-30	
f		$Nb_{0.68}Ti_{0.32}$	20-30	

Appendix B: Rietveld refinement of XRD pattern

B-1. Introduction

In this Appendix, the profile fitting of XRD pattern by Rietveld refinement for residues from different steels is shown in Figure B-1, Figure B-2, Figure B-3, Figure B-4 and Figure B-5, respectively. They corresponds to the profile fitting of XRD pattern for residues from X80-A4B, X80-B4F, X80-A4F, X100-2B and X100-3C, respectively.

B-2. Rietveld refinement of XRD pattern from different steels

Profile fitting of XRD patterns and phase matching for different steels are shown in the following figures. Figure B-1a shows the overall profile fitting and the differences between the calculated and the observed patterns for the residue from the X80-A4B steel. Similar to X70-564 steel, some Ti-rich precipitates, with chemistry $Ti_{0.74}Nb_{0.26}N$, were observed in X80-A4B steel using TEM. This phase was also not identified in the XRD analysis, probably due to the negligible amount. The calculated diffraction patterns for $Ti_{0.52}Nb_{0.48}C_{0.5}N_{0.5}$, $Nb_{0.9}Ti_{0.1}C_{0.5}N_{0.5}$, NaCl (contamination) and amorphous SiO_2 are shown in Figure B-1b, c, d and e, respectively, as shown by arrows. The tick marks in the bottom of the figures indicate the positions of the above phases. During XRD sample preparation, this sample was contaminated by some NaCl. NaCl contamination was also identified in the XRD patterns for residues from X100-2B and X100-3C steels, shown in Figure B-4 and Figure B-5. In Figure B-4, one peak at high angle, about 73º 2θ, is not identified. It does not fit any of the phases being identified.

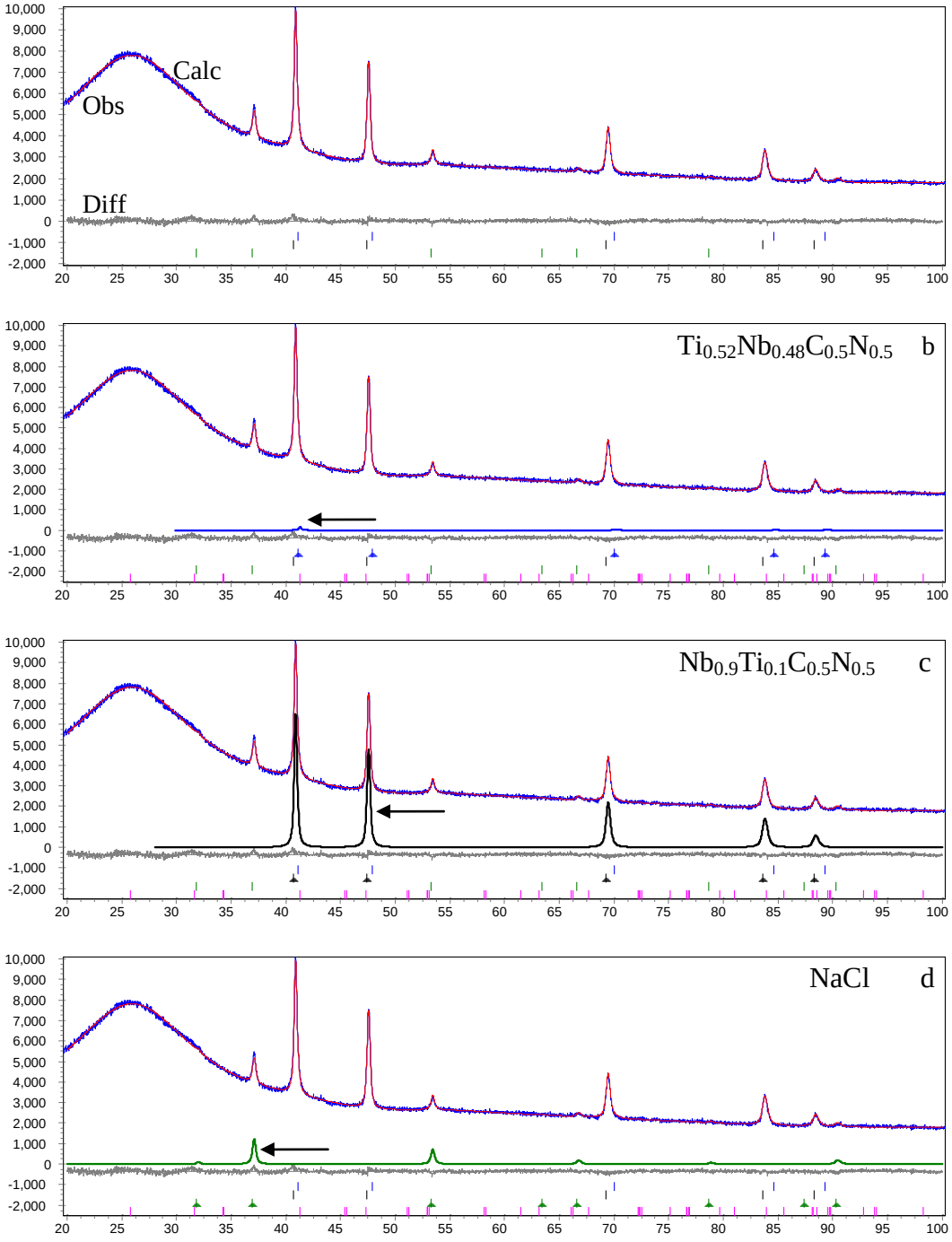
Calc
Obs
Diff
Ti0.52Nb0.48C0.5N0.5 b
Nb0.9Ti0.1C0.5N0.5 c
NaCl d

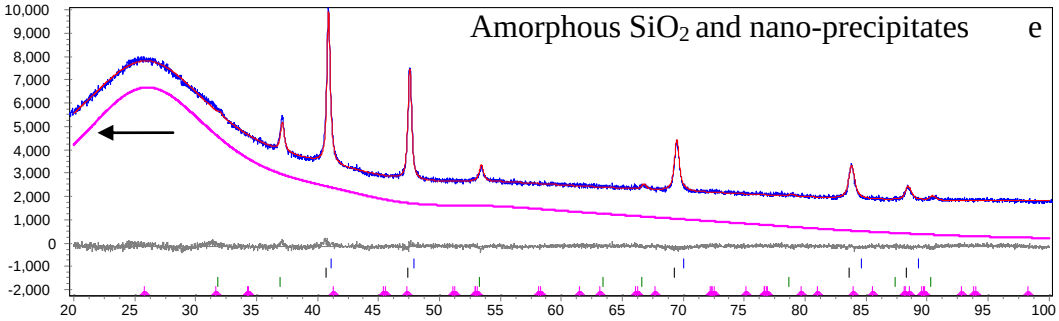

Figure B-1 Profile fitting of XRD pattern by Rietveld refinement for residue extracted from X80-A4B steel by chemical dissolution using HCl.

a) Overall XRD pattern profile fitting;

b) calculated diffraction pattern for $Ti_{0.52}Nb_{0.48}C_{0.5}N_{0.5}$;

c) calculated diffraction pattern for $Nb_{0.9}Ti_{0.1}C_{0.5}N_{0.5}$;

d) calculated diffraction pattern for NaCl (contamination);

e) calculated diffraction pattern for amorphous SiO_2 and nano-precipitates.

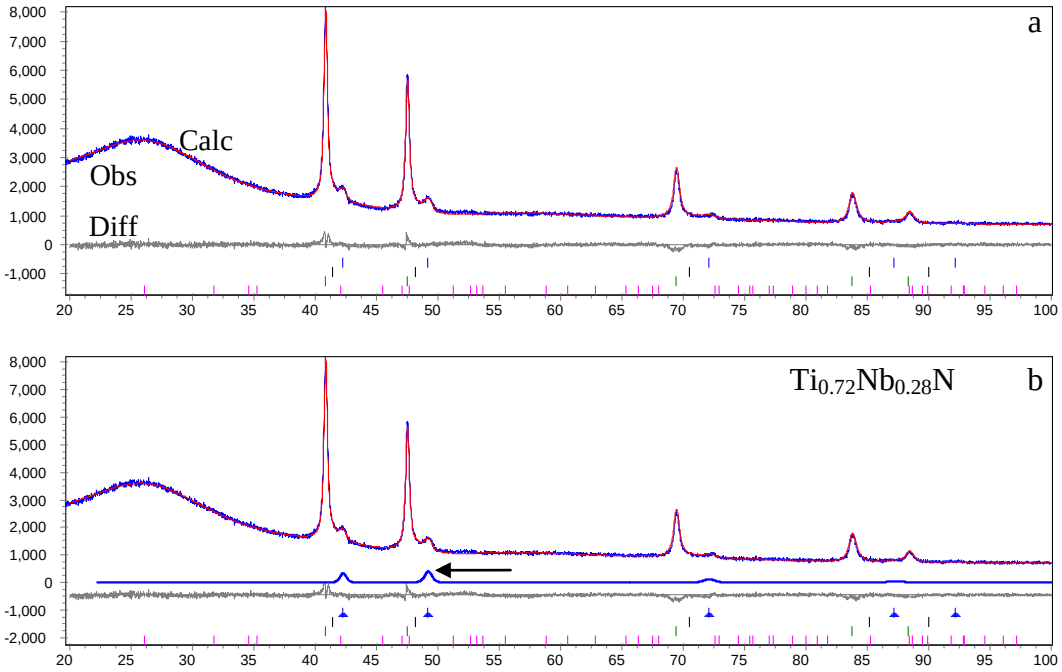

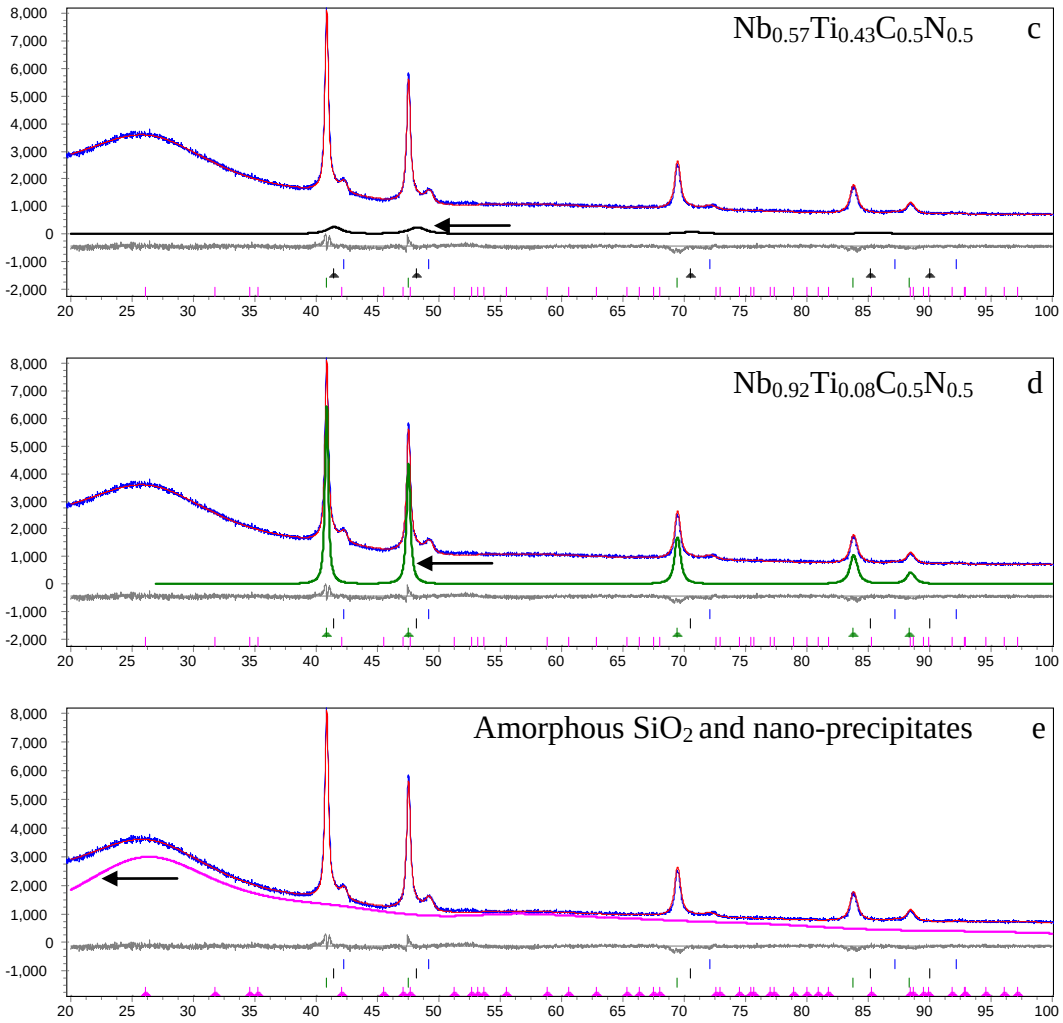

Figure B-2 Profile fitting of XRD pattern by Rietveld refinement for residue extracted from X80-B4F steel by chemical dissolution using HCl.

a) Overall XRD pattern profile fitting;

b) calculated diffraction pattern for $Ti_{0.72}Nb_{0.28}N$;

c) calculated diffraction pattern for $Nb_{0.57}Ti_{0.43}C_{0.5}N_{0.5}$;

d) calculated diffraction pattern for $Nb_{0.92}Ti_{0.08}C_{0.5}N_{0.5}$;

e) calculated diffraction pattern for amorphous SiO_2 and nano-precipitates.

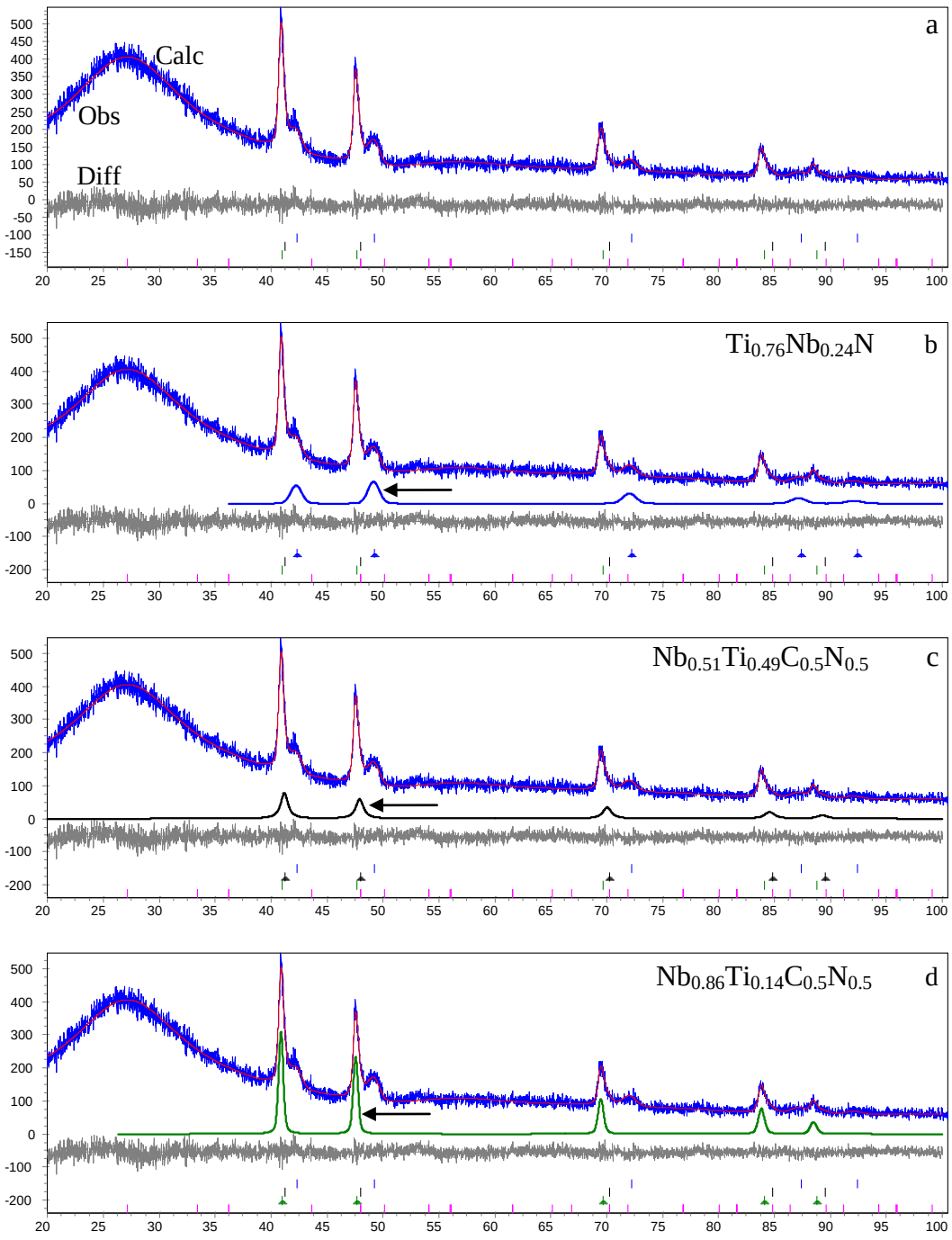
a
Calc
Obs
Diff
b
$Ti_{0.76}Nb_{0.24}N$
c
$Nb_{0.51}Ti_{0.49}C_{0.5}N_{0.5}$
d
$Nb_{0.86}Ti_{0.14}C_{0.5}N_{0.5}$

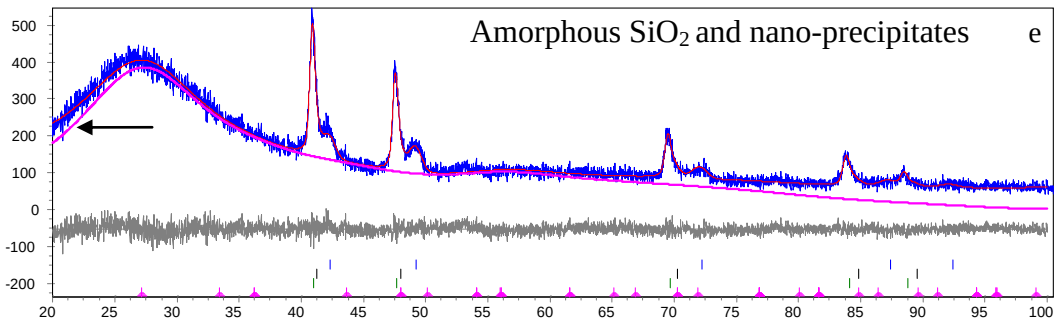

Figure B-3 Profile fitting of XRD pattern by Rietveld refinement for residue extracted from X80-A4F steel by chemical dissolution using HCl.

a) Overall XRD pattern profile fitting;

b) calculated diffraction pattern for $Ti_{0.76}Nb_{0.24}N$;

c) calculated diffraction pattern for $Nb_{0.51}Ti_{0.49}C_{0.5}N_{0.5}$;

d) calculated diffraction pattern for $Nb_{0.86}Ti_{0.14}C_{0.5}N_{0.5}$;

e) calculated diffraction pattern for amorphous SiO_2 and nano-precipitates.

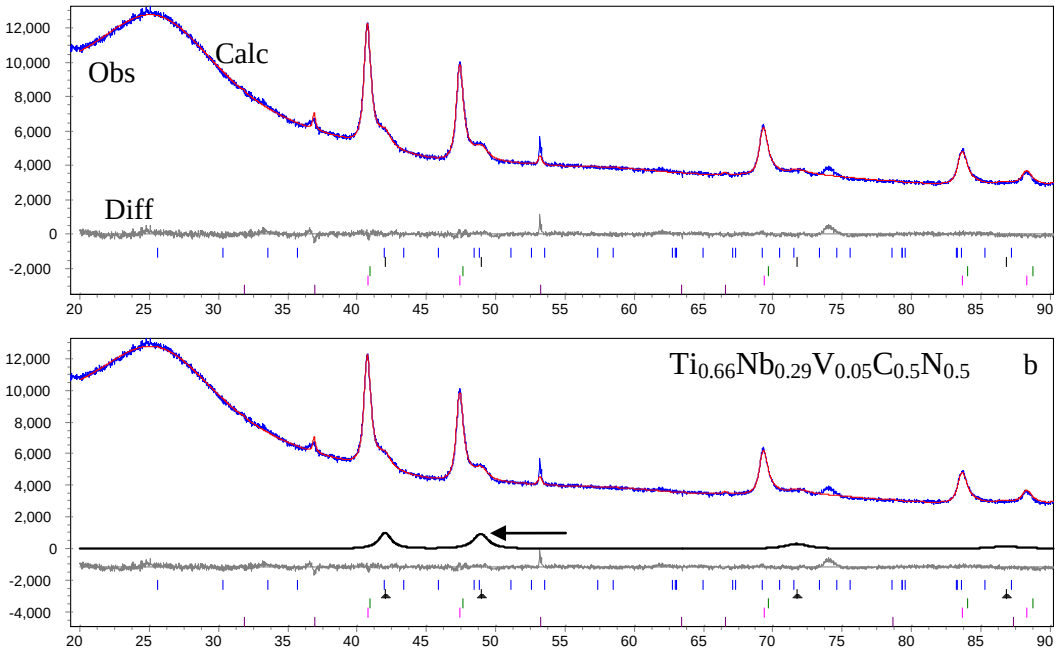

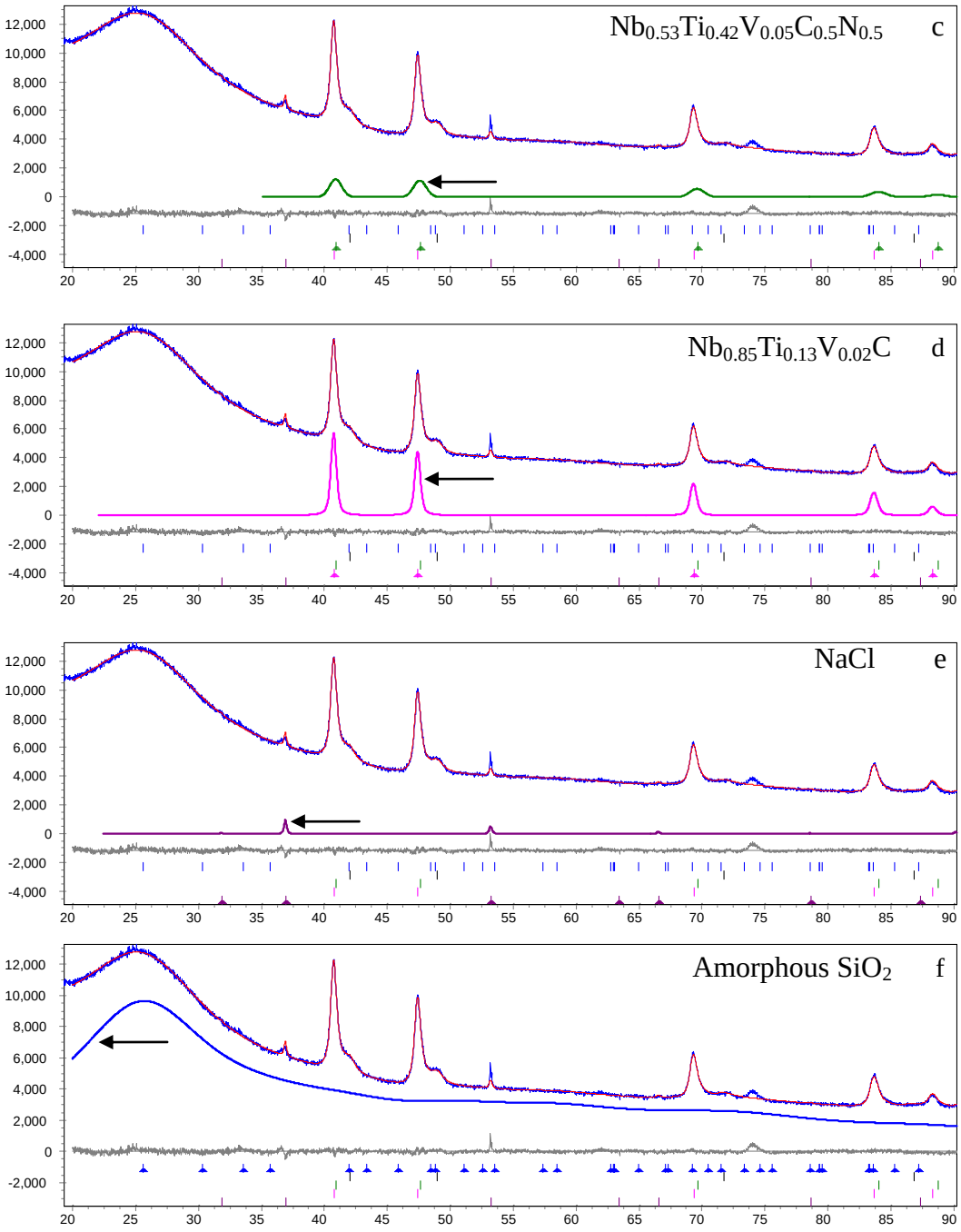

Figure B-4 Profile fitting of XRD pattern by Rietveld refinement for residue extracted from X100-2B steel by chemical dissolution using HCl.

a) Overall XRD pattern profile fitting;

b) calculated diffraction pattern for $Ti_{0.66}Nb_{0.29}V_{0.05}C_{0.5}N_{0.5}$;

c) calculated diffraction pattern for $Nb_{0.53}Ti_{0.42}V_{0.05}C_{0.5}N_{0.5}$;

d) calculated diffraction pattern for $Nb_{0.85}Ti_{0.13}V_{0.02}C$;

e) Calculated diffraction pattern for NaCl (contamination);

f) calculated diffraction pattern for amorphous SiO_2.

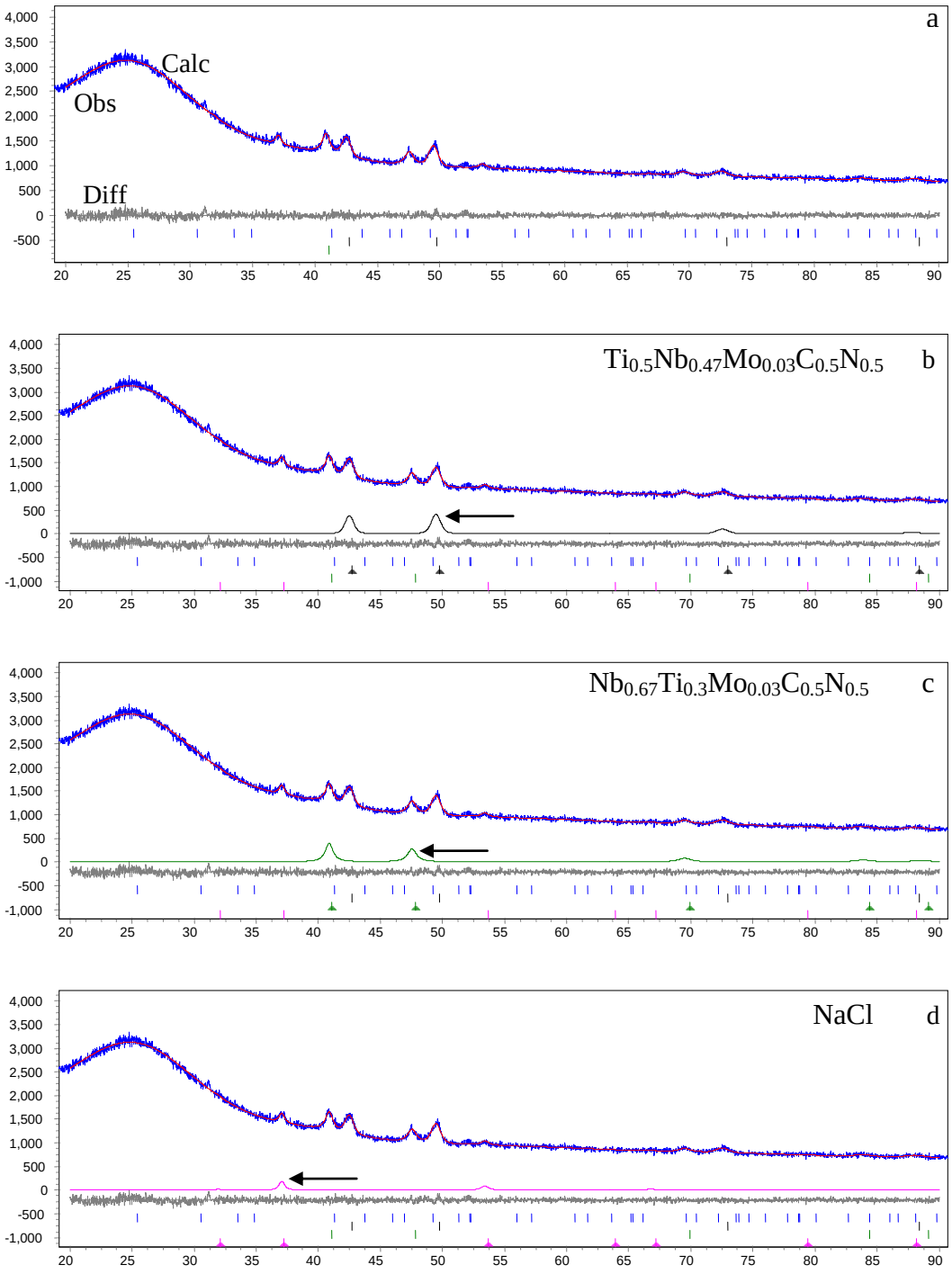

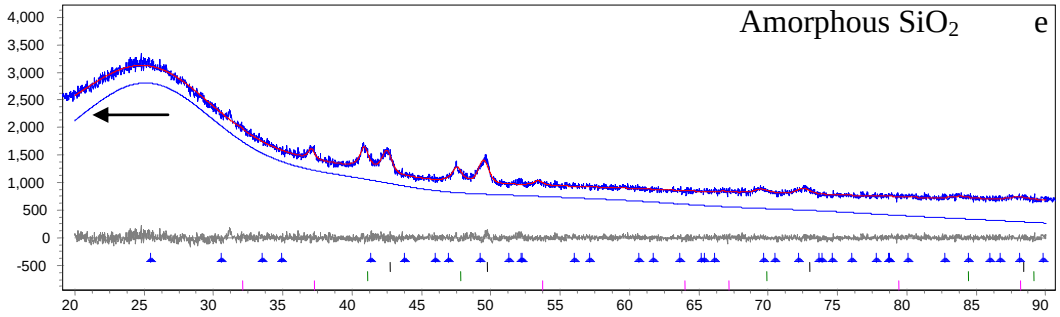

Figure B-5 Profile fitting of XRD pattern by Rietveld refinement for residue extracted from X100-3C steel by chemical dissolution using HCl.

a) Overall XRD pattern profile fitting;

b) calculated diffraction pattern for $Ti_{0.5}Nb_{0.47}Mo_{0.03}C_{0.5}N_{0.5}$;

c) calculated diffraction pattern for $Nb_{0.67}Ti_{0.3}Mo_{0.03}C_{0.5}N_{0.5}$;

d) calculated diffraction pattern for NaCl (contamination);

e) calculated diffraction pattern for amorphous SiO_2.